# Development of Grid-Based Direct Kinetic Method and Hybrid Kinetic-Continuum Modeling of Hall Thruster Discharge Plasmas

by

Kentaro Hara

A dissertation submitted in partial fulfillment
of the requirements for the degree of
Doctor of Philosophy
(Aerospace Engineering)
in The University of Michigan
2015

Doctoral Committee:

Professor Iain D. Boyd, Chair
Professor Alec D. Gallimore
Igor D. Kaganovich, Princeton Plasma Physics Laboratory
Professor Mark J. Kushner

For my family and friends

# ACKNOWLEDGEMENTS

I cannot thank all my mentors, friends, and family enough through my doctoral study at Michigan.

First, I want to acknowledge my advisor, Prof. Iain Boyd, for all the support throughout my doctoral study. I'm grateful for all your support related to research, coursework, raising a child, how to control my motivation, or even the weather differences in Michigan and California. I was always interested in so many things for research and coursework, but you always told me the importance to finalize projects, including journal publications, conferences, and my dissertation.

I also want to thank my committee members. Prof. Mark Kushner taught me how interesting plasma physics is, how to survive in academia, and many other things. It was great to be part of the DOE Plasma Science Center as well as the Michigan Institute for Plasma Science and Engineering (MIPSE) that gave me lots of opportunities to look into many different types of plasmas. I want to thank Prof. Alec Gallimore particularly for the collaboration with Dr. Mike Sekerak. It wouldn't have been such a nice team effort without the support from Michigan/Air Force Center of Excellence for Electric Propulsion (MACEEP). I want to acknowledge Dr. Igor Kaganovich, who taught me how to be critical in pursuing science and provided me several research ideas.

At the University of Michigan, I felt very fortunate to learn CFD, particularly its history, from Prof. Bram Van Leer and Prof. Phil Roe. Other professors I want to thank include Prof. YY Lau, Prof. John Foster, and Prof. Alec Thomas in nuclear engineering as well as Prof. Quentin Stout in computer science for giving me an $A^+$ in the infamous "Parallel Computing" class. Prof. Katsuo Kurabayashi in mechanical engineering helped me writing fellowship applications and gave me many advices. I also want to thank Prof. Joaquim

Martins for being an awesome graduate chair. Special thanks to Denise Phelps in aerospace engineering and Julia Falkovitch-Khain in MIPSE for all your support.

I was also lucky to have so many good collaborations. Dr. Vladimir Kolobov at CFDRC introduced me to kinetic methods and parallel computing. Dr. Richard Berger at LLNL was kind enough to invite a student who knows nothing about ICF plasmas to do a summer internship at LLNL. This was one of the best experiences during my Ph.D. Dr. Jeff Banks has been a great mentor and become one of my role models. Thanks to Cara and Eliana for making our stay at Livermore fun.

Now all my friends. Many thanks go to my officemates in 2211, a.k.a. the best office in FXB, Yuntao Chen, Wai Lee Chan, Brad Maeng, Yee Chee See, and Chang-Kwon Kang. Thanks to all my friends in NGPDL, particularly, Paul Giuliano, Brandon Smith, Maria Choi, Horatiu Dragnea, Abhilasha Anna, and Cyril Galitzine. I already mentioned Mike Sekerak, but I was motivated when we were studying for prelims and doing research together. Thanks to Ann, Aviana, and Max for the awesome dinners. It was fun sharing ideas with Kapil Sawlani and Jerry Wang. Special thanks to my friends from Japan, Motohiro Ohno, Eunkyung Chang, Mitsuhito Hirose, Masahiro Kurata, Takanori Watanabe, and Ryoji Okada. Thanks to Mike Chu, Yayoi, and Lucas for the great photos and friendship.

The reason I came to Michigan was to get my Ph.D in aerospace engineering but it was also because I knew Ann Arbor is a very nice place. The first time I visited Ann Arbor was the spring of 2006 when I was an undergrad at the University of Tokyo. Thanks to John Paul, the head coach of University of Michigan Men's Lacrosse team, for giving me the first opportunity to be part of this fantastic community. I truly feel like Ann Arbor is our second home.

Finally, Mom and Dad, thanks for raising the first Dr. Hara in our family. Thanks to my sister, grandparents, and relatives for making a wonderful family. I cannot appreciate my wife, Sayaka, enough. You decided to take this unusual path with me even in a country where you never lived. Alisa, you make me smile every day. I always feel protected by all of you so that I can take any risk in my life.

# TABLE OF CONTENTS

**DEDICATION** . . . . . ii

**ACKNOWLEDGEMENTS** . . . . . iii

**LIST OF FIGURES** . . . . . ix

**LIST OF TABLES** . . . . . xiv

**LIST OF APPENDICES** . . . . . xv

**LIST OF ABBREVIATIONS** . . . . . xvi

**ABSTRACT** . . . . . xviii

**CHAPTER**

**I. Introduction** . . . . . 1

1.1 Problem Statement . . . . . 1
1.2 Hall Effect Thrusters . . . . . 3
1.2.1 Overview of Electric Propulsion . . . . . 4
1.2.2 Basic Principles . . . . . 5
1.2.3 Challenges . . . . . 6
1.3 Plasmas . . . . . 8
1.4 Research Objectives . . . . . 10
1.5 Thesis Outline . . . . . 13

**II. Numerical Method** . . . . . 15

2.1 First-Principles Governing Equations . . . . . 15
2.2 Particle-based Method . . . . . 17
2.3 Grid-based Kinetic Method . . . . . 18
2.3.1 Comparison with Particle Methods . . . . . 19
2.3.2 Numerical Scheme . . . . . 21
2.3.3 Time Integration . . . . . 24
2.3.4 Parallel Computing Capabilities . . . . . 26
2.4 Continuum Approach . . . . . 27

2.5 Summary . . . 30

**III. Verification of a Grid-Based Direct Kinetic Method** . . . 32

3.1 Implementation of the Vlasov-Poisson solver . . . 32
3.2 Classical Plasma Sheath . . . 36
3.2.1 Theory . . . 37
3.2.2 Boundary Conditions for the Sheath Simulation . . . 39
3.2.3 Numerical Parameters . . . 40
3.2.4 Results obtained from the Vlasov-Poisson solver . . . 41
3.3 Plasma Sheath with Secondary Electron Emission . . . 43
3.3.1 Theory with Secondary Electrons . . . 44
3.3.2 Electron Velocity Distribution Functions . . . 47
3.3.3 Sheath Potential Results . . . 48
3.3.4 Virtual Cathode Analysis . . . 51
3.4 Nonlinear Plasma Waves . . . 54
3.4.1 Landau Damping . . . 55
3.4.2 Electron Plasma Waves . . . 57
3.4.3 Ion Acoustic Waves . . . 61
3.5 Trapped Particle Bunching Instability . . . 64
3.5.1 Numerical Setup and Diagnostic Tools . . . 65
3.5.2 Particle Bunching . . . 66
3.5.3 Comparison with Theory . . . 69
3.6 Summary . . . 72

**IV. One-Dimensional Hybrid Kinetic-Continuum Model of a Hall Thruster Discharge Plasma** . . . 73

4.1 Introduction . . . 73
4.2 SPT-100 Hall Thruster . . . 74
4.3 Hybrid Kinetic-Continuum Simulation . . . 75
4.3.1 Direct Kinetic Method . . . 75
4.3.2 Boundary Conditions and Discretization . . . 76
4.3.3 Simplified Electron Continuum Model . . . 78
4.3.4 Hybrid-PIC Simulation . . . 80
4.3.5 Flowchart . . . 81
4.4 Macroscopic Results . . . 82
4.4.1 Computational Time Comparison . . . 83
4.4.2 Overall Thruster Performance . . . 84
4.4.3 Time-averaged Plasma Properties . . . 85
4.5 Discharge and Plasma Oscillations . . . 89
4.5.1 Ionization Oscillations: $> 10$ kHz . . . 90
4.5.2 Transient-time Oscillations: $> 100$ kHz . . . 91
4.6 Microscopic Results . . . 94
4.6.1 Time-Averaged Ion Energy Distribution Functions . . . 94
4.6.2 Time-Varying Ion Velocity Distribution Functions . . . 96
4.6.3 Instantaneous VDFs . . . 99
4.6.4 Effect of Charge Exchange Collisions . . . 101

4.7 Summary . . . 102

**V. Mode Transition of Discharge Oscillations in Hall Thrusters** . . . 104

5.1 Introduction . . . 104
5.2 Previous Research on Mode Transition . . . 105
5.3 Improved Hybrid-DK Simulation . . . 108
5.4 Mode Transition Results . . . 112
5.4.1 Comparison with Experiments . . . 112
5.4.2 Discharge Current Oscillations . . . 114
5.4.3 Plasma oscillations . . . 116
5.5 Time-averaged Results . . . 120
5.5.1 Excited-state Atoms . . . 120
5.5.2 Ionization Cost . . . 121
5.6 Cause of Mode Transition . . . 123
5.6.1 Electron Transport . . . 124
5.6.2 Electron Energy Contributions . . . 125
5.6.3 Electron Energy Balance . . . 127
5.7 Sensitivity Analysis . . . 128
5.7.1 Emission Rate . . . 129
5.7.2 Anomalous Electron Mobility . . . 130
5.8 Summary . . . 133

**VI. Perturbation Theory of Ionization Oscillations in Hall Thrusters** . 135

6.1 Introduction . . . 135
6.2 Predator-prey model . . . 135
6.2.1 Formulation . . . 136
6.2.2 Time-varying Analysis . . . 137
6.3 Complete Perturbation Theory . . . 139
6.3.1 Heavy Species Transport: Ion and Neutral Atom Continuity Equations . . . 139
6.3.2 Including Ion Momentum and Electron Energy Equations 145
6.4 SPT-100 Results . . . 147
6.4.1 Growth Rate . . . 148
6.4.2 Real Frequency . . . 149
6.5 Discussion . . . 150
6.5.1 Cause of Discharge Oscillations . . . 151
6.5.2 Electron Energy Relaxation Frequency . . . 152
6.5.3 Comparison with Experiments . . . 153
6.5.4 Nonlinear Saturation of Ionization Oscillations . . . 156
6.6 Time-Varying Analysis . . . 157
6.6.1 Damping due to Heavy Species Transport . . . 157
6.6.2 Excitation of Ionization Oscillations . . . 158
6.7 Summary . . . 160

**VII. Two-Dimensional Hybrid Modeling of Plasma Transport in Hall Thrusters** . . . 162

7.1 Introduction . . . 162
7.2 Azimuthal Oscillations . . . 163
7.2.1 High-Frequency Rotating Spokes . . . 163
7.2.2 Low-Frequency Rotating Spokes . . . 164
7.2.3 Hypotheses for Low-Frequency Spokes . . . 166
7.3 2D Kinetic Model . . . 168
7.3.1 2D Axial-Azimuthal Kinetic Simulation . . . 168
7.3.2 Discretized 2D DK Model . . . 169
7.3.3 2D Ion Simulation with a Static Electric Field . . . 171
7.4 2D Electron Continuum Model . . . 177
7.4.1 Electron Momentum . . . 178
7.4.2 Reviewing the One-Dimensional Case . . . 180
7.4.3 2D Charge Conservation Equation . . . 183
7.4.4 Electron Energy . . . 185
7.4.5 Summary of 2D Electron Continuum Model . . . 187
7.5 Test Cases . . . 188
7.6 Mode Transition Results . . . 189
7.6.1 1D Hybrid-DK Simulation . . . 189
7.6.2 Results Including Ion Magnetization . . . 190
7.6.3 Results Without Ion Magnetization . . . 191
7.7 Plasma Oscillations . . . 192
7.7.1 Global Oscillation Mode . . . 192
7.7.2 Local Oscillation Mode . . . 196
7.8 Discussion . . . 200

**VIII. Summary** . . . 202

8.1 Conclusions . . . 202
8.1.1 Part I: Development of a Grid-based DK Solver . . . 202
8.1.2 Part II: Hybrid-DK Simulations of Ionization Oscillations in Hall Thrusters . . . 203
8.2 Contributions . . . 205
8.3 Future Work . . . 205
8.3.1 Improving the Kinetic Method . . . 205
8.3.2 Plasma Sheath and Presheath Simulations . . . 206
8.3.3 Chemistry Models of Hall Thruster Discharge Plasma . . . 206
8.3.4 Hall Thruster Performance Study . . . 207
8.3.5 Ionization Oscillation Theory . . . 207
8.3.6 2D Axial-Azimuthal or Radial-Azimuthal Simulation . . . 208
8.3.7 2D Radial-Axial Hybrid-DK Simulation . . . 208
8.3.8 Multidimensional Time-Varying MHD solver . . . 209

**APPENDICES** . . . 210

**BIBLIOGRAPHY** . . . 239

# LIST OF FIGURES

**Figure**


| | | |
|---|---|---|
| 1.1 | H6 thruster. Reproduced from Refs. 1 and 2. | 6 |
| 1.2 | Schematic of HET operation. | 7 |
| 1.3 | Summary of various plasmas for a wide range of density and temperature. | 11 |
| 2.1 | Stencil of a finite volume scheme. Arrows describe the fluxes at the cell interfaces. | 23 |
| 2.2 | Sweby diagram: The Arora-Roe limiters in this figure are for CFL number $\|c\| = 0.2$. | 25 |
| 2.3 | Computational methods for rarefied flows or plasmas. | 31 |
| 3.1 | Example of the phase space partitioning in the DK/Vlasov solver when using 16 processors in total. | 35 |
| 3.2 | Implementation of the Vlasov-Poisson solver. | 36 |
| 3.3 | Steady-state potential obtained from the Vlasov-Poisson solver. | 41 |
| 3.4 | Ion velocity distribution functions obtained from the Vlasov-Poisson solver in comparison to the theoretical predictions using the potential field in Fig. 3.3. | 42 |
| 3.5 | Electron velocity distribution functions obtained from the Vlasov-Poisson solver in comparison to the theoretical predictions using the potential field in Fig. 3.3. | 43 |
| 3.6 | Electron velocity distribution functions for $\tau = T_e/T_w = 10$. Black and red solid lines illustrate primary and secondary electrons, respectively. | 48 |
| 3.7 | Space charge limited sheath potential versus $\tau = T_e/T_w$ | 50 |
| 3.8 | Sheath potential versus SEE rate for $\tau = 10$ and $\tau = 200$. | 51 |
| 3.9 | Secondary electron velocity distribution functions and potential profile of a virtual cathode near the wall for large $\sigma > \sigma_{SCL}$. This case is for $\tau = 10$ and $\sigma = 1.05$. Dashed line represents the virtual cathode position. | 52 |
| 3.10 | The balance between the ion, primary electron, and secondary electron fluxes in a space charge limited sheath. | 53 |
| 3.11 | Bernstein-Greene-Kruskal (BGK) solution in the wave frame for a given sinusoidal potential. Black line is the separatrix. | 54 |
| 3.12 | Nonlinear Landau damping: PIC vs Vlasov, denoted as DK in the figure, with different number of particles (PIC) and different grid size in velocity space (Vlasov) while the grid size in physical space is kept constant. | 56 |
| 3.13 | Driven EPW for $k_0\lambda_D = 1/3$ | 60 |
| 3.14 | Initially perturbed EPWs for $k_0\lambda_D = 1/3$ | 61 |

3.15 Close-up view of electron VDFs for a sudden case. Here, $k_0\lambda_D = 0.425$ and $\delta n/n_0 = 0.05$. The physical position is normalized by $L = 2\pi/k_0$. . . . . 62
3.16 Driven IAWs for $T_e/T_i = 10$ and $k_0\lambda_D = 0.3$. . . . . 63
3.17 Close-up view of ion VDFs for a driven IAW at $\omega_p t = 4.5\times10^4$ for $ZT_e/T_i = 10$ and $k_0\lambda_D = 0.3$. The physical position is normalized by $L = 2\pi/k_0$. . 64
3.18 Particle bunching for initial conditions $W_0/(e\phi_0) = -0.4$, $e\phi_0/T_e = 0.04$, $v_L = 3.6v_{th}$, and $k_L\lambda_D = 1/3$. Shown are the distribution functions in phase space (a1)-(a6) and those transformed in energy-angle coordinates (b1) - (b6). . . . . 68
3.19 Evolution of trapped particle quantities. (a) Total kinetic energy of trapped particles $E_{K,trap}$ and (b) the bunching amplitude $B = (X_{ave}^2 + V_{ave}^2)^{1/2}$ in logarithmic scale, where $X_{ave}$ and $V_{ave}$ are average normalized position and velocity of the trapped particles. . . . . 70
3.20 Comparison of trapped particle bunching instability between theory and Vlasov simulations for different potential amplitudes. Here, $v_L = 3.6v_{th}$ and $k_L\lambda_D = 1/3$. . . . . 71
4.1 Flowchart of the hybrid model for HET discharge plasmas. . . . . 82
4.2 Time averaged results of macroscopic parameters vs. axial position. Dashed lines: HDK-DK, Solid lines: HV-Cont, Triangles: HPIC . . . . . 86
4.3 Logarithmic plot of electron mobility and ion number density vs. axial position in the acceleration region. Dashed lines: HDK-DK, Solid lines: HDK-Cont. . . . . 87
4.4 Mean velocity of neutral atoms vs. axial position. Dashed line: HDK-DK, Solid line: HDK-Cont. . . . . 88
4.5 Discharge current oscillations of a SPT-100 thruster (a: HDK-DK; b: HDK-Cont; c: HPIC). . . . . 89
4.6 Contour map of the number densities of the heavy species obtained from the HDK-DK case (a: neutral atoms, b: ions). These results correspond to Fig. 4.5(a). The units of the number densities are $m^{-3}$. . . . . 90
4.7 High frequency oscillations of the discharge current (a: Hybrid-PIC, b: HDK-DK). The time range is 20 $\mu s$. . . . . 92
4.8 High frequency data of ion number density in the ionization and acceleration regions, corresponding to Fig. 4.7 (a: Hybrid-PIC, b: HDK-DK) The units are in $m^{-3}$. The instantaneous number densities are sampled every 0.5 $\mu s$ (500 time steps). . . . . 93
4.9 Time-averaged ion EDFs at the channel exit. . . . . 95
4.10 HDK-DK: Time-varying results of ion VDFs as well as the discharge current. 97
4.11 HPIC: Time-varying results of ion VDFs as well as the discharge current.. Note that the neutral atom speed is slightly higher than the other results, $u_n = 300$ m/s. . . . . 98
4.12 Instantaneous VDFs of ions at the channel exit obtained from the hybrid-PIC and HDK-DK simulations. Zero values are not shown since it is a logarithmic plot. . . . . 99
4.13 Velocity distribution function of neutrals at the channel exit . . . . . 102
5.1 Discharge current as a function of magnetic field with constant discharge voltage. The operation modes are categorized into six different regimes. Reproduced from Fig. 5 of Ref. 3. . . . . 105

5.2 Discharge current oscillations reported by Gascon *et al.*. The discharge voltage is 300 V and the anode mass flow rate is 5 mg/s. Top left: borosil, bottom left: alumina, top right: silicon carbide, and bottom right: graphite. Reproduced from Fig. 2 of Ref. 4. . . . . 107
5.3 Discharge current oscillations reported by Barral *et al.* using a 1D continuum simulation. Reproduced from Fig. 10(b) of Ref. 5. . . . . 108
5.4 Discharge current vs. magnetic field: Red symbol plots are the mean discharge current and error bars show the standard deviation. (a) Experimental results of the H6; (b) Experimental data of the SPT-100. Reproduced from Ref. 6; (c) Hybrid-DK simulation results of the SPT-100. . . . . 113
5.5 Discharge current oscillation: (a) $B_r/B_r^* = 0.52$ (H6), (b) $B_r/B_r^* = 0.61$ (H6), (c) B=120 G (Hybrid-DK), (d) B=180 G (Hybrid-DK). . . . . 114
5.6 Breathing mode frequency: (a) H6 experiment,[7] (b) SPT-100 simulation. 115
5.7 Two oscillation cycles (0.1 ms) of the global oscillation mode at B = 120 G. Dashed horizontal lines correspond to the maximum discharge current in Fig. 5.5(c). (From top to bottom) Ground-state atom density, excited-state atom density, ion density, electron axial velocity, and electron total energy. . . . . 117
5.8 The local oscillation mode at B = 180 G. (From top to bottom) Ground-state atom density, excited-state atom density, ion density, electron axial velocity, electron total energy. Note that the range of electron total energy is different from Fig. 5.7(e). . . . . 119
5.9 Discharge current oscillation and the integrated excited-state atom density: (a) B=120 G, (b) B=180 G. . . . . 121
5.10 Correlation between light intensity and total discharge current. The light intensity: $L = n_{Xe^*}/10^{16}$. . . . . 122
5.11 Time-averaged ionization cost. . . . . 123
5.12 Time-averaged axial electron velocity from Figs. 5.7(d) and 5.8(d). . . . 125
5.13 Time-averaged electron energy transfer. Each term in Eq. (5.6) is divided by the electron axial current. (a) B=120 G; (b) B=180 G. . . . . 126
5.14 Time-averaged kinetic energy and thermal energy components in two modes. (a) B=120 G; (b) B=180 G. Vertical axis is shown in terms of effective electron temperature: $T_{e,eff} = \frac{2}{3}\varepsilon$. Horizontal dotted line is the critical electron temperature that forms a SCL sheath. . . . . 127
5.15 Discharge current oscillation with various spontaneous emission frequencies. 129
5.16 Mode transition: $\nu_{ea,in} = \omega_B/64$ and $\nu_{ea,out} = \omega_B/16$ . . . . . 131
5.17 Mode transition: $\nu_{ea,in} = \omega_B/160$ and $\nu_{ea,out} = \omega_B/16$ . . . . . 131
5.18 Global energy balance for $\nu_{ea,in} = \omega_B/160$ and $\nu_{ea,out} = \omega_B/16$ . . . . . 132
5.19 Mode transition: $\nu_{ea,in} = \omega_B/160$ and $\nu_{ea,out} = \omega_B/64$ . . . . . 133
6.1 Lotka-Volterra model: Initial ion density is $1.5N_{i0}$. . . . . 138
6.2 Lotka-Volterra model: Initial ion density is $5N_{i0}$. . . . . 138
6.3 Schematic of the Hall thruster discharge region. . . . . 140
6.4 Minimum $T_e$ required to sustain a plasma. $N_{i,0} > 0$ from Eq. (6.11). The geometric parameters of a SPT-100 thruster are considered: $L_{ch} = 2.5$ cm, $R_\Delta = 2$ cm. . . . . 142

6.5 Ratio of ionization length and channel length for various $V_D$ and $T_e$ obtained from Eq. (6.9). Same geometric parameters as Fig. 6.4 is used. $N_{int} = 1.6 \times 10^{19}$ m$^{-3}$ is considered for $T_{e,min}$ in solid line. Dashed line illustrates $T_{e,min}$ for $N_{int} = 1 \times 10^{19}$ m$^{-3}$. . . . . 144
6.6 Growth rate in units of rad/s for various ($T_{e,0}$, $U_e$). The region where $\gamma < 0$ is not shown since the ionization oscillation is damped. $V_D = 300$ V and $N_{int} = 1.6 \times 10^{19}$ m$^{-3}$. The two stability regimes are labeled as I and II. 149
6.7 Real frequency in units of rad/s for various ($T_{e,0}$, $U_e$). Same condition as Fig. 6.6. . . . . 150
6.8 Electron energy relaxation frequency $\Lambda$ in units of s$^{-1}$ for various ($T_{e,0}$, $U_e$). White region corresponds to $\Lambda > 1.5 \times 10^7$ s$^{-1}$. Same condition as Figs. 6.6 and 6.7. Red line indicates $\gamma = 0$ as shown in Figs. 6.6 and 6.7. . . . 151
6.9 Measurements of discharge current oscillation amplitudes in the H6 thruster. Reproduced from Figs. 4.2 and 4.3 of Ref. 7: . . . . . 154
6.10 Perturbation theory results for different conditions. Note that the electron temperature range (horizontal axis) is different. . . . . 155
6.11 Heavy species transport model with constant ionization rate. Similar condition as Fig. 6.2: Initial ion density is 5 $N_{i0}$, but $N_{int} = 2 \times 10^{19}$ m$^{-3}$ is also used. . . . . 158
6.12 Heavy species transport model with perturbation of ionization rate: 0.1 %. 159
6.13 Heavy species transport model with perturbation of ionization rate: 1 %. 160
6.14 Heavy species transport model with perturbation of ionization rate: 5 %. 160
7.1 Low-frequency azimuthally rotating spokes. Shown is the normalized spoke surface processed from the light intensity obtained from images from a FastCam video. Reproduced from Fig. 5.2 of Ref. 7. . . . . 165
7.2 Possible mechanism of the rotating spokes. Diagram of $z - \theta$ plasma of discharge channel shown exaggerated ionization front. Reproduced from Fig. 5.19 of Ref. 7. . . . . 167
7.3 The 2D setup. (a) Cylindrical Coordinates in an annulus, representing a Hall thruster discharge channel. The dashed line in (a) is the plane of interest, expanded into 2D in (b). . . . . 169
7.4 Static electric field case using the DK simulation. . . . . 174
7.5 Ion mean velocity in the $y$ direction for the static electric field case using the DK simulation. Note that the azimuthal velocities are negative because the direction of the magnetic field lines is pointing inwards. . . . . 175
7.6 The steady-state ion VDFs at the inlet, $x = 0$ m, and the domain exit, $x = 0.035$ m. The color bars are in logarithmic scales. Note that the range of the color bar is different in (a) from the other two. . . . . 176
7.7 Example of a 1D axial case. (Top) Prescribed magnetic field and assumed ion density. $B_{max} = 0.018$ T and $n_{i,max} = 10^{18}$ m$^{-3}$ are assumed. (Bottom) Eigenvalues estimated using the MATLAB EIG function assuming Dirichlet Boundary conditions for potential. The Condition number is 13,240. . . . 182
7.8 Discharge oscillations obtained from the 1D hybrid-DK simulation. Note that y-axis is from $I_d = 0 - 20$ A. . . . . 190
7.9 Discharge oscillations obtained from the 2D hybrid-DK simulation with Lorentz force. Note that y-axis is from $I_d = 0 - 40$ A. . . . . 190
7.10 Discharge oscillations obtained from the 2D hybrid-DK simulation without Lorentz force. Note that y-axis is from $I_d = 0 - 40$ A. . . . . 191

7.11 Ion number density in global oscillation mode: $B = 120$ G. The units are in $m^{-3}$. . . . . 193
7.12 Ground-state neutral atom density in global oscillation mode: $B = 120$ G. The units are in $m^{-3}$. . . . . 193
7.13 Examples of ion VDFs at $y = L_y/2$ in global oscillation mode and $B = 120$ G. . . . . 194
7.14 Azimuthal electric field in global oscillation mode: $B = 120$ G. The units are in V/m. . . . . 195
7.15 Axially-integrated ion number density for each azimuthal location at four different time steps. Note that $\Delta T = 0.5(t_{id,max} - t_{id,min})$ is half of the time difference between $t_{id,max}$ and $t_{id,min}$. . . . . 196
7.16 Ion number density in local oscillation mode: $B = 180$ G. The unit is $m^{-3}$. 197
7.17 Surface plot of the axially-integrated ion number density. . . . . 198
7.18 Normalized surface plot of local mode obtained from the 2D hybrid-DK simulation. A line is manually drawn that indicates an azimuthal structure. 199
D.1 Collisionless neutral atom simulation. . . . . 225
D.2 The VDFs as a function of Y-velocity averaged over X-velocity obtained from the collisionless DK simulation at $(X, Y) = (0.001, 0.04)$, $(0.039, 0.04)$, and $(0.08, 0.04)$ m. Theory curve is a Maxwellian. . . . . 226
D.3 The VDFs as a function of X-velocity averaged over Y-velocity obtained from the collisionless DK simulation at $(X, Y) = (0.001, 0.04)$, $(0.039, 0.04)$, and $(0.08, 0.04)$ m. Theory curve is a Maxwellian biased with the X-velocity. 227

# LIST OF TABLES

**Table**


| | | |
|---|---|---|
| 2.1 | Comparison of grid-based and particle-based kinetic simulations | 20 |
| 2.2 | Comparison of kinetic models and continuum approach | 27 |
| 4.1 | SPT-100 configuration | 74 |
| 4.2 | Thruster performance | 84 |
| 5.1 | Collisions: $Xe$, $Xe^*$, and $Xe^+$ are the ground-state atom, excited-state atom, and ion. | 109 |
| 7.1 | Discretization of 2D DK simulation | 171 |
| 7.2 | Test cases performed using the 2D hybrid-DK simulation | 188 |
| 7.3 | Results of the 2D hybrid-DK simulation | 200 |

# LIST OF APPENDICES

**Appendix**


A. Derivation of Conservation Equations from the Boltzmann Equation . . . . 211

B. Reduction of Kinetic Description to Hobbs and Wesson's Theory for Secondary Electrons . . . . . 217

C. Derivation of Trapped Particle Theory . . . . . 219

D. 2D Collisionless Kinetic Simulation Compared to DSMC . . . . . 223

E. Axial-Azimuthal Electron Continuum Model . . . . . 228

F. Validity of the Quasineutral Assumption . . . . . 235

# LIST OF ABBREVIATIONS

**BBGKY** Bogoliubov-Born-Green-Krikwood-Yvon

**BGK** Bhatnagar- Gross-Krook

**BGK** Bernstein-Greene-Kruskal

**BHT** Busek Hall Thruster

**CEX** Charge Exchange

**CFD** Computational Fluid Dynamics

**CFL** Courant-Freidrich-Lewy

**DK** Direct Kinetic

**DSMC** Direct Simulation Monte Carlo

**EDF** Energy Distribution Function

**EP** Electric Propulsion

**EPW** Electron Plasma Wave

**FFT** Fast Fourier Transform

**FWHM** Full Width at Half Maximum

**GMRES** Generalized Minimum Residual

**HET** Hall Effect Thruster

**IAW** Ion Acoustic Wave

**ICF** Inertial Confinement Fusion

**LIF** Laser Induced Fluorescence

**LLNL** Lawrence Livermore National Laboratory

**MCF** Magnetic Confinement Fusion

**MHD** Magnetohydrodynamic

**MPD** Magneto-Plasma-Dynamic

**MPI** Message Passing Interface

**MUSCL** Monotonic Upwind Scheme for Conservation Laws

**NASA** National Aeronautics and Space Administration

**NMI** Negative Mass Instability

**ODE** Ordinary Differential Equation

**PDE** Partial Differential Equation

**PEPL** Plasmadynamics and Electric Propulsion Laboratory

**PIC** Particle-In-Cell

**SCL** Space Charge Limited

**SEE** Secondary Electron Emission

**SPT** Stationary Plasma Thruster

**TAL** Thruster with Anode Layer

**TVD** Total Variation Diminishing

**VDF** Velocity Distribution Function

# ABSTRACT

Development of Grid-Based Direct Kinetic Method and Hybrid Kinetic-Continuum Modeling of Hall Thruster Discharge Plasmas

by

Kentaro Hara

Chair: Iain D. Boyd

Novel computational methods were developed and used to characterize plasma flows and improve the efficiency of electric propulsion devices. The focus of this doctoral research is on developing a grid-based direct kinetic (DK) simulation method that is an alternative to particle-based kinetic methods. The first part of this dissertation describes development of the grid-based direct kinetic method through verification and benchmarking. The test cases include a plasma-sheath with and without secondary electron emission from a plasma-immersed material as well as trapped particle bunching instability in nonlinear plasma waves. Using a hybrid kinetic-continuum method for the discharge plasma in a Hall effect thruster, the grid-based DK simulation and a standard particle-in-cell (PIC) method are compared. It was found that ionization events and hence ionization oscillations are captured without any statistical noise in the DK simulation in comparison to a particle simulation. In the second part, mode transition of the discharge oscillations in Hall effect thrusters, which are known to affect thruster performance, is investigated using the hybrid-DK method, in which the DK method is used for ions and a continuum method is used for electrons. The numerical simulations show good agreement with experimental data. In addition, a linear perturbation theory of ionization oscillations is derived. It is found that electron transport

and temperature play an important role in such discharge oscillations whereas the common understanding in the community was that the heavy species are the main contributors. In addition, a two-dimensional simulation is developed to investigate the multidimensional ionization oscillation phenomena in the Hall effect thrusters. The effect of ion magnetization due to the magnetic field is included, showing a swirling effect of accelerated ions. Local ionization oscillations in the azimuthal direction are observed.

# CHAPTER I

# Introduction

In this chapter, the motivation and contributions of the dissertation are summarized and the organization of the remaining chapters is introduced.

## 1.1 Problem Statement

Computer simulations of complex gas and plasma flows have become increasingly popular as computational resources exponentially increases.[1] Predictive modeling is required for practical engineering systems to investigate regions where it is difficult to carry out experimental measurements, to reduce the cost of testing new concepts and designs, and to gain deeper understanding of the detailed physical processes of nonlinear, dynamic, nonequilibrium flows. However, controlling and modeling plasma flows still present a significant challenge due to the broad physical processes and the associated temporal and spatial scales.

One of the most important physical mechanisms in gas and plasma flows is collisions. If there are a significant number of elastic collision events without any inelastic collisions, then the velocity distribution function (VDF) and/or energy distribution function (EDF) of gas particles relaxes to a Maxwell-Boltzmann distribution, or often called a Maxwellian distribution. The collisionality of the gas and plasma flows is characterized by the collision frequency or mean free path. Whether the flow is collisional or collisionless is determined

[1] Moore's Law: The number of transistors in an integrated circuit (IC) chip doubles every two years. For instance, the computational speed becomes 32 times faster over a 10-year period and 1024 times faster over a 20-year period.

by the Knudsen number:

$$Kn = \frac{\lambda_{MFP}}{L}, \tag{1.1}$$

where $\lambda_{MFP} \sim v_{th}/\nu$ is the mean free path, $v_{th}$ is the thermal speed, $\nu$ is the collision frequency, and $L$ is the characteristic length of the system of interest. Once the inelastic collisions are activated, the VDFs and EDFs can be non-Maxwellian particularly for electrons.

The flow is collisional when the Knudsen number is much smaller than unity. Conservation equations of mass, momentum, and energy can be used for computational fluid dynamics (CFD). On the other hand, when the Knudsen number is sufficiently large, the VDFs and EDFs become a non-Maxwellian distribution. In other words, the flow is in a nonequilibrium state. Note that the word *equilibrium* refers to near-Maxwellian and *nonequilibrium* is non-Maxwellian in the dissertation. Strictly speaking, there can be non-Maxwellian distribution functions in a *thermally* equilibrium state.

The extreme case where $Kn \to \infty$ is often called the free-molecular flow. In this regime, the particles will not experience any collisions at all, which can, for example, occur in high temperature plasmas as $\lambda_{MFP} \gg L$. The most difficult regime to model is the transitional flow ($0.01 < Kn < 1$) when the gas or plasma experiences some amount of collisions but not enough to achieve an equilibrium state. For transitional and free-molecular flows, kinetic methods that can resolve particle information are required to capture the nonequilibrium effect.

The primary application considered in this dissertation is a Hall effect thruster (HET), a type of electric propulsion (EP) device, used for space missions. This device utilizes ionized gas, or a plasma, to obtain thrust. As will be described in Sec. 1.2, the discharge plasma is known to be in a nonequilibrium state. For instance, ions are accelerated out of the thruster and generated via ionization simultaneously without any structures, *i.e.* grids, that separate the two physical processes. In order to capture such nonequilibrium phenomena, particle-based kinetic methods have been mainly used in the state-of-the-art computational simulations. These simulation methods have been successful in predicting thruster performance, often time-independent or time-averaged data, which is the main in-

terest in the field from an engineering perspective. However, as advancement in HETs has been made, the key challenge of the HET physics has become more and more in understanding time-varying (*dynamic*)[2], nonequilibrium (*kinetic*)[3], and temporally and spatially small-scale plasma phenomena. The statistical noise due to the use of macroparticles in particle simulations may become problematic, making them unable to model all these complex phenomena.

Although particle methods have been widely used, it has been known that directly solving the kinetic equations is a more deterministic kinetic approach, which is called the grid-based direct kinetic method in this dissertation. Such grid-based kinetic methods have already been developed and used due to their significantly low noise level in other fields, such as applied mathematics and high temperature plasma physics. While particle methods are easy to implement, grid-based kinetic methods require more advanced knowledge in numerical algebra, particularly of hyperbolic partial differential equations (PDEs).[4] Such hyperbolic PDEs have been mainly studied and computational methods have been developed by the aerospace community, in which a high-fidelity CFD model has been required for analyzing high speed flows and designing aircraft. In this dissertation, a grid-based kinetic method, aimed to be used for an EP device, is developed based on advanced computational algorithms developed in the CFD community.

## 1.2 Hall Effect Thrusters

In Hall effect thrusters (HETs), ions are accelerated to generate thrust. There are some magnetized effects on ion motion, including the swirl torque,[8] but HETs are designed such that ions accelerate out of the channel before a complete ion gyration occurs. On the other hand, electrons are fully magnetized so that electron transport, *i.e.* mobility and diffusion, is suppressed due to the magnetic fields.

[2]Dynamic (time-varying) vs. static (time-independent)

[3]Kinetic (nonequilibrium) vs continuum (equilibrium)

[4]Partially differential equations (PDEs) can be categorized into hyperbolic, parabolic, and elliptic equations. (1) Hyperbolic: wave equations that describes the advection of a wave. $u_{tt} - u_{xx} = 0$, where subscripts denote the derivative in either time $t$ or space $x$. This equation can be reduced into $u_t \pm u_x = 0$. (2) Parabolic: heat equations that describes the evolution of a diffusion process. $u_t - u_{xx} = 0$. (3) Elliptic: time-independent diffusion equations, in which the time derivative in parabolic equations is zero. $u_{xx} = 0$.

Magnetization of charged species is characterized by the Larmor radius, or gyroradius, as well as the cyclotron frequency, given by

$$r_L = \frac{mv_\perp}{qB}, \tag{1.2}$$

$$\omega_B = \frac{qB}{m}, \tag{1.3}$$

where $B$ is the magnetic field strength and $v_\perp$ is the velocity perpendicular to the magnetic field lines. The Larmor radius of an ion is much larger than that of electrons due to the difference in mass. On the other hand, the cyclotron frequency of an ion is much smaller than that of electrons. The dimensions of HETs satisfy $r_{L,e} \ll L$ and $r_{L,i} \gg L$, where subscripts $e$ and $i$ denote electrons and ions, respectively. In addition, electrons are magnetized as $\omega_{B,e} > \nu_m$, where $\nu_m$ is the momentum transfer collision frequency. Ions are nonmagnetized since $\omega_{B,i} \ll \nu_m$.

### 1.2.1 Overview of Electric Propulsion

One of the most important thruster metrics is called the specific impulse, given by

$$I_{sp} = \frac{v_{exit}}{g}, \tag{1.4}$$

where $v_{exit}$ is the exhaust speed and $g$ is the gravitational acceleration constant. Rocket engines using chemical propulsion have a large thrust[5] level, as they are used for launching to escape Earth's gravitational field, but the specific impulse is limited to $< 500$ s due to their acceleration mechanism.

EP devices employ electricity to ionize the gas to produce thrust in comparison to using chemical reactions, *i.e.* combustion, in chemical propulsion. EP can be categorized into three categories based on their acceleration mechanisms. First, *electrothermal* systems employ an electrical current or radiation to directly heat the propellant and the heated gas will gain thrust through a nozzle. Examples include arcjets, which generate a plasma via arc

[5]Thrust is essentially the force or the momentum: $F = ma = \dot{m}v_{exit}$, where $m$ is the mass, $a$ is the acceleration, $\dot{m}$ is the mass flow rate.

discharge, and resistojets, in which a resistor such as a filament heats the gas. The specific impulse is comparable to chemical systems but additional gas, *i.e.* oxygen, is not required for EP devices. Second, *electrostatic* devices accelerate ionized propellant through an electric field without magnetization of the ions. The electric field is generated by acceleration grids in ion thrusters and potential drop due to reduced electron mobility in HETs, which will be discussed later. The specific impulse can reach above 3000 sec as $v_{exit}$ increases through electrostatic forces. Third, *electromagnetic* thrusters employ the electromagnetic force to accelerate the plasma. Examples include MagnetoPlasmaDynamic (MPD) thrusters and helicon discharge thrusters. The specific impulse as well as the thrust can be larger than electrostatic thrusters.

### 1.2.2 Basic Principles

The H6 thruster, developed at the Plasmadynamics and Electric Propulsion Laboratory (PEPL) at the University of Michigan, is shown in Fig. 1.1(a). Also illustrated are the direction of the electromagnetic fields and $E \times B$ drift as well as the two major types of low-frequency oscillations: axial breathing mode and azimuthally rotating spokes. Figure 1.1(b) illustrates the profile picture of the H6 operating at nominal conditions with magnetic field stream lines overlaid and discharge channel outlined. The design of the magnetic field is critical in the electron transport and hence the acceleration and ionization of the propellant.

HETs consist of a set of anode and cathode as well as coils to generate magnetic fields in the radial direction of an annular channel. As shown in Fig. 1.2, electrons are emitted from the cathode and some enter the channel due to the more positive potential at the anode, while others in the plume contribute to neutralizing the ion flow from the channel. The channel width of HETs is designed to be smaller than the Larmor radius of electrons, so that they are captured within the discharge channel. Due to the axial electric field and radial magnetic field, the electrons drift in the azimuthal direction, which is known as the $E \times B$ drift. The drifting electrons ionize the propellant injected from the anode and generates the discharge plasma. As soon as the plasma is generated, the ions accelerate through the electric field.

Dielectric materials are used on the walls for standard HETs due to their high thermal

resistivity and electric insulation. These thrusters are often called the stationary plasma thruster (SPT). Another type of HET is the anode layer thruster (TAL) which employs a shorter acceleration channel and metallic wall materials. The purpose of a TAL is to increase the electron temperature since the heat flux to the channel walls can be much lower than SPTs as the rate of electron-induced secondary electron emission of metal materials is significantly lower than that of insulators.

### 1.2.3 Challenges

The principal goal of developing HETs is to improve thruster performance metrics such as thruster efficiency and specific impulse. There are three main problems that must be investigated in order to achieve this goal: 1) to understand the effects of plasma oscillations on thruster performance, 2) to improve efficiency by enhancing ionization and acceleration,

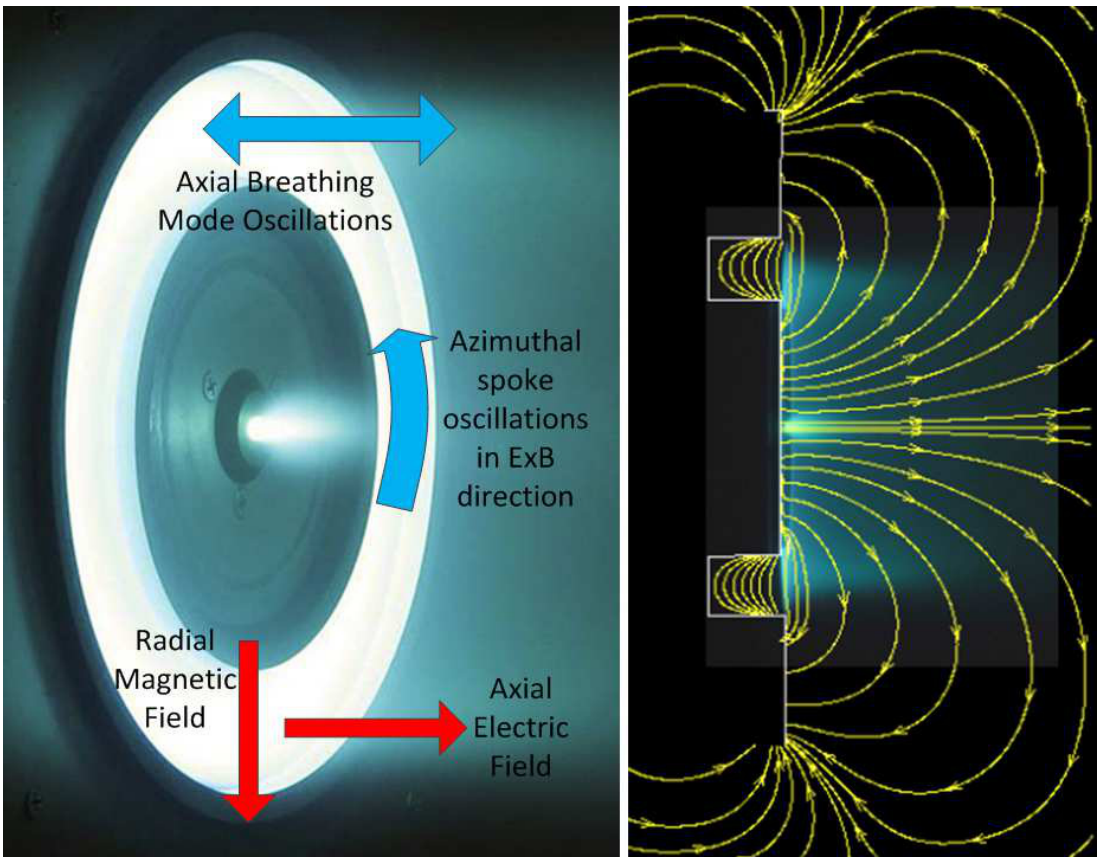


(a) HET operation (b) Magnetic field lines

Figure 1.1: H6 thruster. Reproduced from Refs. 1 and 2.

and 3) to maximize the lifetime of the thruster.

First, there is a wide spectrum of plasma oscillations ranging from 10 kHz to 1 GHz in HETs.[9] One of the most important oscillation modes for actual operation is the low-frequency discharge oscillation, often called the breathing mode.[10, 11] Rotating spokes or density fluctuations in the azimuthal direction also play an important role in electron transport.[12] It has been recently observed by Sekerak[7] that thruster efficiency is optimized when the low-frequency breathing mode is stabilized depending on the operation conditions, including discharge voltage, magnetic field strength, and anode and cathode mass flow rates. It was also found that azimuthally rotating spokes appear in the stable discharge mode whereas the breathing mode is associated with an axial ionization oscillation. For a better understanding of these phenomena, the plasma properties such as density and temperature must be well resolved both temporally and spatially.

Second, the ionization rate of neutral gas and the electric field that accelerates ions are mainly determined by the electron transport.[13, 14] Specifically, ionization and other reactions depend on the electron energy and the potential profile is determined by electron conductivity. Electrons in an HET experience various physical phenomena, including collisions

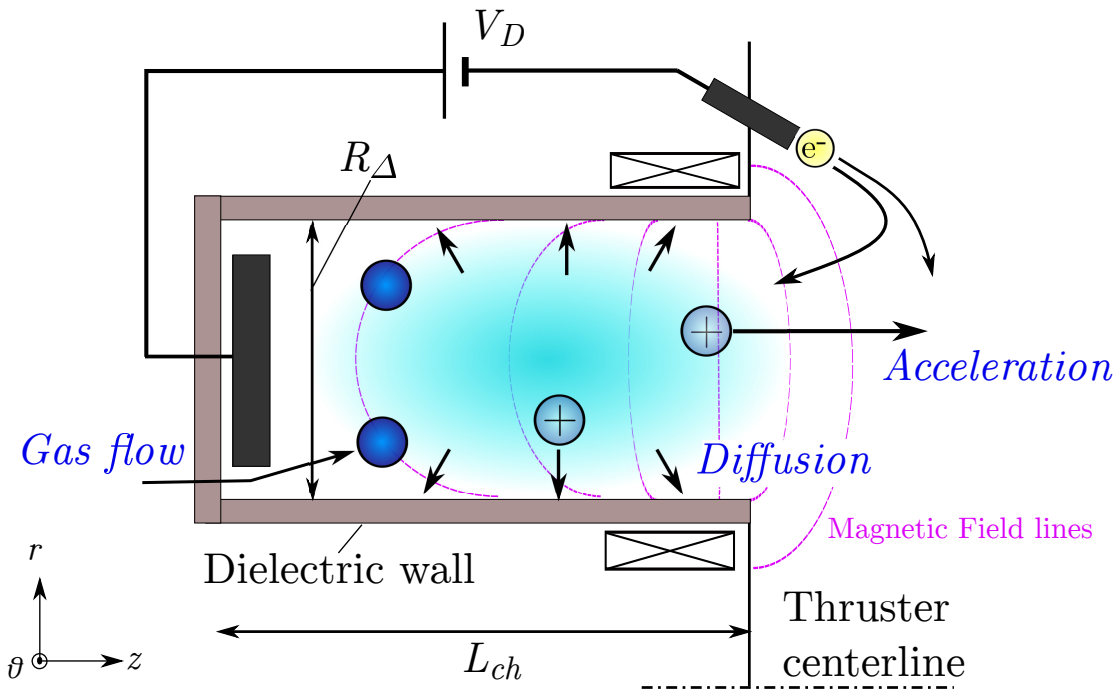


Figure 1.2: Schematic of HET operation.

with channel walls,[15, 16, 17] inelastic collisions such as ionization and excitation,[2, 18, 19] and anomalous diffusion in the presence of a magnetic field.[20, 21, 22] It is very difficult to experimentally obtain time-resolved properties of electrons due to their high characteristic speed in comparison to heavy species. Computational modeling of such plasma flows is extremely useful to investigate small-scale phenomena that cannot be resolved in experiments.

Third, plasma-wall interactions are unavoidable in plasma applications. There are two main processes that play an important role: sputtering and secondary electron emission (SEE).[23] Erosion of the wall material, which is often a dielectric material such as boron nitride in an HET, limits the lifetime of the thruster. The operation of an HET fails when the magnetic coils and pole pieces covered by the channel walls are exposed to the plasma. Molecular dynamics simulations of the sputtering process have shown promising results to accurately estimate the erosion rate.[24, 25] It is also likely that the wall properties, such as wall temperature, composition, and surface roughness, affect the plasma behavior.[26] Therefore, understanding of the material itself as well as the plasma-wall interaction is important for precise control of the discharge plasma. One promising technique is the magnetic shielding of HETs demonstrated at NASA Jet Propulsion Laboratory.[27] Sputtering of the wall material is significantly reduced by controlling the shape of the magnetic fields.

In order to investigate all such phenomena of the HETs, high-fidelity computational modeling of the discharge plasma would be helpful. The dynamic, kinetic, small-scale nature of the plasma transport needs to be understood so that the flow can be characterized and controlled effectively, ultimately to design high-power and highly-efficient thrusters. The purpose of this dissertation is to develop a noiseless kinetic simulation that can capture these complex phenomena.

## 1.3 Plasmas

Plasma is a quasineutral ionized gas that possesses both electromagnetic properties and characteristics of a gas. The flow characteristics, including the balance between ionization and diffusion, determine the plasma properties.

Research on low temperature plasmas has primarily started with the work by Irving

Langmuir, who developed several important devices, including light bulbs, filaments, and plasma probes. The most common plasma phenomena that we see in daily life may be fluorescence lamps, in which ultraviolet photons emitted from excited mercury atoms hit the fluorescent coating and emit a visible photon. The plasma processing community has developed various plasma sources, such as capacitively and inductively coupled plasmas, using a radio frequency power supply. These devices are used for atomic emission spectroscopy, reactive-ion etching, and deposition. Recently, atmospheric-pressure plasmas have gained popularity since such plasmas do not require any vacuum system. Plasma jets and dielectric barrier discharges are being investigated for wound treatment and cancer therapy in the biomedical sciences.

On the other hand, high temperature plasma physics include astrophysical plasmas and fusion plasmas. These plasmas can reach up to 10,000 eV and become fully ionized.[6] Since the magnetic field is dynamic in high temperature plasmas, there are strong interactions between the plasma and electromagnetic forces, which can be described using Maxwell's equations. There are two types of fusion plasmas: magnetic confinement fusion (MCF) and inertial confinement fusion (ICF). The most popular magnetic confinement system is a tokamak, in which the plasma is confined by toroidal magnetic fields. ICF employs high power laser beams to ignite high temperature plasmas. One example of an ICF is the National Ignition Facility at Lawrence Livermore National Laboratory (LLNL).

Most of the electric propulsion devices, including HETs, operate in the low temperature regime, $T_e = O(10)$ eV. However, for instance, it has been shown that increased discharge voltage can increase the maximum electron temperature to about 60 eV.[28] Other measurements suggest that electron temperature is less than 5 eV in the plume.[29] As can be discussed in terms of electron temperature, the HET plasma is multiscale and multiphysics in nature. Plume modeling has been performed by several researchers[30, 31] and it has been shown that the computational results agree well with experimental data. Part of the reason is that the plasma is nonmagnetized in this region, while the electron modeling of the discharge plasma remains challenging. In this dissertation, a new kinetic simulation

[6]Low temperature plasmas are sometimes categorized as *partially ionized gases* since neutral atoms are not completely ionized while high temperature plasmas are *fully ionized*.

method is introduced to model such discharge plasmas.

Figure 1.3 shows a summary of various plasmas in nature depending on the electron density and temperature. Plasmas can be categorized by temperature, *i.e.* low and high temperature plasmas, ionization fraction, *i.e.* fully or partially ionized plasmas, and the effect of magnetic fields, *i.e.* magnetized or nonmagnetized. $\lambda_D$ is the Debye length, which is the length scale associated with Coulomb shielding of the plasma, given by,

$$\lambda_D = \sqrt{\frac{\epsilon_0 k_B T_e}{e^2 n_e}},$$

where $\epsilon_0$ is the permittivity, $k_B$ is the Boltzmann constant, $e$ is the elementary charge, and $T_e$ and $n_e$ are the temperature and number density of electrons. The Debye number is a parameter given by the average number of electrons in a Debye sphere: $N_D = (4/3)\pi n_e \lambda_D^3$. For $N_D \gg 1$, *collective* electrostatic interactions from all other particles in the Debye sphere dominate over binary collisions. The plasmas in this regime are often called weakly coupled plasmas as opposed to strongly coupled plasmas for $N_D \ll 1$, in which the binary electrostatic influence is stronger than the kinetic energy of the particles.[7] When the Debye length is much smaller than the characteristic length, a quasineutral assumption holds as charge separation only occurs in a short range, *e.g.* plasma sheaths.

## 1.4 Research Objectives

This dissertation focuses on development of a grid-based kinetic method that can be used as an alternative to particle-based kinetic methods. In developing a new simulation technique or method, there are four important processes to be taken into account.

- **Verification**: It is necessary to check if the code is correctly implemented. This is done by comparing the numerical results with analytic (*exact*) solutions. Only limited problems have analytic solutions, so it becomes important to understand the test problems from a mathematical perspective. Once the code is verified, the numerical solvers can be also used to verify the theory.

[7] Examples of strongly coupled plasmas include laser ablated plasmas, high pressure arc discharge, white dwarf, neutron starts, and inertial confinement fusion plasmas.

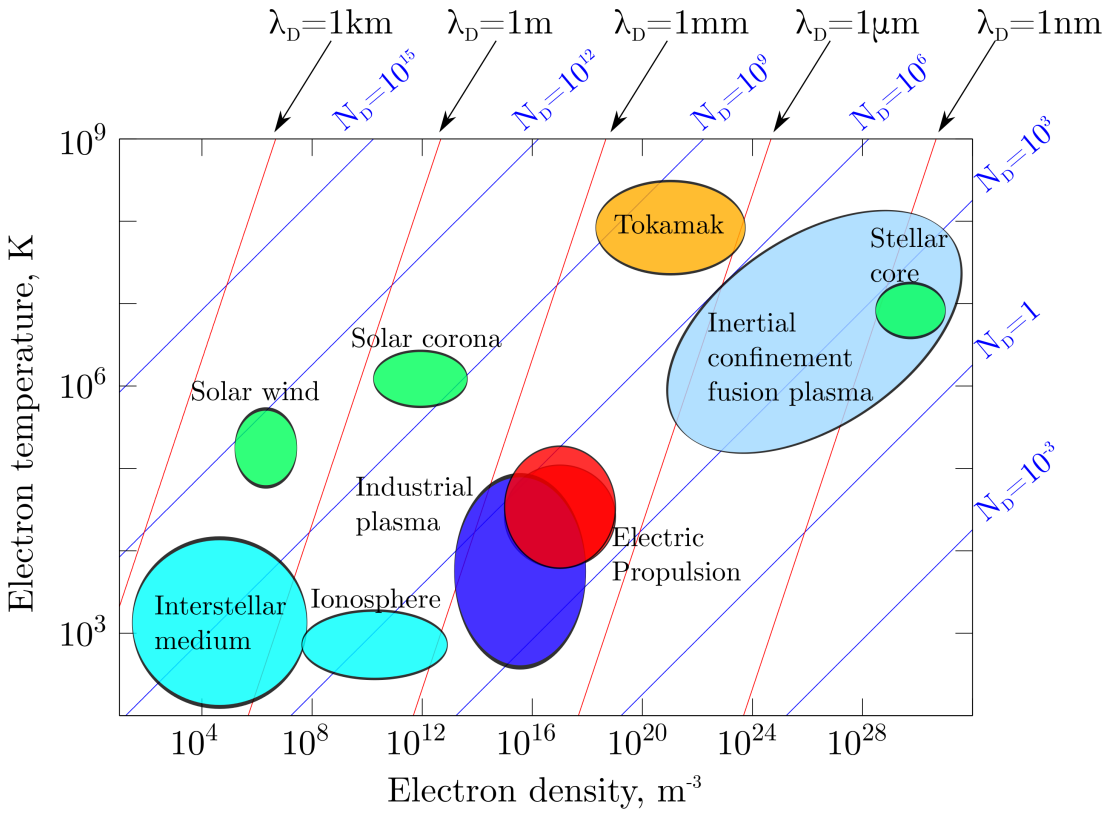


Figure 1.3: Summary of various plasmas for a wide range of density and temperature.

- **Benchmarking**: There may be a variety of solvers that solve the exact same equations. It is important to benchmark a code against other codes to understand the performance of a numerical method. In addition, for development of a grid-based kinetic method, it is important to show the similarities and differences with the existing particle-based methods.

- **Validation**: Computer simulations can be used to analyze and predict measurements or experimental observations. While verification is often mathematical as analytic solutions are required, validation is a process to compare the numerical results with something that is *close* to the exact solutions.[8] It is important to keep in mind that experiments also include uncertainties through measurements, making them not *exact*.[9]

- **Computational Efficiency**: As computation time and memory are finite, it is important to minimize the computational cost either by improving the numerical scheme or utilizing large-scale parallel computers. Currently, several parallel computing techniques are available, including distributed-memory[10] or shared-memory[11] systems. Recent advancement on graphic processing units[12] possesses a large potential in making parallel computation faster and cheaper.

In this dissertation, a grid-based kinetic simulation method is discussed. It is important to test and verify the code before applying it to complex engineering problems. In the first part of the dissertation, a numerical scheme is chosen by considering its properties and understanding the problems to solve. Once the solver is developed, verification, benchmarking, and validation can be performed. It is important to note that the key disadvantage of

[8]Validation can be both ways. There are computational validation of an experiment as well as experimental validation of a computer simulation. For a code development, one validates the simulations with experiments.

[9]The main difference between verification and validation is whether the solutions to be compared are *exact* or not. These two are often used without any distinctions.

[10]The most used distributed-memory parallel computation is Message Passing Interface (MPI), in which multiple cores (*processors*) on an IC chip (*node*) communicate among each other. As each processor has its own memory, the memory is not shared but distributed. A set of multiple nodes is often called a cluster.

[11]An example of shared-memory systems is Open Multi-Processing (OpenMP). Multiple threads within a processor share memory and other resources. One drawback is the synchronization, which occurs when multiple threads in a device perform multiple operations at the same time.

[12]General-Purpose computing on graphics processing units (GPGPU) includes CUDA and OpenCL. This is also one type of shared-memory architecture.

using a grid-based kinetic method has been the large computational cost associated with the discretized velocity space, which is discussed in Sec.2.3.1. This has been improved by the use of parallel computation, making large-scale simulations feasible. All of the abovementioned processes are taken into account in this dissertation to construct a computational framework using grid-based kinetic methods.

The second part of the dissertation focuses on the physics of Hall thruster discharge plasmas. Modeling of such plasmas poses a significant challenge due to the broad spectrum of physical phenomena as well as the associated temporal and spatial scales. A hybrid kinetic-continuum method was developed to model heavy species and electrons that have orders of magnitude difference in their time scales. In addition, the transport of electronically-excited atoms is taken into account and the multispecies reaction effects are discussed. As recent advancement of experimental techniques enables accurate measurements on low-frequency plasma oscillations, computational and theoretical frameworks are developed to investigate such dynamic plasma transport. The goal of the second part of this dissertation is to understand the mechanism of the low-frequency ionization oscillations in a HET using the hybrid simulation technique and a perturbation theory.

## 1.5 Thesis Outline

In Chapter II, an overview of different types of plasmas and plasma modeling techniques is presented. The development of a grid-based kinetic method is also discussed. Chapter III discusses the two verification test problems for developing the grid-based kinetic method, including the plasma-sheath problem and nonlinear plasma waves. Chapter IV focuses on the hybrid kinetic-continuum method developed to model the Hall thruster discharge plasma and benchmarking of the grid-based kinetic method with a particle-based simulation. In Chapter V, mode transition of discharge oscillations in Hall thrusters is investigated using an improved hybrid kinetic-continuum model. Several improvements in the electron continuum model are made and detailed multispecies reactions are taken into consideration. Chapter VI presents a linear perturbation theory of ionization oscillations in Hall thrusters. The computational and theoretical framework are both compared with experimental data

and the mechanisms of discharge oscillations are discussed. Chapter VII describes the development of a two-dimensional grid-based kinetic model. This is coupled with a two-dimensional electron continuum model to investigate the ionization oscillations in the axial and azimuthal directions of a Hall thruster. Finally, in Chapter VIII, conclusions and future directions of this dissertation are presented.

# CHAPTER II

# Numerical Method

In this chapter, an overview of governing equations is presented. Three major plasma simulation techniques, including particle- and grid-based kinetic simulation and continuum model, are discussed and compared.

## 2.1 First-Principles Governing Equations

Kinetic theory of gas and plasma flows describes the time evolution of the phase space distribution function of particles. The Liouville equation, in which the Hamiltonian dynamics of $N$ particles is considered, can be transformed into a chain of equations of multiple particle distribution functions, called the Bogoliubov-Born-Green-Krikwood-Yvon (BBGKY) hierarchy. Detailed derivations and assumptions are described in Ref. 32. The Boltzmann equation can be derived by assuming that only binary collisions occur[1] and the velocities of two colliding particles are uncorrelated.[2] The Boltzmann equation is given by:

$$\frac{\partial f}{\partial t} + \mathbf{v} \cdot \frac{\partial f}{\partial \mathbf{x}} + \mathbf{a} \cdot \frac{\partial f}{\partial \mathbf{v}} = S, \tag{2.1}$$

where $f$ is the VDF, $\mathbf{v}$ is the velocity, $\mathbf{x}$ is the physical space, $t$ is time, $\mathbf{a}$ is the acceleration, which can be written as $\mathbf{a} = q(\mathbf{E}+\mathbf{v}\times\mathbf{B})/m$ for nonrelativistic plasmas,[3] $q$ is the elementary charge, $m$ is the mass, $\mathbf{E}$ is the electric field, $\mathbf{B}$ is the magnetic field, and $S$ is the collision

[1] Also called dilute gas approximation. Three-body collisions are neglected.

[2] Molecular chaos assumption. The two-particle distribution function $f_{12}$ can be written as a product of one-particle distribution functions: $f_{12} = f_1 f_2$

[3] For relativistic plasmas, $\mathbf{a} = q[\mathbf{E} + (\mathbf{v} \times \mathbf{B})/\gamma_r]/m$, where $\gamma_r$ is the relativistic factor given by $\gamma_r = (1 + v^2/c^2)$ with $c$ being the speed of light.

term. In the plasma community, the collisionless Boltzmann equation is often called the Vlasov equation: $S = 0$ in Eq. (2.1).

Macroscopic quantities can be obtained by evaluating moments of the VDFs. For instance, the number density, mean velocity, and mean energy are obtained from

$$n(\mathbf{x}, t) = \int_{-\infty}^{\infty} f(\mathbf{x}, \mathbf{v}, t) d\mathbf{v}, \tag{2.2}$$

$$\mathbf{u}(\mathbf{x}, t) = \int_{-\infty}^{\infty} \mathbf{v} \hat{f}(\mathbf{x}, \mathbf{v}, t) d\mathbf{v}, \tag{2.3}$$

$$\epsilon(\mathbf{x}, t) = \int_{-\infty}^{\infty} \frac{1}{2} m |\mathbf{v}|^2 \hat{f}(\mathbf{x}, \mathbf{v}, t) d\mathbf{v}, \tag{2.4}$$

where $\hat{f}$ is the normalized VDF: $\hat{f} = f/n$. Note that the conventional fluid conservation equations can be derived by taking moments of the collisional invariants in Eq. (2.1) and by assuming that the VDFs are Maxwellian. The derivation is shown in Appendix A.

Modeling collision terms can be the most challenging component in kinetic modeling. In particular, elastic collisions are described by the Boltzmann collision integral:

$$S_{boltz} = \int \int g\sigma(f'_A f'_B - f_A f_B) d\Omega d^3\mathbf{v}, \tag{2.5}$$

where $g = |\mathbf{v}_A - \mathbf{v}_B|$ is the relative speed between particles $A$ and $B$, $\sigma = \sigma(g, \Omega)$ is the differential cross section, superscript $'$ denotes the information after a collision event, subscripts $A$ and $B$ denote the two particles colliding in this event, and $d\Omega$ is the solid angle. Solving the Boltzmann integral is computationally expensive, so the simplified Bhatnagar-Gross-Krook (BGK)[4] collision operator has also been used to account for some scattering processes. The BGK operator is given by

$$S_{bgk} = \nu(f - f_M), \tag{2.6}$$

where $\nu$ is the collision frequency and $f_M$ is the Maxwellian with the macroscopic properties, such as mean velocity and temperature, the same as those obtained from $f$. It is based on

[4]This is different from the Bernstein-Greene-Kruskal (BGK) solution for nonlinear plasma waves, shown in Sec. 3.4

the assumption that the non-Maxwellian components will eventually relax to a Maxwellian with conservation of momentum and energy. Another collision model that is important in plasma physics is the Fokker-Planck collision integral that assumes the effect of charged-particle interactions such as elastic Coulomb collisions:

$$S_{fp} = -\frac{\partial}{\partial \mathbf{v}} \cdot (\mathbf{A}f) + \frac{1}{2}\frac{\partial}{\partial \mathbf{v}} \cdot \left[\frac{\partial}{\partial \mathbf{v}} \cdot (\mathbf{D}f)\right], \tag{2.7}$$

where $\mathbf{A}$ and $\mathbf{D}$ are the dynamical friction vector and the diffusion tensor, respectively. Investigation and development of the collision models are reserved for future work.

In the present study, the collision reactions involved in the DK simulation are ionization processes and charge exchange collisions. For instance, the ion source term via ionization can be described as

$$S_{ion} = \nu_{ion} f_{neutral}, \tag{2.8}$$

where $\nu_{ion}$ is the ionization frequency and $f_{neutral}$ is the neutral atom VDF. The charge exchange collisions between ions and neutral atoms are modeled as

$$S_{CEX} = \nu_{CEX}(f_{neutral} - f_{ion}), \tag{2.9}$$

where $\nu_{CEX}$ is the charge exchange collision frequency and $f_{ion}$ is the ion VDF. This will be explained later in Sec. 4.3.

## 2.2 Particle-based Method

In particle simulations, the kinetic equation is not directly solved but the equations of motion are solved for each macroparticle. The equations of motion for each particle $j$ are written as

$$\frac{d\mathbf{x}_j}{dt} = \mathbf{v}_j, \frac{d\mathbf{v}_j}{dt} = \mathbf{a}_j. \tag{2.10}$$

The most common integration scheme used for particle simulations is a leap-frog scheme, which is a second-order accurate method without any numerical dissipation error.[5] The

[5]In numerical simulations, dissipation error is the magnitude of error, while dispersion error is the phase error. These errors can be quantified using Von Neumann analysis, where a numerical solution can be written

macroscopic quantities are obtained by sampling the particle information. For instance, the number density and the mean velocity can be obtained by

$$n(\xi) = \frac{1}{V} \sum_j s(\mathbf{x}_j - \xi), \tag{2.11}$$

$$\mathbf{u}(\xi) = \frac{1}{V} \sum_j \mathbf{v}_j s(\mathbf{x}_j - \xi), \tag{2.12}$$

where $\xi$ is the physical coordinate of a cell, $V$ is the cell size, and $s$ is the shape function, or the particle weight. The statistical noise, $\epsilon_S$, due to the use of discrete macroparticles can be reduced with an increased number of macroparticles $N_p$, *i.e.* $\epsilon_S \sim N_p^{-1/2}$, but there is always statistical noise in the system that may affect estimation of the collision integral and alter high frequency plasma oscillations. Collision processes are often taken into account probabilistically using random numbers. The collision probability within a fixed time step $\Delta t$ is given by

$$P = \nu \Delta t, \tag{2.13}$$

where $\nu$ is the collision frequency and $P$ is the collision probability, which is compared with a random number to determine if the collision event occurs or not.

## 2.3 Grid-based Kinetic Method

A grid-based kinetic method employs discretized phase space in which the kinetic equations are solved directly. In this thesis, the grid-based kinetic method is referred to as the direct kinetic (DK) method. As the collisionless Boltzmann equation is often called the Vlasov equation in the plasma community, we refer to the collisionless DK simulation as the Vlasov simulation.

Since Eq. (2.1) is a multidimensional first-order hyperbolic partial differential equation (PDE), the numerical methods for advection problems developed in the computational fluid dynamics (CFD) community can be used effectively. In the applied mathematics community, development of high-order accurate Vlasov simulation technique has also been a popular

as $G = \exp(-i\omega t)$ in simple equations.

research topic. The first Vlasov simulation developed was a finite difference scheme using cubic spline interpolation.[33] Since then, many researchers have developed other methods including semi-Lagrangian methods,[34] Weighted Essentially Non-Oscillatory (WENO) schemes,[35] Discontinuous Galerkin methods,[36] and finite volume methods using Runge-Kutta methods for time integration.[37] Other Vlasov models have been used in the plasma community. For instance, the gyrokinetic approach, in which the gyrophase-averaged Vlasov equation is solved, is frequently employed in the tokamak plasma community.[38]

### 2.3.1 Comparison with Particle Methods

Table 2.1 summarizes the comparison of grid-based and particle-based kinetic simulations. In particle simulations, the kinetic equation is not directly solved but the equations of motion, shown in Eq. (2.10), are solved for each macroparticle. Eq. (2.10) is a set of two first-order ordinary differential equations (ODE). The macroscopic quantities are obtained by sampling the particle information. Collision processes are often taken into account probabilistically using random numbers. There is always statistical noise in the system that may affect estimation of the collision integral and alter high frequency plasma oscillations.

On the other hand, grid-based methods eliminate the statistical noise in particle simulations and calculate the collision integral using discretized VDFs directly. In comparison to the particle-based kinetic method being a probabilistic approach, the grid-based simulation is often called a deterministic kinetic method. Particle simulations can also be categorized as Lagrangian while grid-based methods are Eulerian.

Memory requirements can be larger for grid-based kinetic simulations since the phase space needs to be discretized in all dimensions. Let us assume that the discretization in the physical coordinate is identical in grid- and particle-based kinetic simulations. In general, the total number of cells per one physical cell is $N_v^d$, where the number of grid points in the velocity space is $N_v$ and $d$ is the number of dimensions in velocity space. For particle simulations, each macroparticle has $(2d)$-dimensional information, so the total number of degrees of freedom is $2dN_p$, where $N_p$ is the number of particles per cell. The computational memory required is directly associated with the resolution of the VDFs, which also affects the macroscopic quantities.

Table 2.1: Comparison of grid-based and particle-based kinetic simulations

| | **Grid-based** | **Particle-based** |
|---|---|---|
| **Model** | Solve for VDFs in phase space | Solve for motions of macroparticles |
| **Differential equation** | Hyperbolic PDE | ODE |
| **Specification** | Eulerian | Lagrangian |
| **Macroscopic quantities** | Moments of VDFs | Sampling particle information |
| **Collision rates** | Integral of collision operator | Collision probability |
| **Computational memory per physical cell ($d$ is the number of dimensions)** | $N_v^d$ ($N_v$: number of grid points in the velocity space) | $2dN_p$ ($N_p$: number of particles per cell) |
| **Numerical error** | Global truncation error: $\epsilon_T \sim O[(N_v)^{-p}]$ ($p$ is the order of accuracy of the scheme) | Statistical noise: $\epsilon_S \sim O[(N_p)^{-1/2}]$ |

Finally, the most critical comparison may be the error associated with either kinetic method. The truncation error is the source of the error in numerically solving a differential equation system.[39] For instance, consider a first-order differential equation: $\frac{du}{dt} = ku$. The analytic solution is $u = u_0 \exp(kt)$, where $u_0 = u(t = 0)$. From another perspective, for a given level $t = t_0$, the solution at $t = t_0 + h$ can be described using Taylor expansion as

$$u(t_0 + h) = u(t_0) \left[ 1 + kh + \sum_{m=2}^{\infty} \frac{k^m}{m!} h^m \right]. \tag{2.14}$$

For numerical calculations, the left hand side must be discretized and we apply a numerical scheme. For instance, a first-order forward Euler integration method is employed to advance one numerical step $h$ from the level $n$ to $n + 1$.

$$U^{n+1} = U^n \left( 1 + kh \right). \tag{2.15}$$

It can be seen that the numerical scheme neglects the high order terms in Eq. (2.14) when

comparing Eqs. (2.14) and (2.15). This is exactly the *local* truncation error, the numerical error introduced in one numerical step, of a numerically-discretized scheme: $O(h^{p+1})$ for a $p$th-order method. The *global* truncation error is the accumulative error through multiple integration steps, *i.e.* a sum of many local truncation errors. For a total length of $L$,[6] the total number of integration steps will be $L/h$. Hence, the global truncation error, $\epsilon_T$, of a $p$-th order accurate scheme is on the order of $O(h^p)$. Note that there are temporal errors when integrating the time derivative as well as spatial errors when discretizing spatial derivatives. In Table 2.1, the numerical error in the grid-based method is shown to be proportional to $O(N_v^{-p})$ as the grid size $h$ can be given by $h = L_v/N_v$ for a given system size $L_v$. The error level can be reduced by choosing a large number of grid points or a higher order accurate numerical method.

The numerical error in particle-based methods[7] is associated with the statistical noise, $\epsilon_S$, due to the use of discrete macroparticles.[32] The statistical noise arises when sampling the particle information using averaging techniques and can be reduced with an increased number of macroparticles $N_p$, *i.e.* $\epsilon_S \sim N_p^{-1/2}$. The error level can be reduced by increasing the number of particles for the particle simulations. For a steady-state calculation, as the flows are static, a large time window can be chosen for particle sampling. This will reduce the statistical noise since macroscopic quantities can be sampled from a larger number of macroparticles. Therefore, it can be expected that the grid-based simulation works better if the flows are dynamically moving and a smaller sampling time is required as there is no need for sampling in the grid-based methods.

### 2.3.2 Numerical Scheme

When choosing the numerical scheme for the grid-based solver, several important properties must be considered.

1. *Positivity:* VDFs must be positive since the probability of particles in the phase space is bounded between zero and one. $0 \leq \hat{f} \leq 1$, where $\hat{f}$ is the normalized VDF, *i.e.* $\int \hat{f} dv = 1$.

[6] $L$ can be either time, spatial length, or any other dimensions that are discretized.

[7] A leap-frog method used for advancing particle position and velocity is typically second-order in time and space or velocity.

2. *Mass Conservation:* The number of particles must be conserved in the system. Finite volume methods inherently satisfy conservation of particles whereas other methods often neglect this property.

3. *Accuracy:* The accuracy of the scheme should be high enough, usually higher than first order, to reduce the numerical errors and obtain a converged solution.[8]

4. *Efficiency:* Since grid-based kinetic simulations can be computationally expensive, as discussed in Table 2.1, the computational efficiency should also be improved for practical use.

5. *Momentum/Energy Conservation:* Such conservation is important since the collision rate coefficients are calculated using the VDFs or EDFs. For instance, if the electrons gain energy from numerical errors, the inelastic collision terms may be calculated less accurately.

In this thesis, a finite volume DK solver is developed using a modified Arora-Roe scheme,[40] which gives second-order accuracy, for flux reconstruction. All the properties except for the momentum/energy conservation are achieved using the present numerical scheme. Finite volume methods solve for the cell-averaged quantity by estimating the flux that goes in and out of the cell. An example of the numerical stencil for a finite volume method is shown in Fig. 2.1. Assume a one-dimensional linear advection equation,

$$\frac{\partial u}{\partial t} + v\frac{\partial u}{\partial x} = 0, \tag{2.16}$$

where $u = u(x)$ is the conserved quantity and $v$ is the characteristic speed, which is constant in a linear advection equation. The discretized equation can be written as

$$\frac{U_j^{n+1} - U_j^n}{\Delta t} = -\frac{1}{\Delta x}(F_{j+1/2} - F_{j-1/2}), \tag{2.17}$$

where $U$ is the cell-averaged quantity, $F$ is the discretized flux, $\Delta t$ is the time step, $\Delta x$ is the cell size, and superscript $n$ and subscript $i$ denote the indices of time step and cell,

[8] Solutions obtained from a numerical method should approach the *exact* solution of the differential equation when the error level is small enough $\epsilon_T \to 0$.

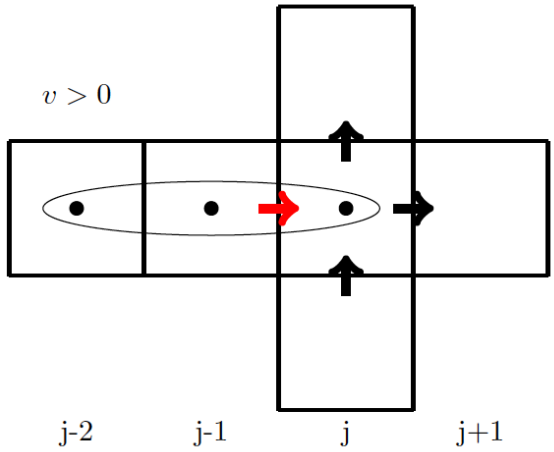


Figure 2.1: Stencil of a finite volume scheme. Arrows describe the fluxes at the cell interfaces.

respectively.

In order to calculate the flux terms higher than first-order accuracy in Eq. (2.17), the Monotonic Upwind Scheme for Conservation Laws (MUSCL) is used.[41] Godunov's theorem states that no linear numerical scheme that is better than first-order accuracy ($p \geq 2$) can preserve monotonicity.[9] The use of nonlinear flux limiter functions in the MUSCL framework can limit any numerical extrema, *i.e.* undershoot and overshoot, while achieving order of accuracy higher than first order. For $v > 0$, the flux at the cell interface $j + 1/2$ can be written as

$$F_{i+1/2} = cU_i + \frac{(1 - |c|)c}{2}(U_{i+1} - U_i)\Psi(r_{i+1/2}), \tag{2.18}$$

where $c = v\Delta t/\Delta x$ is the Courant number, or often called the Courant-Freidrich-Lewy (CFL) number, $\Psi(r)$ is the nonlinear limiter function, and $r_{i+1/2} = (U_i - U_{i-1})/(U_{i+1} - U_i)$ is the slope factor, which indicates the smoothness of the neighboring values. In addition to the modified Arora-Roe limiter employed in this dissertation, various nonlinear flux limiters are shown in Fig. 2.2. For instance, the harmonic limiter works well for smooth functions, the superbee limiter tends to capture a discontinuity well due to the steepening of solutions,

[9] This property can be described by the total variation: $TV(U^n) = \sum |U_{j+1} - U_j|$. A total variation diminishing (TVD) scheme satisfies $TV(U^{n+1}) \leq TV(U^n)$.

and the Arora-Roe scheme is based on the third-order accurate discretization:

$$\Psi^{3rd}(r) = \frac{1+|c|}{3}(r-1)+1.$$

The original Arora-Roe limiter uses

$$\Psi(r) = \begin{cases} 0 & r < 0 \\ \min\left[\frac{2}{|c|}r, \Psi^{3rd}(r)\right] & 0 \le r < 1 \\ \min\left[\frac{2}{1-|c|}, \Psi^{3rd}(r)\right] & r \ge 1. \end{cases} \tag{2.19}$$

The limits $\Psi = 2r/|c|$ and $\Psi = 2/(1-|c|)$ are the strongest conditions for monotonicity, *i.e.* satisfying TVD properties. It was found that the tail of a smooth distribution can be corrupted due to these strong limiters. In this study, a modified Arora-Roe limiter is used, given by

$$\Psi(r) = \begin{cases} 0 & r < 0 \\ \min[2r, \Psi^{3rd}(r)] & 0 \le r < 1 \\ \min[2, \Psi^{3rd}(r)] & r \ge 1. \end{cases} \tag{2.20}$$

### 2.3.3 Time Integration

For the time integration on the left hand side in Eq. (2.17), a second-order Runge-Kutta method or Strang's time splitting technique is used. A higher order time integration scheme can be used, but second-order accuracy is sufficient since the spatial discretization of the flux calculations is second-order accurate. Note that higher order time integration is needed for collision dominated flows in order to maintain the nonlinearity of the evolution.[42] Let us assume a time-dependent equation:

$$\frac{du}{dt} = L(u),$$

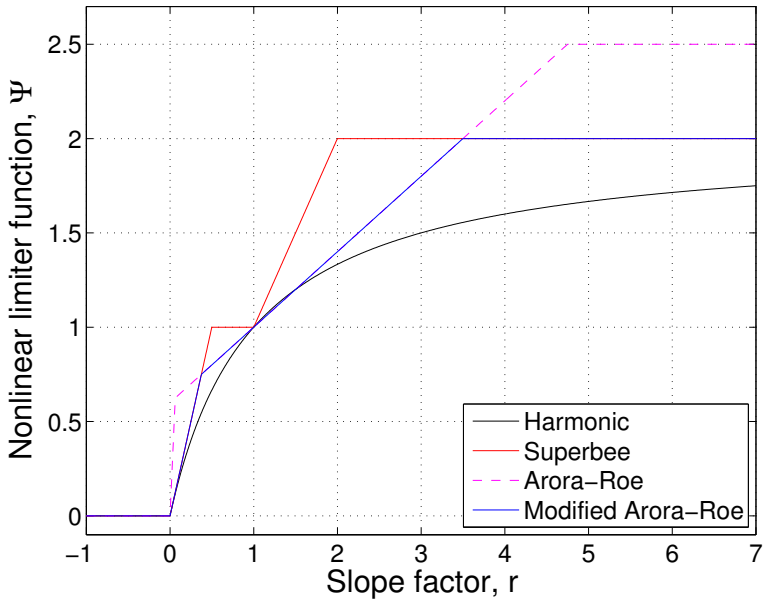


Figure 2.2: Sweby diagram: The Arora-Roe limiters in this figure are for CFL number $|c| = 0.2$.

where $L(u)$ is an operator for the quantity $u$. A second-order Runge-Kutta scheme can be written as a two-step integration method:

$$u^* = u^n + \Delta t L(u^n),$$

$$u^{n+1} = u^n + \frac{\Delta t}{2}\left[L(u^n) + L(u^*)\right].$$

Strang's time splitting technique works for multidimensional equations. Let us assume a two-dimensional time-dependent equation:

$$\frac{du}{dt} = L_x(u) + L_y(u),$$

where $L_x(u)$ and $L_y(u)$ are differential operators in the x and y directions. Then, the time integration can be given by

$$u^* = u^n + \frac{\Delta t}{2} L_x(u^n),$$

$$u^{**} = u^* + \Delta t L_y(u^*),$$

$$u^{n+1} = u^{**} + \frac{\Delta t}{2} L_x(u^{**}).$$

The time step must satisfy the Courant-Freidrich-Lewy (CFL) condition in order to achieve numerical stability. For a second-order explicit RK integration,

$$\sum_i \left( \frac{\max |v|_i \Delta t}{\Delta x_i} + \frac{\max |a|_i \Delta t}{\Delta v_i} \right) \leq 1 \tag{2.21}$$

where $v$ is the characteristic velocity, $a$ is the characteristic acceleration, $\Delta t$ is the time step, $\Delta x$ and $\Delta v$ are the cell size in physical and velocity space, and $i$ denotes the dimension. The time step must be chosen small enough to satisfy Eq. (2.21) for a certain spatial discretization. Typically, on the right hand side, we can set a safety factor which is less than 1 in order to satisfy numerical stability. The right hand side is also dependent on the time integration scheme. For instance, the maximum Courant number is above 2 for a fourth-order Runge-Kutta scheme. For Strang's time splitting method, the CFL condition needs to be satisfied independently in each direction. Note that the source term can be easily added on the right hand side of Eq. (2.17) for collisional problems.

The challenge of grid-based kinetic simulations lies in the choice of the numerical scheme to solve the discretized governing equation. Additional important properties include conservation of momentum and energy,[43] which may be critical when including collision terms. Investigation of other numerical methods is reserved for future work.

### 2.3.4 Parallel Computing Capabilities

The DK simulation can be used on a signal processor or multiple processors using Message Passing Interface (MPI). For instance, the 1D1V (one dimensional in physical space and one dimensional in velocity space) DK simulation partitions the domain and assigns each of those sub-domains to different processors. Information is sent and received between the neighboring processors using MPI_Send and MPI_Recv. As the DK simulation employs a MUSCL scheme, each processor requires two extra cells from the neighbors. If a higher-order numerical method is used and a larger stencil is required, then the communication required in MPI will also increase. The macroscopic quantities can be integrated using collective

communication routines, such as MPI_Allgather and MPI_Bcast. When the 1D1V Vlasov solver is coupled with a Poisson solver, then the Poisson solver runs on a single processor.

For the 2D2V DK simulation, the 2D domain in the physical space is partitioned among the processors while all processors possess the same 2D velocity space. The macroscopic quantities can be integrated locally on each processor, and they can be sent to the neighboring processors. MPI communications are used when passing the macroscopic quantities and VDFs between processors. For a 2D Poisson solver or continuum solver, linear algebra software can be used. In this thesis, hypre, software developed at LLNL, is used. This is a library of high performance preconditioners that can be used for parallel computing.

## 2.4 Continuum Approach

Although kinetic simulations can capture nonequilibrium effects, a CFD-type fluid modeling is also popular since the computational cost is significantly lower than kinetic methods. Like grid-based kinetic methods, continuum methods avoid the statistical noise associated with particle-based methods. Continuum models are useful for equilibrium or near-equilibrium flows, but become less accurate when modeling strong nonequilibrium flows such as non-Mawellian and beam distributions.

Table 2.2: Comparison of kinetic models and continuum approach

| | **Kinetic** | **Continuum (fluid)** |
|---|---|---|
| **Nonequilibrium effects** | Yes | Assumes equilibrium or near-equilibrium |
| **Velocity space discretization** | Yes | No |
| **Computational cost ($N_c$ is the total number of cells in physical coordinate)** | $N_c N_{v,tot}$ ($N_{v,tot}$ is the total degrees of freedom that represents velocity space) | $N_c$ |
| **Models** | PIC, DSMC, Vlasov, DK, Gyrokinetic | Euler, Navier-Stokes, Burnet, MHD |

For continuum modeling, conservation equations are derived by taking moments of the

Boltzmann equation in Eq. (2.1). If the gas is not ionized, the flow can be described using the Euler equations or Navier-Stokes equations. There are also some fluid equations that takes higher order moments into account, such as the Burnett equations. In the presence of nonequilibrium effects and electromagnetic forces, the generalized magnetohydrodynamic (MHD) equations can then be given by

$$\frac{\partial n}{\partial t} + \nabla \cdot (n\vec{u}) = S, \tag{2.22}$$

$$\frac{\partial}{\partial t}(mn\vec{u}) + \nabla(mn\vec{u}.\vec{u} + p) = q(\vec{E} + \vec{u} \times \vec{B}) + \nabla\tau + \vec{R}, \tag{2.23}$$

$$\frac{\partial}{\partial t}(n\epsilon) + \nabla \cdot (n\vec{u}\epsilon + p\vec{u}) = \nabla \cdot \vec{Q} + qn\vec{u} \cdot \vec{E} + S_{elas} - S_{inelas} + \Phi, \tag{2.24}$$

where $m$ is the mass, $n$ is the number density, $\vec{u}$ is the mean velocity, $S$ is the sum of source and sink terms for particles, $p$ is the pressure, $\tau$ is the viscous stress, $\vec{R}$ is the collisional friction, $\epsilon$ is the mean energy, $\vec{Q}$ is the conductive heat flux, $S_{elas}$ is the energy source due to elastic collisions, $S_{inelas}$ is the energy loss due to inelastic collisions, and $\Phi$ is the energy dissipation function due to viscous stress. For the Euler equations, all of the right hand sides are zero. The Navier-Stokes equations retain the viscous terms including $\nabla\tau$ in Eq. (2.23) and $\Phi$ in Eq. (2.24) as well as the heat conduction, $\nabla \cdot \vec{Q}$. For reactive multispecies flows, $S$ in Eq. (2.22) is also included. Note that the derivation of the continuum equations is shown in Appendix A. It can be seen that these equations can be exact at any Knudsen number if the VDFs of the gas species are known.

For plasma simulations, it is typically assumed that the electromagnetic forces are dominant over the viscous terms. Typically, the source and sink terms in the mass conservation equation can be given as

$$S = \sum_{\text{reaction}} \dot{n},$$

where $\dot{n}$ is the change in the density due to reactions. The collisional friction term is often given by a Krook operator:[44, 45]

$$\vec{R} = -mn\nu_m(\vec{u} - \vec{u}_j),$$

where $\nu_m$ is the momentum transfer collision frequency and $\vec{u}_j$ is the mean velocity of a colliding particle, $j$. Note that this approximation employs an assumption that the mean velocity of the flow is much smaller than the thermal speed. To our knowledge, this is only discussed in Ref. 45. Finally, the energy transfer terms are written as

$$S_{elas} = \sum_j \frac{2m}{m_j}\frac{3}{2}k_B(T - T_j)\nu_j,$$

$$S_{inelas} = \sum_k n\Delta\epsilon_k\nu_k,$$

where $m_j$ and $T_j$ are the mass and temperature of the colliding particle, $j$, $\nu_j$ is the elastic collision frequency, and $\Delta\epsilon_k$ and $\nu_k$ are the energy required and collision frequency of inelastic process, $k$. The collision frequency can be calculated from

$$\nu = n\int \hat{f}(\varepsilon)\sigma(\varepsilon)\sqrt{\frac{2\varepsilon}{m}}d\varepsilon,$$

where $n$ is the number density of the target gas species, $\hat{f}(\varepsilon)$ is the energy distribution function, $\sigma(\varepsilon)$ is the collision cross section, and $\varepsilon$ is the energy of the colliding particle. Collision frequencies can be a function of temperature when the EDF is a function of temperature, such as a Maxwellian: $f(\varepsilon) \sim \exp(-\varepsilon/T)$.

For the momentum equation in Eq. (2.23), the most used approach is called the drift-diffusion approximation.[46] If the collision terms, electromagnetic forces, and pressure gradient are dominant, the inertial term and the time derivative can be neglected. From the drift-diffusion approximation, the momentum equation in Eq. (2.23) reduces to an equation in which a simple form of flux is obtained. This is then inserted in Eq. (2.22) and the spatiotemporal evolution of the density is solved for.[42] Assuming that the gas species are in an equilibrium state, the temperature is obtained from Eq. (2.24). Note that the mean energy is a sum of kinetic and thermal energy. For an isotropic distribution,

$$\epsilon = \frac{3}{2}k_BT + \frac{1}{2}m|\vec{u}|^2, \tag{2.25}$$

where $k_B$ is the Boltzmann constant and $T$ is the temperature. In the low temperature

plasma community, it is common to assume that the kinetic energy is negligible compared to the thermal energy. This is valid as long as there is no strong directed flow in the plasma or the drift-diffusion approximation holds. As discussed later, it was recently found that the kinetic energy of electrons cannot not be neglected in Hall thruster plasmas since a strong $E \times B$ drift exists in the system. As the numerical methods for solving continuum equations depend on what assumptions are used, they are discussed later in the dissertation.

## 2.5 Summary

The aim of this research is to develop a grid-based direct kinetic (DK) simulation where the kinetic equations, such as the Boltzmann equation and Vlasov equation, are solved directly in discretized phase space. The statistical noise in particle-based methods is essentially eliminated in the DK simulation, making it useful for investigating plasma oscillations and small-scale physics. In comparison to continuum models, the nonequilibrium nature of the plasma flow can be obtained more accurately using a kinetic method. The differences between continuum, particle-based kinetic, and grid-based kinetic simulations are illustrated in Fig. 2.3.

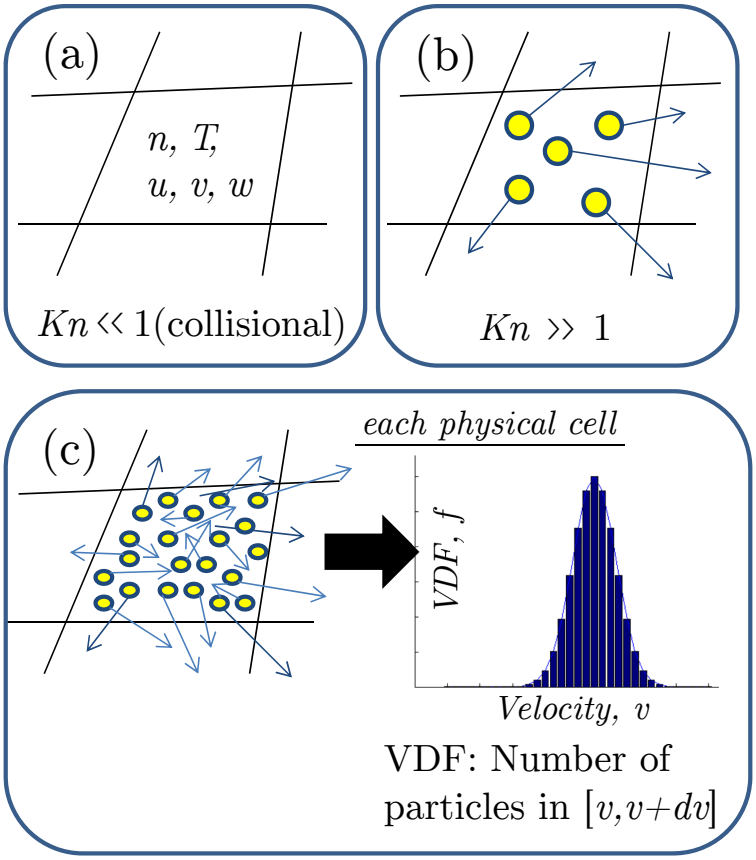


Figure 2.3: Computational methods for rarefied flows or plasmas.

# CHAPTER III

# Verification of a Grid-Based Direct Kinetic Method

A grid-based direct kinetic (DK) simulation is constructed by first developing a collisionless Vlasov solver, since analytic solutions can be derived in some particular problems from the collisionless Vlasov-Poisson equations. In this chapter, code verification is performed and the verification test problems including plasma sheath and trapped particle instabilities are discussed.

## 3.1 Implementation of the Vlasov-Poisson solver

For developing a new kinetic method, it is important to verify the solver. Verification is a technique where the results obtained from numerical simulations are compared with analytic solutions of a mathematical model. Inclusion of the source term in kinetic modeling introduces complexity and it is often difficult to derive an analytic solution. Therefore, collisionless problems are considered and the Vlasov-Poisson solver is used to verify the grid-based kinetic method.

### Formulation

For a nonmagnetized plasma, the electric field can be written as $\mathbf{E} = -\nabla\phi$, where $\phi$ is the plasma potential. Gauss's law, one of Maxwell's equations, reduces to the Poisson equation. The 1D Poisson equation is given by

$$-\frac{d}{dx}\left(\epsilon_0 \frac{d\phi}{dx}\right) = e(n_i - n_e), \tag{3.1}$$

where $\epsilon_0$ is the permittivity, $n_i$ is the positively charged ion density, and $n_e$ is the electron density.[1] This is a second order elliptic PDE that requires boundary conditions.Three main boundary conditions include Dirichlet, Neumann, and periodic conditions. The electric field calculated from the potential, $E_x = -d\phi/dx$, is then used in the Vlasov equation:

$$\frac{\partial f}{\partial t} + v_x \frac{\partial f}{\partial x} + \frac{qE_x}{m} \frac{\partial f}{\partial v_x} = 0, \tag{3.2}$$

where $q$ is the charge. $q = -e$ for electrons and $q = +e$ for positively charged species. The densities integrated from the VDFs are then used in the Poisson equation. Here, this simulation is called the Vlasov-Poisson solver.

The Vlasov equation is solved using a finite-volume method with MUSCL framework using a modified Arora-Roe limiter, as shown in Chapter II. The 1D Poisson equation is solved using a fast Fourier Transform (FFT) method for periodic boundary conditions and a Tridiagonal matrix solver is used for the other boundary conditions.

**DK/Vlasov Procedure**

The 1D1V DK solver is written in C.[2] For the DK/Vlasov subroutine, a 1D1V solver has a 2D array. Strang's time splitting allows one to separate the 2D advection into a set of 1D advection equations. The 1D1V Vlasov equation becomes a set of two linear advection equations because the velocity is identical in the same velocity bin for the $x$-advection and the electric field is identical in the same physical cell for the $v$-advection. The procedure of the kinetic update is as follows.

1. Store the old values. $u_{old}[i] = u[i][j]$ for $j$, where $i = 0, \ldots, n$ with the total number of cells in one direction, $n$.

2. Initialize an array for the flux at the cell interfaces. $flux[i]$, where $i = 0, \ldots, n+1$.

3. Calculate the flux using the old values. $flux[i] = \text{muscl}(u_{old})$. The CFL number for the $x$-advection is $v\Delta t/\Delta x$ and that for the $v$-advection is $a\Delta t/\Delta v$, where $a$ is the acceleration.

[1] If negatively charge ions exist, those will contribute to the negative charges as well.
[2] A Fortran version of the Vlasov solver is also developed.

4. Update the values. $u[i][j] = u_{old}[i] - (flux[i+1] - flux[i])$ for each $j$.

5. Repeat for all $j$.

**Boundary Conditions**

The boundary conditions for the DK/Vlasov solver are twofold. There are boundaries for the $x$-advection and $v$-advection. The boundary conditions for the $v$-advection are straightforward as long as the domain is large enough and there are essentially no VDFs at the first and last cells in the $v$ direction. Otherwise, there may be particles with lower or higher velocity outside the domain in the velocity space. If the VDFs at the cell interfaces of the maximum and minimum velocities are small enough, either a Dirichlet boundary condition, *i.e.* specifying a zero value for the ghost cell, or a Neumann condition, *i.e.* specifying the gradient of the VDFs to be zero, works.

The boundary conditions for the $x$-advection require more consideration. First, the VDFs of $v \geq 0$ at $x = 0$ and those of $v < 0$ at $x = L$ must be assigned as the characteristics stem from outside the inner domain. For a non-emitting wall, the VDFs of the emitting particles at the wall are fixed at zero. Thus, the fluxes at these cell interfaces are zero. On the other hand, the VDFs of the particles that leave the domain, *i.e.* $v < 0$ at $x = 0$ and $v \geq 0$ at $x = L$, will not be affected by the information outside the domain. The flux calculation must be performed using only the interior information. Most importantly, it was found that the order of accuracy for the flux at these cell interfaces needs to be matched to that of the interior numerical schemes. A Neumann condition for the VDFs only results in first order accuracy as the flux is calculated from piecewise constant data from the interior cell adjacent to the boundary. At least a first-order extrapolation is required for the ghost cells outside the domain for these outgoing particles. This results in second-order accurate flux calculation at those interfaces.

**Parallel Computation**

Message-Passing Interface (MPI) is used for parallel computation. A Cartesian mesh is used for the phase space discretization and partitioned among multiple processors. Typi-

cally, the partition is performed as shown in Fig. 3.1. The global numbers of cells in the $x$ and $v$ directions are first defined, from which the cell size is determined, *i.e.* $\Delta x$ and $\Delta v$. The cell-centered VDFs are cell-averaged as a finite volume method is used for the DK/Vlasov solver.

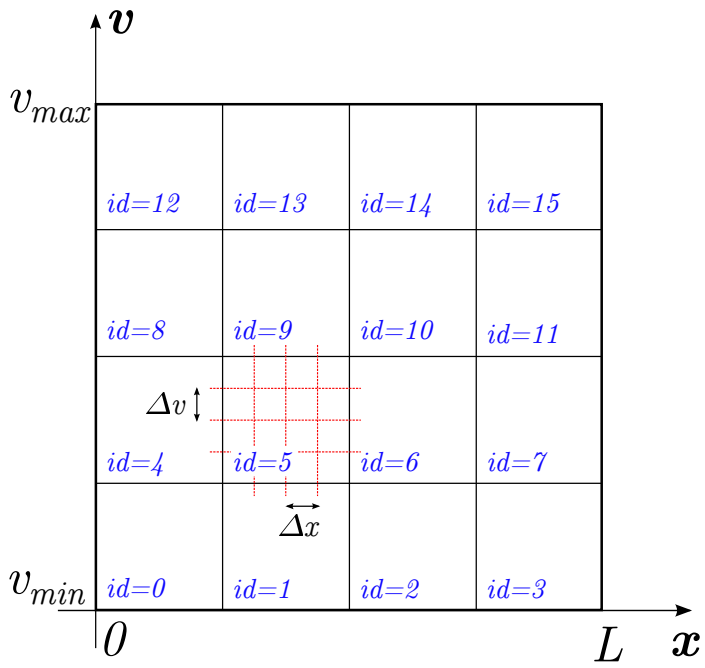


Figure 3.1: Example of the phase space partitioning in the DK/Vlasov solver when using 16 processors in total.

Each processor has partitioned phase space with 2 ghost cells, which are required due to the use of a finite volume method. These ghost cells are assigned physical quantities using a Dirichlet or Neumann condition at the boundaries of the global domain. However, the quantities from the neighboring processors must be exchanged for the interior region of the global domain. All processors store the array elements that are sent to the neighboring processors. Then, the elements are sent using MPI_Send. Simultaneously, the processors receive the information sent to themselves using MPI_Recv.

The number density in each physical cell is required for the Poisson solver. Each processor calculates the density from the moment of the VDFs and stores it into a local array. Then, these local arrays are summed together and stored into a global array using MPI_Allgather or MPI_Gather. Typically, the global array that summed the number den-

sity information from all processors is stored on the root processor, where the potential and the electric field are calculated. Then, the electric fields are copied to all processors using MPI_Bcast. The flowchart of the Vlasov-Poisson solver is shown in Fig. 3.2.

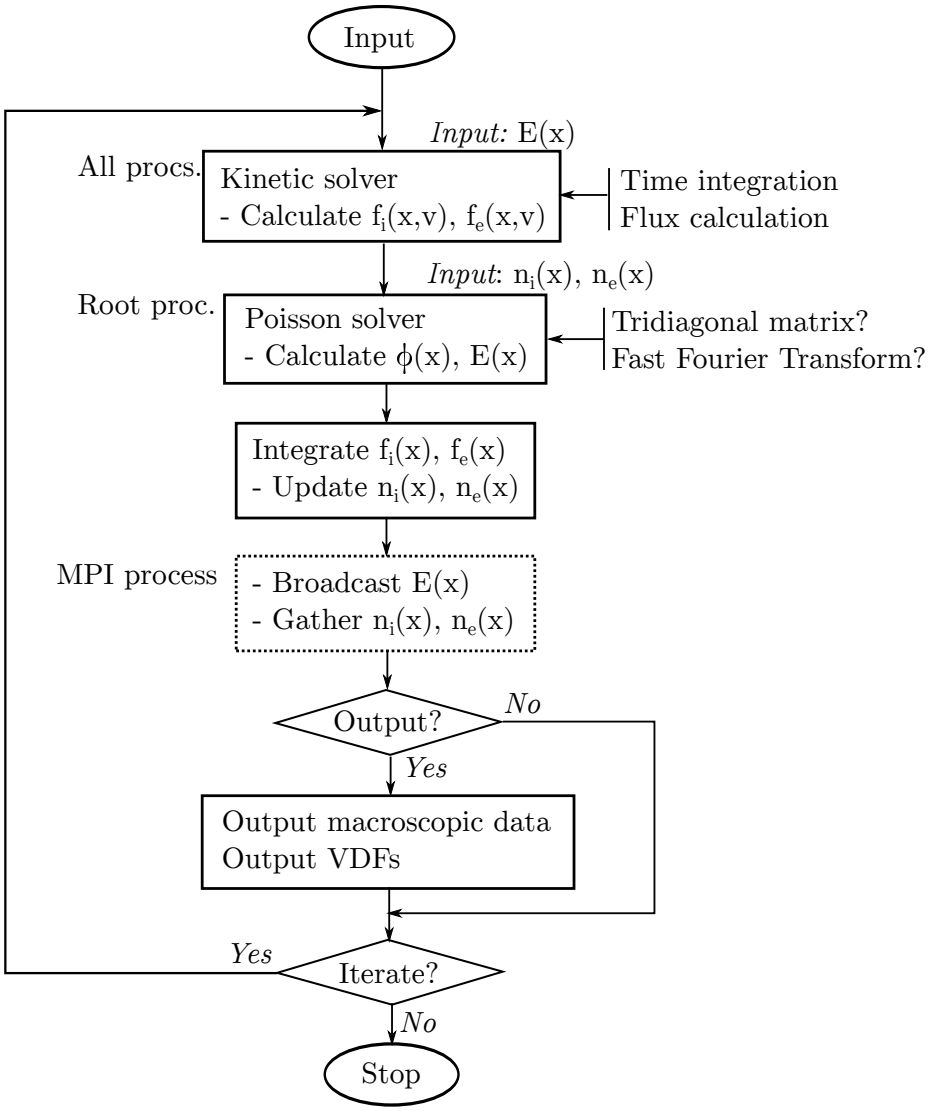


Figure 3.2: Implementation of the Vlasov-Poisson solver.

## 3.2 Classical Plasma Sheath

A plasma sheath is a boundary layer-type structure near plasma-immersed materials. When the potential at the material is fixed, then the difference between the plasma potential

and the wall potential determines the current balance.[3] On the other hand, for a material with floating potential, a plasma sheath will be formed to maintain the charge balance at the wall. When $T_e \gg T_i$, where $T_e$ and $T_i$ are the electron and ion temperatures, respectively, more hot electrons collide with the wall, therefore the wall initially becomes negatively charged, which will attract positive ions until the charges at the wall are balanced. As the standard HETs employ dielectric materials for the channel wall, the plasma sheath of a material with floating potential is investigated in this section.

### 3.2.1 Theory

Ions are assumed to be a monoenergetic beam and have a finite speed entering the sheath, $u_0$. Primary electrons are assumed to be thermalized, Boltzmann electrons. The sheath edge is assumed to be at $x = L$ and the wall is at $x = 0$, where $L$ is the sheath width. The potential at the sheath edge is assumed to be $\phi(x = L) = 0$. As $T_e \gg T_i$, we investigate a positive sheath, where $\phi(x) < \phi(x = 0) = 0$. A quasineutral assumption is used at the sheath edge: $n_i(x = L) = n_e(x = L) = n_0$, where $n_0$ is a constant. From the ion continuity and energy conservation equations, the ion density is described as

$$n_i = n_0 \left(1 + \frac{2e\phi}{m_i u_0^2}\right)^{-\frac{1}{2}} \tag{3.3}$$

where $\phi$ is the potential, $m_i$ is the ion mass, and $e$ is the elementary charge. The ion flux is simply $J_i = n_0 u_0$ throughout the sheath as there are no collisions. In addition, the analytic ion VDFs can be obtained from the Bohm-velocity shifted Maxwellian at the sheath edge, given by

$$f_i(x, v_x) = \begin{cases} n_0 \left(\frac{m_i}{2\pi k T_i}\right)^{1/2} \exp\left[-\frac{m_i}{2kT_i}\left(\sqrt{v_x^2 + \frac{2e\phi}{m_i}} - u_0\right)^2\right] & v_x \le -\sqrt{2e|\phi|/m_i} \\ 0 & v_x > -\sqrt{2e|\phi|/m_i} \end{cases} \tag{3.4}$$

The number density and flux of electrons can be calculated assuming a Maxwellian VDF

[3] For instance, when $\phi_w \ll \phi_p$, where $\phi_w$ is the wall potential and $\phi_p$ is the plasma potential, the electron density is significantly smaller near the wall and the ion current will be space charge limited: $J_i \sim V^{3/2}/d^2$, where $J_i$ is the ion flux, $V$ is the potential drop, and $d$ is the sheath width. This is often called the Child-Langmuir sheath.

at the sheath edge. Thus, the electron VDF inside the sheath can be given as,

$$f_e(x,v) = \begin{cases} n_{0,e}\left(\frac{m_e}{2\pi kT_e}\right)^{1/2} \exp\left(-\frac{mv^2}{2kT_e} + \frac{e\phi}{kT_e}\right) & v \le v_c \\ 0 & v > v_c \end{cases} \tag{3.5}$$

where $v_c = \sqrt{2e(\phi - \phi_w)/m_e}$ is the cutoff velocity of the truncated electrons due to the potential drop in the sheath, $m_e$ is the electron mass, and $\phi_w$ is the wall temperature. Note that the potential field obtained from the simulation results can be used for the potential $\phi$ in order to obtain the analytic solutions for ion and electron VDFs in Eqs. (3.4) and (3.5), respectively. The electron number density and flux can be calculated by taking the moment of Eq. 3.5:

$$n_e = \frac{n_{0,e}}{2}\left(1 + \mathrm{erf}\sqrt{\frac{e(\phi - \phi_w)}{kT_e}}\right) \exp\left(\frac{e\phi}{kT_e}\right), \tag{3.6}$$

$$J_e = \frac{n_{0,e}}{4}\sqrt{\frac{8kT_e}{\pi m_e}} \exp\left(\frac{e\phi_w}{kT_e}\right) \quad (= \text{const.}) \tag{3.7}$$

From Eq. (3.6), $n_e(x = L) = n_0$. Note that $\phi(x = L) = 0$ and $\phi_w < 0$. Thus, in order to maintain quasineutrality at the sheath edge, strictly speaking, $n_{e0}$ must satisfy

$$n_0 = \frac{n_{0,e}}{2}\left(1 + \mathrm{erf}\sqrt{\frac{e|\phi_w|}{kT_e}}\right). \tag{3.8}$$

For $|e\phi_w/kT_e| \gg 1$, it can be seen that the quasineutral assumption holds: $n_0 \approx n_{0,e}$. Thus, the electron density in Eq. (3.6) can be approximated as following the Boltzmann relation: $n_e = n_0 \exp(e\phi/kT_e)$.

The Bohm condition can be derived by taking the linear perturbation of the Poisson equation around $\phi(x = L) = 0$ and that of the ion and electron densities. From this linear perturbation equation evaluated at the sheath edge, $u_0 \ge c_s$, where $c_s = \sqrt{kT_e/m_i}$ is the ion acoustic speed. This is also called the Bohm speed. In addition, the sheath potential

$\phi_w$ obtained by the flux balance, $J_i = J_e$,[4] can be given by

$$\phi_w = -\frac{kT_e}{e} \ln \left( \frac{1}{\sqrt{2\pi m_e/m_i}} \right) \tag{3.9}$$

### 3.2.2 Boundary Conditions for the Sheath Simulation

At the wall, ions and electrons are absorbed and no particles are emitted or reflected. The electric field at the wall is determined by the charge accumulated by the ion and electron fluxes,[47] given by

$$E_w = E(x=0) = \frac{Q}{\epsilon_0} = \frac{e}{\epsilon_0} \int_{t'=0}^{t'=t} [J_{iw}(t') - J_{ew}(t')] dt', \tag{3.10}$$

where $E_w$ is the electric field at the wall, $Q$ is the charge accumulated at the wall, and $J_{iw}$ and $J_{ew}$ are the ion and electron fluxes at the wall, $x = 0$. From Gauss's law,[5] which is equivalent to the Poisson equation, the electric field at the sheath edge, $x = L$, and that at the wall, $x = 0$, are balanced by the charge inside the sheath region:

$$\epsilon_0(E_s - E_w) = e \int_{x=0}^{x=L} (n_i - n_e) dx, \tag{3.11}$$

where subscript $s$ denotes the sheath edge at $x = L$. Integrating the continuity equation[6] both in time and space can be expressed as $\int n dx = \int J_s dt - \int J_w dt$. Eq. (3.10) can be substituted into Eq. (3.11) to obtain the electric field at the sheath edge:

$$E_s = -\frac{e}{\epsilon_0} \int_{t'=0}^{t'=t} (J_{is} - J_{es}) dt'. \tag{3.12}$$

Therefore, if one wants to obtain $E_s(t) = 0$ at the sheath edge, the electron and ion fluxes at the sheath edge need to be adjusted accordingly. This can be done by assigning a boundary condition in the kinetic solver. At the sheath edge, the outgoing flux from the sheath region is not influenced by the information outside the domain, but the incoming flux

[4] Particle flux is $J = nu$ while the current density is $j = enu = eJ$, which is the flux of the charge. In addition, the current is $jA$, where $A$ is the area so that the units are $C/s = Amps$.

[5] Gauss's Law: $\nabla \cdot (\epsilon_0 \mathbf{E}) = e(n_i - n_e)$

[6] Continuity equation: $\partial n/\partial t = \nabla \cdot \mathbf{J}$

needs to be chosen carefully. It can be seen from Eq. (3.12) that the ion and electron fluxes that come into the sheath from the sheath edge essentially determine the electric field at the sheath edge. Here, we use a circular boundary condition, a boundary condition proposed by Shoucri[48] and Kolobov[49], for the electrons at the sheath edge. The boundary condition for the ions at the sheath edge is a Bohm velocity shifted Maxwellian.

The electric field at the sheath edge has been problematic for previous sheath simulations. Previous numerical results using a fixed ion VDF and a fixed half-Maxwellian electron VDF have shown that there will be a source sheath type structure at the sheath edge.[50, 51] The electron VDFs can be more accurately assigned from Eq. (3.12) in order to prevent the source sheath. The circular boundary condition works well and no source sheath type structure was found in our simulations, but it has been reported that this boundary condition does not work for higher order Vlasov methods. The implementation of a generalized boundary condition that prevents a source sheath will be reserved for future work.

### 3.2.3 Numerical Parameters

The grid size in the $x$ and $v$ directions are $N_x = 400$ and $N_v = 400$, respectively. The domain size in physical space is $L = 40\lambda_D$. The ion and electron velocity domains are $v_i \in [-5c_s, c_s]$ and $v_e \in [-6v_{th,e}6v_{th,e}]$, respectively, where $v_{th,e}$ is the electron thermal velocity. The cell size is $\Delta x = L/N_x = 0.1\lambda_D$ in the physical space, $\Delta v_i = (v_{i,max} - v_{i,min})/N_v = 0.015c_s$ in the $v$ direction for ions, and $\Delta v_e = (v_{e,max} - v_{e,min})/N_v = 0.3v_{th,e}$ in the $v$ direction for electrons. The time step is $\omega_p \Delta t = 0.001$ and the total time of simulation is $\omega_p T = 30$, $\omega_p$ is the electron plasma frequency, $\Delta t$ is the time step, and $T$ is the maximum time. Another parameter is the electron-to-ion temperature ratio: $T_e/T_i$. Here, $T_e/T_i = 10$ is assumed. The ions are assumed to be hydrogen molecule, *i.e.* $m_i/m_e = 2\beta$, where $\beta = 1836$ is the proton-to-electron mass ratio. Note that $v_{th,e}/c_s = \sqrt{m_i/m_e}\sqrt{T_e/T_i}$.

In the simulations, a Dirichlet boundary condition is used for the Poisson solver at the sheath edge, *i.e.* $\phi = 0$, and a Neumann condition is used at the wall, $\partial\phi/\partial x = -E_w$, as shown in Eq. (3.10). A Thomas Tridiagonal matrix solver is used to solve for the potential. Second-order central differencing is used to calculate the electric field from the potential. Note that the electric field interpolation must also employ a higher order differencing method

if higher order Vlasov simulation techniques are used.

Finally, the velocity, position, potential, and time are normalized by the ion acoustic speed, Debyle length, primary electron temperature, and electron plasma frequency, respectively.

### 3.2.4 Results obtained from the Vlasov-Poisson solver

The potential field obtained from the Vlasov-Poisson solver is shown in Fig. 3.3. The sheath potential is $e\phi_w = -3.17k_BT_e$. The difference between the sheath potential obtained from the Vlasov-Poisson solver and the theoretical prediction in Eq. (3.9), $e\phi_w = -3.18k_BT_e$, is approximately 1 %. This is possibly due to the use of the quasineutral assumption. In this simulation, quasineutrality is satisfied at the initial condition but not in every time step. A small density difference ($\sim 0.1\%$) and the discretization error may yield this small discrepancy in the sheath potential.

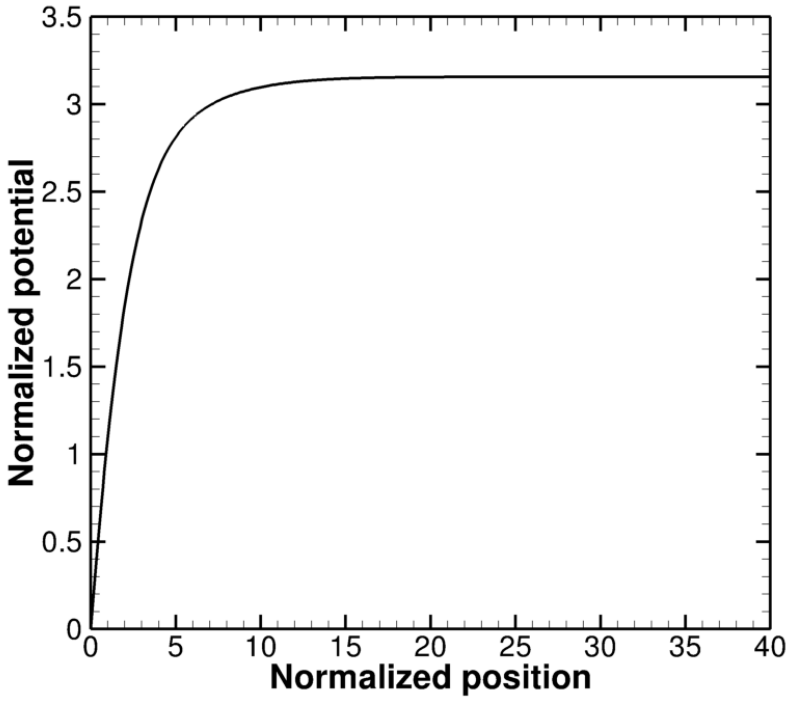


Figure 3.3: Steady-state potential obtained from the Vlasov-Poisson solver.

Figure 3.4 shows good agreement between the steady-state ion VDFs obtained from the Vlasov-Poisson solver and the theoretical predictions from Eq. (3.4), shown as solid

lines for each location. The theory curves employ the numerically-calculated potential field, $\phi(x)$, which is used in Eq. (3.4). Here, $x = 0$ corresponds to the wall and $x = 40\lambda_D$ is the sheath edge.[7] It can be seen that the numerical results near the wall differ slightly from the theory. The ion VDFs become narrower as ions are accelerated through the electric field as the total energy of ions, *i.e.* the sum of kinetic and thermal energies, needs to be conserved. There are some discrepancies between the numerical and theoretical predictions because the VDFs calculated from the Vlasov-Poisson solver become poorly resolved near the wall due to the fixed discrete phase space. In order to obtain better agreement with theory, a higher order method and/or smaller grid size can be used so that the numerical error is reduced.

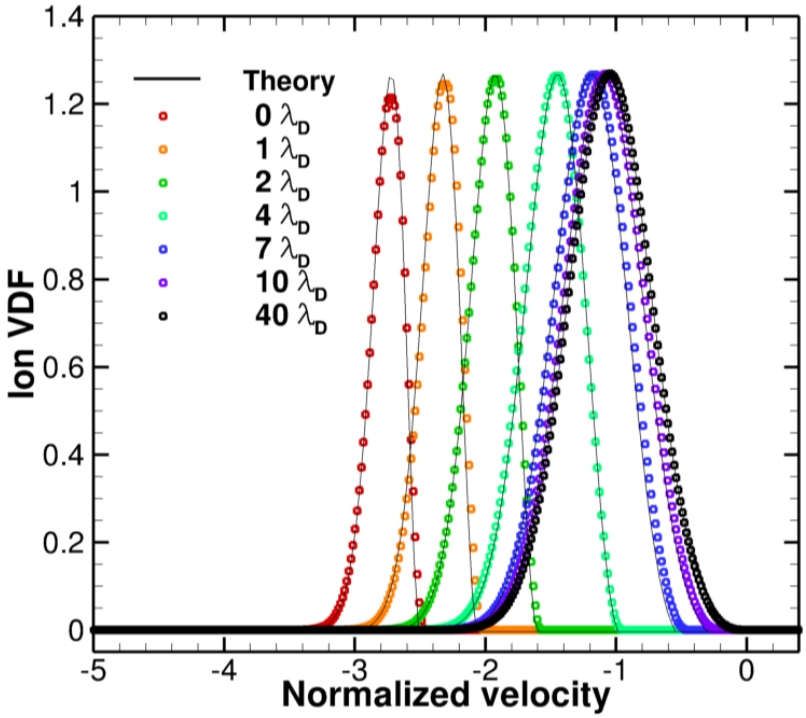


Figure 3.4: Ion velocity distribution functions obtained from the Vlasov-Poisson solver in comparison to the theoretical predictions using the potential field in Fig. 3.3.

The steady-state electron VDFs are shown in Fig. 3.5. Again, the potential field obtained from the Vlasov-Poisson solver is used to calculate the theoretical curves from Eq. (3.5). Good agreement between the numerical simulations and theory is shown, particularly

[7]The size of sheath region has been changed but the results are the same for $L \geq 30\lambda_D$.

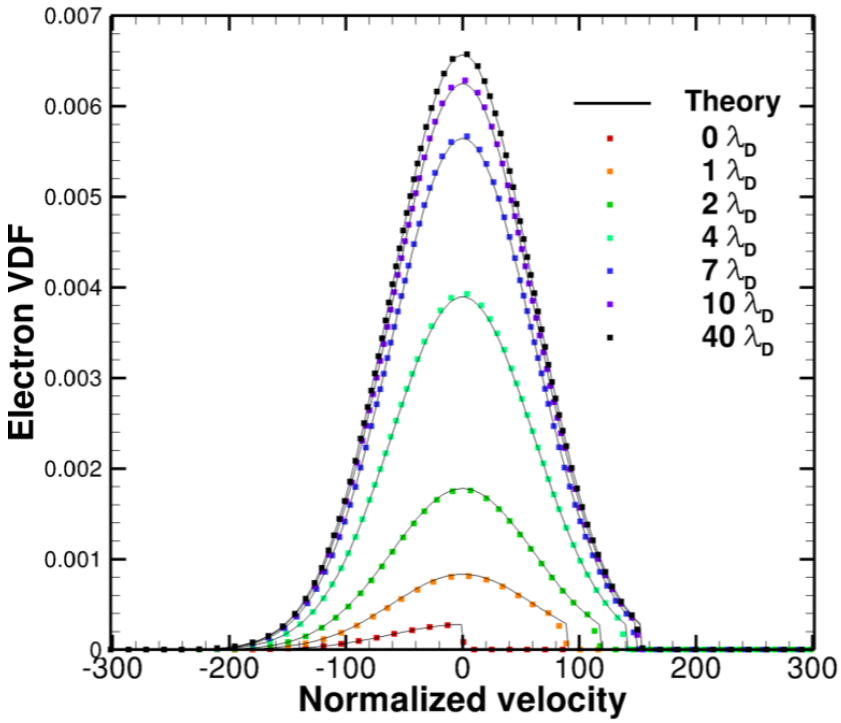


Figure 3.5: Electron velocity distribution functions obtained from the Vlasov-Poisson solver in comparison to the theoretical predictions using the potential field in Fig. 3.3.

in terms of the truncation of the EVDFs. The high positive velocity components that are flowing out of the sheath region are truncated due to the potential barrier. Note that these VDFs are not time-averaged results. It can be seen that there is no statistical noise in the simulation.

## 3.3 Plasma Sheath with Secondary Electron Emission

It has been known that electrons can be emitted from a plasma-immersed surface due to impacts of ions, electrons, and photons. This phenomenon is called secondary electron emission (SEE), which plays an important role in lowering the sheath potential and increasing the heat flux to the materials. For a dielectric material at $T_e$ = 10-50 eV, it is known that the rate of electron-induced SEE is dominant over the other SEE processes. Thus, in this dissertation, electron-induced SEE is investigated.

Hobbs and Wesson[52] proposed a fluid type theory and predicted a space charge limited (SCL) sheath, which acts as a virtual cathode that prevents excessive SEE from the wall.

A theory has been recently proposed by Sheehan *et al.*[51] to investigate the SCL regime using a kinetic description.

In the fluid and kinetic theories, the SEE coefficient $\sigma$ is defined as the ratio of the flux of secondary electrons to that of primary electrons.

$$\sigma = \frac{J_{see}}{J_e} \tag{3.13}$$

Hence, the steady-state flux balance between ions, primary electrons, and secondary electrons can be written as,

$$J_e - J_{see} = J_i, \tag{3.14}$$

where $J_{see}$ is the flux of secondary electrons. Ions and primary electrons follow the same expressions as Sec. 3.2. In Hobbs and Wesson's theory, secondary electrons are modeled as a cold electron beam emitted from the wall. In Sheehan's kinetic theory, they are modeled as half-Maxwellian with temperature $T_w$.

### 3.3.1 Theory with Secondary Electrons

The secondary electron flux is given by the product of the SEE rate and the primary electron flux that is constant in the sheath. For a monotonically decreasing sheath potential, the VDF of secondary electrons (SEVDF) can be described as

$$f_{see}(x, v_x) = \begin{cases} 2n_{see0}\left(\frac{m_e}{2\pi kT_w}\right)^{1/2} \exp\left(-\frac{mv^2}{2kT_w} + \frac{e(\phi-\phi_w)}{kT_w}\right) & v \geq v_c \\ 0, & v < v_c \end{cases} \tag{3.15}$$

where $n_{see0}$ is the number density of secondary electrons at the wall, $T_w$ is the temperature of the emitted electrons, and $v_c = [2e(\phi - \phi_w)/m_e]^{1/2}$ is the truncation velocity. Note that there is a coefficient, 2, in Eq. (3.15) due to normalization. At the wall, the SEVDF is a half-Maxwellian since $\phi = \phi_w$ and $v_c = 0$. The number density and flux of secondary electrons are given by,

$$n_{see} = n_{see0} \exp\left[\frac{-e(\phi - \phi_w)}{kT_w}\right] \left[1 - \mathrm{erf}\sqrt{\frac{e(\phi - \phi_w)}{kT_w}}\right], \tag{3.16}$$

$$J_{see} = J_{see,wall} = \frac{n_{see0}}{2}\sqrt{\frac{8kT_w}{\pi m_e}} \quad (= \text{const.}). \tag{3.17}$$

In order to evaluate $n_{see0}$, the relation $|J_{see}| = \sigma|J_e|$ at the wall, *i.e.* Eq. (3.13), is considered. Using the relation between the primary and secondary electron fluxes in Eqs. (3.7) and (3.17),

$$n_{see0} = \sigma\frac{n_{0e}}{2}\exp\left(\frac{e\phi_w}{kT_e}\right)\sqrt{\tau}, \tag{3.18}$$

where $\tau = T_e/T_w$. If the temperature of secondary electrons is very small, $T_w \to 0$, then the SEVDF in Eq. (3.15) reduces to a delta function and the number density at the wall is infinite. However, it can be shown that the number density from the kinetic description in Eq. (3.16) reduces to the expression proposed by Hobbs and Wesson[52] in the limit of $T_w \to 0$, given by

$$n_{see}^{HW} = \frac{\sigma}{1-\sigma}n_0\left[\frac{m_e u_0^2}{2e(\phi-\phi_w)}\right]^{1/2}. \tag{3.19}$$

The derivation is shown in Appendix B. Hobbs and Wesson's estimate for secondary electron density in Eq. (3.19) is different from Eq. (3.16) but still works well for small $T_w$. The kinetic formulation plays an important role when $T_w \to T_e$ and for smaller sheath potential, $|\phi_w| \to O(1)$.

#### 3.3.1.1 Bohm Condition

In order to obtain the sheath condition, the electron number density needs to be linearized. Linearization for a quantity $Q(x)$ can be described as $Q(x=0) + xQ'(x=0)$. The linearized natural exponential function for $\phi \ll 1$ is $\exp(\phi) \approx 1+\phi$ and the linearized error function is $\text{erf}(\phi) \approx \phi[\text{erf}(\phi)]'$, where $[\text{erf}(\phi)]' = 2\exp(-\phi^2)/\sqrt{\pi}$. From Eqs. 3.6 and 3.16, the linearized primary and secondary electron number densities can be written as

$$\frac{n_e}{n_0} \approx \frac{1}{2}\left[1 + \text{erf}\sqrt{|\Phi_w|} + \Phi H_1 + O(\Phi^2)\right]\frac{n_{0,e}}{n_0}, \tag{3.20}$$

$$\frac{n_{see}}{n_0} \approx \frac{A}{2}\left[1 - \text{erf}\sqrt{|\Phi_w|\tau} + \Phi H_2 + O(\Phi^2)\right]\frac{n_{0,e}}{n_0}, \tag{3.21}$$

where $\Phi = e\phi/kT_e$, $\Phi_w = e\phi_w/kT_e$, $O(\Phi^2)$ represents the higher order terms that are neglected in the linear perturbation equations, and

$$A = \sigma \exp\left[\Phi_w(1-\tau)\right]\sqrt{\tau},$$

$$H_1 = 1 + \mathrm{erf}\sqrt{|\Phi_w|} + \frac{\exp(\Phi_w)}{\sqrt{\pi|\Phi_w|}},$$

$$H_2 = \tau\left[1 - \mathrm{erf}\sqrt{|\Phi_w|\tau} - \frac{\exp\left(-|\Phi_w|\tau\right)}{\sqrt{\pi|\Phi_w|\tau}}\right].$$

From the linearized number densities of ions from Eq. (3.3), primary electrons in Eq. (3.20), and secondary electrons in Eq. (3.21), the linearized Poisson equation can be written as

$$\frac{1}{n_0}\frac{d^2\Phi}{dx^2} = -\Phi\left(\frac{1}{2E_0} - \frac{H_1 + AH_2}{n_0/n_{0,e}}\right), \tag{3.22}$$

where $E_0 = m_i u_0^2/2$ is the ion energy at the sheath edge. The ion mean velocity at the sheath edge can be obtained as

$$u_0 \geq c_s\left(\frac{H_1 + AH_2}{n_0/n_{0,e}}\right)^{-1/2}. \tag{3.23}$$

The minimum $u_0$ is a function of $\tau$ and $\phi_w$. In solving Eq. 3.23, $n_0/n_{oe}$ must be calculated. In order to satisfy quasineutrality at the sheath edge, the electron number density there must be equal to the ion number density. The quasineutral assumption can be written as $n_{see}(x = L) + n_{e0} = n_0$, where $x = L$ is the sheath edge. $\phi = 0$ at the sheath edge is inserted in Eqs. (3.6) and (3.16) to obtain

$$\frac{n_0}{n_{0,e}} = \frac{1}{2}\left[1 + \mathrm{erf}\sqrt{|\Phi_w|}\right] + \frac{A}{2}\left[1 - \mathrm{erf}\sqrt{|\Phi_w|\tau}\right], \tag{3.24}$$

which is a function of $\phi_w$ and $\tau$ as well. The maximum value of the function in Eq. (3.23) is approximately 1.16, which agrees with Hobbs and Wesson's theory.

#### 3.3.1.2 Sheath Potential

The sheath potential is calculated from the flux conservation in Eq. (3.14) that can be written as

$$\frac{n_{0,e}}{\sqrt{2\pi}} \exp\left(\frac{e\phi_w}{kT_e}\right) \sqrt{\frac{kT_e}{m_e}} = \frac{1}{1-\sigma} n_0 u_0. \tag{3.25}$$

Therefore, the sheath potential is given by

$$\phi_w = -\frac{kT_e}{e} \ln\left(\frac{n_{0,e}}{n_0} \frac{1-\sigma}{u_0\sqrt{2\pi m_e/m_i}}\right), \tag{3.26}$$

where $u_0$ and $n_{0e}/n_0$ are from Eq. (3.23) and Eq. (3.24), respectively. As the right hand side of Eq. (3.26) is a function of $\tau$ and $\phi_w$, this needs to be solved using an iterative solution finder, such as Newton's method.

There are two correction terms in the sheath potential from Hobbs and Wesson's theory. The quasineutrality condition needs to be obtained from Eq. (3.24), and the ion mean velocity at the sheath edge is obtained from Eq. (3.23). These corrections are very important to obtain the relation in a very special case when the sheath collapses for $\sigma = 1$ and $T_e = T_w$.[51] The number density ratio cannot be zero or infinity. The numerator in the logarithm in Eq. (3.26) reaches zero in the limit $\sigma \to 1$. Using L'Hospital's rule, $u_0$ needs to be zero at $\sigma \to 1$ so that $\phi_w$ has a finite value. Therefore, the Bohm condition is violated at $\sigma \to 1$ for $T_e = T_w$.

### 3.3.2 Electron Velocity Distribution Functions

The numerical setup is similar to Sec. 3.2. The boundary conditions for ions and electrons in the Vlasov-Poisson solver are kept the same and secondary electrons are added as an additional species. The boundary condition for SEVDFs is a half-Maxwellian with a temperature $T_w$ at the wall. There is no electron flux inflow from the sheath edge for the secondary electrons. In this set of simulations, $\tau = T_e/T_w$ and $\sigma$ are varied and the sheath potential is investigated.

Figure 3.6 shows the VDFs of primary and secondary electrons at the sheath edge with various SEE rates for $\tau = 10$. It can be seen that the truncation velocity of the primary

electrons agree with that of the secondary electrons in Eq. (3.15). It can be also seen that the peak of the SEVDF increases as $\sigma$ increases. Thus, the number density of secondary electrons also increases. It was not observed in the simulation, but a larger beam-type component from the secondary electrons may trigger bump-on-tail type instabilities in the presheath or bulk plasma.

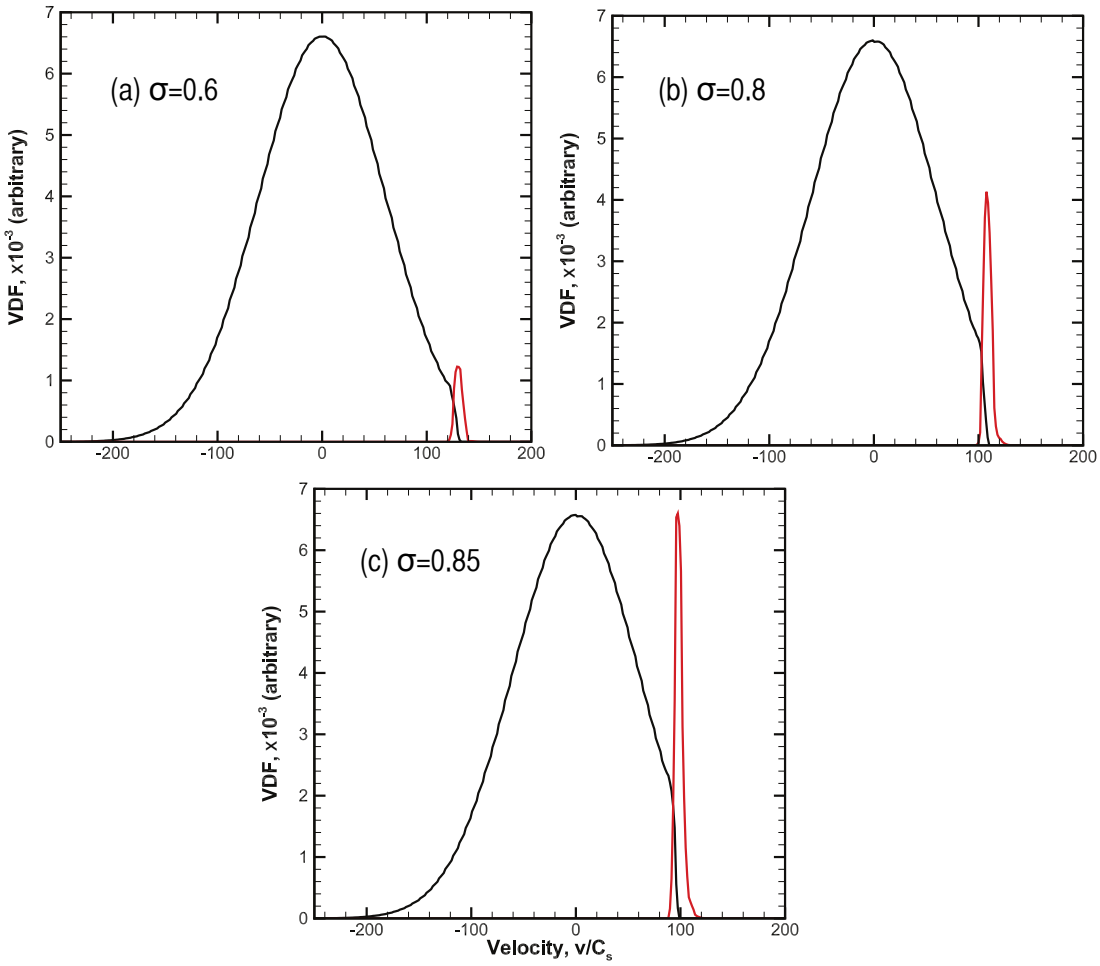


Figure 3.6: Electron velocity distribution functions for $\tau = T_e/T_w = 10$. Black and red solid lines illustrate primary and secondary electrons, respectively.

### 3.3.3 Sheath Potential Results

For a SEE rate larger than the critical rate, the secondary electrons are reflected back to the material in order to satisfy flux conservation inside the sheath. A virtual cathode type structure can be formed near the plasma-immersed material. This is also often called the

space charge limited (SCL) sheath. Critical SEE coefficients, where SCL sheath occurs, in Hobbs and Wesson's theory[52] are obtained by solving the flux conservation, the integrated Poisson equation evaluated at the sheath edge and at the wall. There are three equations to solve for three variables: $u_0$, $\phi_w$, and $\sigma$. Solving the system, the critical values are

$$u_0 = 1.16\sqrt{\frac{k_B T_e}{m_i}} \tag{3.27}$$

$$\phi_{w,SCL} = -1.02\frac{k_B T_e}{e} \tag{3.28}$$

And, inserting these values into the Eq. 3.14, the SCL SEE rate can be derived as

$$\sigma_{SCL} = 1 - 8.3\sqrt{\frac{m_e}{m_i}}$$

Sheehan *et al.* found that these values can be corrected using the VDF of secondary electrons instead of a cold electron beam. As can be seen from Eq. (3.26), the SCL sheath potential is a function of $\tau$. It was found that the SCL sheath potential decreases as $\tau = T_e/T_w$ decreases. In particular, the sheath potential for $\tau = T_e/T_w \to \infty$ is

$$\phi_{w,SCL} = -0.87\frac{kT_e}{e}. \tag{3.29}$$

Figure 3.7 shows good agreement between the SCL sheath potential obtained from the Vlasov-Poisson solver and from Sheehan *et al.*'s theory. There is a larger discrepancy at higher $\tau$ primarily due to the constant grid size. At higher $\tau$, $T_w$ is small and hence the distribution functions of secondary electrons become more beam-like. The Vlasov simulation yields more accurate results for VDFs with a wide distribution rather than a narrow beam-like distribution since the grid size needs to be smaller to resolve a narrow distribution.

The cases for $\tau < 2$ were not studied using the Vlasov-Poisson solver since the Bohm condition must be modified. The ions no longer require velocities larger than ion acoustic speed, as shown in Eq. (3.27). In order to study $\tau \to 1$, the boundary condition for ions needs to be changed according to the theory. Otherwise, a simulation that includes the presheath region is required as the ion Bohm speed is no longer an input parameter, making

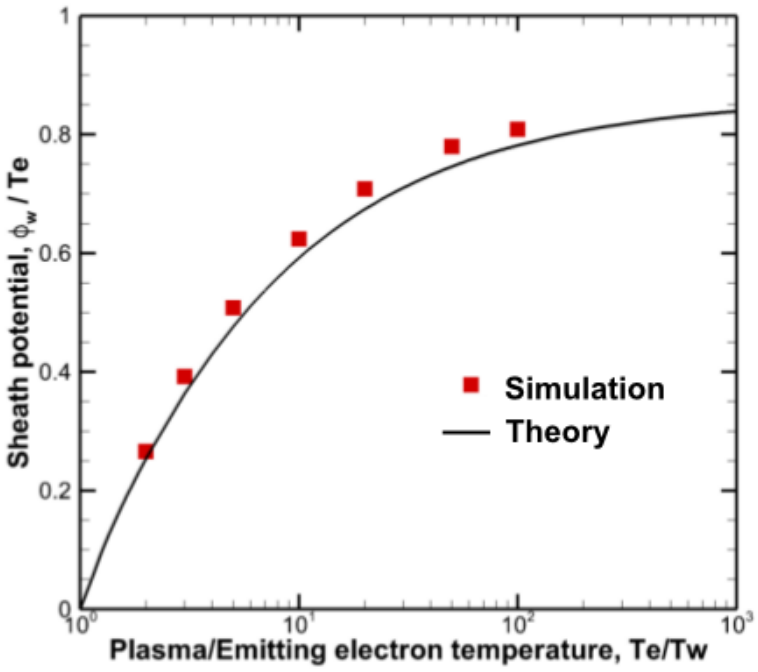


Figure 3.7: Space charge limited sheath potential versus $\tau = T_e/T_w$

it possible to investigate whether the Bohm condition is actually satisfied across a wide range of parameters. However, this also introduces some other physical phenomena, namely, collisions. It is observed by Oksuz and Hershkowithz[53] that the presheath length is on the order of the ion-neutral collision mean free path. A DK simulation that includes charge exchange collisions for ions has been developed and the numerical simulations including the presheath, sheath, and wall are discussed in Ref. [54]. Further analysis and development will be reserved for future work.

Figure 3.8 shows the numerically- and theoretically-predicted sheath potential across a wide range of SEE rates. A good agreement is shown for different $\tau = T_e/T_w$, *e.g.* $\tau = 10$ and 200. The kinetic theory curve for $\sigma < \sigma_{SCL}$ is almost identical to Hobbs and Wesson's theory. This means that the cold electron beam assumption for secondary electrons in Eq. (3.19) is valid for $\sigma < \sigma_{SCL}$. However, the difference appears in the SCL sheath that occurs at different SEE rates and consequently different sheath potentials. For instance, the theory and numerical simulations show that the SCL region occurs at lower sheath potential than Hobbs and Wesson's theory in Eq. (3.28). The Vlasov-Poisson solver accurately captures

the transition to the SCL sheath as a function of $\tau$. There is a slight increase in the sheath potential in the SCL region as $\sigma$ increases. This is primarily due to the discretization error since the virtual cathode, *i.e.* the potential drop between the wall potential and the minimum potential, is small and may be comparable to the grid size. Although a finer grid size is required to resolve such small-scale phenomena near the wall, the virtual cathode is captured well, as shown in the next section.

### 3.3.4 Virtual Cathode Analysis

As shown in Fig. 3.9, the Vlasov-Poisson solver also predicts a small potential drop near the wall for a large $\sigma$. First, the minimum potential $\phi_{drop}$ is determined by the SCL values. Thus, $\phi_{drop} = \phi_{w,SCL}$. The virtual cathode potential $\Delta\phi = \phi_w - \phi_{drop}$ is on the order of the wall temperature $T_w$, which can be calculated analytically.

The flux balance is illustrated in Fig. 3.10. The secondary electron flux emitted from the wall $J_{see}^{tot}$ is determined by $J_{see}^{tot} = \sigma J_e$. The primary electron flux is space charge limited

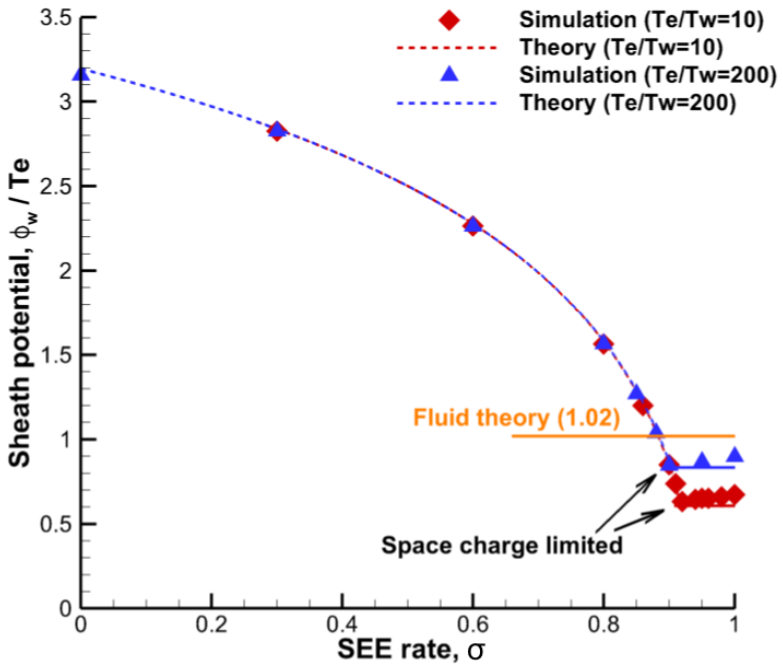


Figure 3.8: Sheath potential versus SEE rate for $\tau = 10$ and $\tau = 200$.

and determined by $\phi_{drop} = \phi_{w,SCL}$ in Eq. (3.7) for $\sigma > \sigma_{SCL}$. Thus, $J_{see}^{tot} = \sigma J_{e,SCL}$. However, the secondary electron flux that reaches the sheath edge, $J_{see}$, is determined by the critical SEE rate $\sigma_{SCL}$: *i.e.* $J_{see} = \sigma_{SCL} J_{e,SCL}$. The secondary electron flux that is reflected back to the material $J_{see}^{refl.} = J_{see}^{tot} - J_{see}$ can also be calculated by taking the first moment of Eq. (3.15) from $v = \sqrt{2e\Delta\phi/m_e}$ to $v = \infty$ at the wall, where $\phi = \phi_w$:

$$J_{see}^{refl.} = \frac{n_{see0}}{2}\sqrt{\frac{8k_B T_w}{\pi m_e}}\left[1 - \exp\left(-\frac{e\Delta\phi}{k_B T_w}\right)\right],$$

which has a correction term that reduces the emitted electron flux in comparison to Eq. (3.17). The relation between $n_{see0}$ and $n_{0e}$ in Eq. (3.18) holds for $\sigma$ and $\phi_w$ is replaced by

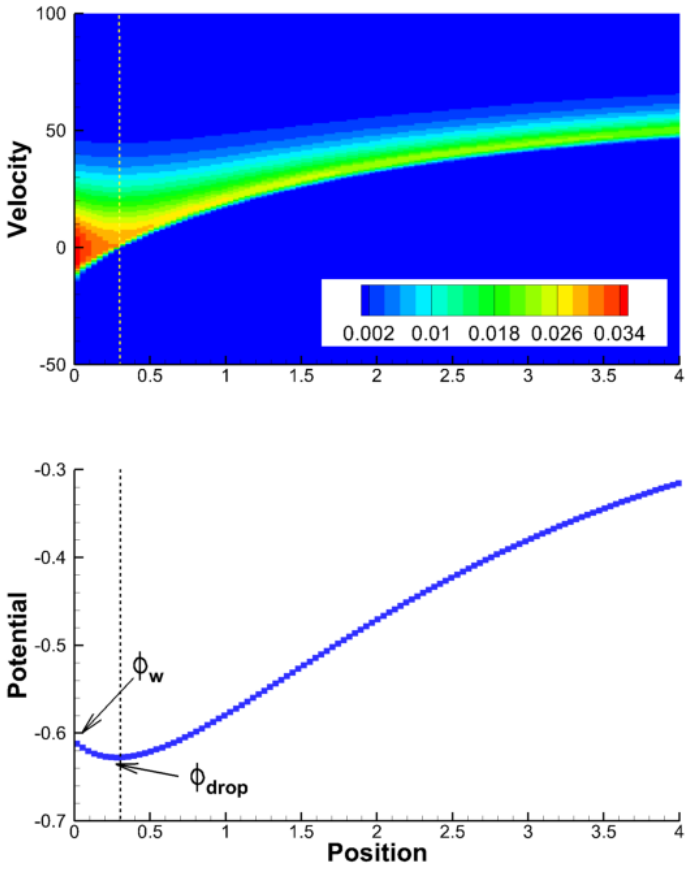


Figure 3.9: Secondary electron velocity distribution functions and potential profile of a virtual cathode near the wall for large $\sigma > \sigma_{SCL}$. This case is for $\tau = 10$ and $\sigma = 1.05$. Dashed line represents the virtual cathode position.

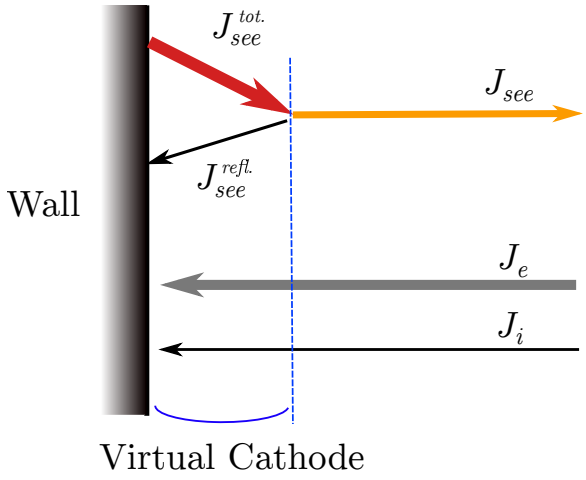


Figure 3.10: The balance between the ion, primary electron, and secondary electron fluxes in a space charge limited sheath.

$\phi_{w,SCL}$. Therefore,

$$(\sigma - \sigma_{SCL})J_{e,SCL} = \sigma J_{e,SCL}\left[1 - \exp\left(-\frac{e\Delta\phi}{k_B T_w}\right)\right]$$

Hence, the virtual cathode potential drop can be written as,

$$\Delta\phi = \frac{k_B T_w}{e}\ln\left(\frac{\sigma}{\sigma_{SCL}}\right) \quad \text{for } \sigma \geq \sigma_{SCL}. \tag{3.30}$$

In terms of the primary electron temperature,

$$\frac{e\Delta\phi}{k_B T_e} = \frac{1}{\tau}\ln\left(\frac{\sigma}{\sigma_{SCL}}\right) \quad \text{for } \sigma \geq \sigma_{SCL}. \tag{3.31}$$

In the limit of $\tau \to \infty$, the virtual cathode potential drop is essentially negligible relative to the sheath potential. It can also be seen that $\Delta\phi = 0$ is satisfied for $\sigma = \sigma_{SCL}$ and the virtual cathode is typically smaller than the sheath potential. The results shown in Fig. 3.9 are for $\tau = 10$ and $\sigma = 1.05$. Thus, $e\Delta\phi/k_B T_e \approx 0.015$ from Eq. (3.31). This agrees well with the results obtained from the Vlasov-Poisson solver, $e\Delta\phi/k_B T_e \sim 0.02$, as shown in Fig. 3.9.

## 3.4 Nonlinear Plasma Waves

Landau damping has served as a good verification test problem in the plasma community, both for particle- and grid-based kinetic methods. However, the physics of particle-wave interactions is quite complicated and is found to be important in laser-induced fusion plasmas and astrophysical plasmas. Here, starting from Landau damping, the electron plasma waves (EPWs), ion acoustic waves (IAWs), and trapped particle bunching instability, a newly found instability, are investigated using the Vlasov-Poisson solver.

Plasma waves may trap particles in traveling potential wells, leading to instabilities such as sideband instability.[55] This is found to be important in nonlinear saturation of scattering light process in laser-plasma interactions and in astrophysical plasmas. For a sinusoidal electric field, the particle VDFs near the phase velocity can be illustrated as Fig. 3.11. This stationary, nonlinear wave solution is called the Bernstein-Greene-Kruskal (BGK)[8] wave.[56] The red lines describe the trapped particles while the green lines show untrapped particles. The black solid line is the separatrix, where the velocity in the wave frame is zero.

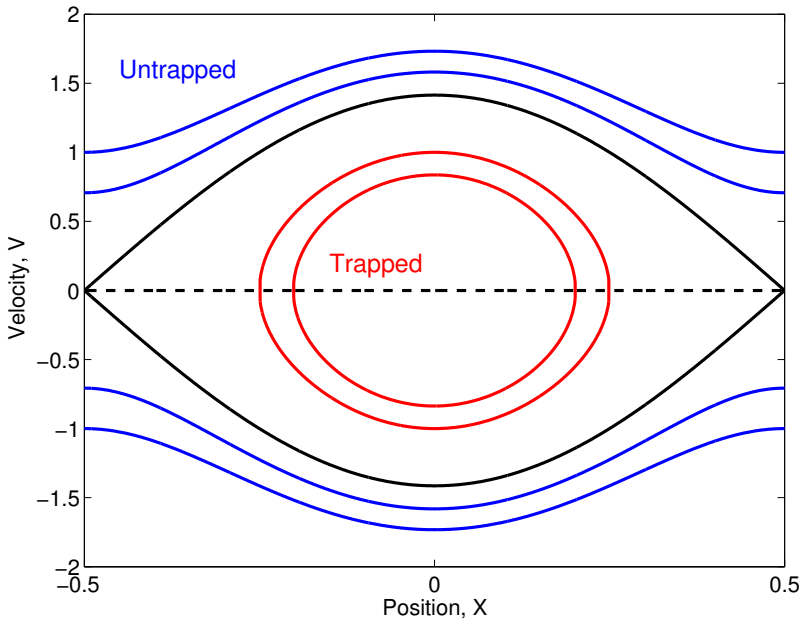


Figure 3.11: Bernstein-Greene-Kruskal (BGK) solution in the wave frame for a given sinusoidal potential. Black line is the separatrix.

[8]This is different from the Bhatnagar-Gross-Krook (BGK) collision operator in Sec. 2.1.

### 3.4.1 Landau Damping

The Landau damping problem has served as a good verification test case for the Vlasov simulation community. This is primarily because the problem is easy to setup and the damping rate can be derived analytically. Landau damping rate, $\gamma_L$, for an arbitrary distribution can be given by

$$\gamma_L = -\frac{\pi}{2}\frac{\omega_p^2}{k_0}\left[v\frac{\partial \hat{f}_0}{\partial v}\right]_{v=v_\phi}, \tag{3.32}$$

where $k_0 = 2\pi/\lambda_0$ is the wavenumber, $\lambda_0$ is the wave length, $\hat{f}_0$ is the initial normalized VDF, and $v_\phi = \omega/k_0$ is the phase velocity. In the case of a Maxwellian distribution,

$$\gamma_L = \sqrt{\frac{\pi}{8}}\frac{1}{(k_0\lambda_D)^3}\frac{\omega}{\omega_p}\exp\left[-\frac{1}{2}\left(\frac{\omega}{k_0 v_{th,e}}\right)^2\right], \tag{3.33}$$

where $\lambda_D = v_{th,e}/\omega_p$ is the Debye length and $v_{th,e}$ is the electron thermal velocity.

Numerically, Landau damping can be tested by allowing a density perturbation. For simplicity, it is assumed that ions are immobile and the ion density is constant throughout the domain. The initial condition of the electron VDFs is given by,

$$f(x,v) = \left[1 + \frac{\delta n}{n_0}\cos(k_0 x)\right] f_M(v), \tag{3.34}$$

where $\delta n/n_0$ is the magnitude of the density perturbation and $f_M(v)$ is a Maxwellian distribution: $f_M(v) = (2\pi)^{-1/2}\exp(-v^2/2)$ .

The numerical parameters are $\delta n/n_0 = 0.5$, $k_0\lambda_D = 0.5$, $N_x = 128$, and $\omega_p\Delta t = 0.001$, where $N_x$ is the number of cells in the $x$ direction. One wavelength system, $L = \lambda_0 = 2\pi/k_0 = \pi\lambda_D$, is considered and a periodic boundary condition is used in physical space. The velocity space is $v \in [-8v_{th}, 8v_{th}]$. For the Poisson equation with a periodic boundary condition, a fast Fourier transform (FFT) algorithm is used. Landau damping is often studied by analyzing the total electrostatic energy:

$$\Sigma E = \int \frac{\epsilon_0 |E_x(x)|^2}{2} dx,$$

which is the integral of the field energy in the plasma wave. Note that the total energy, the sum of the total kinetic energy and the total electrostatic energy, is conserved. Thus, particles gain kinetic energy while the plasma wave is Landau damped. As Landau damping occurs, the total electrostatic energy damps $\Sigma E \sim \exp(\gamma t)$.

Figure 3.12 shows a direct comparison of the Vlasov-Poisson solver, shown as DK, and a standard particle-in-cell (PIC) simulation. It can be seen that the initial decay is due to Landau damping and electrostatic energy increases again due to the bounce motion of trapped particles. If the initial perturbation is small enough, the trapped particle region becomes small and Landau damping occurs for a longer time down to a smaller electrostatic energy.

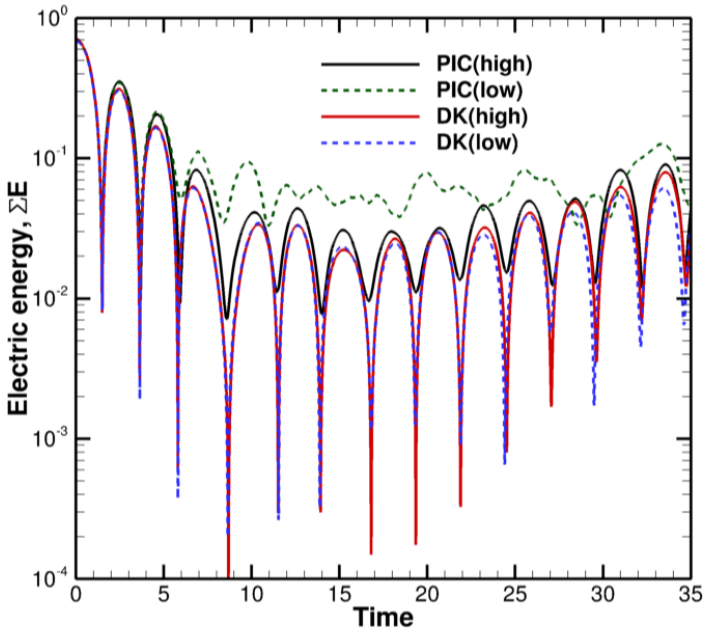


Figure 3.12: Nonlinear Landau damping: PIC vs Vlasov, denoted as DK in the figure, with different number of particles (PIC) and different grid size in velocity space (Vlasov) while the grid size in physical space is kept constant.

Here, high and low resolution PIC correspond to $N_p = 1000$ and $N_p = 64$, respectively, where $N_p$ is the number of particles per cell. High and low resolution DK correspond to $N_v = 256$ and $N_v = 32$, respectively. The spatial discretization is unchanged: $N_x = 128$ in all four cases. Note that $N_p = 64$ is very small for a particle method, but the purpose was

to compare the same order of degrees of freedom as the Vlasov solver. A good convergence[9] of the numerical simulation is shown for the Vlasov simulation. A small number of velocity space bins can capture the nonlinear trapping phenomena while some deviations can be seen at later time $\omega_p t \sim 40$.

On the other hand, numerical convergence is not fully achieved by the PIC simulations. Even the low resolution PIC case can capture some of the linear Landau damping effect, but the nonlinear bounce motion is not obtained accurately. While a qualitative agreement can be seen from the high resolution PIC and the Vlasov simulations, $N_p = 1000$ may still not be sufficient for numerical convergence. For instance, the large negative peaks of the electrostatic energy in the Vlasov results are not captured by the PIC simulations due to statistical noise. This is because the presence of statistical noise yields a non-zero electric field. This figure shows the advantage of a grid-based DK method over a particle-based kinetic simulation, particularly for nonlinear particle trapping in plasma waves.

### 3.4.2 Electron Plasma Waves

The Vlasov-Poisson solver is compared with an analytic theory of the frequency shift in nonlinear plasma waves. From the linearized Vlasov equation, the kinetic dielectric function of the plasma waves can be written as,

$$\frac{\epsilon_L(k,\omega)}{\epsilon_0} = 1 - \sum_{\text{species}} \frac{\omega_p^2}{k_0} \int dv \frac{\partial \hat{f}_0/\partial v}{v - \omega/k_0}. \tag{3.35}$$

A linear perturbation in the dispersion relation can be taken in terms of a small frequency shift about the linear frequency, $\omega_L = \omega_L(k)$, at which the dielectric function is zero: $\epsilon_L(k,\omega_L) = 0$. The dispersion relation can be written as $\epsilon_L(k,\omega) = \epsilon_L(k,\omega_L) + (\omega - \omega_L)(\epsilon_L)' = -\sum \Delta\epsilon_{NL}$, where $\Delta\epsilon_{NL}$ is the nonlinear correction from each species to the kinetic dispersion relation due to particle trapping. The nonlinear frequency shift can be written as

$$\delta\omega_{NL} = \omega - \omega_L = -\left[\left(\frac{\partial \epsilon_L}{\partial \omega}\right)_{\omega=\omega_L}\right]^{-1} \sum_{\text{species}} \Delta\epsilon_{NL}. \tag{3.36}$$

[9]Convergence: the numerical solution converges to an *exact* solution in the limit of $h \to 0$, where $h$ is the discretized time step or grid size.

$\Delta\epsilon_{NL}$ is dependent on how the wave is generated. The two extrema are *sudden* and *adiabatic* distributions.[57] The sudden distribution is when the initial distribution instantly becomes trapped by the finite amplitude field. The adiabatic distribution occurs when the wave is driven up and the particles are trapped sufficiently slowly. The nonlinear frequency shift is then given by

$$\delta\omega_{NL} \approx -\left[\left(\frac{\partial\epsilon_L}{\partial\omega}\right)_{\omega=\omega_L}\right]^{-1} \sum_{\text{species}} \alpha\frac{\omega_p^2}{k_0^2}\,\Delta v_{tr}\frac{d^2\hat{f}_0}{dv^2}\bigg|_{v=v_\phi}, \tag{3.37}$$

where $\alpha = 0.823$ is the sudden and $\alpha = 0.544$ is the adiabatic wave generation, $\Delta v_{tr}$ is the trapping velocity width, and $\phi_0$ is the amplitude of a sinusoidal potential. Note that $\Delta v_{tr} = \Delta v_{th,e}$ for electrons in the EPW cases, where $\Delta v_{th,e} = (2e\phi_0/m_e)^{1/2}$ and $\Delta v_{tr} = \Delta c_s$ for ions in the IAW cases, where $\Delta c_s = (2e\phi_0/m_i)^{1/2}$. Finally, in order to estimate the nonlinear frequency shift, $\partial\epsilon_L/\partial\omega$ can be calculated from either the fluid or kinetic dispersion relation. For instance, the dielectric function for thermal electrons is given by $\epsilon_L(k,\omega) = 1-(\omega_p/\omega)^2 - 3(kv_{th,e})^2\omega_p^2/\omega^4$. Assuming that $k\lambda_D \ll 1$, the linear frequency can be written as $\omega_L^2 = \omega_p^2 + 3(kv_{th})^2$, which is often called the Bohm-Gross relation, and the derivative of $\epsilon_L$ can be estimated as,

$$\left(\frac{\partial\epsilon_L}{\partial\omega}\right)_{\omega=\omega_L} \approx \frac{2}{\omega_p}. \tag{3.38}$$

For verification of the Vlasov solvers, a plasma wave can be generated either by using an external force that mimics the ponderomotive force that occurs due to light wave beating in ICF plasmas or by assigning a density perturbation to investigate the nonlinear trapping via Landau damping. For a driven wave, an external force drives the wave, given by

$$E_{ext} = E_0(t)\cos(\omega_{ext}t - k_0x), \tag{3.39}$$

where $\omega_{ext}$ is chosen from the dispersion relation for a given $k_0$ and $E_0(t)$ contains ramp-up,

constant driver, and ramp-down, given as

$$E_0(t) = \begin{cases} \frac{1}{2}\left[1 + \tanh\left(4\left\{\frac{2t}{t_r} - 1\right\}\right)\right] & \text{if } t < t_r \\ \frac{1}{2}\left[1 + \tanh\left(4\left\{\frac{2[(t-t_d)}{t_r} - 1\right\}\right)\right] & \text{if } t_r \le t < t_r + t_d \\ 0 & \text{otherwise} \end{cases} \tag{3.40}$$

Ramp up and down times, $t_r$, are found to be insensitive to the plasma wave generation[10] whereas the time at which the maximum amplitude of the driver is turned on, $t_d$, affects the plasma wave. The shape of the driver is chosen such that the plasma wave is slowly and adiabatically driven, otherwise some high order harmonic wave may be generated. The ramp-up and ramp down time of the external driver are $\omega_p t_r = 25$ and the constant driver time is $\omega_p t_d = 200$. The amplitudes of $E_0$ are varied so that the trapping velocity width $\Delta v_{tr}$ varies. All EPW simulations are performed with time step $\omega_p \Delta t = 2.5 \times 10^{-5}$, cell size in physical space $\Delta x = L/N_x$, cell size in velocity space $\Delta v = (v_{max} - v_{min})/N_v$, with $N_x = 1028$ and $N_v = 4000$, $L = 2\pi/k_0$, and $k_0\lambda_D = 1/3$. The frequency of the external driver is found from the kinetic dispersion relation: $\omega_{ext} = 1.2\omega_p$ for $k_0\lambda_D = 1/3$. These simulations are run on Dawson clusters in the Princeton Plasma Physics Laboratory and Flux clusters in the University of Michigan. A typical simulation on the Flux clusters takes 3 hours using 16 processors.

The nonlinear plasma frequency $\omega_{NL} = \omega - \omega_L$ is plotted against the trapping velocity width in Fig. 3.13 for a driven EPW case. The plasma-wave frequency $\omega$ is obtained over a time window after the driver is turned off and the wave is settled. A Hilbert transform technique is used to find the frequency. The trapping velocity width is measured from the magnitude of the potential field obtained from the simulations. For the reference frequency of the nonlinear frequency shift, $\omega_L$ is obtained by extrapolating the simulation results to $\Delta v_{tr} \to 0$, which is described in Ref. 58.

It can be seen that the numerical results agree with the theoretical estimate of an adiabatic distribution over a wide range of parameters. This is because the particles are

[10]There are some high order harmonic waves that can be excited for a very fast ramp up, but typically such harmonic waves are $\omega = n\omega_L$ with $n = 1, 2, \ldots$. As the phase velocity is $n$ times larger than that of the fundamental frequency, the number of trapped particles is also small since the trapped region is in the tail of the distribution.

trapped sufficiently slowly by the external driver. Hence, the trapped particles follow the adiabatic distribution without any higher order harmonics generated. In addition, the linear frequency obtained by the extrapolation technique $\omega_L$ agrees well with the initial driver frequency $\omega_{ext}$ within 0.1 %.

Figure 3.14 shows the nonlinear Landau damping case. The magnitude of the initial density perturbation is varied and the wave frequency and the trapping velocity width are obtained from the numerical simulations. Simulation results show qualitative agreement with the theory curve in Eq. (3.37) where a sudden distribution is assumed. The larger frequency shift is due to the larger number of particles being trapped by the sudden wave generation. The dispersion relation is significantly modified, and hence the $\alpha$-parameter in Eq. (3.37) is larger than that of the adiabatic case.

However, the agreement between numerical simulations and theory for the initial perturbation case is not as good as the driven case, possibly due to the higher order nonlinear plasma waves generated. This can be seen from the calculated electron VDF, as shown in Fig. 3.15, for $\delta n/n_0 = 0.05$ and $k_0\lambda_D = 0.425$. The trapping region becomes more

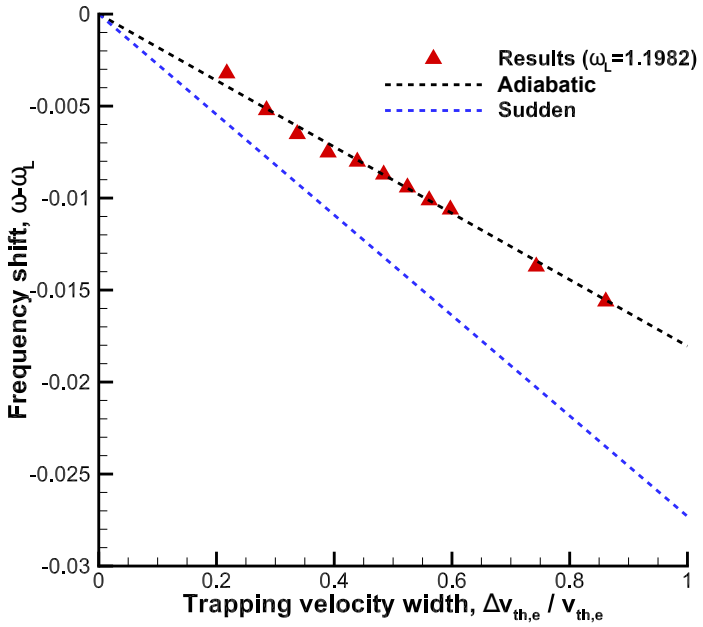


Figure 3.13: Driven EPW for $k_0\lambda_D = 1/3$

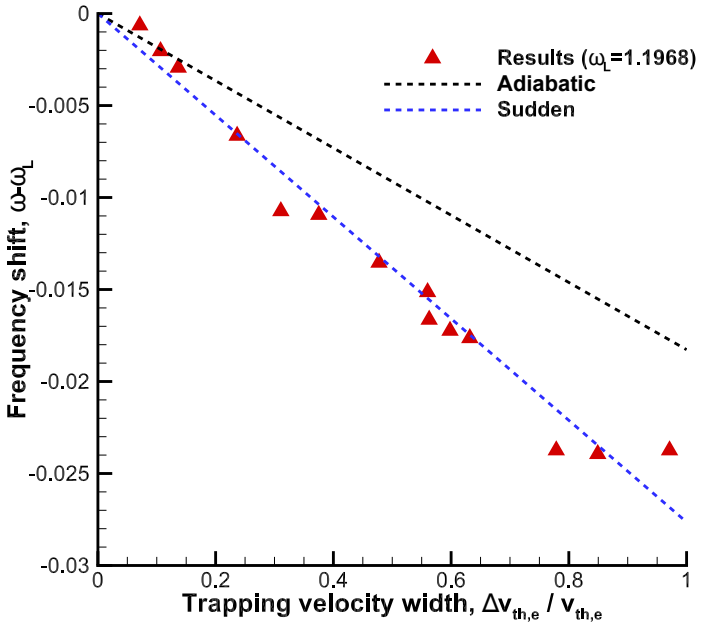


Figure 3.14: Initially perturbed EPWs for $k_0\lambda_D = 1/3$

complicated than the simple BGK model in Fig. 3.11. For instance, there are more complex structures in the EPW, including bunched trapped particles near the separatrix, small islands inside the eye region, and also a separate trapped region at higher velocity around $v/v_{th,e} = 3.9$.

### 3.4.3 Ion Acoustic Waves

The dispersion relation in Eq. (3.37) can be extended to include another charged species. Therefore, IAWs can also serve as a good verification problem for the multispecies Vlasov-Poisson solvers. IAWs have a much smaller characteristic plasma frequency as $v_\phi = \omega/k = c_s$, where $c_s = (k_B T_e/m_i)^{1/2}$ is the ion acoustic speed. Due to the difference in mass, $c_s$ can be more than 40 times smaller than the electron thermal velocity. From Eq. (3.37), the electron components contribute to positive frequency shift since the second derivative of the VDF is positive as the phase velocity is smaller than the electron thermal velocity. On the other hand, the ion components will shift the frequency negatively. As the ion temperature increases, the negative frequency shift will be larger, as shown in Ref. 58.

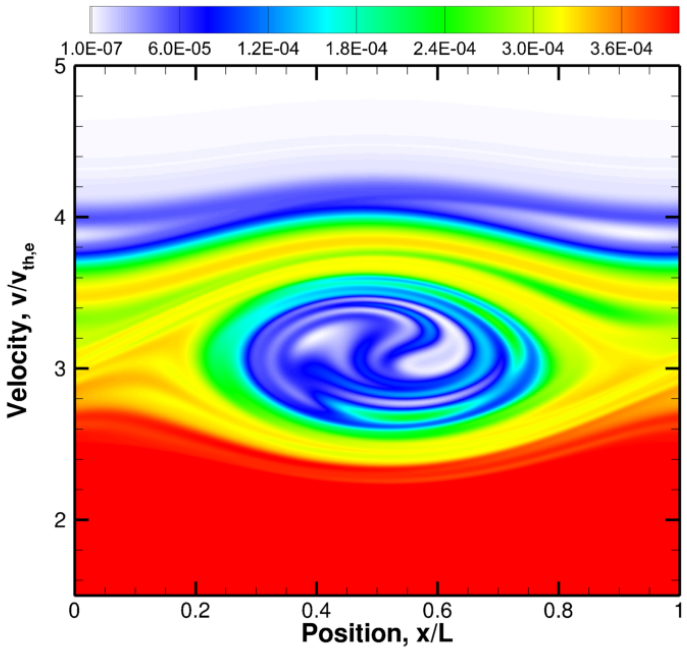


Figure 3.15: Close-up view of electron VDFs for a sudden case. Here, $k_0\lambda_D = 0.425$ and $\delta n/n_0 = 0.05$. The physical position is normalized by $L = 2\pi/k_0$.

The same number of grid points are used for the ion and electron VDFs: $N_x = 1028$ and $N_v = 2000$. For the ions, $v_{max} = 6v_{th,i}$ and $v_{min} = -6v_{th,i}$, where $v_{th,i} = (eT_i/m_i)^{1/2} = c_s\sqrt{T_i/T_e}$ is the ion thermal velocity, which is also related to the electron thermal velocity by $v_{th,i}/v_{th,e} = [(T_i/T_e)(m_e/m_i)]^{1/2}$. Electron trapping occurs at low phase velocity, so the maximum and minimum velocities for electrons are chosen smaller than the EPW cases: $v_{max} = 5v_{th,e}$ and $v_{min} = -5v_{th,e}$. The ramp-up and ramp-down time are $\omega_p t_r = 50$ and the time at which the driver is constant is $\omega_p t = 1.5 \times 10^4$. The simulation ends at $\omega_p t = 4.5 \times 10^4$. The driver amplitude $E_0$ is varied so that the size of the trapping region varies. A fully-ionized hydrogen plasma is assumed: $Z = 1$ and $m_i/m_e = 1836$.

Figure 3.16 shows the numerical results of the IAW for $k_0\lambda_D = 0.3$ and $ZT_e/T_i = 10$ in comparison to several theory curves. In order to excite IAWs, the electrons are first driven with a frequency that satisfies the kinetic dispersion relation for an IAW: the frequency of the external driver is given by $\omega_{ext} = 8.032 \times 10^{-3}\omega_p$. The sudden distribution and adiabatic distribution in Eq. (3.37) are plotted, but there is a discrepancy between the numerical

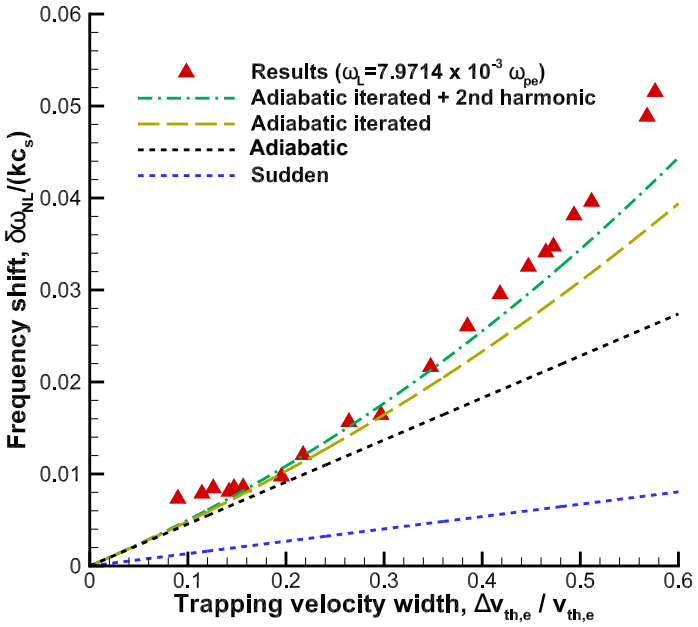


Figure 3.16: Driven IAWs for $T_e/T_i = 10$ and $k_0\lambda_D = 0.3$.

simulations and these theory curves, in which the frequency shift is linearly proportional to the trapping width. There are two reasons that can explain the discrepancies.

1. Trapped ions shift the phase velocity up and trap more ions. In particular, increased phase velocity affects the second derivative of the initial VDF in Eq. (3.37). IAWs trap ions around the acoustic speed, which is not in the tail of the distribution, leading to a large number of trapped particles in comparison to the EPWs where particle trapping occurs in the high velocity tail.

2. The nonlinear frequency shift obtained in Eq. (3.37) accounts for the first-order kinetic effects of trapped particles. It was suggested by Berger *et al.*[58] that there are fluid-type effects on top of the kinetic effects, which add second and higher harmonic type terms into the frequency shift.

As can be seen from Fig. 3.16, the numerical results agree better with the iterated solution in addition to the second harmonic mode associated with the fluid effects. Note that the ratio of electron trapping velocity width to the electron thermal velocity, $\Delta v_{th,e}/v_{th,e} =$

$\sqrt{2e\phi/m_e}/\sqrt{eT_e/m_e} = \sqrt{2\phi/T_e}$, is equal to that of ion trapping velocity width to the ion acoustic speed, $\Delta c_s/c_s = \sqrt{2e\phi/m_i}/\sqrt{eT_e/m_i} = \sqrt{2\phi/T_e}$.

Figure 3.17 shows a close-up view of an ion VDF for the driven IAW case at the final time step. The initial condition is $E_0 = 0.009$, which corresponds to the case shown at $\Delta v_{th,e}/v_{th,e} = 0.5$ in Fig. 3.16. The velocity and physical location are normalized by the ion acoustic speed, $c_s$, and $L = 2\pi/k_0$, respectively. The shape of the trapped region is no longer like a standard BGK mode in Fig. 3.11 assuming a sinusoidal potential field. It can also be seen that there are long-lasting structures inside the trapping regions that result in higher-order fluid-type harmonics.

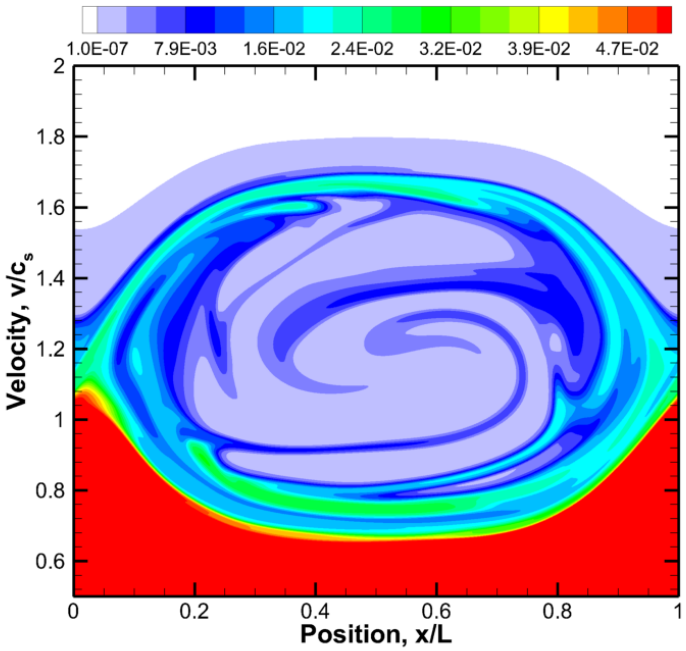


Figure 3.17: Close-up view of ion VDFs for a driven IAW at $\omega_p t = 4.5\times10^4$ for $ZT_e/T_i = 10$ and $k_0\lambda_D = 0.3$. The physical position is normalized by $L = 2\pi/k_0$.

## 3.5 Trapped Particle Bunching Instability

Another verification test problem is described in this section. Dodin *et al.*[59] recently proposed the negative mass instability (NMI) of a nonlinear plasma wave. Here, the NMI is called the trapped particle bunching instability. Its mechanism is as follows: trapped

particles in a traveling potential well perform bounce oscillations with a frequency $\Omega = \Omega(W)$ that decreases with increasing wave-frame particle energy $W$, *i.e.* $d\Omega/dW < 0$. Through Coulomb repulsion, among a set of trapped particles with similar energy $W_0$, trailing particles in the bounce motion are pushed to lower $W$ and therefore higher $\Omega$ by those leading, and *vice versa*. The result is a bunching of particles, with respect to their bounce phase, performing trapped orbits. In Ref. 59, the theory was compared with a PIC simulation of a magnetic compression plasma. Although the results indicate that there is particle bunching, it was unclear due to the statistical noise of the PIC simulation and the numerical setup was not identical to the theory.

### 3.5.1 Numerical Setup and Diagnostic Tools

To enable direct comparison with theory,[59, 60] simulations are initialized using a freely-propagating plasma wave whose trapped electron population approximates a delta function in the wave-frame energy. The algorithm is as follows.

1. One considers an analytically constructed BGK mode[56] in the wave frame with phase velocity $v_L$, wavelength $\lambda_L$, and an assumed sinusoidal potential of amplitude $\phi_0$. In this study, the frequency $\omega_L \equiv k_L v_L$ is chosen from the linear kinetic dispersion relation[58] with $k_L \equiv 2\pi/\lambda_L$.

2. An adiabatic distribution[57] generated from an initial Maxwellian is considered.

3. All trapped particles from this state are gathered into a narrow Gaussian so that the trapped particle distribution is $f_{trap}(W) \simeq \delta(W - W_0)$ where $W_0$ is the wave-frame energy of the initial BGK mode.

4. The particle distribution is then transformed to the laboratory frame or $(x, v)$ phase space, $f_{trap}(x, v)$, and the fraction of trapped particles, $f_t = n_t/n_p$, where $n_t$ is the number density of trapped particles and $n_p$ is the plasma density, is adjusted iteratively such that the relative error between calculated and assumed electric field is below a tolerance, 0.001 in this case.

The width of the Gaussian in this process is chosen so that the FWHM of the resulting ring distribution function occupies at least 3 points on the Vlasov simulation grid. For all cases, the grid size is $\Delta x = \lambda_L/N_x$ where $N_x = 1024$ in physical space and $\Delta v = (v_{max} - v_{min})/N_v$ where $v_{max} = -v_{min} = 10v_{th}$ and $N_v = 4000$. The time step is $\omega_p \Delta t = 2.5 \times 10^{-5}$. The wave frame energy varies from $W/(e\phi(t)) = -1$ to $+1$, where the potential amplitude varies in time as $\phi(t) = (1/2)(\max[\Phi(x,t)] - \min[\Phi(x,t)])$ with $\phi_0 = \phi(t = 0)$. The discrete representation in $W/(e\phi(t))$ and $\theta$, for generating Figs. 3.18(b1)-(b6), employ 50 and 45 cells, respectively.

### 3.5.2 Particle Bunching

Figure 3.18 shows the evolution of particle bunching in phase space (a1)-(a6) and the results transformed in energy-angle coordinates (b1)-(b6) at $\omega_p t = 0$, 600, 900, 1200, 1600, and 2400, respectively. For $k_L \lambda_D = 1/3$, $\omega_L/\omega_p = 1.2$ is chosen from the kinetic dispersion relation, and hence $v_L = 3.6v_{th}$. The initial wave amplitude is $e\phi_0/T_e = 0.04$ and the fraction of trapped particles is $f_t = 6.66 \times 10^{-5}$. The energy in the wave frame is $W = m(v - v_\phi)^2/2 - e\Phi(x,t)$ and the geometric angle is used: $\theta = \tan^{-1}(V/X)$, where $v_\phi$ is the phase velocity of the wave, $\Phi(x,t)$ is the potential in physical space, $V = v/\Delta v_{trap}$ and $X = x/\lambda_L$ are the normalized velocity and position in the wave frame, and $\Delta v_{trap}/v_{th} \simeq 2\sqrt{e\phi/T_e}$ is the trapping half-width, defined as the maximum excursion from $v_L$ that a particle may make while remaining trapped where $\phi$ is the instantaneous potential well depth. The plasma frequency obtained at $\omega_p t \in [0, 1200]$ is $1.192\omega_p$, which matches the initially prescribed frequency within 0.7%. Thus, the phase velocity is assumed to be constant at $v_\phi \simeq v_L = 3.6v_{th}$.

Figures 3.18(a1) and (b1) illustrate the initial condition in phase space and in the energy-angle coordinates, respectively. The initial ring is a narrow Gaussian in the wave frame energy and relaxes modestly due to numerical dissipation. Figs. 3.18(a2) - (a4) clearly show that particle bunching develops in phase space, which can also be seen in the energy-angle coordinates in Figs. 3.18(b2)-(b4). The uniform distribution function at the initial time step modulates in energy and angle. As particles with higher $W$ move slower in angle, those with lower $W$ move faster. At $\omega_p t = 1200$ in Fig. 3.18(b4), the distribution

function that was initially uniform in angle at constant $W$ in Fig. 3.18(b1) is now vertically oriented. This corresponds to the optimum state in the bounce phase bunching process and thus to the saturation of the bunching instability.

In the nonlinear stage, as shown in Figs. 3.18(a5) and (a6), the trapped particles form a macroparticle while spreading out in phase space due to filamentation and their average kinetic energy in the wave frame $\langle W \rangle$ is higher than the initial $W_0$, which can be seen from the corresponding plots in energy-angle coordinates. Similar macroparticle formation has also been observed in beam-plasma instabilities.[61] In Figs. 3.18(b5) and (b6), it can be seen that filamentation occurs inside the trapped region due to deeply trapped particles that have the largest bounce frequency. Note that some particles leak through the separatrix due to numerical dissipation and physical processes, *i.e.* shearing effect at the discontinuity leads to phase space mixing.

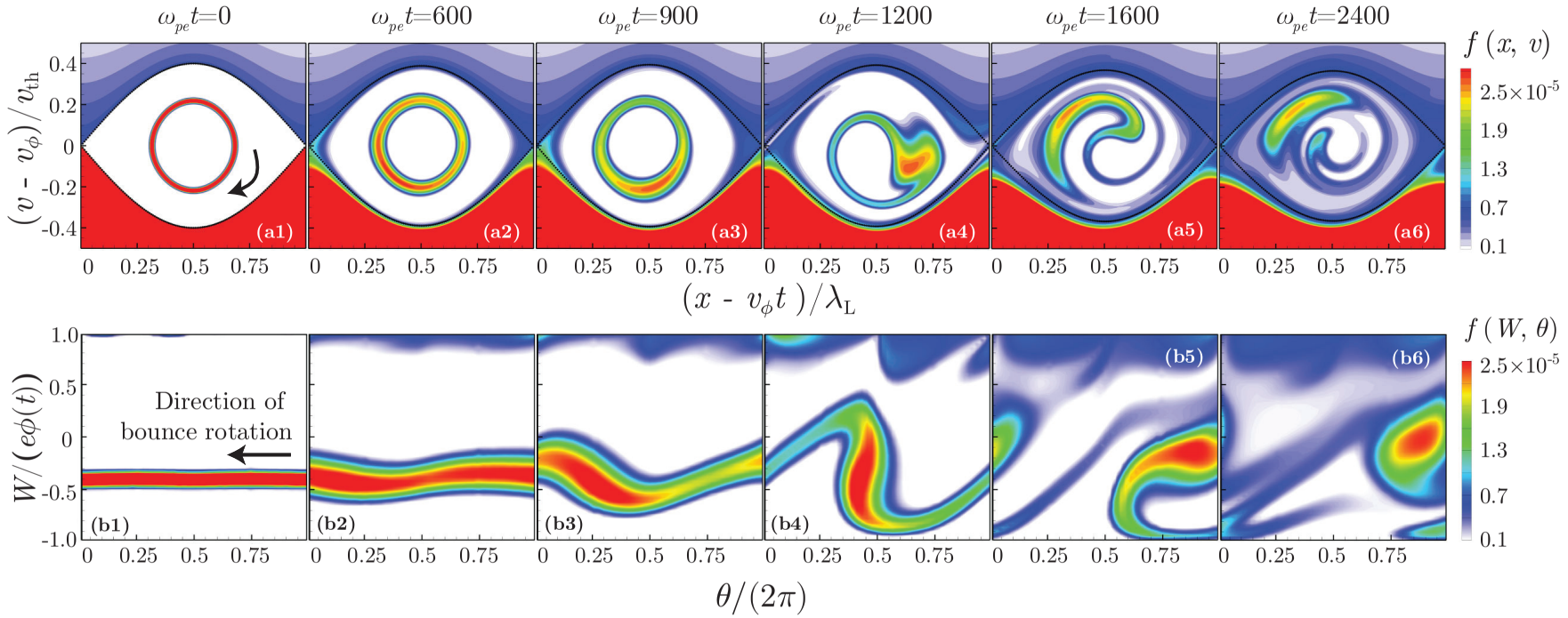


Figure 3.18: Particle bunching for initial conditions $W_0/(e\phi_0) = -0.4$, $e\phi_0/T_e = 0.04$, $v_L = 3.6v_{th}$, and $k_L\lambda_D = 1/3$. Shown are the distribution functions in phase space (a1)-(a6) and those transformed in energy-angle coordinates (b1) - (b6).

### 3.5.3 Comparison with Theory

Figure 3.19 shows that the envelope of trapped particle kinetic energy in the laboratory frame $E_{K,trap}$ exhibits an exponential growth, as does the bunching amplitude $B = \sqrt{X_{ave}^2 + V_{ave}^2}$, where $X_{ave}$ and $V_{ave}$ are the moments of the trapped particle distribution:

$$X_{ave} = \int (x - 0.5\lambda_0) f_{trap}(x, v) dx, \tag{3.41}$$

$$V_{ave} = \int (v - v_\phi) f_{trap}(x, v) dv, \tag{3.42}$$

where $f_{trap}$ is the trapped particle distributions. Note that $E_{K,trap}$ and $B$ are both integrated from the bottom of the potential well to 70% of the potential depth, $W/(e\phi(t)) = 0.4$, in order to exclude the particle leakage through the separatrix. These quantities are only useful in the linear stage while the trapped particles and those leaking through the separatrix are well-separated.

Figure 3.19(b) shows that $B$ is initially very small since the particles are uniformly distributed in phase space. As the instability develops, a particle bunch rotates in phase space. The bunching instability growth rate is calculated by extracting the envelope of $B$ and performing a least-square fit as shown in Fig. 3.19(b). For the case in Fig. 3.18, the growth rate is $\gamma = 3.29 \times 10^{-3}\omega_p$, which also agrees with the growth rate obtained from the envelope of the $E_{K,trap}$, shown in Fig. 3.19(a), $\gamma = 3.25 \times 10^{-3}\omega_p$.

To enable the description of the bunching instability as well, one must account for the energy dependence of $\Omega = \Omega(W)$, or equivalently the dependence $\Omega = \Omega(J)$ in the action $J$, in the potential wells. We consider a single wavelength system with periodicity, *i.e.* $\delta k = 0$ and thus $k_n = nk_L$. The dispersion relation of a trapped particle distribution can be given as

$$1 + 2M_0\omega_t^2\sqrt{J_0}\int_0^{J_{max}} \frac{\sqrt{J\Omega/\Omega_0}}{\delta\omega_S^2 - \Omega(J)^2} F'(J) dJ = 0, \tag{3.43}$$

where $J = m\Omega\Lambda^2/2$ is the canonical action for deeply trapped particles assuming harmonic oscillation, $F(J) = 2\pi f(J)/(mn_t)$ is the normalized distribution function, $\omega_t = (n_t/n_p)^{1/2}\omega_p$ is the trapped particle frequency, $n_t$ and $n_p$ are the number density of trapped particles and the plasma density, respectively, $M_0 = 16/(3\pi k_L\Lambda_0) \approx 1.70/(k_L\Lambda_0)$, $J_0 =$

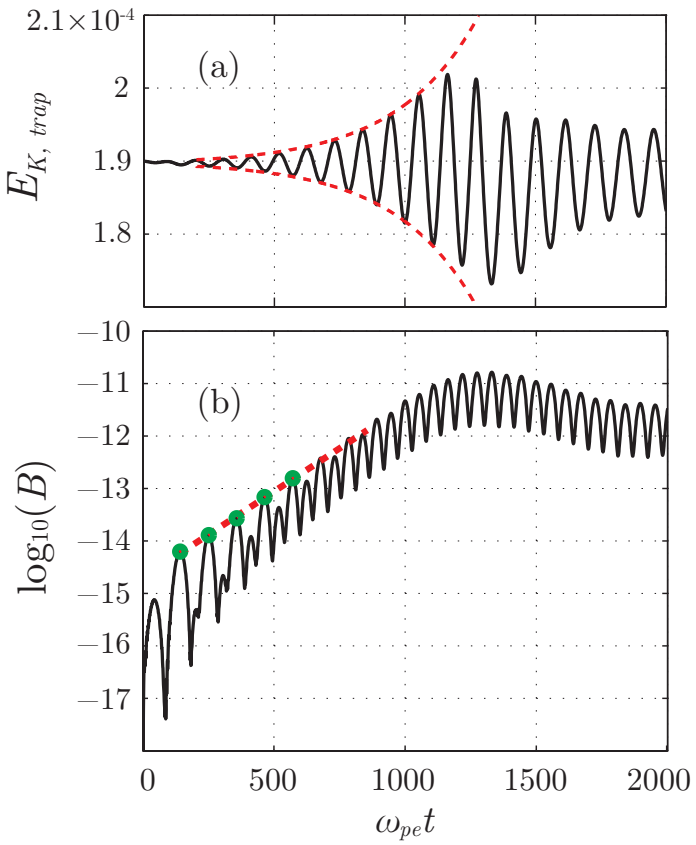


Figure 3.19: Evolution of trapped particle quantities. (a) Total kinetic energy of trapped particles $E_{K,trap}$ and (b) the bunching amplitude $B = (X_{ave}^2 + V_{ave}^2)^{1/2}$ in logarithmic scale, where $X_{ave}$ and $V_{ave}$ are average normalized position and velocity of the trapped particles.

$m\Omega_0\Lambda_0^2/2$, $\Omega_0 = \Omega(J = J_0)$, and $\Lambda_0 = \Lambda(J = J_0)$. The detailed derivation is shown in Appendix C.

Equation (3.43) can be analytically solved when $F(J) = \delta(J - J_0)$.[59, 60] Using integration by parts assuming $F(J) = 0$ at the limits,

$$1 - \frac{(1-\alpha_0)\beta_0}{w} + \frac{4\alpha_0\beta_0}{w^2} = 0, \tag{3.44}$$

where $w = (\delta\omega/\Omega_0)^2 - 1$, $\alpha_0 = \alpha(J = J_0)$, and $\beta_0 = M_0\omega_t^2/\Omega_0^2$ with $\alpha(J) = -J/\Omega(d\Omega/dJ)$. The solution to Eq. (3.44) can be found as $\delta\omega \simeq \pm\Omega_0(1 + \beta_0/4) + i\gamma$, where the growth

rate is

$$\gamma = \omega_t \left[ M_0 \alpha_0 \left( 1 - \frac{\beta_0}{16\alpha_0} \right) \right]^{1/2} \tag{3.45}$$

when $\alpha_0 > \beta_0/16$. If $\beta_0$ is negligible, $\gamma \simeq \omega_t \left(\alpha_0 M_0\right)^{1/2} = \left(f_t \alpha_0 M_0\right)^{1/2} \omega_p$ from which one can see that the bunching instability growth rate is primarily dependent on $f_t$, $W_0 = W(J_0)$ via $\alpha_0$, and $M_0$. We have improved the calculation of the coefficient $M_0$ compared with Refs. 59 and 60.

Figure 3.20 shows excellent agreement of the growth rates between the Vlasov simulations and theory. The potential amplitude of the initial BGK mode, $\phi_0$, and the energy level of the initially trapped particles, $W_0$, are prescribed for the numerical simulations. The initial fraction of trapped particles, $f_t = n_t/n_p$, is also shown in Fig. 3.20. The growth rates obtained from the numerical simulations are primarily dependent on $f_t$ over the range of parameters investigated.

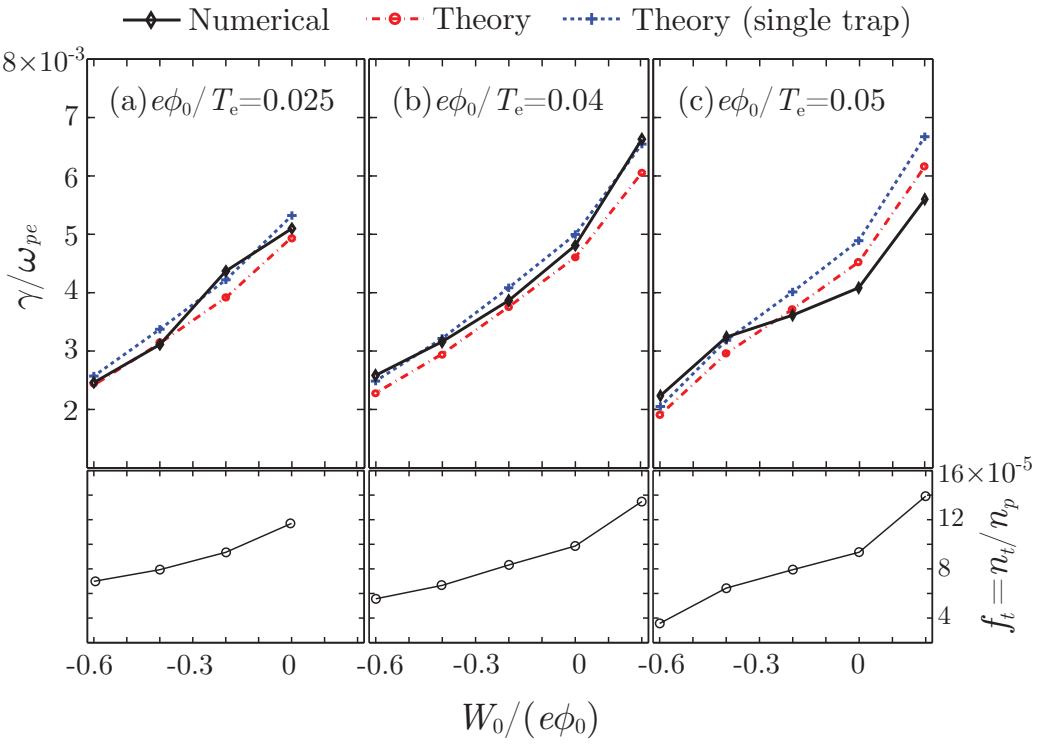


Figure 3.20: Comparison of trapped particle bunching instability between theory and Vlasov simulations for different potential amplitudes. Here, $v_L = 3.6 v_{th}$ and $k_L \lambda_D = 1/3$.

The growth rate is calculated from the bunching amplitude $B$ as shown in Fig. 3.19(b). The theoretical estimate of the growth rate is derived in Eq. (3.45) using $M_0 = 1.70/(k_L\Lambda_0)$. Also shown in Fig. 3.20 is the growth rate of Dodin's single trap model,[59] which assumes a single potential well in an infinitely long 1D system, no untrapped particles, and the linearized Vlasov-Poisson equation in the canonical action-angle coordinates. This corresponds to $M_0 = 2/(k_L\Lambda_0)$ in Eq. (3.45). The results are not shown for $W_0/(e\phi_0) > 0$ in Fig. 3.20(a) since the bounce frequency is low due to the small potential amplitude while $\gamma$ is high and it is difficult to extract the growth rate. For all other cases, there are at least three bounce cycles during the linear phase of bunching instability. The results of trapped particle bunching instability are discussed in Ref. 62.

## 3.6 Summary

Several verification test problems were used to test the Vlasov-Poisson simulation. The test problems include plasma sheath with and without secondary electron emission from a plasma-immersed material, nonlinear plasma waves, and trapped particle bunching instability. As all of these problems have analytic solutions, the simulation results are compared with those solutions and good agreement was found for all cases. In addition, the present Vlasov-Poisson solver is tested for various boundary conditions. The sheath cases employed Dirichlet and Neumann boundary conditions and the plasma wave simulations use a periodic boundary condition.

# CHAPTER IV

# One-Dimensional Hybrid Kinetic-Continuum Model of a Hall Thruster Discharge Plasma

## 4.1 Introduction

The discharge plasma of a Hall thruster is known to be in a nonequilibrium state. Laser-induced-fluorescence (LIF) measurements for the Hall thruster discharge plasma have shown that (i) the VDFs ions and neutral atoms in the discharge channel are non-Maxwellian; [63, 64] (ii) the plume jet consists of interactions between multiple ion streams; [65] and (iii) the VDFs of ions vary spatially and temporally. [66]

Two methods have mainly been used for numerical simulations of a Hall thruster plasma. A continuum approach solves the conservation equations of mass, momentum, and energy, and assumes the VDFs are close to a Maxwellian. [15, 24, 67, 68] This method has been well developed and is relatively efficient in terms of computational cost. The other approach involves particle methods, such as particle-in-cell (PIC) and direct simulation Monte Carlo (DSMC), that are able to capture non-equilibrium phenomena. So far, several fully kinetic simulation methods [16, 21, 69, 70, 71, 72] and hybrid-PIC methods [10, 13, 14, 73, 74, 75, 76] have been developed. However, due to the use of macroparticles, particle methods suffer from statistical noise. Possible problems of the numerical noise include the nonlinear effect on plasma oscillations and the inability to resolve the high energy tail of the electrons.

By comparison, the plasma kinetic equation can be solved directly to obtain the VDFs without any numerical noise. [49] In the HET community, the first grid-based kinetic simulation was developed by Boeuf and Garrigues.[11] It was briefly mentioned that the calculated

VDFs had negative values but the details of the method were not described. Fox *et al.*[77] developed a full-PIC simulation utilizing the concept of a grid-based kinetic method. The resolution of VDFs in velocity space was improved by an adaptive mesh technique. These techniques led to development of a grid-based direct kinetic (DK) method to model the Hall thruster discharge plasma.

The purposes of this chapter are (1) to show the development of the hybrid-DK simulation method, in which the DK solver is used for ions and neutral atoms while a continuum model is used for electrons, and (2) to compare the hybrid-DK simulation with a hybrid-PIC simulation to benchmark the two simulation codes. Benchmarking is performed by using an identical electron continuum model.

## 4.2 SPT-100 Hall Thruster

As the present model focuses on the axial transport, the radial and azimuthal transport of the discharge plasma are not considered, and only the radial magnetic field and axial electric field are taken into consideration. The configuration of the SPT-100 thruster considered here is summarized in Table 4.1. The propellant is xenon gas, so the mass of the neutral atoms and ions is 131 amu, where 1 amu = $1.67 \times 10^{-27}$ kg. Only singly charged ions are taken into consideration.

Table 4.1: SPT-100 configuration

| | | |
|---|---|---|
| Axial length | $L$ | 4 cm |
| Inner Radius | $r_{in}$ | 3 cm |
| Outer Radius | $r_{out}$ | 5 cm |
| Mass flow rate | $\dot{m}$ | 5 mg/s |
| Discharge voltage | $V_d$ | 300 V |
| Discharge current | $I_d$ | 4.5 A |
| Maximum Magnetic field | $B_0$ | 160 G |

Garrigues *et al.* used two different magnetic field profiles for their numerical simulation and showed that the mean discharge current is similar but the amplitude and shape of the oscillations vary significantly. [78] Since the main goal of this paper is developing the DK simulation and demonstrating its capability for application to a Hall thruster, the effect of the curvature of magnetic field distribution is not considered due to the one-dimensional

assumption.

## 4.3 Hybrid Kinetic-Continuum Simulation

The hybrid approach consists of a kinetic solver for ions and neutral atoms, and a continuum model for electrons. For the ion kinetic component, a DK solver and a standard PIC solver are used for benchmarking purposes. The electron continuum model is simplified so that we can make the benchmarking of the two kinetic methods more tractable.

In order to investigate the effects of modeling neutral atoms, two methods are compared: a DK solver is used or the continuity equation is solved. In the present model, collision mechanisms such as single-charge ionization and charge exchange are included for heavy species.

### 4.3.1 Direct Kinetic Method

The present 1D simulation includes one dimension in both space and velocity (1D1V). Additionally, the Lorentz force can be neglected for ions in the channel of a Hall thruster since the magnetic field is chosen so that they are relatively non-magnetized. The 1D transport equation for the heavy species is given by

$$\frac{\partial f_s}{\partial t} + v_x \frac{\partial f_s}{\partial x} + \frac{eE_s}{m_s} \frac{\partial f_s}{\partial v_x} = S_s \tag{4.1}$$

where $E_s$ is the electric field, $e$ is the elementary charge, $m_s$ is the mass of species $s$, $f_s$ and $S_s$ are the VDF and the collision term respectively, which are functions of the axial position, $x$, the axial velocity $v_x$, and time $t$. For neutral atoms, due to the absence of any external forces, the acceleration term in Eq. (4.1) is omitted. Macroscopic quantities, such as number density and mean velocity, are obtained by calculating the moments of the VDFs.

Depending on the processes that are accounted for, the collision terms can be calculated as the sum of each collision process. The rate of change in VDFs due to collisions, the right

hand side of Eq. (4.1), can be written as

$$S_s = \sum_c \beta \dot{n}_c(x,t) \hat{f}_{s'}(x, v_x, t) \tag{4.2}$$

where $\dot{n}_c$ is the collision rate, $\hat{f}_{s'}$ is the normalized VDF of species $s'$ that is involved in the collision process, $c$. Here, $\beta$ is plus or minus depending on the species of interest. For instance, ions are created ($\beta = " + "$) and neutral atoms are deleted ($\beta = " - "$) via an ionization event. Single-charge ionization and charge exchange collisions (CEX) are included in the present model. The CEX cross section employs the expression proposed by Pullins *et al.*[79] and the ionization cross section is given by Rapp.[80]

Equation (4.1) is solved using Strang's time splitting,[33] where the position advection and velocity update are performed separately. The second-order finite-volume MUSCL scheme with a modified Arora-Roe limiter is used for flux calculation. The stability condition is the most restrictive criterion for solving the left hand side of the plasma kinetic equation, given by

$$\frac{v\Delta t}{\Delta x} \leq 1 \quad \text{and} \quad \frac{a\Delta t}{\Delta v} \leq 1, \tag{4.3}$$

where $v$ and $a$ are the velocity and acceleration. In Ref. 81, a bounded upwind scheme was used. This employs a cubic spline interpolation method but the numerical method switches to a first-order upwind method whenever the updated value is negative in order to preserve monotonicity and positivity. It is found that the numerical dissipation of the bounded upwind scheme was severe and the ion VDFs obtained is significantly smoothed out. The DK component is later updated to a second-order MUSCL scheme with nonlinear flux limiters, and the calculation of VDFs is improved.

### 4.3.2 Boundary Conditions and Discretization

At the channel exit, there is no influence from outside the domain for the particles that are leaving. Since the characteristic speed is their own speed, the flux for the outlet boundary should be calculated using an interpolation from the inner information. It is found that a zeroth-order condition, *i.e.* Neumann boundary condition, for the ghost cell

introduces a large error because the flux at the channel exit essentially becomes always first order accurate. Therefore, an improved boundary condition where the ghost cell is linearly extrapolated from the inner cells is used. The flux calculated is second-order accurate, which matches the accuracy of the numerical scheme for all other interior cells.

Background neutral atoms as well as ions are neglected, so no neutral atoms and ions enter the channel from the channel exit. For the anode boundary condition, assuming a diameter of 0.5 mm for the anode orifice and a neutral number density of $10^{19}$ $m^{-3}$, the Knudsen number is larger than 100. Thus, the inlet neutral flow can be assumed to be in a free molecular region. A half-Maxwellian VDF is applied at the anode inlet and the neutral-neutral collisions are neglected. Since the anode sheath is not included in the present model, the ions require a boundary condition at the anode that represents the actual plasma flow. Dorf *et al.* visually observed a plasma jet structure from the anode holes in the presence of anode coating. [82] Keidar also indicated that the gas ionization inside the anode holes plays an important role and a plasma jet is generated. [83] A half-Maxwellian VDF is also applied for ions. It is assumed that the number density of ions is $10^{15}$ $m^{-3}$.

In order to capture the unsteady phenomena of Hall thrusters, where strong plasma oscillations may occur, velocity space should be discretized carefully. If the domain is too small in the velocity space, the mean properties calculated by integrating the moments of the VDFs will be underestimated due to truncated VDFs. Considering the mean velocity of ions, which is approximately 200 m/s at the anode and 20,000 m/s at the channel exit, the range for ion velocities must be selected large enough to capture the time-varying VDFs. We choose the maximum and minimum velocity to be 70000 m/s and -10000 m/s, respectively. Note that the maximum velocity is too large and usually 35,000 m/s is enough. This already corresponds to 800 eV, which is significantly larger than the applied discharge voltage, but the discretization error of the DK simulation generates VDFs at large velocities as will be discussed later. Most importantly, the size of the velocity bins must be chosen carefully in order to discretize the VDFs accurately. While satisfying the stability condition, the phase space must be discretized finely enough such that the VDFs are well resolved. For the present case, it is found that $\Delta v \leq 250$ m/s is required.

### 4.3.3 Simplified Electron Continuum Model

The cross-field transport in the axial direction for electrons is obtained using a continuum model. Since the characteristic time scales of electrons are much smaller than those of ions due to the large difference in mass, the electrons are assumed to be steady state in the time scale of ions.

For the momentum equation, shown in Eq. (2.23), the left hand side is neglected due to the small mass of electrons. The pressure term is also neglected to derive a simplified electron continuum model so that benchmarking of the kinetic solvers is easier. Physically, the pressure term plays an important role near the anode since the plasma diffuses to the walls. At the channel exit, there is a density gradient in the axial direction due to acceleration, but it can be assumed that the electromagnetic forces dominate over the pressure term. Note that the pressure term is included in Chapter V. As shown later, the inclusion of the pressure term introduces some noise, possibly physical and numerical. A simple electron continuum model is assumed, making the benchmarking of ion kinetic solvers easier. The electric field is calculated by the steady-state momentum equation,

$$0 = -n\mu_{\perp}E + nu_e, \tag{4.4}$$

where $\mu_{\perp}$ is the effective electron mobility, $n$ is the plasma density obtained from ion number density via a quasineutral assumption, and $u_e$ is the axial electron mean velocity. Assuming only singly charged ions and a quasineutral plasma, the charge conservation equation can be written as

$$0 = \frac{\partial}{\partial x}J_i + \frac{\partial}{\partial x}J_e \tag{4.5}$$

where $J_i = en_iu_i$ and $J_e = -en_eu_e$ are the ion and electron current densities, respectively. Integrating this equation once over $x$ gives

$$J_d = J_i + J_e, \tag{4.6}$$

where $J_d$ is the total discharge current density, or the anode current density. Using Eq.

(4.4), Eq. (4.6) can be further integrated[1] to obtain the fundamental relation between the discharge current and the discharge voltage $V_d$, given by

$$J_d = \left[\int \frac{1}{n_e \mu_e} dx\right]^{-1} \left(V_d + \int \frac{n_i u_i}{n_e \mu_e} dx\right), \tag{4.7}$$

where $n_i = n_e = n$. The electron axial mean velocity and the electric field can be calculated from Eq. (4.6) once $J_d$ is calculated. Note that electron mobility across the magnetic field plays an important role in the electron continuum model. The transverse electron mobility in the cross-field direction follows the classical description and can be written as

$$\mu = \frac{e}{m_e \nu_m} \frac{1}{1 + \omega_B^2/\nu_m^2} \tag{4.8}$$

where $\omega_B$ is the electron cyclotron frequency and $\nu_m$ is the total electron momentum transfer frequency, which is written as the sum of contributions from electron-neutral collisions and electron-wall collisions. [11] Note that electron-ion collisions are orders of magnitude smaller for the electron temperature range, *i.e.* $> 5$ eV, in HETs.

The mean electron energy, $\varepsilon$, is obtained from the steady-state energy equation:

$$\frac{5}{3} \frac{\partial}{\partial x} \left(n u_e \varepsilon\right) = -e n u_e E - n\Gamma_w - n\Gamma_c \tag{4.9}$$

where $\Gamma_w$ is the energy loss to the channel wall and $\Gamma_c$ is the energy loss due to electron-neutral collisions. It is assumed that the axial thermal conductivity is negligible. Assuming the electron energy distribution function to be Maxwellian, the electron temperature and the mean electron energy are related as $\varepsilon = 3/2 k_B T_e$, where $T_e$ is the electron temperature. The kinetic energy components are neglected.[2] The energy loss to the channel wall is modeled as follows:

$$\Gamma_w = \Gamma_{w0} \exp\left(-\frac{U_0}{\varepsilon}\right) \cdot \varepsilon, \tag{4.10}$$

where $\Gamma_{w0}$ and $U_0$ are parameters taken to be equal to $0.2 \times 10^7$ and 20 eV, respectively. [11,

[1] Eq. (4.5) with Eq. (4.4) gives a second order PDE for plasma potential using $E_x = -\nabla_x \phi$. However, it will be shown in Chapter VII that there are numerical difficulties to solve the PDE.

[2] The kinetic energy of electrons are included in Chapter V.

13, 74, 84] The energy loss due to inelastic collisions reads:

$$\Gamma_c = n_n \xi(\varepsilon) \cdot \varepsilon \tag{4.11}$$

where $n_n$ is the number density of neutral atoms and $\xi$ is the energy loss coefficient which consists of contributions from ionization and excitation. The energy loss coefficients are calculated using the cross sections of Puech and Mizzi. [85]

The mean electron energy at the channel exit is set to 10 eV, *i.e.* the electron temperature is 6.7 eV. As can be seen from Eq. (4.9), the steady-state 1D electron energy equation reduces down to an ordinary differential equation. Hence, a fourth-order Runge-Kutta method is used to calculate the mean electron energy. The potential is set to 0 V at the channel exit and the anode potential is equal to the discharge voltage. Note that the anode sheath and the plume are neglected in this model.

### 4.3.4 Hybrid-PIC Simulation

A hybrid-PIC simulation, developed by Boeuf and Garrigues,[11, 18] uses a PIC method for ions, an electron continuum model, and a continuity equation solver for neutral atoms. The position and velocity of the macroparticles are updated by a leap-frog scheme, which is second-order accurate. The maximum number of macroparticles used in the hybrid-PIC simulation is approximately 300,000 particles. The total number of macroparticles is fixed instead of keeping it constant in each cell. Ions are generated due to ionization when the total number of macroparticles is smaller than the maximum limit. Otherwise, the ionization rate is stored and a new ion is generated whenever the number of macroparticles decreases to a satisfactory level. The number density and ion current are obtained every time step by integrating the particle information, which are used for the electron continuum model, discussed in Sec. 4.3.3.

The continuity equation is solved for neutral atoms with constant speed, which is set equal to the mean velocity of a half-Maxwellian assigned at the anode in the DK simulation. This is necessary to obtain identical neutral atom density from the inlet as the anode mass flow is kept the same. It was observed that any discharge oscillations damp when the

velocity of ions generated via ionization is sampled from a Maxwellian distribution, *i.e.* half-Maxwellian or shifted-Maxwellian. This is because slow ions that are sampled from the VDF stay longer than the fast ions. As the total number of particles is fixed, the slow ions will be preferentially filled in the ionization region where the electric field is small. Therefore, in this study, the velocity of the ions generated by an ionization event are assigned a constant speed.

### 4.3.5 Flowchart

The implementation of the hybrid-DK simulation is illustrated in Fig. 4.1. The input parameters, domain information, and initial conditions are assigned before the main iteration.

First, the ion and neutral atom kinetic solvers are called. Here, the input parameters for the ion kinetic solver are the electric field and the collision terms on the right hand side of the kinetic equation. For the neutral atom solver, only the collision terms are needed.

Next, the electron continuum module is called. The discharge current is calculated first from the charge conservation equation along with the drift-diffusion approximation for the electron momentum equation. Inputs for this module are the ion number density, ion flux (or the mean velocity), and the electron mobility. Once the discharge current is calculated, the electric field is calculated. The electron mean velocity can then also be calculated from the current conservation. The steady-state electron energy equation is solved to obtain the electron mean energy, $\varepsilon$. In this chapter, the azimuthal electron drift is neglected so the electron temperature in electron-volts is simply $T_e = (2/3)\varepsilon$.

Finally, the ion and neutral atom VDFs obtained from the kinetic solver are integrated to update the number densities and the velocities. This integration process must be performed after the electron module so that the input for the electron module is the information at the old time step.

Data output is performed typically every 500 time steps, *i.e.* 500 ns. The simulation stops when the simulation time is 1 ms. Therefore, the hybrid model is iterated for $10^6$ time steps.

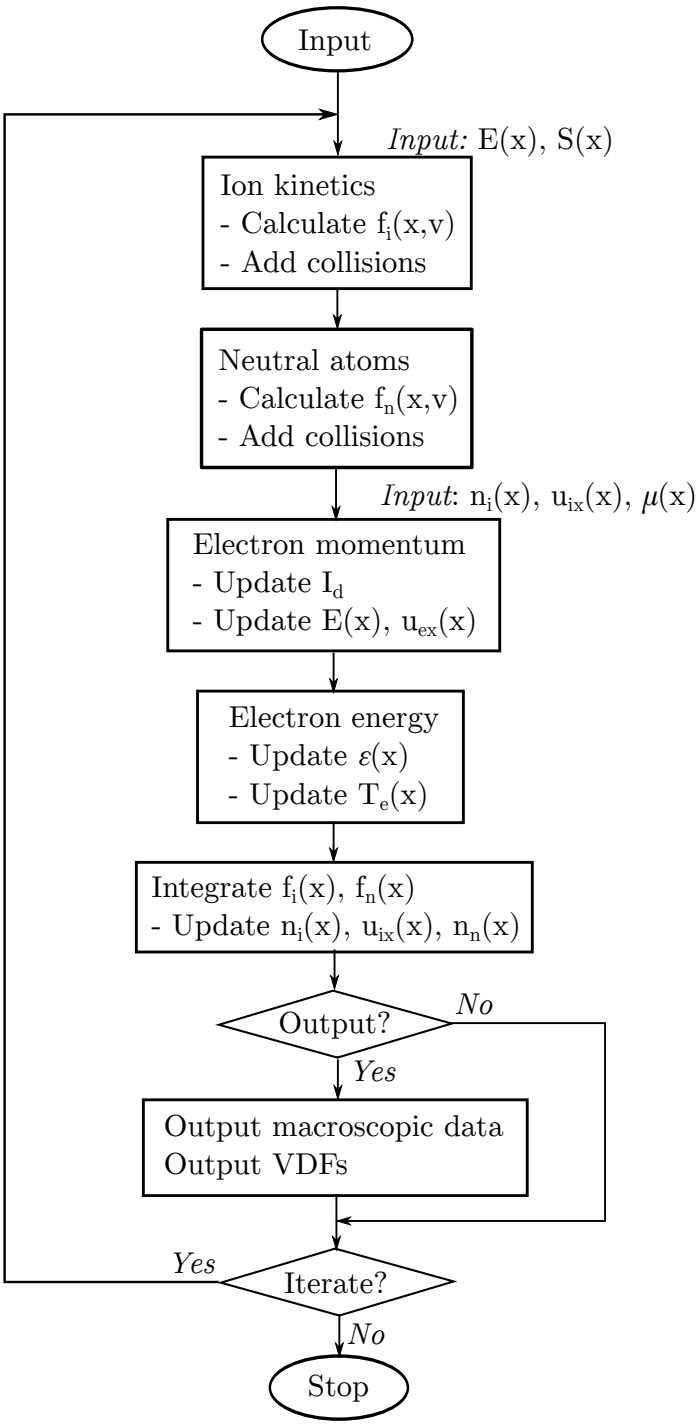


Figure 4.1: Flowchart of the hybrid model for HET discharge plasmas.

## 4.4 Macroscopic Results

The results obtained from the 1D hybrid-DK simulation are compared with those obtained from the 1D hybrid-PIC simulation. For the hybrid-DK simulation, the time step

size used for the xenon particles is $1 \times 10^{-9}$ seconds and the cell size is [$4 \times 10^{-4}$ m, 200 m/s] in order to satisfy the stability condition. The phase space is divided into $100 \times 400$ cells in the physical space and velocity space, respectively. The time step and phase space discretization are chosen to satisfy the stability condition in Eq. (4.3). In order to investigate the effect of neutral atom modeling, a DK simulation and a continuum model are employed. The results are described as HDK-DK and HDK-Cont, respectively.

For the hybrid-PIC simulation, a time step smaller than $1 \times 10^{-8}$ seconds is required due to the CFL condition in physical space.[3] However, a time step of $1 \times 10^{-9}$ seconds is used to match the hybrid-DK simulation. The number of cells in the physical space is fixed at 100, which is the same as the hybrid-DK simulation. The hybrid-PIC simulation is indicated as HPIC.

### 4.4.1 Computational Time Comparison

On a 3.2 GHz processor, the HDK-DK completes 1 ms in 3.3 hours while the HDK-Cont finishes in 1.9 hours. The computational time required for the HPIC case is 3.6 hours using the same time step. For the time integration of the DK simulation, it is required to

1. store the old values,

2. calculate the fluxes at cell interfaces, and

3. update the VDFs.

Thus, the computational time per velocity bin in DK solvers is about three times more expensive than that per particle in PIC methods. The ratio of the computational steps between PIC and DK methods can be estimated as

$$\frac{\text{3000 particles per cell (PIC)}}{\text{400 velocity bins per cell } \times \text{3 steps (DK)}} = 2.5. \tag{4.12}$$

This agrees with the computational time difference: 3.6 / 1.9 = 1.8. Using a DK solver for neutral atoms will approximately require twice more computational steps as the DK simulation is used for two species. Therefore, for an identical time step, the ratio of the

[3]Note that particle methods do not require the CFL condition in velocity space.

number of particles per cell, $N_p$ for the PIC method to the number of velocity bins per cell, $N_v$, for the DK method should be

$$N_p = 3N_v \tag{4.13}$$

in order for the computational wall time to be similar.

### 4.4.2 Overall Thruster Performance

The thrust, $T$, specific impulse, $I_{sp}$, and thruster efficiency, $\eta$, are calculated from

$$T = \dot{m} v_{exit} \tag{4.14}$$

$$I_{sp} = \frac{T}{\dot{m} g} = \frac{v_{exit}}{g} \tag{4.15}$$

$$\eta = \frac{\dot{m} v_{exit}^2}{2 I_d V_d} \tag{4.16}$$

where $v_{exit}$ is the exhaust velocity at the channel exit and $g$ is the acceleration due to gravity (=9.8 m/s$^2$).

Table 4.2: Thruster performance

| | HDK-DK | HDK-Cont | HPIC | Experiment [86] |
|---|---|---|---|---|
| Mean discharge current, $I_d$ | 3.59 A | 4.03 A | 3.94 A | 4.5 A |
| Thrust, $T$ | 88.7 mN | 89.0 mN | 90.8 mN | 80 mN |
| Specific impulse, $I_{sp}$ | 1810 s | 1810 s | 1850 s | 1600 s |
| Efficiency, $\eta$ | 0.74 | 0.67 | 0.69 | 0.5 |

As shown in Table 4.2, the results obtained from the hybrid-DK simulations are in good agreement with the hybrid-PIC results. However, the simulation results show higher specific impulse and thrust than the experimental data of Mikellides *et al.*. [86] It can be seen from Eqs. (4.14) and (4.15) that the exhaust velocity, or the ion mean velocity at the channel exit, is overestimated. This is because the potential boundary condition of zero is set at the channel exit in the current simulation instead of at the cathode. In the real thruster, the potential drop will extend into the plume so that the ion mean velocity accelerates in the plume as well as inside the channel. This effect is taken into account in the improved hybrid-DK simulation in Chapter V. In addition, plume divergence is not included in the

current 1D model that may impact the thrust performance.

### 4.4.3 Time-averaged Plasma Properties

Figure 4.2 shows the macroscopic plasma properties averaged over several oscillation cycles. Although it can be seen that all simulations provide similar trends, the similarities and disparities in the thruster performance using three different simulation models, seen in Table 4.2, can be explained by the time averaged plasma results.

First, the potential drop, seen in the bottom part of Fig. 4.2, shows good quantitative agreement in the acceleration region. This determines the acceleration of ions and provides similar exhaust velocity. Therefore, the thrust and specific impulse are in good agreement for all three simulations.

Second, HDK-Cont and HPIC results are in good agreement except for the ion number density in the ionization region. The DK simulation accounts for the neutral atom VDFs while the PIC simulation employs a constant velocity for the ions generated via an ionization event. The use of a Maxwellian distribution, for example, for newly generated ions in the PIC simulation yielded different quantitative results. This is due to the slow ions remaining in the system in a unphysical manner longer than the fast ions since the total number of macroparticles is fixed constant.

The discrepancy in the ion number density in the ionization region is mainly due to how the simulations treat ionization events. The DK simulation handles the collision processes at each time step and in every velocity bin. On the other hand, in the PIC simulation, the total number of the macroparticles in the system is fixed so that ions are not created when there are too many particles due to the computational memory restriction. It is found in our simulation that ions are not generated in one out of four time steps. Although the particle weight is calculated properly from the ionization rate, the ionization rate depends on the number density of the accumulated ions. At the time step that skips the ion production, the ion number density is slightly underestimated, and so is the ionization rate.

Lastly, the mean discharge current influences the thrust efficiency, in Eq. (4.16). The second integration in Eq. (4.7) is independent of the number densities since quasineutrality is assumed. As mentioned previously, the distribution of plasma potential gives a similar

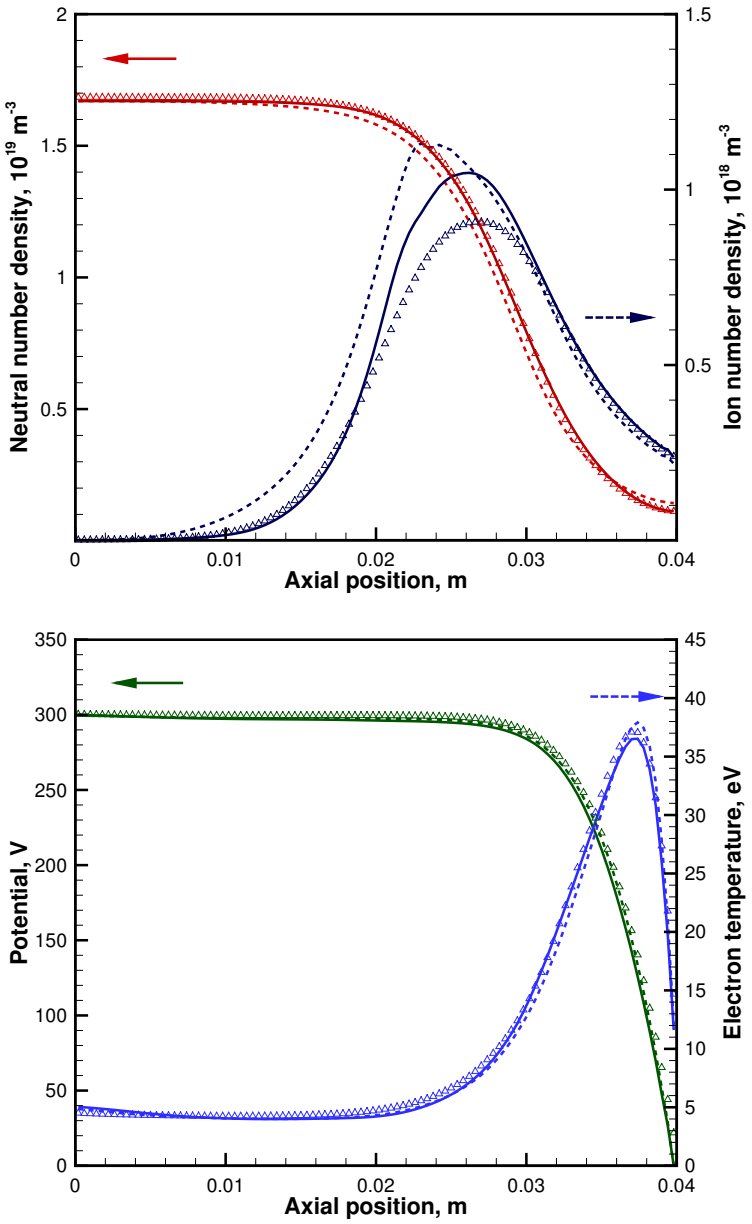


Figure 4.2: Time averaged results of macroscopic parameters vs. axial position. Dashed lines: HDK-DK, Solid lines: HV-Cont, Triangles: HPIC

trend for the ion mean velocity so that the second integration does not vary much. Thus, the first integration mostly determines the total mean current. In the acceleration region, where the electron mobility is small due to the large magnetic field, the magnitude of the first integration is mainly determined by the ion number density near the channel exit. As shown in Fig. 4.3, the ion number density of the HDK-DK case is smaller in comparison to

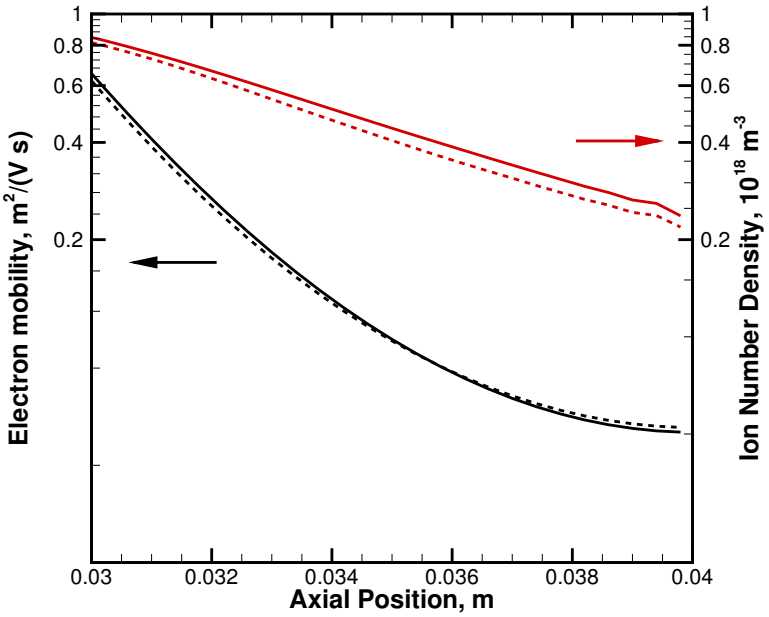


Figure 4.3: Logarithmic plot of electron mobility and ion number density vs. axial position in the acceleration region. Dashed lines: HDK-DK, Solid lines: HDK-Cont.

the HDK-Cont case. This is due to the lower electron temperature, shown in the bottom part of Fig. 4.2. Due to a lower ion number density in the acceleration region, the mean discharge current for HDK-DK is smaller than the other two simulations that employ a neutral continuity solver. Although the ion and electron transport determine the plasma behavior as well as the thruster performance, it can be seen that the modeling of neutral atoms plays an important role.

Figure 4.4 shows the calculated mean velocity from the neutral DK simulation in comparison to the continuity solver with constant velocity. The results obtained from the DK neutral solver (HDK-DK) yield an acceleration of neutral atoms towards the channel exit. This phenomenon is also observed in the LIF experiments by Huang *et al.*[64] Their explanations for this phenomenon included (a) the effects of the channel wall, (b) charge-exchange collisions, and (c) selective ionization in which slower neutrals are more likely to be ionized than the faster neutral atoms. In the present models, (a) is not included due to the one-dimensional approximation and (b) is described in Section 4.6.4 and shows that the effect

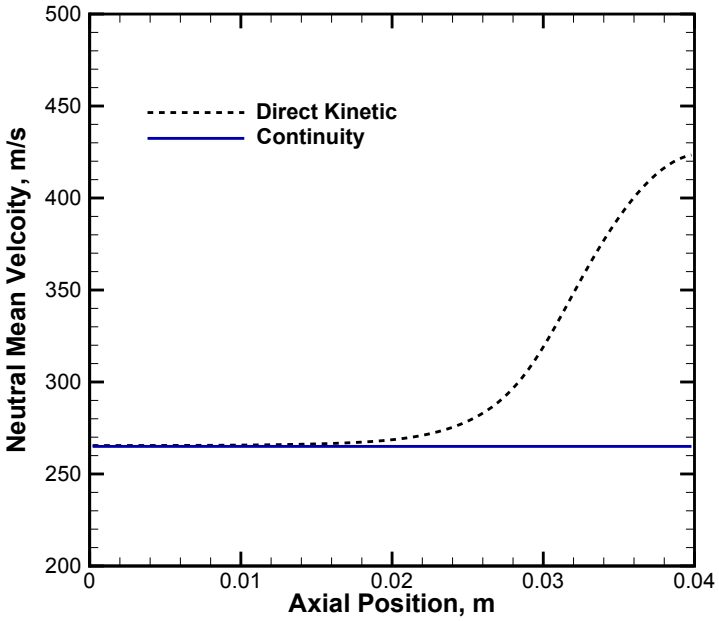


Figure 4.4: Mean velocity of neutral atoms vs. axial position. Dashed line: HDK-DK, Solid line: HDK-Cont.

of CEX is small inside the channel. Therefore, the kinetic simulation results presented here reinforce the physical mechanism that selective ionization causes the apparent acceleration of neutral atoms inside the discharge channel.

Selective ionization plays an important role in determining the ion number density. The lower ion number density produced by the HDK-DK case in the acceleration region is mainly due to the selective ionization. The ions generated via an ionization event have larger bulk velocity so that more ions can escape from the domain and the ion number density decreases near the channel exit. As well as the electron temperature, the kinetic description of neutral atoms provides another physical mechanism of the smaller mean discharge current in the HDK-DK results. In addition, selective ionization explains the larger ion number density produced in the diffusion and ionization regions. As opposed to the acceleration region, there is a larger amount of slow ions due to the shape of neutral VDFs near the anode. Since there are more slow ions, more ions stay in that region and the number density becomes larger than using a neutral continuity solver which assumes constant velocity.

## 4.5 Discharge and Plasma Oscillations

Plasma oscillations are observed in the unsteady calculations. All of the simulations produced ionization oscillations, often referred to as the breathing mode, that are known to be a low-frequency mode present in Hall thruster operation. For the high-frequency oscillations, the DK simulation captures the unsteady phenomenon well.

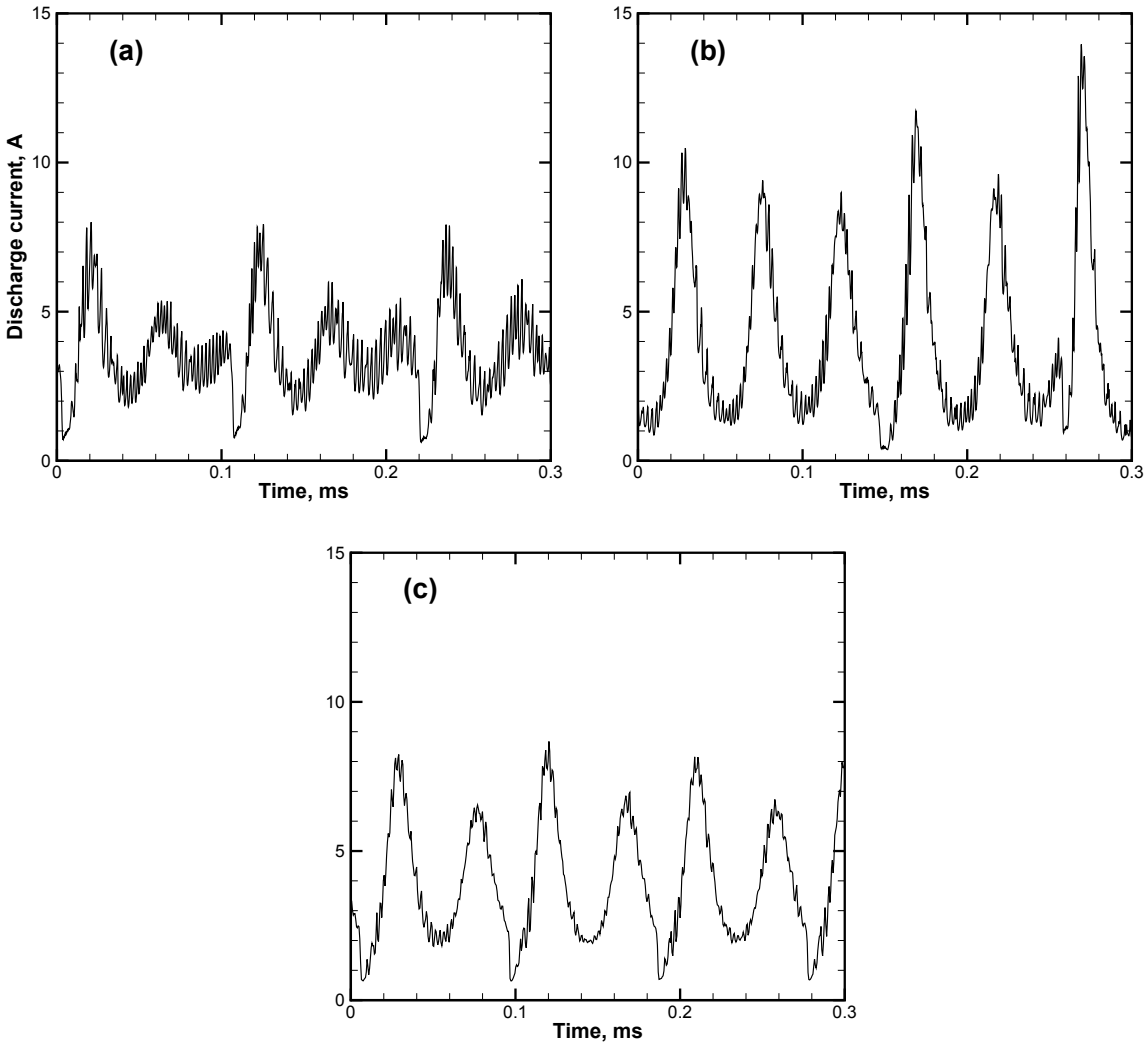


Figure 4.5: Discharge current oscillations of a SPT-100 thruster (a: HDK-DK; b: HDK-Cont; c: HPIC).

### 4.5.1 Ionization Oscillations: > 10 kHz

Figure 4.5 shows the discharge current oscillations obtained from the three different simulations. The mean discharge current matches the values shown in Table 4.2. The overall shape of the discharge current oscillations looks similar, producing plasma oscillations related to ionization. This low-frequency oscillation mode is often referred to as the breathing mode and the oscillations in the number densities of neutral atoms and ions are shown in Fig. 4.6.

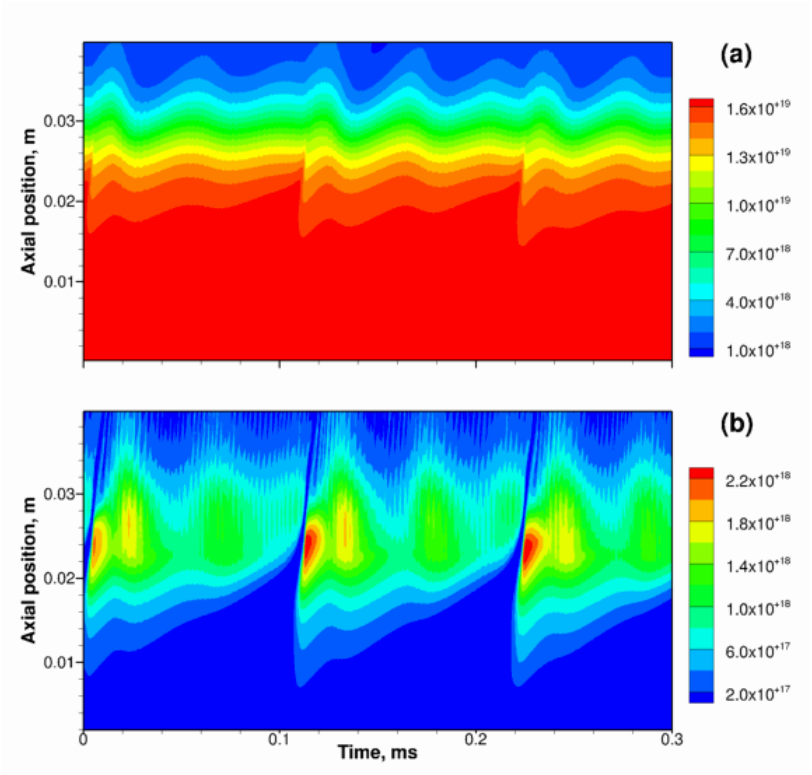


Figure 4.6: Contour map of the number densities of the heavy species obtained from the HDK-DK case (a: neutral atoms, b: ions). These results correspond to Fig. 4.5(a). The units of the number densities are $m^{-3}$.

The frequency of the breathing mode is 19 kHz in the HDK-DK case and 20 kHz in the HDK-Cont and Hybrid-PIC cases. A simple physical model for breathing mode oscillations is proposed by Fife [10]:

$$f_B = \frac{\sqrt{V_i V_n}}{2\pi L_i} \tag{4.17}$$

where $f_B$ is the breathing mode frequency, $V_i$ and $V_n$ are the characteristic velocities of ions

and neutral atoms, respectively, and $L_i$ is the characteristic length of the ionization region. For $V_i = 18,000$ m/s, $V_n = 300$ m/s, and $L_i = 0.02$ m, the breathing mode frequency from Eq. (4.17) is $f_B = 19$ kHz. The experiment of Mikellides *et al.* [86] shows a breathing mode frequency of 17 kHz. The breathing mode frequencies obtained from the simulations are in good agreement with the theory and experiment.

The simulation results show that there is another unique mode at the minimum discharge currents. Its mechanism is due to the diffusion region being filled with neutral atoms that are injected from the anode and consequently the ionization front moves towards the channel exit. One period of this cycle is 105 $\mu$s from the hybrid-DK results compared to 95 $\mu s$ from the hybrid-PIC result. This corresponds to the transit time of neutral atoms in the diffusion and ionization regions which is given by

$$\tau_n = \frac{L_i}{V_n}.$$

Using the values above, this gives $\tau_n = 70$ $\mu$s and shows quantitative agreement with the time needed to fill the channel with neutral atoms obtained from the simulations.

There are two different peaks in the mean discharge current from the simulations. In the HDK-DK case, the larger peak is approximately 7.5 A whereas the smaller peak is about 5.5 A. The difference in the mean discharge current can again be explained by the magnitude of the ion number density, as described in the previous section (Section 4.4.3). In the acceleration region, the ion number density is smaller at the second peak than at the first peak, seen in Fig. 4.6(b). Although the discharge current is calculated based on the simplified 1D Ohm's law and only by using the plasma parameters obtained from ion transport in the present hybrid simulations, the simulations provide reasonable results.

### 4.5.2 Transient-time Oscillations: > 100 kHz

As shown in Figs. 4.7 and 4.8, the high-frequency discharge oscillations are well captured in both simulations. Similar to the ionization oscillations, shown in the previous section, a high-frequency ionization oscillation mode, which is often referred to as the transient-time mode, is also present in the Hall thruster discharge plasma. [3, 9]

Transient-time oscillations have frequencies that correspond to $u_i/L_a$, or the ion residence time scale, where $L_a$ is the acceleration characteristic length. [9] For $U_i = 10000$ m/s and $L_a = 0.01$ m, this frequency is 100 kHz. In the example shown in Fig. 4.7, the transient-time frequency is 350-400 kHz from the simulations. Tilinin showed that the transient-time oscillations occur in any operation conditions when changing the magnitude of the magnetic field, mass flow rate, and the discharge voltage. Particularly, in the optimum regime where the Hall thruster operates stably, it is shown that the high-frequency transient-time oscillations are confined to a region near the maximum magnetic field. [3]

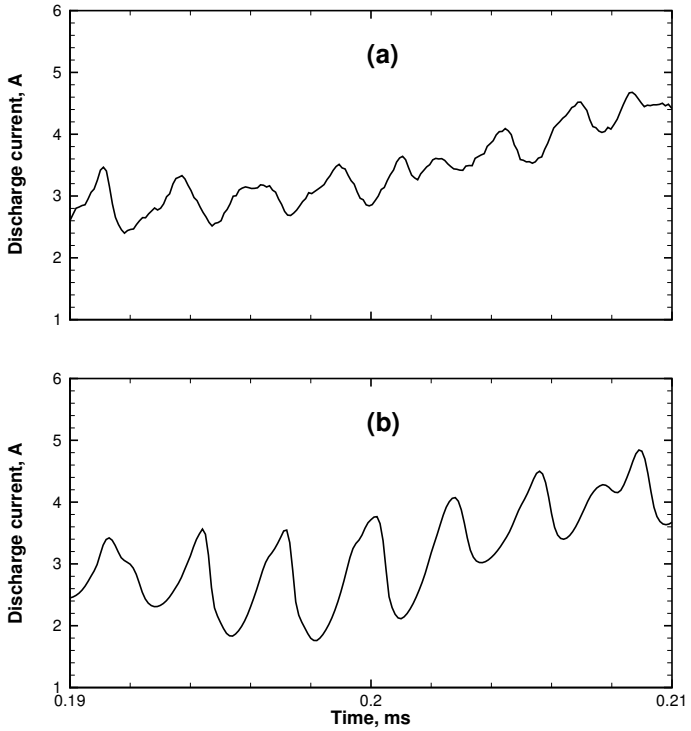


Figure 4.7: High frequency oscillations of the discharge current (a: Hybrid-PIC, b: HDK-DK). The time range is 20 $\mu s$.

The numerical results obtained from the hybrid simulations match the experimental observation that the plasma density fluctuations are confined in the acceleration region. The HPIC results show numerical fluctuations in the discharge current whereas the HDK-DK results are smooth even in the short time scale. The maximum peak of the discharge current again corresponds to the time step at which the ion number density is large in the

near-exit region. It can be seen that the hybrid-DK simulation resolves the temporal plasma fluctuations without the statistical noise in comparison to the hybrid-PIC simulation.

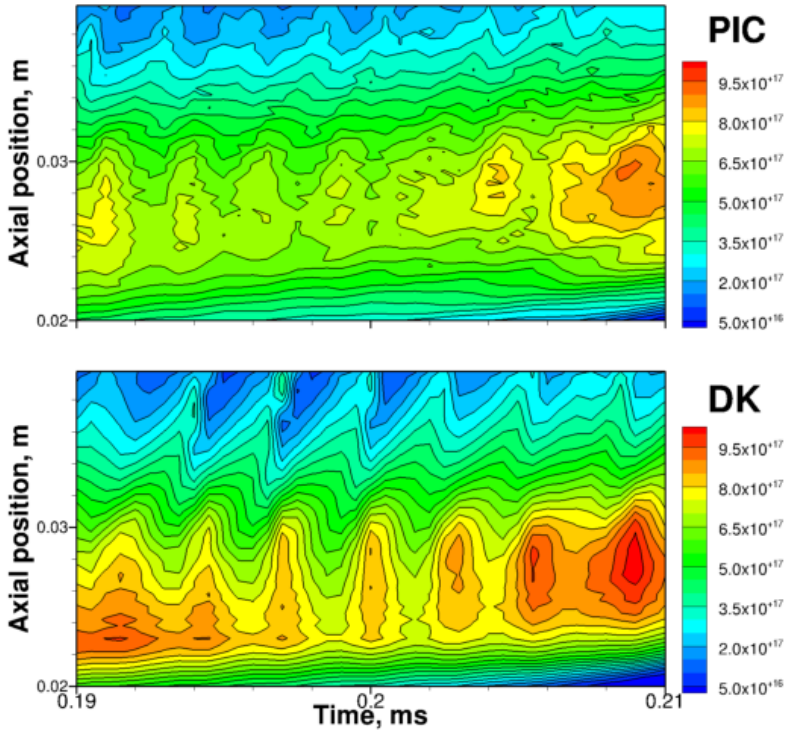


Figure 4.8: High frequency data of ion number density in the ionization and acceleration regions, corresponding to Fig. 4.7 (a: Hybrid-PIC, b: HDK-DK) The units are in $m^{-3}$. The instantaneous number densities are sampled every 0.5 $\mu s$ (500 time steps).

In addition to the temporal resolution, the Vlasov simulation provides a better resolution in physical space. As an example, the PIC simulation shows not only temporal but also spatial non-smoothness. There are two possible explanations regarding the spatial fluctuations. One is the effect of ionization. As described previously, in order to maintain the total number of macroparticles in the PIC simulation, ions are not generated at every time step. During 100 time steps (0.1 $\mu$s), the generation of ions is skipped in approximately 26 steps. Secondly, the spatial fluctuation comes from representing particles in a discrete manner. This is due to the statistical noise in the particle simulations and will be discussed in the next section.

Since the transient-time oscillations are considered to play an important role in the

turbulent conductivity of the discharge plasma in Hall thrusters,[3] the DK simulations can be very useful in understanding the small-scale physics in comparison to particle methods. In addition, usually in particle simulations, time averaging techniques are commonly used in order to obtain good statistics. Although no time averaging is used in the current hybrid-PIC simulation and instead an offset for the ion number density is set to $10^{15}$ m$^{-3}$, either numerical procedure may alter the plasma physics in the low density regions.

## 4.6 Microscopic Results

One of the primary objectives of developing a direct kinetic simulation is to obtain a better resolution for the VDFs of plasma species. In the previous section, statistical noise in the ion number density predicted by the PIC simulation is observed even when the total number of macroparticles is set relatively large. In this section, VDFs are constructed from the information of discrete particles, namely, the location and velocity of each macroparticle, in the HPIC results. Identical cell sizes are used in the HPIC and HDK-DK cases for the discretization of phase space.

### 4.6.1 Time-Averaged Ion Energy Distribution Functions

Figure 4.9 shows the time-averaged energy distribution functions (EDFs) of the ions at the channel exit compared with the measurements of Bareilles *et al.*[74]. Good qualitative agreement between the two kinetic methods and the experimental data is shown. The DK simulation shows a slightly better agreement with the experimental data than the PIC simulation.

For both kinetic methods, it can be seen that there are ions exceeding the prescribed discharge voltage, $V_d = 300$ V. This is due to the dynamic oscillations generating high velocity ions and this phenomenon is often referred to as the *wave-riding* effect.[72, 74] In the presence of discharge oscillations, the ion distribution functions shift back and forth, which generates some spread of the ion EDFs around the discharge voltage. Surprisingly, this spread, particularly the high energy components, can be observed in the experiment. The HPIC results slightly over-predict the high energy tail of ions, which is possibly due to

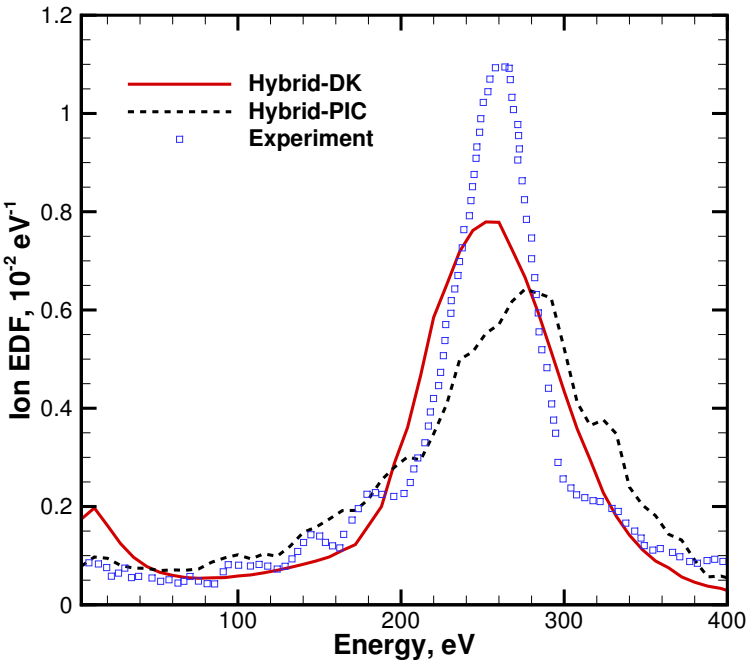


Figure 4.9: Time-averaged ion EDFs at the channel exit.

the statistical noise near the channel exit. The average number of macroparticles for the HPIC method is 3000, but the number of macroparticles in the cells near the channel exit is sometimes less than 20. This is due to the ions being significantly accelerated from the ionization region, where a large number of macroparticles exist. If the statistical noise due to the small number of macroparticles in the acceleration region feeds back into the electron continuum model, the electric field may oscillate more strongly due to such numerical errors, which then can generate high energy ions.

There is a bump in the low energy component obtained from the HDK simulation. This is due to the ionization that is captured in the low velocity tail of the distribution of ions near the channel exit. It can be seen in Sec. 4.6.2 that some ionization events are captured more in the HDK results near the channel exit compared to the HPIC results. These slow ions are generated during the *wave-riding* cycle. The low energy ions may be a real physical phenomenon as a recent experiment by Young *et al.* detected a slow ion population during the breathing mode oscillation from an LIF measurement. This is discussed in the next

section in more detail. In real operation, there may be doubly charged ions generated and those might be accelerated twice as much as singly charged ions. The high velocity tail of ions may be due to the doubly charged ions or other species which went through charge exchange collisions with the doubly charged ions.[87] However, such effects are not captured in the present simulations. This will be reserved for future work.

### 4.6.2 Time-Varying Ion Velocity Distribution Functions

Figures 4.10 and 4.11 show the time-varying ion VDFs in phase space at various times. The indices of five contour figures correspond to the five points shown in the discharge current plots in Figs. 4.10 and 4.11. The color scale of the two figures is identical.

Figures 4.10(a) and 4.11(a) describe the ion VDFs when the discharge current rises. The ion VDFs look like a strong double layer since there is another set of slow ions in the region where the ions are accelerated. This structure has been recently observed in experiments by a LIF technique by Young *et al.*[88]. They concluded that the slow ions in the acceleration region are related with CEX collisions. However, the present simulation results suggest the slow ion population can occur without CEX. As the discharge voltage is fixed in the system, whenever there is a strong potential drop, the electric field in other regions must be reduced. Since ionization still occurs in the acceleration region, slow ions may populate the region where the electric field is small, which generates the slow ion population near the channel exit during the discharge oscillation.

The double layer type structure moves and pushes the slow ions out of the channel. After the slow ions near the channel exit disappear, smooth ion acceleration can be again achieved, as shown in Figs. 4.10(b)-(e). It can be seen from these figures that the discharge current oscillations are mainly due to the number density fluctuation rather than the ion acceleration mechanism. It can also be seen that the plasma near the anode gradually moves towards the channel exit. As neutral atoms are consumed, the ionization rate drops and hence the ion density also decreases.

A similar trend is also shown in Fig. 4.11 for HPIC results. The major difference between the HDK-DK and HPIC results can be seen from the magnitude of the slow ion density near the channel exit. The ionization events are captured better in the HDK simulations than

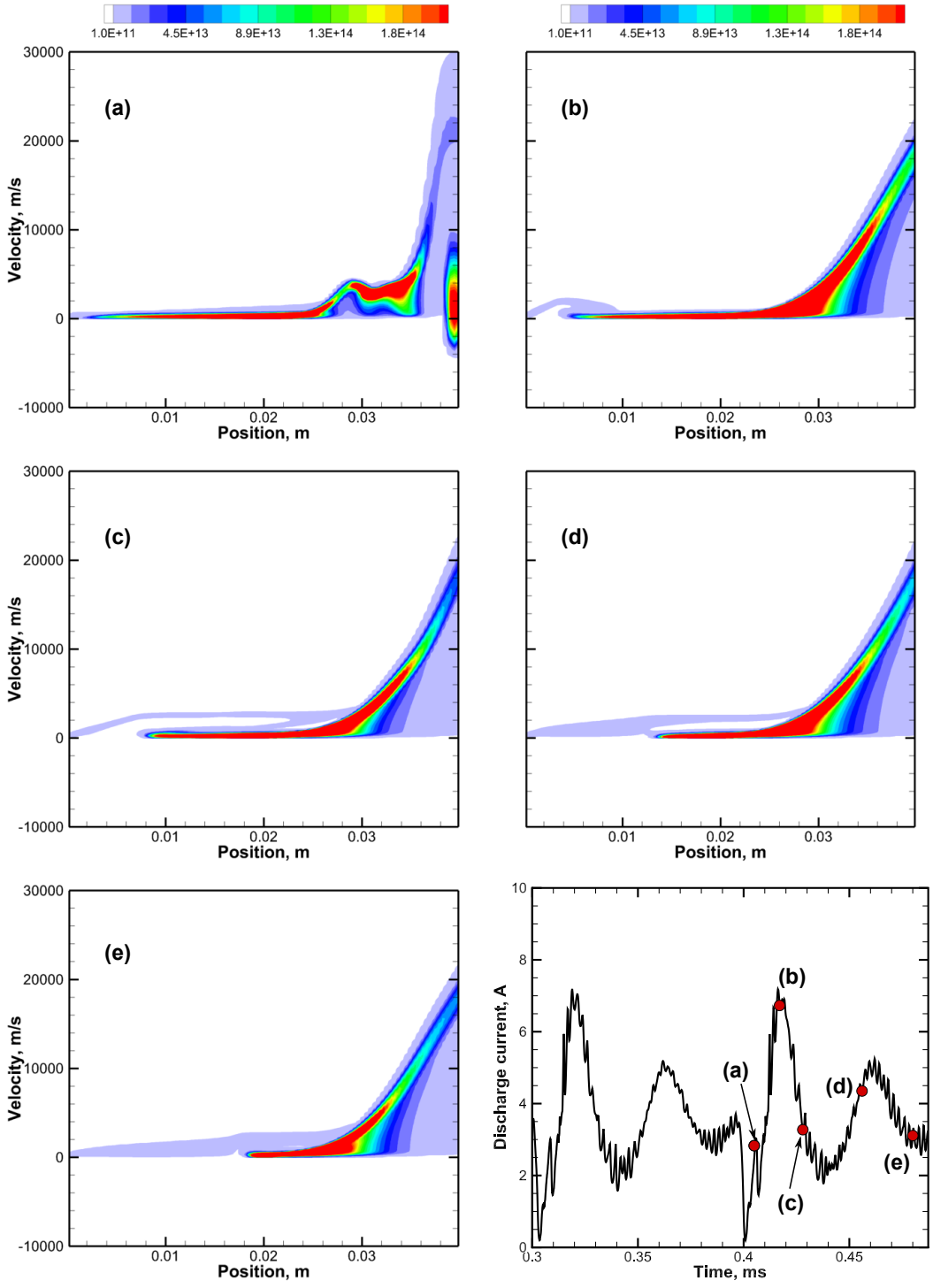


Figure 4.10: HDK-DK: Time-varying results of ion VDFs as well as the discharge current.

in the HPIC results. This can be seen from all the figures that there are empty velocity bins in the HPIC results in comparison to HDK results, where even rare ionization events

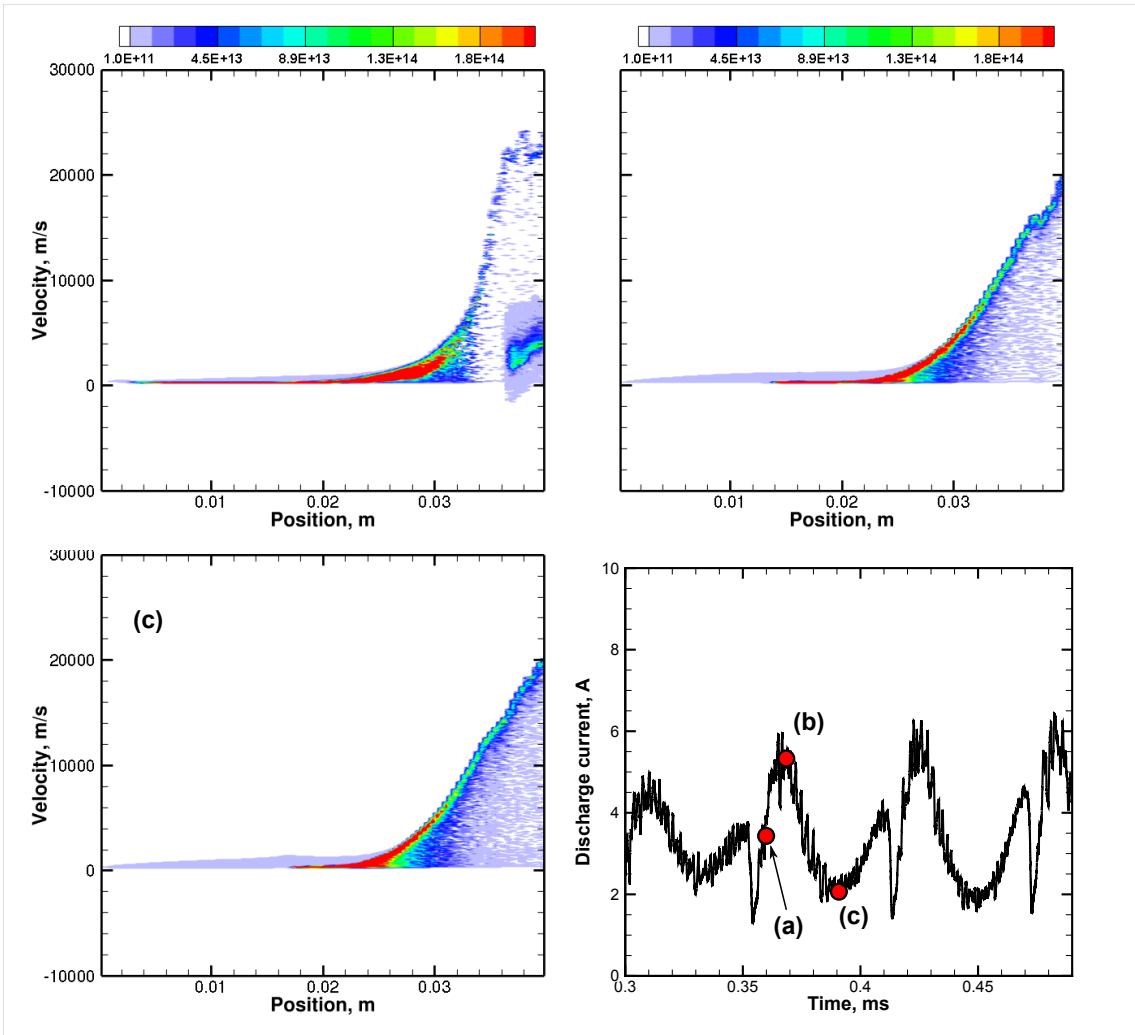


Figure 4.11: HPIC: Time-varying results of ion VDFs as well as the discharge current.. Note that the neutral atom speed is slightly higher than the other results, $u_n = 300$ m/s.

are captured in the low velocity region. Also, the slow ion population in Fig. 4.10(a) and Fig. 4.11(a) shows a clear difference in the magnitude of the ion VDFs. For instance, there are no particles in the region where ions significantly accelerate, *i.e.* in the strong double layer, at $x = 0.34 - 0.36$ m in Fig. 4.11(a). Note that the results shown in Fig. 4.11 employ a slightly different neutral atom velocity in comparison to Fig. 4.5(c). The macroscopic results are not affected by the neutral atom velocity but the breathing mode frequency is, as shown in Eq. (4.17).

### 4.6.3 Instantaneous VDFs

Figure 4.12 shows the instantaneous VDFs of ions at the channel exit. The time at which the data are chosen is at a maximum peak of the discharge current. Therefore, the time corresponds to Figs. 4.10(b) and 4.11(b). The overall shape and the most probable

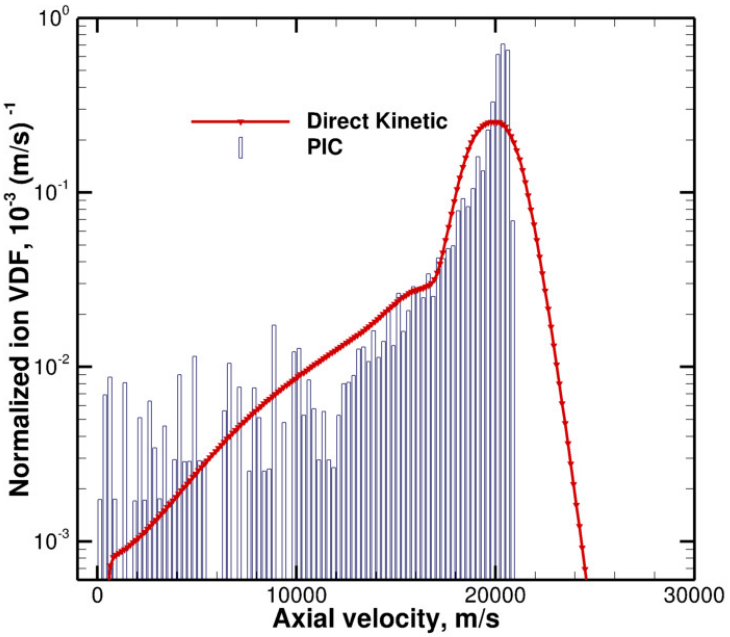


Figure 4.12: Instantaneous VDFs of ions at the channel exit obtained from the hybrid-PIC and HDK-DK simulations. Zero values are not shown since it is a logarithmic plot.

velocities of the VDFs at the channel exit agree well in both simulations. The most probable velocities are approximately 20 km/s. One notable feature is that the DK simulation resolves any level of the VDFs whereas the PIC simulation uses discrete particles with a numerical weight so that there is a minimum limit in the VDFs that can be resolved. The ion VDFs obtained from the particle simulation are not well resolved in the low density region as can be seen from Fig. 4.12 where there are several velocity bins that are empty. This is also problematic in the near-anode region where the ionization rate is small and there may be cells that have no macroparticles. The number of ions in one physical cell near the channel exit can be estimated as $N = nA\Delta x \approx 10^{17}\pi/4(0.05^2 - 0.03^2)4 \times 10^{-3} = 5 \times 10^{11}$.

Assuming that each velocity bin is $\Delta v \approx 100$ m/s and the particles are equally distributed in the velocity space, each velocity bin contains $N\Delta v/v_{max} = 2.5 \times 10^9$ number of particles, where $v_{max} = 20000$ m/s. Therefore, the velocity bins at low velocities are not likely to be empty from this estimate.

For hybrid simulations in which quasineutrality is assumed, a number density of zero crashes the simulation. In order to avoid zero number density, the hybrid-PIC simulation employs an offset for ion number densities of $10^{15}$ m$^{-3}$. In addition, the hybrid-PIC results exhibit a steep discontinuity in the velocity space at high energy. The absence of high energy particles may be attributed to the beam-type VDFs when ions are generated in the ionization region. For the HPIC simulations, the ions generated via an ionization event have constant velocity, which is not sampled from a Maxwellian–type distribution. Assuming initial velocity to be small ($\sim 200$ m/s), the ion velocity at the channel exit can be calculated from energy conservation:

$$v = \sqrt{\frac{2eV_d}{M}}$$

The ion velocity is 21,000 m/s for a discharge voltage of 300 V, and this matches the maximum limit of velocity obtained from the HPIC simulation.

One major disadvantage of the DK simulations is the resolution of the sharp discontinuity in velocity space that particle methods can capture. Although the VDFs obtained from the DK simulation are smooth and contain no statistical noise, the use of a second-order finite-volume method and fixed Cartesian grids cause broadening of the VDFs. The high energy tail of the distribution is mainly due to the numerical dissipation of the scheme used. For instance, the results shown in this dissertation exhibit great improvement over those shown in Ref. 81. The high energy tail, for instance, was around $2.8 \times 10^4$ m/s in the previous model whereas it is approximately $2.4 \times 10^4$ m/s in the present results. The use of higher-order numerical methods is reserved for future work. The numerical dissipation leads to the increase in the temperature, *i.e.* the width of the VDFs. This was not critical for the ions, as the collisions depending on the ion temperature are not important in the Hall thruster discharge, but may become important for electron kinetic modeling.

It is observed from the present investigation that the effect of the high energy tail of ion VDFs on the time-averaged and time-resolved macroscopic results is small, particularly in comparison to other components of the hybrid approach including the electron continuum model, boundary conditions, and neutral atom solver. The most important region in the ion VDFs is the peak, as most of the macroscopic quantities lie near the peak of the VDFs. In addition, several advancements on time-resolved LIF measurements have been made by Mazouffre *et al.*[66] and Durot *et al.*[89]. In those results, the high energy tail of ions is often observed, which is possibly caused by some physical mechanisms, such as CEX or beam-type instability, and/or measurement uncertainties. The experimental measurements suggest that the high energy tail of the ions may be an issue related to not only numerical errors but also some physical processes.

### 4.6.4 Effect of Charge Exchange Collisions

The collision frequency due to CEX collisions is given by:

$$\nu_{\text{CEX}} = n_n \int \hat{f}_i \hat{f}_n |g| \sigma_{\text{CEX}} dv \tag{4.18}$$

where $\hat{f}$ is the normalized VDFs and $\sigma_{\text{CEX}}$ is the cross section due to CEX collisions. Here, the CEX cross section employs the expression proposed by Pullins *et al.*[79]:

$$\sigma_{CEX}(v) = (a - b \log_{10} v) \left( \frac{I}{I_0} \right)^{-1.5},$$

where $a$ and $b$ are coefficients fit to the measured data, which are given by $a = 188.81 \pm 5.64$ and $b = 23.30 \pm 1.02$, $I/I_0$ is the ratio of the xenon ionization potential, $I = 12.13$ eV, to that of hydrogen, $I_0 = 13.6$ eV.

In the diffusion and ionization regions, the relative velocity of neutral atoms and ions is small so that the CEX frequency is negligible. CEX collisions become important in the acceleration region where the ions have larger velocity than neutral atoms. If the VDFs of ions and neutral atoms are assumed to be a delta function at 20 km/s and 0 m/s, respectively, at the channel exit, the CEX frequency is $\nu_{\text{CEX}} \approx 1 \times 10^4$ Hz. CEX collisions

are known to be important in the plume where the ionization rate is small. An accurate prediction of the slow ions due to CEX collisions is required for spacecraft integration in the actual missions and well-resolved VDFs of ions can be used as inputs for plume simulations. [30]

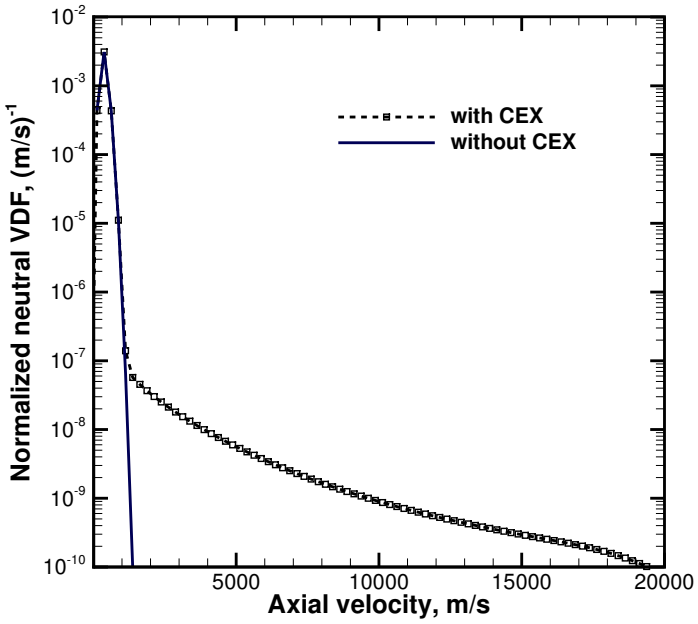


Figure 4.13: Velocity distribution function of neutrals at the channel exit

## 4.7 Summary

The grid-based DK simulation method discussed in Chapter III is now integrated into a hybrid framework, where an electron continuum model is used and the DK method is employed for the heavy species. The DK method is compared with a PIC method using the hybrid kinetic-continuum model as well as experimental data.

Time averaged and time resolved plasma parameters are compared in order to investigate the usefulness of the DK simulation. The breathing mode is observed and its frequency agrees well with theories and experiments. High frequency oscillations show similar trends in the DK and PIC simulations yet the DK simulation exhibits the ability of achieving temporally and spatially resolved plasma parameters. By comparison, the hybrid-PIC sim-

ulation suffers from inherent statistical noise. Two mechanisms have been greatly improved in the hybrid-DK simulation:

- The treatment of ionization events, for which the particle simulation is unable to generate ion particles at each time step and every velocity bin,
- the resolution of VDFs, and hence that of the plasma properties.

The new kinetic approach provides an alternative to particle simulations that contain statistical noise even when the number of macroparticles is large.

The direct kinetic simulation that achieves a better resolution of VDFs and the plasma parameters will be implemented for the electrons as well as the heavy particles. One challenge of a fully-kinetic simulation is the computational cost. Firstly, the spatial discretization must be chosen smaller than the local Debye length, which is similar to particle methods. Secondly, the effect of the magnetic field will be included in the electron DK solver. Lastly, due to the discrepancy in the masses of electrons and ions, the time step for electrons should be taken much smaller than that for ions. In order to reduce the computational time, numerical techniques such as GPU computing and adaptive mesh refinement can be employed. [49]

# CHAPTER V

# Mode Transition of Discharge Oscillations in Hall Thrusters

## 5.1 Introduction

A wide spectrum of oscillation modes exists in Hall thruster discharge plasmas. Understanding and controlling the low-frequency oscillation modes is critical for development of HETs.

Two important types of low-frequency oscillation modes in the range of 10-30 kHz include an axial breathing mode and an azimuthal rotating spoke mode. The breathing mode has been observed in several numerical studies[5, 10, 11, 90] but differences between the oscillation modes have not been discussed. The two low-frequency oscillation modes have also been observed in experiments using high speed Langmuir probe systems [91] and high speed camera systems,[1, 92] in which emitted light from the discharge plasma is measured to analyze the oscillation modes. Excited states of atoms and ions often play an important role as a different path of ionization and hence nonlinear mechanism of electron energy loss. Although excited atoms have been modeled in PIC methods,[93] the effect of excited atoms on discharge oscillations has never been explicitly discussed in the previous Hall thruster simulation models.

State-of-the-art particle simulations[10, 13, 14, 94] employ time averaging techniques to obtain smooth macroscopic profiles that may numerically alter the oscillation behaviors. Additionally, due to restriction of the computational memory, ionization events are often not captured every time step in such particle methods whereas a DK simulation can model the ionization at every time step and on every phase space cell.[81] Continuum models

[5, 68, 90] cannot capture the non-equilibrium nature of the discharge plasma which may affect the plasma oscillations. Hence, it is expected that a DK simulation can capture oscillations of the discharge plasma more accurately.

In this chapter, an improved version of the 1D hybrid-DK simulation[81, 95] is developed, including an improved electron fluid model as well as ground- and excited-state neutral atom transport models in addition to the hybrid model presented in Chapter IV. Although radial and azimuthal plasma transport is not solved directly, the characteristics of axial plasma oscillations that determine the global discharge oscillation can be investigated. The purpose of this study is to analyze the mode transition that occurs in a standard SPT-type Hall thruster comparing experimental observations with numerical simulations.

## 5.2 Previous Research on Mode Transition

The first research conducted on mode transition was by Tilinin[3] in 1977. Figure 5.1 shows the discharge current as a function of magnetic field strength. Note that these definitions were developed using an older SPT type thruster and the *loop* oscillations refer to what are currently called breathing mode oscillations.

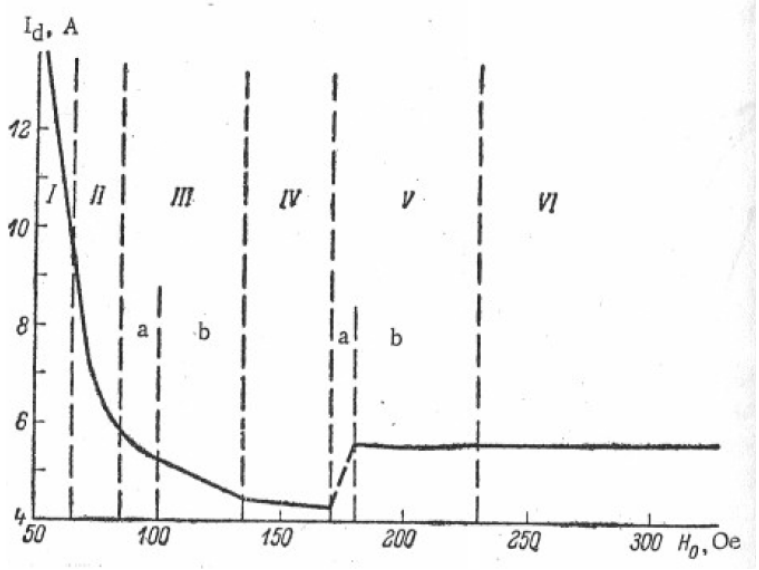


Figure 5.1: Discharge current as a function of magnetic field with constant discharge voltage. The operation modes are categorized into six different regimes. Reproduced from Fig. 5 of Ref. 3.

I **Collisional (classical) conductivity**: The weak magnetic field causes the electron Larmour radius to be comparable to the effective dimensions of the channel.

II **Regular electron drift wave**: Dominated by an azimuthal drift wave that propagates at 0.4−0.8 $v_{E\times B}$.

III **Transition**: Moderate amplitude loop oscillations due to poor conductivity in the discharge channel.

IV **Optimal**: Discharge current and loop oscillations are minimized. The electron drift wave is detectable, but of lower amplitude.

V **Macroscopic instability**: Discharge current abruptly increases and loop oscillations become strong with visible instabilities in the thruster. Drift waves are absent.

VI **Magnetic saturation**: Discharge is again stabilized and loop oscillations are minimized. Transit time oscillations dominate.

In terms of the actual HET operation, operating in the optimal region (Region IV) is best because the discharge current and breathing mode oscillations are minimized. Therefore, research on mode transition has focused mainly on Regions III and IV.

Bechu *et al.*[96] investigated the operating mode transition of an SPT-100ML thruster. Four discharge current oscillation modes are identified. Irregular mode at discharge voltage of 100 V, fluctuating mode at 300 V, oscillating mode at 400 V, and pulsed mode at 600 V. The effect of discharge current on the oscillation modes has been also shown by Gascon *et al.* in Ref. 4.

Gascon *et al.*[4] studied the discharge current oscillations in an SPT-100ML thruster, using various materials for the channel wall for the discharge voltage of 300V, as shown in Fig. 5.2. Regions I and II are not shown and Regions V and VI are not observed due to the improvements in the design of HETs. The result for borosil in Fig. 5.2(a) shows a qualitative agreement with Fig. 5.1. The oscillation modes for an alumina channel wall show a similar trend but the stable discharge region (Region IV) is observed at a lower magnetic field strength. Silicon carbide and graphite do not exhibit any optimal region in

the range of magnetic field strengths shown in the figures. The large discharge oscillations for silicon carbide and graphite were attributed to the short circuit effect near the wall in Ref. 4.

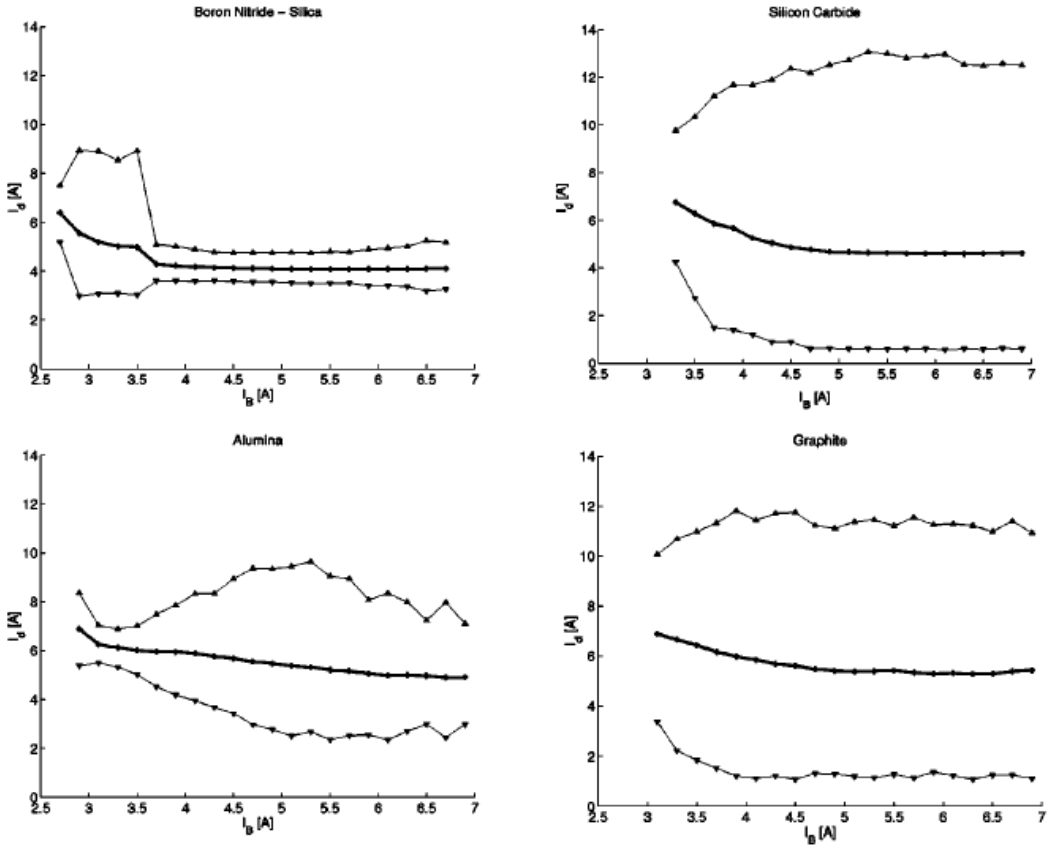


Figure 5.2: Discharge current oscillations reported by Gascon *et al.*. The discharge voltage is 300 V and the anode mass flow rate is 5 mg/s. Top left: borosil, bottom left: alumina, top right: silicon carbide, and bottom right: graphite. Reproduced from Fig. 2 of Ref. 4.

Barral *et al.*[5] performed a 1D continuum simulation of the Hall thruster discharge plasma. In Ref. 5, good agreement of the trend of mean discharge current shows with experimental data and Tilinin's observations is shown. The discharge current increases as the electron current increases for a smaller magnetic field. It was indicated that the mode transition is attributed to the wall effects, namely the space charge limited (SCL) sheath, or space charge saturated (SCS) sheath as illustrated in Fig. 5.3. In Ref. 5, the amplitude of discharge current oscillations as well as the breathing mode frequency are not shown and discussed. Thus, the cause of the mode transition of discharge oscillation is not completely

understood.

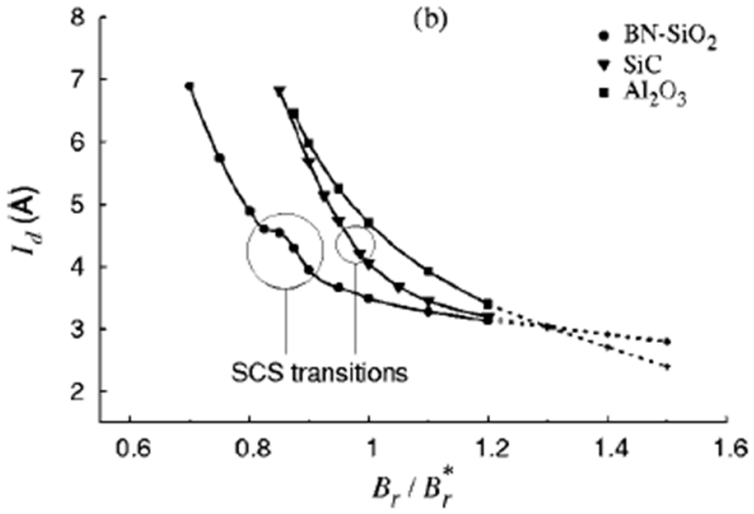


Figure 5.3: Discharge current oscillations reported by Barral *et al.* using a 1D continuum simulation. Reproduced from Fig. 10(b) of Ref. 5.

## 5.3 Improved Hybrid-DK Simulation

The discharge plasma of a SPT-100 Hall thruster is modeled using a 1D hybrid-DK simulation. The SPT-100 is chosen for modeling as a typical, well-characterized Hall thruster. A DK simulation is used for ions, a fluid model which solves the momentum and energy equations is used for electrons, and neutral atoms are modeled solving the continuity equation. Singly charged ions and one electronically excited state of xenon atoms are taken into account in the model. The implementation of the hybrid-DK simulation is identical to that in Chapter IV as illustrated in Fig. 4.1.

The configuration is identical to the SPT-100ML thrusters.[4, 5] The calculation domain is taken from $x = 0$ cm, the anode, to $x = 3.5$ cm, which is assumed to be the cathode line where the electron total energy is chosen as 10 eV and the potential is 0 V. The channel length is 2.5 cm. The discharge voltage is 300 V, anode mass flow rate is 5.0 mg/s, and the peak magnetic field is varied. Background pressure is not accounted for in the present model and charge exchange collisions are neglected.

The transport of ground-state and electronically excited atoms are modeled by solving

the continuity equation.

$$\frac{\partial n_n}{\partial t} + \frac{\partial}{\partial x}(n_n u_n) = \sum_{\text{reactions}} \dot{n}_n, \tag{5.1}$$

where $\dot{n}_n$ is the source term due to collisional reactions. The axial neutral atom velocity is assumed to be constant: $u_n = 250$ m/s. For the ground-state neutral atoms, electron-impact excitation, electron-impact ionization, and wall diffusion are taken into consideration. For the excited-state neutral atoms, electron-impact excitation, and electron-impact stepwise ionization are included in the model. The ion diffusion rate to the walls is determined by

$$\dot{n}_{iw} = n \frac{1}{R_o - R_i} \sqrt{\frac{eT_e}{m_i}},$$

where $R_o$ and $R_i$ are the outer and inner radii, respectively. The ions are assumed to approach the sheath edge at the ion acoustic speed, *i.e.* the Bohm condition. The rate coefficients of various processes are tabulated assuming a Maxwellian electron distribution using the cross section data cited in Table 5.1. Note that several assumptions are made in this model, including neglecting energy loss due to the elastic collisions, resonance radiation trapping[97], and doubly-charged ions, but it is still an improvement over state-of-the-art simulation methods. Inclusion of detailed collision models is reserved for future work.

Table 5.1: Collisions: $Xe$, $Xe^*$, and $Xe^+$ are the ground-state atom, excited-state atom, and ion.

| | | | | Energy loss |
|---|---|---|---|---|
| Excitation [85] | $Xe + e$ | $\rightarrow$ | $Xe^* + e$ | 8.3 eV |
| Direct ionization [80] | $Xe + e$ | $\rightarrow$ | $Xe^+ + 2e$ | 12.1 eV |
| Stepwise ionization [98] | $Xe^* + e$ | $\rightarrow$ | $Xe^+ + 2e$ | 3.8 eV |
| Radiation [99] | $Xe^*$ | $\rightarrow$ | $Xe + h\nu$ | - |
| Elastic collisions [100] | $Xe + e$ | $\rightarrow$ | $Xe + e$ | - |

The pressure term is included in the new electron fluid model. The 1D electron momentum equation is written as

$$v_{ex} = \mu_{eff} \left[ E_x - \frac{1}{n_e} \frac{\partial}{\partial x} (n_e T_e) \right] \tag{5.2}$$

where $\mu_{eff}$ is the effective electron mobility and $v_{ex}$ is the axial electron drift velocity

which is obtained from current conservation. The effective electron mobility is determined by the magnetic field and effective momentum transfer collision frequency, $\nu_{eff}$, that is described as the sum of electron-neutral elastic collisions, electron-impact inelastic collisions, electron-wall collisions, Coulomb collisions, and any contributions from anomalous transport. Coulomb collisions are not important under the plasma parameters in the Hall thruster discharge. The momentum transfer collision frequencies due to elastic and inelastic collisions are obtained from Table 5.1.

In this model, it is assumed that the effective electron mobility has some contributions from the nonmagnetized mobility, $\mu = e/m\nu_m$, near the anode.

$$\mu_{eff} = \alpha\ \mu_\perp + (1-\alpha)\mu, \tag{5.3}$$

where $\alpha = x/L_c$ and $\mu_\perp = \mu(1+\Omega^2)^{-1}$ with $L_c = 0.5L_{ch}$, the Hall parameter $\Omega = \omega_B/\nu_m$, and the electron gyro-frequency $\omega_B = eB/m_e$. By setting the electron mobility large near the anode, the electric field and hence the electron heating are reduced. It has been suggested by Hofer *et al.*[14] that additional anomalous contributions are required for the electron mobility near the anode. An anomalous electron collision frequency results in increased electron mobility so that the electric field decreases. Thus, the nonmagnetized electron mobility term assumed in this study is similar to the anomalous mobility near the anode assumed by Hofer *et al.*

The electron-wall collision frequency is given by

$$\nu_{ew} = \frac{1}{R_o - R_i}\sqrt{\frac{T_e}{m_i}}\frac{1}{1-\sigma} \tag{5.4}$$

where $\sigma$ is the effective secondary electron emission (SEE) rate, which is a function of the electron temperature. The SEE model is identical to that of Barral *et al.*[5, 90] in which the wall material is borosil and the effective SEE coefficient is assumed to be $\sigma = \max(T_e/25, \sigma_{SCL})$ where $T_e$ is the electron temperature. $\sigma_{SCL} = 0.986$ is the space charge limited (SCL) SEE coefficient of a xenon plasma and $T_e = 24.6$ eV is assumed to be the critical electron temperature that forms an SCL sheath.

A two-region model is used for the anomalous cross-field mobility.[13, 73] Different anomalous mobility coefficients are chosen for outside and inside the channel such that the predicted mean discharge current agrees with the experimental data.

$$\nu_{ea,out} = \frac{1}{16}\omega_B, \quad \nu_{ea,in} = \frac{1}{160}\omega_B, \tag{5.5}$$

where $\nu_{ea,out}$ and $\nu_{ea,in}$ are the anomalous mobility outside and inside the channel. It is not the focus of the present investigation to find the anomalous mobility coefficients that agree with experimentally measured thruster performance as has been demonstrated for the H6 thruster.[14] The main focus of this study is to investigate the cause of the mode transition in a Hall thruster under the assumption that the anomalous electron mobility components remain the same across the mode transition. However, it is worth noting that the mode transition is observed for different cross-field mobility coefficients in the hybrid kinetic-continuum model, as discussed in Sec. 5.7. For the mode transition study, the values are chosen such that the mean discharge current agrees with the experimental results. In order to fully understand and capture the behavior of the discharge plasma, a self-consistent model that accounts for the anomalous diffusion without using empirical coefficients is required.

The electron energy equation is described by the balance between convective heat flux, Joule heating, wall losses, and inelastic collisions.[74]

$$\frac{\partial}{\partial x}\left(\frac{5}{3}nv_{ex}\varepsilon\right) = n_e v_{ex} E_\perp - n_e\left[\nu_{ew}\Delta\varepsilon_w + \sum_j \nu_j \Delta\varepsilon_j\right] \tag{5.6}$$

where $\varepsilon$ is the mean electron energy, $\nu_{ew}$ is the electron-wall collision frequency given in Eq. (5.4), $\Delta\varepsilon_w$ is the energy loss to the wall, $\nu_j$ is the collision frequency and $\Delta\varepsilon_j$ is the energy loss due to an inelastic collision, $j$. The mean electron energy can be decomposed into

$$\varepsilon = \frac{3}{2}T_{eV} + K_{eV} \tag{5.7}$$

where $T_{eV}$ is the electron temperature in electron-volts, $K_{eV} = \frac{1}{2}m_e(v_{ex}^2 + v_{e\theta}^2)/e$ is the kinetic energy in electron-volts, and $v_{e\theta} = v_{ex}\Omega$ is the azimuthal velocity. The energy loss

to the wall is given by $\Delta\varepsilon_w = 2T_{eV} + K_{eV} + |\phi_w|$ where $\phi_w$ is the sheath potential. As the experiments by Raitses *et al.*[101] showed that the effective electron temperature measured by Langmuir probes can exceed the electron temperature of the SCL sheath, it has been suggested that there is an anisotropy in the electron temperature. This has also be suggested by Barral *et al.*[5, 90]. In the present model, it is assumed that the electron temperature is isotropic, i.e. $T_e = T_{e,\perp} = T_{e,\parallel}$ where $T_{e,\perp}$ and $T_{e,\parallel}$ are the electron temperatures across and along the magnetic field, respectively. However, it can be considered that the kinetic energy is the source of the isotropy, as the energy in the parallel direction is not modified but that in the perpendicular direction contains the kinetic energy due to the $E \times B$ drift.

## 5.4 Mode Transition Results

Mode transition in the mean discharge current as well as the magnitude of the discharge current oscillation is observed from the numerical simulation showing good agreement with experiments. In this study, although the 1D axial simulation cannot capture the azimuthally rotating structure as described in Ref. 7, the discharge oscillation mode and stable discharge mode obtained from the simulation are categorized as *global* and *local* modes, respectively. From experiments, it was found that ionization oscillations occur simultaneously in the entire channel during the global mode whereas the oscillations are localized and propagate in the azimuthal direction during the local mode. Mode transition when varying the discharge voltage or the mass flow rate lies outside the scope of the present study.

### 5.4.1 Comparison with Experiments

Figure 5.4 shows the discharge mean current and the standard deviation of the oscillation. The numerical results of the SPT-100 thruster obtained from the hybrid-DK simulation agree with the experimental data obtained in the H6 and SPT-100 thrusters. The experimental data of the H6 thruster show the same trend as those of the SPT-100 thruster reported in Ref. 4. It can be seen from the two experiments that global and local ionization modes correspond to transient and optimal modes, respectively, which are categorized by Tilinin.[3] The relation between the experimental coil current and the magnetic

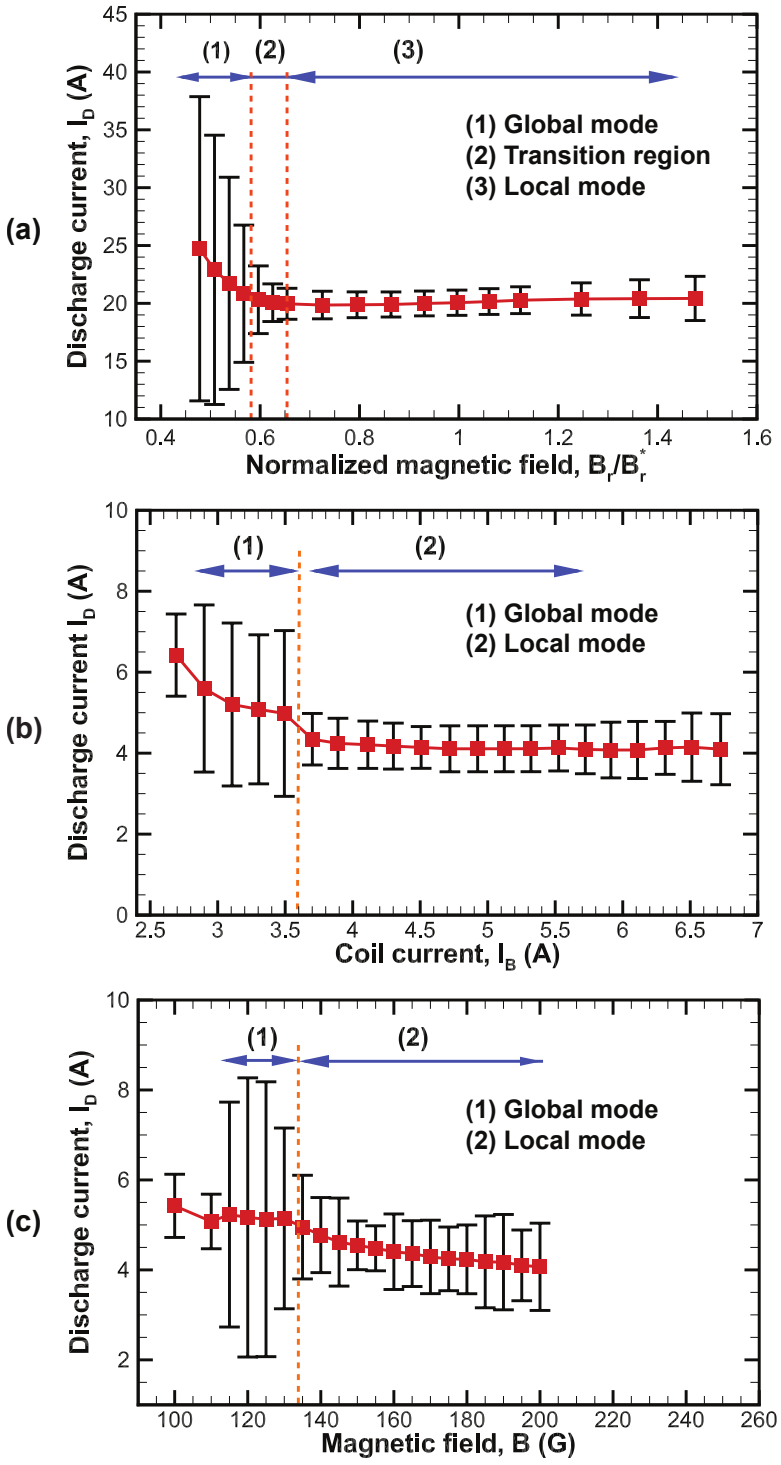


Figure 5.4: Discharge current vs. magnetic field: Red symbol plots are the mean discharge current and error bars show the standard deviation. (a) Experimental results of the H6; (b) Experimental data of the SPT-100. Reproduced from Ref. 6; (c) Hybrid-DK simulation results of the SPT-100.

field strength is not explicitly given but it is often linearly correlated.

### 5.4.2 Discharge Current Oscillations

The discharge current oscillations of the global and local modes in both the H6 experiment and the SPT-100 simulation are shown in Fig. 5.5. Figures 5.5(a) and 5.5(b)

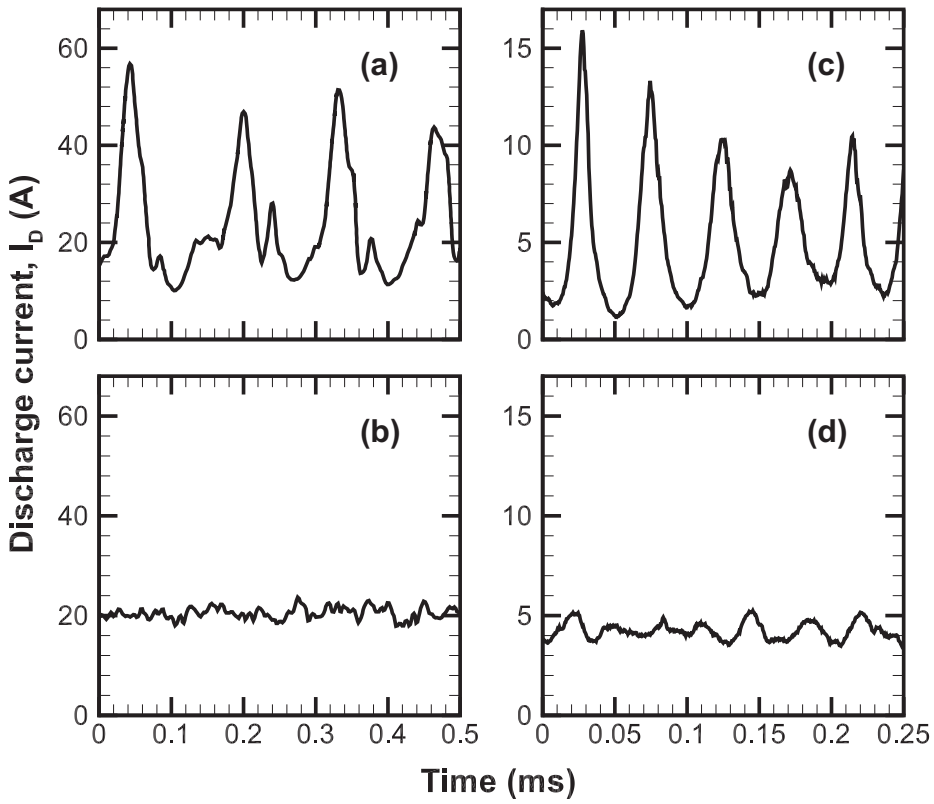


Figure 5.5: Discharge current oscillation: (a) $B_r/B_r^* = 0.52$ (H6), (b) $B_r/B_r^* = 0.61$ (H6), (c) B=120 G (Hybrid-DK), (d) B=180 G (Hybrid-DK).

correspond to $B_r/B_r^* = 0.52$ and 0.61 shown in Fig. 5.4(a), and Figs 5.5(c) and 5.5(d) correspond to $B = 120$ G and 180 G shown in Fig. 5.4(c), respectively. The shape of the discharge current oscillation exhibits excellent agreement between the two data sets. The global mode is a non-sinusoidal oscillation in which the maximum current is almost three times larger than the mean discharge current. In the local mode, the discharge current is not completely stationary but exhibits a small amplitude oscillation that is a superposition of several modes. Note that there are high frequency noise present in some regions during the breathing mode oscillation in the numerical results. These oscillations come from the

pressure gradient in the electron continuum model as the first derivative of the product of the number density and the electron temperature is taken and the electric field is calculated. This may be numerical but can also be physical in that the pressure gradient can cause acoustic type waves in the system.

Figure 5.6 shows the breathing mode frequency obtained from the discharge current oscillations of the H6 experiment and the SPT-100 simulation. The frequencies in Fig. 5.6(a) are determined by fitting a Lorentzian[102] to the discharge current power spectral density in order to identify the peak frequency. The standard deviation of data points to the averaged frequency versus magnetic field trace is 200 Hz. An agreement of the trend between the experimental data and the simulation results is shown although the magnitude of the frequency does not agree due to the difference in the thruster geometry and operational point. The breathing mode frequency of 20 - 25 kHz from the simulation of the SPT-100 thruster agrees with the previous experiment by Gascon *et al.*[4]

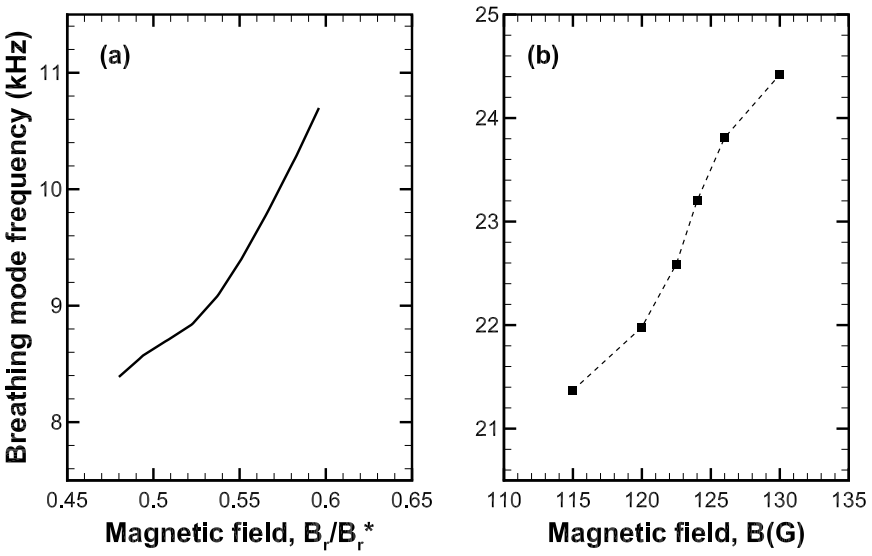


Figure 5.6: Breathing mode frequency: (a) H6 experiment,[7] (b) SPT-100 simulation.

The breathing mode frequency, first proposed by Fife,[10] is explained as a harmonic oscillation between the neutral atoms and ions:

$$\omega = \frac{\sqrt{V_i V_n}}{L_i} \tag{5.8}$$

where $V_i$ is the ion velocity, $V_n$ is the neutral velocity, and $L_i$ is the ionization length. This expression is also supported by the theoretical work of Barral and Ahedo[90] suggesting that the standing wave components of both ions and neutral atoms contribute to the breathing mode oscillation based on their fluid simulations so that a 0D model can be used to explain the breathing mode oscillation. However, in both papers, the damping or stabilization of the discharge oscillation mode has not been discussed. In Chapter VI, a linear perturbation theory is presented and the criteria for mode transition are discussed. In addition, the present simulation accounts for important physical effects that have been neglected in their fluid model including noiseless ion kinetic model and the transport of excited state atoms.

The ionization length is difficult to define since the discharge plasma is generated and confined dynamically due to the balance between ionization and acceleration as well as diffusion to the wall and the anode in Hall thrusters. In Eq. (5.8), the effect of electron transport is simplified using the ionization length, which is often considered to be on the order of the channel length. It is shown that the ionization length becomes smaller as the oscillations become stable, which is consistent with the observation in Fig. 5.6.

### 5.4.3 Plasma oscillations

The spatio-temporal evolutions of the global and local oscillation modes are shown in Figs. 5.7 and 5.8, respectively. The electron total energy is a sum of the electron temperature and electron kinetic energy as shown in Eq. (5.6), thus it is different from the electron temperature alone.

In the global mode, a periodic oscillation is exhibited for all of the plasma properties. The unique feature of the global oscillation mode is that the oscillation is non-sinusoidal. Ground-state atoms are consumed, shown in Fig. 5.7(a), while excited-state atoms and ions are generated during the ionization burst, shown in Figs. 5.7(b) and (c). The characteristic time of ionization and excitation, $t \simeq 20\ \mu s$, is shorter than that of resupply of neutral atoms from the anode, $t \simeq 25\ \mu s$. The rate of spontaneous emission, or de-excitation, of the excited-state atoms, $10^7$ Hz, is much faster than their transport across the channel. As the ion current at the channel exit increases during the ionization burst, the electron current toward the anode increases simultaneously in order to balance the total current.

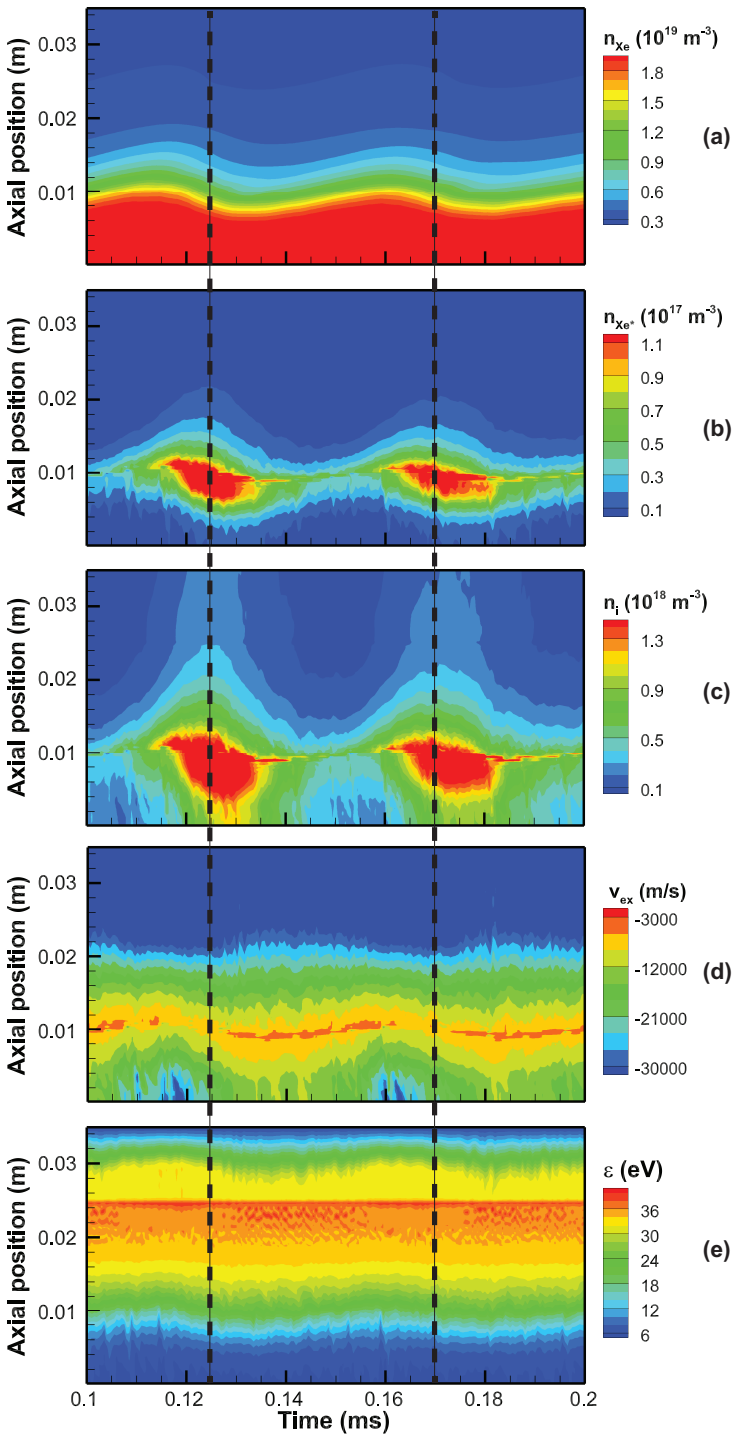


Figure 5.7: Two oscillation cycles (0.1 ms) of the global oscillation mode at B = 120 G. Dashed horizontal lines correspond to the maximum discharge current in Fig. 5.5(c). (From top to bottom) Ground-state atom density, excited-state atom density, ion density, electron axial velocity, and electron total energy.

After a large electron flux toward the anode and a large ion current toward the channel exit are generated, the plasma density decreases inside the channel and ionization occurs to produce electrons. A periodic ionization oscillation occurs due to the balance between plasma production and transport. Thus, the electron transport inside the channel plays an important role in the global oscillation mode. Note that the electron total energy is not continuous at the channel exit ($x = 2.5$ cm) due to artificially setting different anomalous mobility coefficients discontinuously inside and outside the channel. The high frequency oscillations result from the pressure gradient in the electron continuum model, which may be caused by numerical or physical effects. As can be seen, these oscillations are more present near the anode than the channel exit.

The plasma oscillation is stabilized in the local mode as shown in Fig. 5.8 although there is still a weak oscillation in the 10-30 kHz range. The discharge current oscillation is stabilized in comparison to the global oscillation mode as shown in Figs. 5.5(b) and 5.5(d) since the ionization and ion transport are stabilized. In this study, it is assumed that the SEE characteristics are determined by the electron temperature. The SCL sheath is observed at larger magnetic fields due to the increase in electron temperature, which is shown later. As shown in Fig. 5.8(e), the electron total energy exhibits unsteady behavior near the channel exit. When the SCL sheath occurs due to a large $T_e$, the wall collision frequency increases due to the small sheath potential so that the electron axial drift increases.

As the electric field ($v_{ex} \sim \mu E$) and the electron azimuthal drift increase, $T_e$ decreases, so the SCL sheath does not occur continuously in time and space. The unsteady behavior of the SCL sheath is also observed in other fully-kinetic simulations.[23, 103] It is worth noting that the increase in momentum transfer collision frequency due to the SCL sheath does not directly mean that the electron current increases in the axial direction. As discussed in Section 5.6.2, the electron axial velocity near the channel exit is determined by the balance between the magnetic field strength and the momentum transfer collision frequency. As the magnetic field strength increases and the momentum transfer collision frequency is enhanced due to the increase in $T_e$, it is suggested that there is a stable electron drift in the axial direction that results in a wide range of stable mode operation.

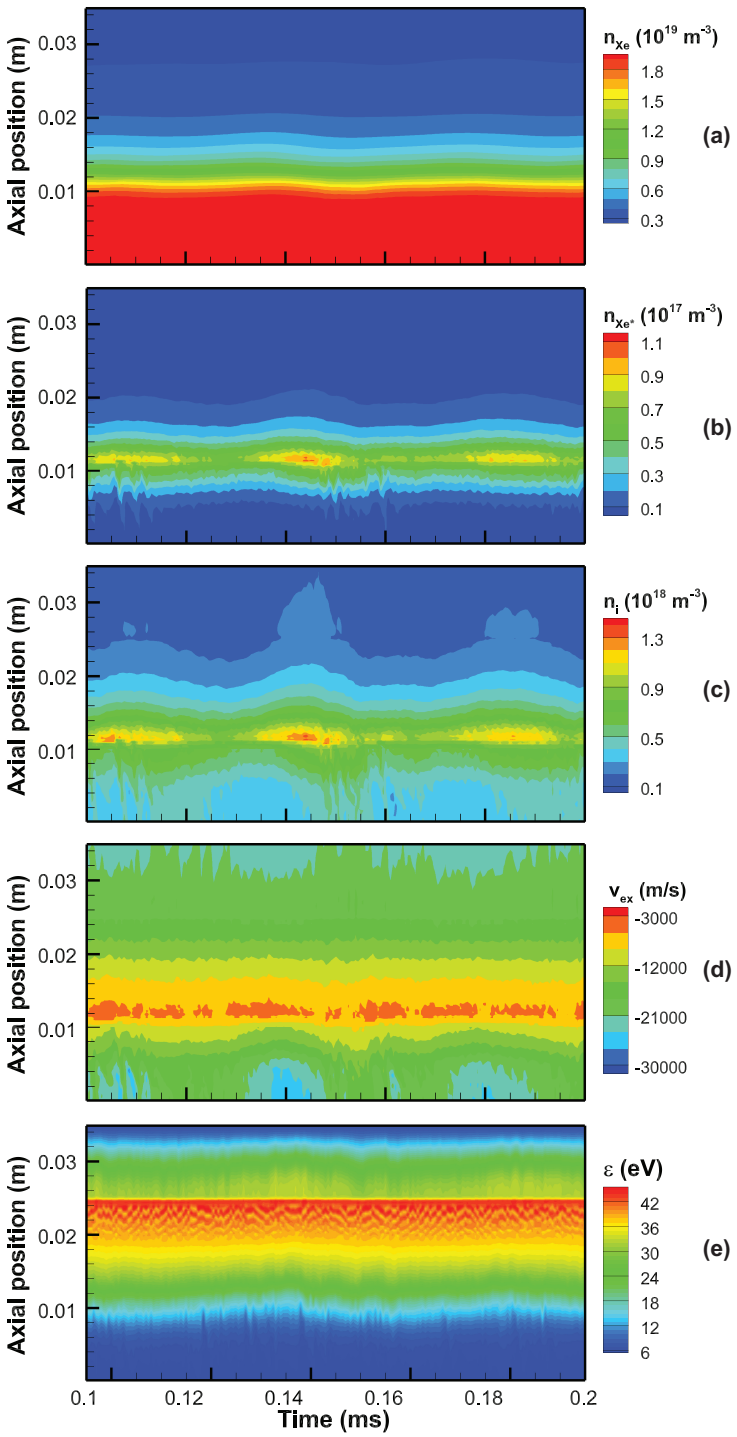


Figure 5.8: The local oscillation mode at B = 180 G. (From top to bottom) Ground-state atom density, excited-state atom density, ion density, electron axial velocity, electron total energy. Note that the range of electron total energy is different from Fig. 5.7(e).

## 5.5 Time-averaged Results

The time-averaged results of excited-state atoms and ionization cost are discussed in this section. The dynamic transport of excited-state atoms has not been performed in prior state-of-the-art HET simulations. The light intensity calculated from the deexcitation process exhibits a strong correlation with the plasma oscillations, which has been observed in experiments. In addition, the ionization cost has been chosen as a constant value in previous HET simulations, but the inclusion of additional excited-atom species allows one to examine the effects of such reactions on the global energy loss.

### 5.5.1 Excited-state Atoms

The excited-state atom density is strongly correlated with the discharge current and the plasma density as shown in Figs. 5.7(b) and 5.8(b), which indicates the correlation between light intensity and the discharge current. This agrees with recent experimental observations in which a strong linear correlation between global light intensity and total discharge current is observed.[1, 104] This may be of great interest to the experimentalists since measurement of visible light can be used to analyze the plasma oscillation without direct measurement. Inclusion of additional electronically excited states will be performed in future work.

Figure 5.9 shows the correlation between the excited-state atom density integrated over the channel length and the discharge current oscillation. The peak intensity is twice as large in the global mode as in the local mode. Assuming the excited-state atom density modeled in the present numerical simulation correlates with the visible light in the Hall thruster discharge plasma, the double peak intensity agrees with an experiment of the SPT-100 thruster.[105] In addition, the time-averaged excited-state atom densities are $1.7 \times 10^{16}$ $m^{-3}$ and $1.8 \times 10^{16}$ $m^{-3}$ in the global and local oscillation modes, respectively. A stable discharge operation generates excited state atoms as well as ions more efficiently than the global oscillation mode, which is also observed in experiments. The high frequency oscillations in the excited-state atom density are likely to be related to the noise in electron energy due to the pressure gradient in the electron continuum model. However, there are

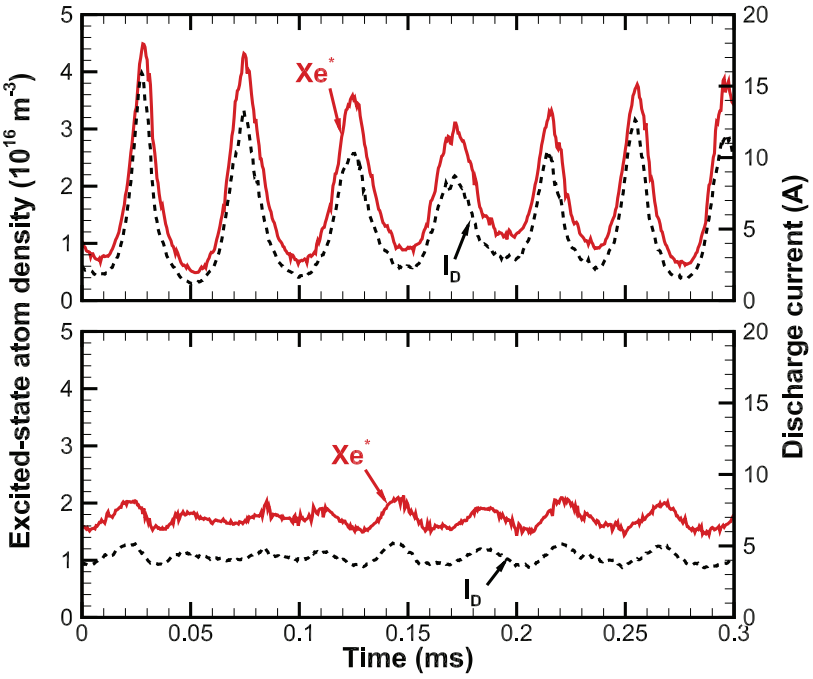


Figure 5.9: Discharge current oscillation and the integrated excited-state atom density: (a) B=120 G, (b) B=180 G.

also contributions from the collision rate on the right hand side of the neutral atom rate equations. The decay rate of the excited-state atom density may be too fast in the absence of radiation trapping,[97] leading to numerical noise in the excited-state atom density.

Figure 5.10 depicts the correlation between the light intensity and discharge current where a linear correlation is shown by a least squares fit. The light intensity is obtained from the normalized excited-state atom density ($n^*/1 \times 10^{16}$ m$^{-3}$), where $n^*$ is the excited-state atom density. Strong light emission corresponds to a large discharge current. It can be seen that the correlation coefficient is different in each mode. The global mode exhibits a larger discharge current than the local mode at the same light intensity. This suggests that the global mode is less efficient in terms of the thruster performance.

### 5.5.2 Ionization Cost

Figure 5.11 shows the time-averaged ionization cost in the discharge plasma. In the literature,[90] a constant ionization cost is usually assigned. The ionization cost is defined

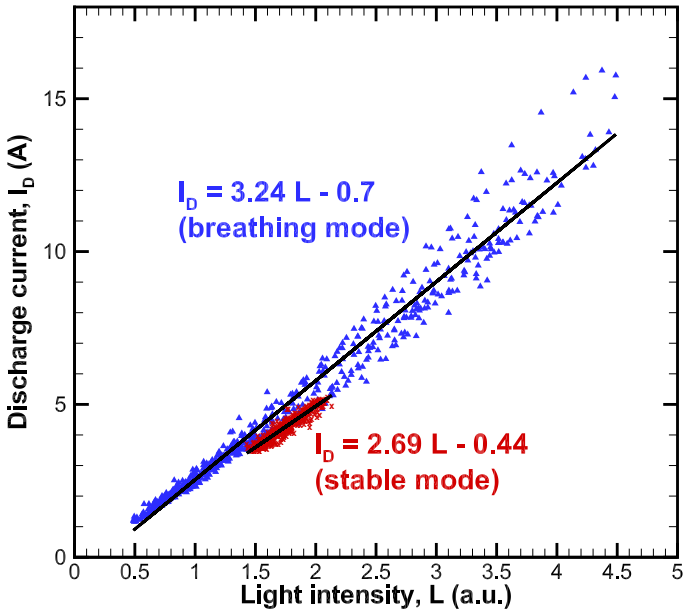


Figure 5.10: Correlation between light intensity and total discharge current. The light intensity: $L = n_{Xe^*}/10^{16}$.

as

$$\xi = \frac{\sum_j N_j k_j \Delta\varepsilon_j}{N_n k_{ion} \Delta\varepsilon_{ion}} \tag{5.9}$$

where $N_j$, $k_j$, and $\Delta\varepsilon_j$ are the heavy species atom density, the rate coefficient, and the threshold energy for reaction, $j$. The denominator is the energy transfer rate due to direct ionization. Since the excited-state atom density is smaller than that for the ion density, the contribution of stepwise ionization is the smallest among the inelastic collisions. Ionization cost essentially describes the ratio of ionization and excitation collisions that are mainly determined by the electron total energy. The larger the ionization cost, the larger the rate of excitation relative to ionization.

The ionization cost is approximately 1.4 in the ionization region where the electron energy is large. When the electron total energy is below 10 eV, the rate coefficient of excitation becomes larger than that of ionization. Thus, the location where $\xi = 2$ corresponds to the electron total energy of 10 eV. Since a small ionization cost corresponds to a large electron total energy, Fig. 5.11 shows that the stabilization of the global oscillation mode

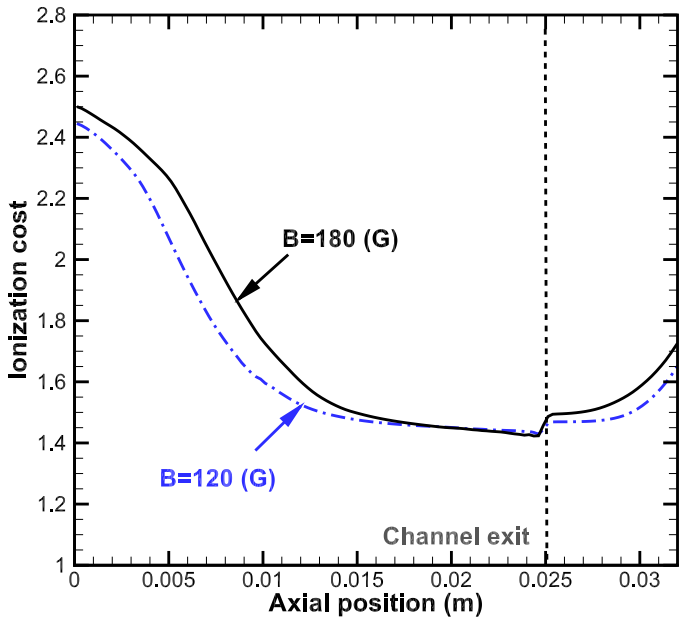


Figure 5.11: Time-averaged ionization cost.

is associated with the suppression of electron energy near the anode. The ionization cost may be too small as only one excited state is considered. In order to obtain an accurate estimate of the ionization cost, a detailed collision model is required including more excited states. Ionization is suppressed near the anode ($x < 8$ mm) and hence the discharge plasma is confined inside the channel away from the anode. Thus, the ionization length decreases as the breathing mode oscillation weakens. This is consistent with Eq. (5.8) and with the increase in the breathing mode frequency as the magnetic field strength is increased, as shown in Fig. 5.6.

## 5.6 Cause of Mode Transition

In this section, it is proposed that electron transport is critical to understanding the mode transition between the global and local modes. First, the electron axial velocity near the channel exit is neither too large nor too small when a stable operation is achieved. The stabilization of the global discharge oscillation is associated with the reduction of electron drift in both the axial and azimuthal directions. This behavior has been also suggested

by Hofer and Gallimore for the NASA-173Mv2 thruster[106], namely that the electron current remains unchanged when the discharge oscillation is stabilized. Second, it is shown that the global mode occurs when the Joule heating exceeds the other electron energy loss mechanisms. Thus, the electron energy balance is critical to stabilization of the discharge oscillation. Finally, the transfer between electron kinetic and thermal energy across the mode transition is discussed.

Barral *et al.* proposed that the mode transition is attributed to the SCL sheath using a 1D fluid code.[5] In their work, it was indicated that the mode transition from the local mode to the global mode is due to the formation of an SCL sheath under the assumption that the electron total energy including both thermal and kinetic energies contribute to SEE. This assumption is not necessarily true in that the azimuthal drift may not reach the wall when there is a large sheath potential formed. Only when the radial component of the electron drift is larger than the sheath potential can the kinetic energy affect the SEE from the wall. In addition, their simulation results have been validated in terms of the mean discharge current, but the amplitude of the discharge oscillation has not been discussed. In our study, the agreement in mode transition has been shown in terms of the mean discharge current, the RMS of the discharge current oscillation, and the breathing mode frequency. In this section, it is shown that electron transport plays an important role in the transition and stabilization of the discharge oscillation.

### 5.6.1 Electron Transport

Figure 5.12 shows a comparison of the time-averaged axial electron velocities for the two oscillation modes. As shown in Figs. 5.7(d) and 5.8(d), the point at which the electron axial drift is smallest is stationary in local mode whereas it moves periodically about 2 mm in global mode. In local mode, the location of the minimum electron axial drift at which the ion density is maximum is shifted away from the anode and thus it is indicated that the ionization region is more confined. The electron axial drift plays an important role in electron energy gain via Joule heating ($\vec{j} \cdot \vec{E}$) and the energy loss due to wall collisions depending on the electron temperature. Note that electron axial velocity is on the order of 0.001 eV, thus the axial component of the electron drift is negligible in the kinetic energy.

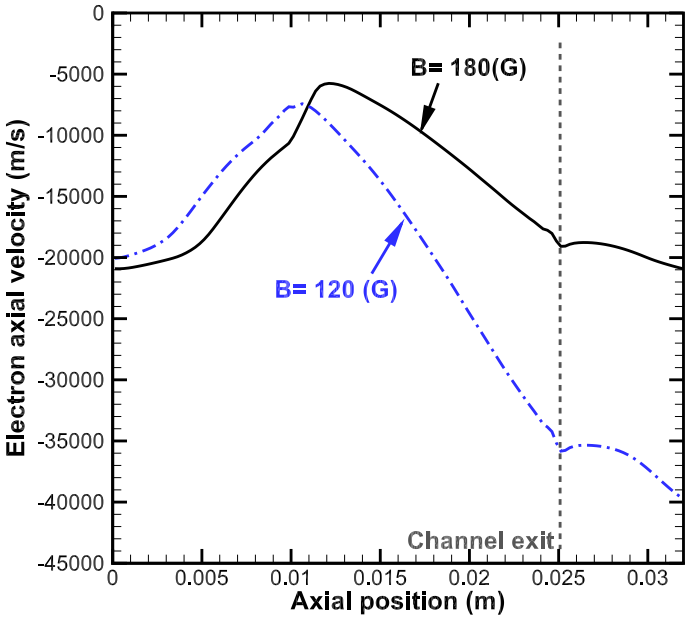


Figure 5.12: Time-averaged axial electron velocity from Figs. 5.7(d) and 5.8(d).

A smaller electron axial velocity was observed for an increases magnetic field strength by Tilinin.[3] Figure 5.12 supports Tilinin's observation, Region III in Fig. 5.1, that the insufficient electron current is related to the oscillatory discharge mode.

### 5.6.2 Electron Energy Contributions

The time-averaged energy contributions as a function of axial position in the two operation modes are shown in Fig. 5.13. In the global mode, the convective heat flux, which is the energy transfer due to the electron axial velocity, is large and balances the Joule heating. The electrons are poorly confined and the plasma oscillation occurs. In the local mode, as the magnetic field strength increases, the electron axial drift is reduced and the convective heat flux decreases such that the wall losses balance the Joule heating. The plasma-wall interaction plays an important role due to the increase in the electron thermal energy, as shown in Fig. 5.14. It is worth noting that a large wall loss in the local mode does not directly mean that the electron energy is smaller since all quantities are determined nonlinearly and dynamically. As shown in Eq. (5.6), the transport of electron total

energy is considered rather than that of the thermal energy in a Hall thruster where the kinetic energy cannot be neglected. Although not shown in this study, it is also observed that a much reduced electron axial drift results in another ionization oscillation due to the lack of electron current that provides a stable plasma. It is therefore suggested that the stabilization of discharge oscillation is associated with the balance between energy gain and loss and that there is an axial electron drift required for a stable operation mode.

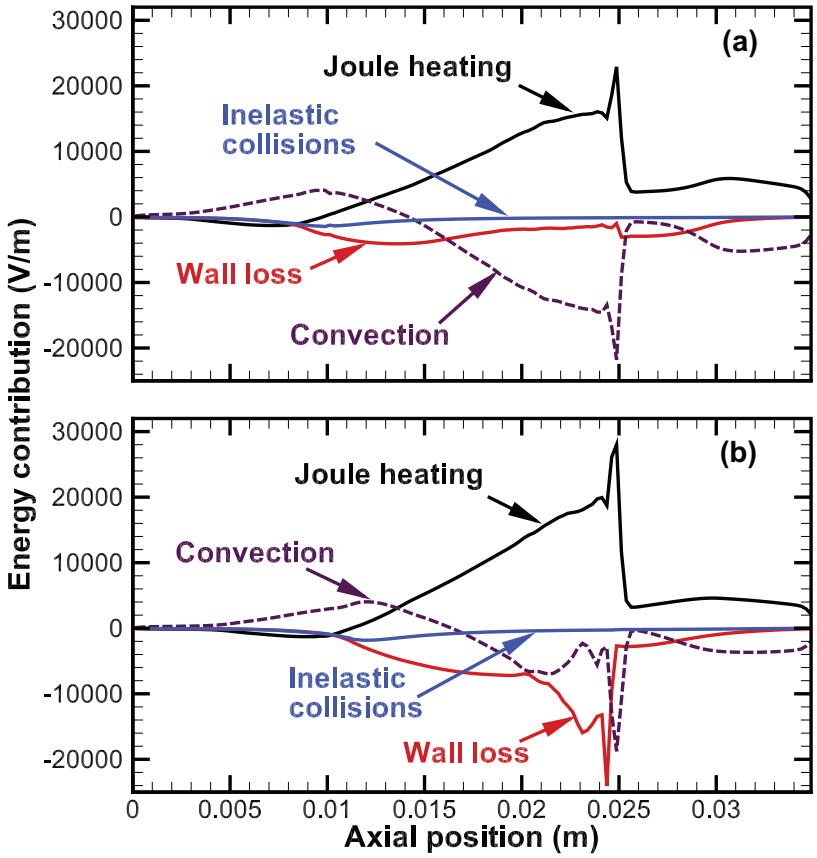


Figure 5.13: Time-averaged electron energy transfer. Each term in Eq. (5.6) is divided by the electron axial current. (a) B=120 G; (b) B=180 G.

In addition, although the value may be small in Fig. 5.13, the contribution of inelastic collisions is also important particularly near the anode. The inelastic collision contribution is about 2% of the wall loss near the channel exit but is on the same order near the anode. The locations at which the energy loss from inelastic collisions is largest are $x = 9$ mm and $x = 11.5$ mm in the global and local modes, respectively. Thus, it is indicated that the diffusion region, in which electron-impact excitation dominates over ionization near the

anode, contributes to confinement of ionization and stabilization of the plasma oscillations. This observation is consistent with the ionization cost shown in Fig. 5.11.

### 5.6.3 Electron Energy Balance

Although the global oscillation mode is a low-frequency oscillation that results in the transport of slow neutral atoms interacting with ions and electrons, the ionization oscillation is strongly associated with the electron transport and hence the electron energy.

Figure 5.14 shows the time-averaged kinetic and thermal energy distributions in the global and local modes. The electron kinetic energy is largest near the channel exit inside the channel where the $E \times B$ drift is strongest. As the electric field weakens inside the channel, the electron kinetic energy due to the azimuthal drift decreases. The sharp transition of the kinetic energy near the channel exit is due to the artificial two-region anomalous mobility

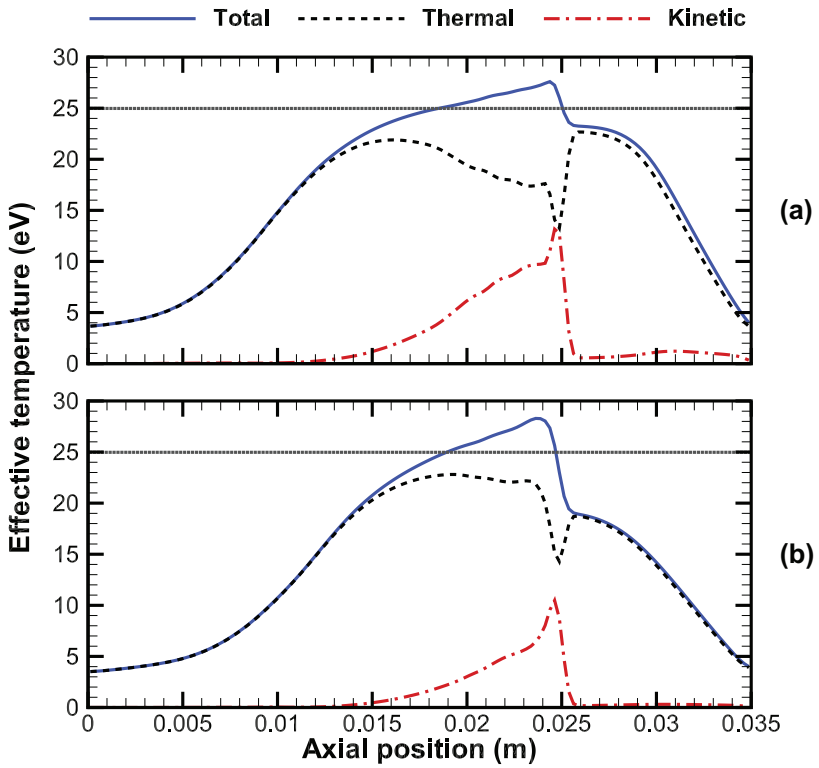


Figure 5.14: Time-averaged kinetic energy and thermal energy components in two modes. (a) B=120 G; (b) B=180 G. Vertical axis is shown in terms of effective electron temperature: $T_{e,eff} = \frac{2}{3}\varepsilon$. Horizontal dotted line is the critical electron temperature that forms a SCL sheath.

model allowing a smaller electric field in the plume outside the channel. The time-averaged electron temperature is below 25 eV, which is the critical electron temperature, since the SCL sheath is not formed stationary as discussed in Sec. 5.4.3.

In the acceleration region, assuming that the effect of thermal pressure can be neglected relative to the electric field and the Hall parameter is large, Eq. (5.2) reduces to

$$|u_{ex}| \sim \mu_e E \sim \frac{m}{eB^2}\nu_{eff}E. \tag{5.10}$$

As the magnetic field decreases, in the global oscillation mode, the electron axial and azimuthal drift velocities increase. Since $T_e$ decreases due to the increase in kinetic energy, a normal sheath is formed on the channel walls. A normal sheath below the SCL region has a large potential drop that reduces the energy loss to the channel walls in the radial direction. In this situation, the sheath potential is $\phi_w \simeq 2 - 5T_e$.

On the other hand, the local mode is achieved when the contribution from $T_e$ increases near the channel exit and the SCL sheath is likely to be formed: $\phi_w \simeq T_e$. When the SEE effect is large, the momentum transfer collision frequency increases as described in Eq. (5.4) and the energy loss due to the wall increases as discussed in Fig. 5.13. As $T_e$ increases and the SCL sheath forms, the time-averaged thermal energy approaches but is below its threshold energy due to the unsteady behavior as explained in Sec. 5.4.3. In addition, as can be seen from Eq. (5.10), the larger SEE effect enhances $\nu_{eff}$ which cancels out the increased magnetic field strength ($B$) so that $u_{ex}$ stays unchanged in the local mode. Thus, the local mode is achieved due to the optimized electron flow over a wide range of magnetic fields. It is also suggested that the plasma-wall interaction plays an important role in formation of the azimuthally rotating spokes. However, this is out of the scope of the present investigation and will be investigated in future work.

## 5.7 Sensitivity Analysis

Several sensitivity analyses are performed in order to gain deeper understanding of the effects of the collision frequencies, *i.e.* the spontaneous emission rate of the excited-state atoms as well as the anomalous electron mobility terms, on the transition of discharge

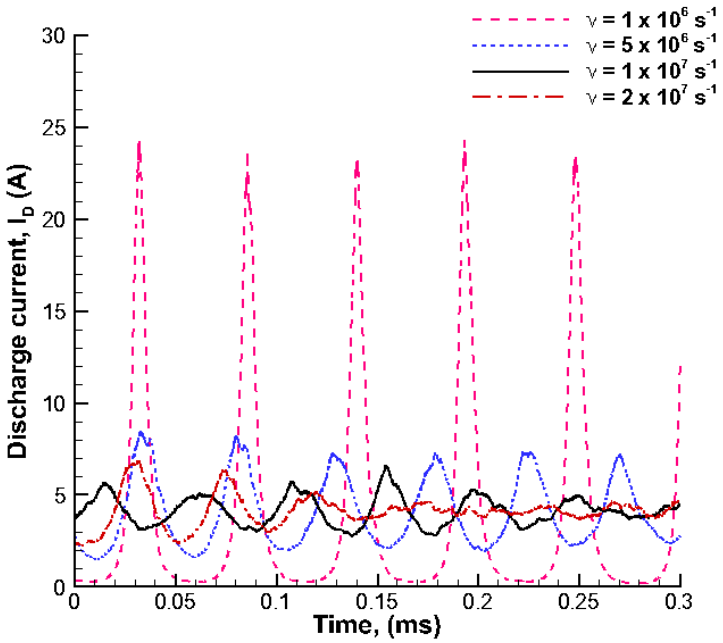


Figure 5.15: Discharge current oscillation with various spontaneous emission frequencies.

oscillation modes.

### 5.7.1 Emission Rate

The spontaneous emission frequency from the excited-state to the ground-state atoms is chosen to be $\nu = 1 \times 10^7$ s$^{-1}$ from Ref. 99 for the mode transition study. In this section, the sensitivity of the emission rate is analyzed to study the effect of excited-state atoms on the discharge oscillations.

As shown in Fig. 5.15, large discharge oscillations are observed for a small rate of spontaneous emission, which is a deexcitation process of excited-state atoms to ground-state atoms that involves emission of photons. When the emission rate is small, the excited-state atoms can live long inside the channel. Since the energy required for stepwise ionization from $Xe^*$ to $Xe^+$ is smaller than that for direct ionization from $Xe$, the ions can be more easily generated, which will result in consumption of neutral atoms. Thus, it is likely that a breathing mode oscillation occurs.

On the other hand, a higher spontaneous emission rate can stabilize the plasma oscilla-

tions. This is mainly due to the electron energy being consumed more via the excitation-deexcitation process. When the spontaneous emission rate is large enough, the excited-state atoms generated via electron-impact excitation will immediately turn back into the ground state. Thus, the deexcitation process essentially serves as an energy sink for the electrons, which is discussed in Sec. 5.5.2. In the local mode, where the discharge oscillations are stabilized, the ionization cost increases, meaning that the electron energy is lowered near the anode region, in comparison to the global mode.

This illustrates the importance of multispecies plasma reactions in HETs. Simply modeling ground-state atoms and ions may not simulate the discharge plasma accurately. There are multiple electronically excited states for xenon neutral atoms as well as those for the ions. Including other excited states and the detailed reactions is reserved for future work.

### 5.7.2 Anomalous Electron Mobility

It was found that the mode transition of discharge oscillations can occur for a wide range of anomalous electron mobilities. The three cases shown here are (1) $\nu_{ea,in} = \omega_B/64$ and $\nu_{ea,out} = \omega_B/16$, (2) $\nu_{ea,in} = \omega_B/160$ and $\nu_{ea,out} = \omega_B/16$, and (3) $\nu_{ea,in} = \omega_B/160$ and $\nu_{ea,out} = \omega_B/64$. The second case, in Fig. 5.17, is the baseline anomalous mobility model used for the mode transition study.

Figure 5.16 shows the first case. The inner anomalous electron mobility is larger than the baseline case, making it less sensitive to the fluctuations of other frequencies, such as wall collisions and inelastic collisions. Therefore, the discharge oscillations are stabilized across a wide range of magnetic field strengths.

Figure 5.17 shows the baseline case. Although not shown in Fig. 5.4(c), the baseline case yields another discharge oscillation mode at higher magnetic fields, $B > 200$ G. This has not been observed in the H6 and SPT-100 thrusters with a boron nitride material for walls. However, the second ionization oscillation mode has been reported in older thrusters[3] and for other materials.[4] The present numerical simulations suggest that this mode is associated with the plasma diffusion and acceleration toward the anode. For instance, ions and electrons become more confined as the magnetic field strength increases even near the channel. The ion velocity toward the anode can be about 2000 to 4000 m/s from the present

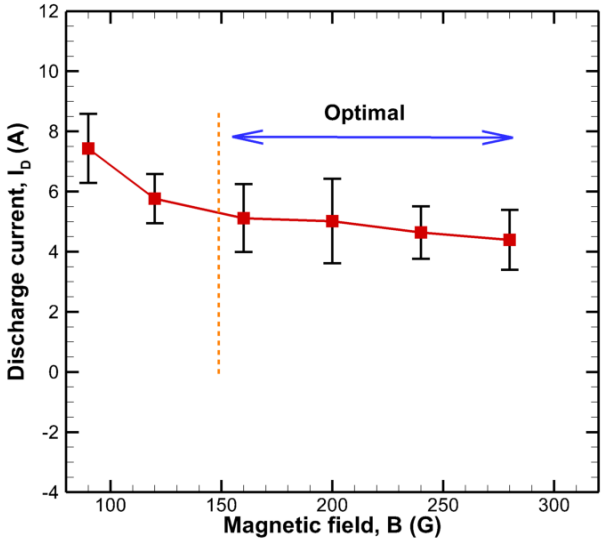


Figure 5.16: Mode transition: $\nu_{ea,in} = \omega_B/64$ and $\nu_{ea,out} = \omega_B/16$

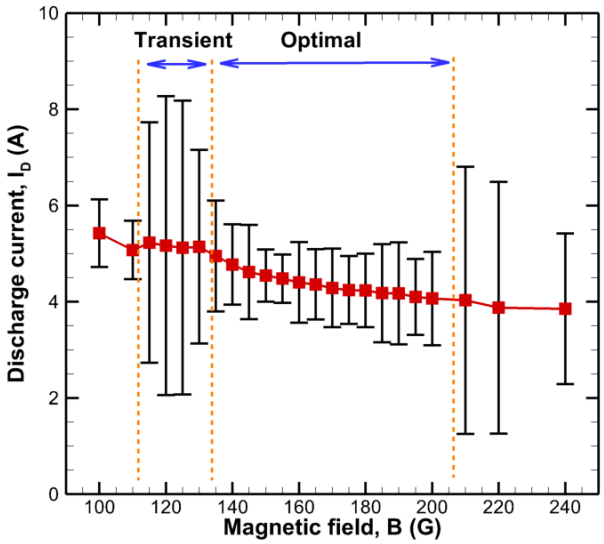


Figure 5.17: Mode transition: $\nu_{ea,in} = \omega_B/160$ and $\nu_{ea,out} = \omega_B/16$

simulations. Such phenomena might contribute to the ionization and discharge oscillations.

Another possibility of the second ionization oscillation mode may be explained from the balance of source and sink terms for the electron energy. Figure 5.18 shows the energy gain and loss terms for the baseline case. Due to the large $E \times B$ drift in the azimuthal drift, the axial electron velocity is also likely to increase at smaller magnetic field strengths as

$v_{ex} = v_{e\theta}/\Omega \sim E\nu_m/B^2$. Thus, the Joule heating increases as the magnetic field strength decreases. On the other hand, the wall loss is small since the electron thermal energy is small as shown in Fig. 5.14. The imbalance between the source term, *i.e.* Joule heating, and the sink term, *i.e.* wall heat loss, is likely to be responsible for additional energy transfer via convective heat flux, as discussed in Fig. 5.13.

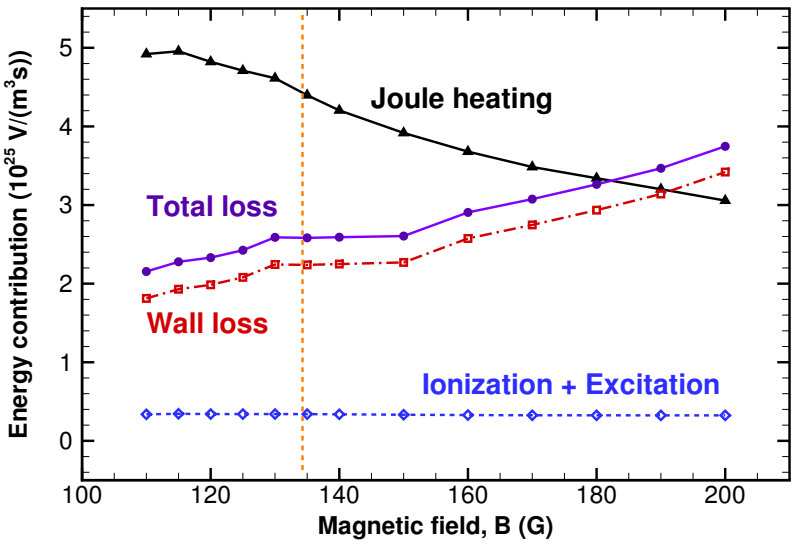


Figure 5.18: Global energy balance for $\nu_{ea,in} = \omega_B/160$ and $\nu_{ea,out} = \omega_B/16$

As the magnetic field increases, the electron thermal energy increases as the electron kinetic energy decreases since the $E \times B$ drift weakens. If the source term is much smaller than the sink term, then there needs to be an additional process to heat the plasma. Convective heat flux may be responsible for such a heating process. In addition, the gyro-frequency $\omega_B = eB/m_e$ increases and the Larmor radius $r_L = mv_\perp/eB$ decreases. Therefore, the electron transport via magnetization becomes a small-scale phenomenon, which may lead to turbulence. If turbulence occurs, it is expected that there is an additional source term in the momentum equation, *e.g.* Reynolds stress due to the high frequency oscillations. In order to resolve the small-scale phenomena, a direct numerical simulation (DNS) type simulation is required.

Finally, Fig. 5.19 shows the third case where the outer anomalous electron mobility is smaller than the baseline case. The qualitative trend of the mode transition is obtained, *i.e.*

discharge oscillation mode at low $B$, stable mode at intermediate $B$, and another oscillation mode at high $B$. However, the stable discharge oscillation mode occurs at lower magnetic field strength in comparison to Fig. 5.17.

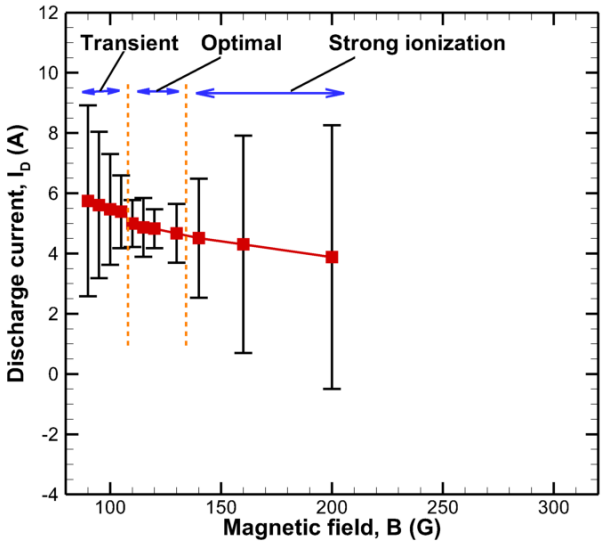


Figure 5.19: Mode transition: $\nu_{ea,in} = \omega_B/160$ and $\nu_{ea,out} = \omega_B/64$

It is also likely that the anomalous electron mobility contribution varies as the structure of the plasma discharge may change as the magnetic field strength increases. In order to understand the effect of plasma properties on the anomalous mobility, a deterministic electron mobility model or a high-fidelity simulation that can resolve small-scale phenomena is required.

## 5.8 Summary

The transition of oscillation modes in a Hall thruster is investigated using a hybrid-DK simulation. The numerical results are validated against published experimental results of the SPT-100 in Ref. 4 and experimental data of the H6. Comparisons in the mean discharge current, the RMS of the discharge current oscillation, and the breathing mode frequency are shown. It is suggested that the mechanisms of stabilization of the global mode include the reduction of electron drift as well as suppression of ionization near the anode.

First, in the local mode, the ionization cost increases and the electron total energy de-

creases near the anode so that ionization is stabilized. When the electron total energy is smaller than 10 eV, electron-impact excitation is dominant over ionization. Since spontaneous emission of the excited-state atoms is a fast process, the excited atoms deexcite back to the ground-state more frequently and hence results in damping of the global oscillation mode. Therefore, it is suggested that electronically excited state atoms play an important role in the ionization oscillation.

Second, the electron energy balance also varies during the mode transition. In the global mode, convection of the electron energy due to a large electron axial velocity balances the Joule heating. On the other hand, the electron axial drift is reduced while the wall loss increases due to the increase in the electron thermal energy in the local mode.

Finally, it is indicated that the SCL sheath is not the direct cause of the mode transition but the stable discharge oscillation mode is supported by the formation of a SCL sheath over a wide range of magnetic field strengths. The momentum transfer collision frequency increases due to wall collisions and balances the increase in the gyro-frequency so that the electron axial velocity is stabilized as the magnetic field is increased. If the momentum transfer is not enhanced, the electron axial velocity can be much smaller, the heating of electron energy is not enough to sustain a stable plasma, and another ionization oscillation may occur.

The sensitivity analysis on the deexcitation rate of excited-state atoms suggests that inclusion of excited states of atoms and even ions is required for the discharge plasma modeling. In addition, an empirical coefficient for the anomalous electron mobility is used in this dissertation. A deterministic high-fidelity model that can calculate the anomalous mobility is required to fully understand the electron transport mechanism.

# CHAPTER VI

# Perturbation Theory of Ionization Oscillations in Hall Thrusters

## 6.1 Introduction

In Chapter V, mode transition of discharge oscillations in HETs was discussed using a hybrid-DK simulation with comparison to experimental data.[2, 7] In this section, a theoretical framework is constructed to investigate the damping and excitation of such discharge and plasma oscillations.

Although several theoretical frameworks have been developed,[10, 90, 107] no complete theoretical justification and explanation of the discharge and plasma oscillations have been made. Yamamoto *et al.*[107] have extended the predator-prey model proposed by Fife[10] and allowed perturbation in the electron current. Barral *et al.*[90, 108] have developed a theoretical framework in which the growth rate of the discharge current is inherently assumed so that the criteria for growth and damping effects cannot be discussed. Peradzyński *et al.*[109] have developed a simplified theory and shown implications that instability may be excited when including perturbation in the electron temperature.

## 6.2 Predator-prey model

The mechanism of ionization oscillations in HETs has been explained by insufficient neutral flow.[10, 11, 110] Theory has been formulated using the transport of heavy species, *i.e.* neutral atoms and ions. In the HET community, the predator-prey model,[10] of which

the simplest form is also known as the Lotka-Volterra model, has been widely used and it has often been attempted to obtain a more correct scaling of the ionization length.[111, 112] In this section, we review the predator-prey model.

### 6.2.1 Formulation

The predator-prey model assumes that the plasma is contained in an ionization box whose length is $L$ and the spatial variation is neglected, *i.e.* $\partial/\partial x \sim 1/L$. The ionization rate coefficient $\xi_{ion}$ and the velocities of ions and neutral atoms are constant in time. There is no ion flux entering the box and no neutral flux escaping the box. Using these assumptions, the continuity equations are written as

$$\frac{\partial N_i}{\partial t} + \frac{N_i U_i}{L} = \quad N_i N_n \xi_{ion} \tag{6.1}$$

$$\frac{\partial N_n}{\partial t} - \frac{N_n U_n}{L} = \quad -N_i N_n \xi_{ion}, \tag{6.2}$$

where $N$ and $U$ are the number density and mean velocity, and subscripts $i$ and $n$ denote ions and neutral atoms, respectively. To study the linear perturbation, a quantity follows the form: $Q = Q_0 + Q' \exp(-i\omega t)$, where $Q_0$ and $Q'$ are equilibrium and perturbation quantities, respectively. The equilibrium quantities can be derived as

$$\frac{U_i}{L} = \quad N_{n,0} \xi_{ion} \tag{6.3}$$

$$\frac{U_n}{L} = \quad -N_{i,0} \xi_{ion}, \tag{6.4}$$

where subscript 0 denotes the equilibrium quantities. Using this first-order perturbation, an equation that exhibits a harmonic oscillation can be derived as

$$\frac{\partial^2 N_i'}{\partial t^2} = -N_{n,0} N_{i,0} \xi_{ion}^2 N_i', \tag{6.5}$$

and the harmonic oscillator frequency is given by

$$\omega = (N_{n,0} N_{i,0} \xi_{ion}^2)^{1/2}. \tag{6.6}$$

Using the zeroth-order equilibrium condition, one obtains $\omega = (U_i U_n)^{1/2}/L$, where $U_i = (eV_D/M_i)^{1/2}$ is a function of the discharge voltage $V_D$. Although ionization oscillations depend on other parameters such as the mass flow rate, magnetic field topology, and channel wall material, it is assumed that these are incorporated into the ionization length $L$.

### 6.2.2 Time-varying Analysis

Figures 6.1 and 6.2 show the Lotka-Volterra model for two different initial conditions. For the equilibrium quantities, $N_{n0} = 1 \times 10^{19}$ m$^{-3}$ and $N_{i0} = 1 \times 10^{17}$ m$^{-3}$ are considered. From Eqs. (6.3) and (6.4), $U_i/L$ and $U_n/L$ can be calculated for a given ionization rate coefficient, which is assumed to be $\xi_{ion} = 2 \times 10^{-13}$ m$^{-6}$s$^{-1}$. The predator-prey model gives oscillations as long as the initial conditions differ from the equilibrium values. Thus, a perturbation in the ion density is prescribed in the figures. In Fig. 6.1, the initial ion density is $1.5N_{i0}$ while the initial neutral atom density is $N_{n0}$. It can be seen that neutral atoms are initially consumed due to the excess in ion (electron) density. As the neutral atom density decreases, the ionization process weakens. The ion density (*predator*) increases again as the neutral atoms (*prey*) repopulate. The initial density perturbation is not too large so that the evolution of the predator and prey follows a sinusoidal. It can be seen from Fig. 6.1 that $N_i \sim \cos(t)$ while $N_n \sim -\sin(t)$. Thus, there is a 90 degree phase shift. The frequency from Eq. (6.6) is 31.8 kHz, or $\omega = 2 \times 10^6$ rad/s. The frequency obtained from the numerical integration also yields 31.8 kHz, as there are almost 7 periods during 0.22 ms.

In Fig. 6.2, the initial ion density is $5N_{i0}$, so the initial deviation from the equilibrium density is large. Neutral atoms are consumed quickly and the ion density decreases. Once the neutral atoms repopulate, the ionization process starts again and thus the phenomenon occurs periodic in time. However, the major difference from the small initial perturbation case in Fig. 6.1 is that the time evolution of ion and neutral atom densities is non-sinusoidal. The non-sinusoidal discharge oscillation is identified as a *nonlinear* mode in comparison to the small perturbation case that yields sinusoidal discharge oscillations is *linear* mode in Ref. 90. The frequency obtained from the numerical integration is 27.3 kHz, as there are only 6 periods during 0.22 ms. This disagrees with Eq. (6.6), which is obtained by assuming a linear perturbation $\exp(-i\omega t)$. It can be considered that in a strongly perturbed case, the

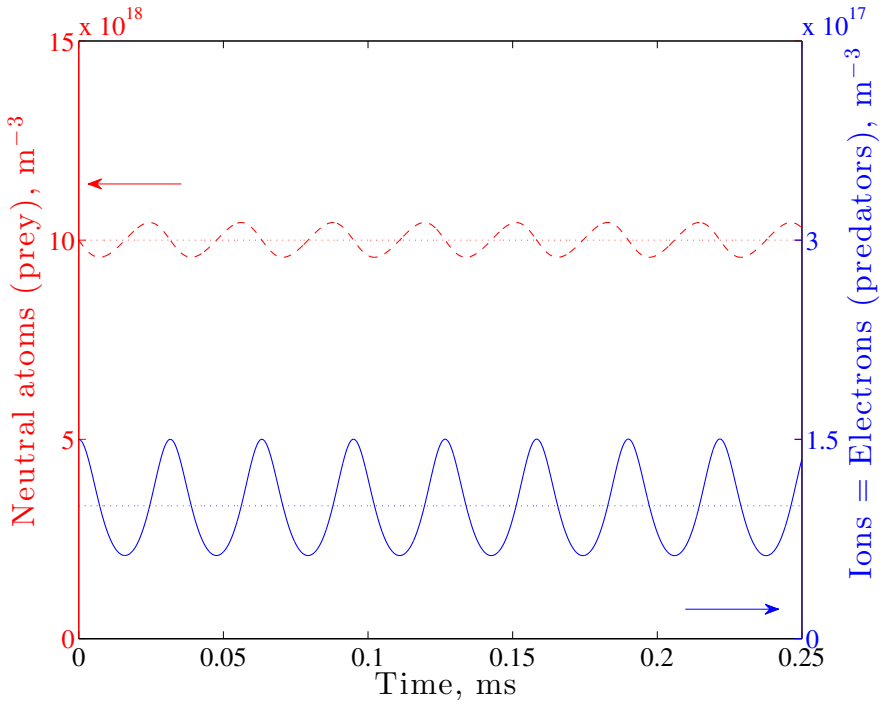


Figure 6.1: Lotka-Volterra model: Initial ion density is $1.5N_{i0}$.

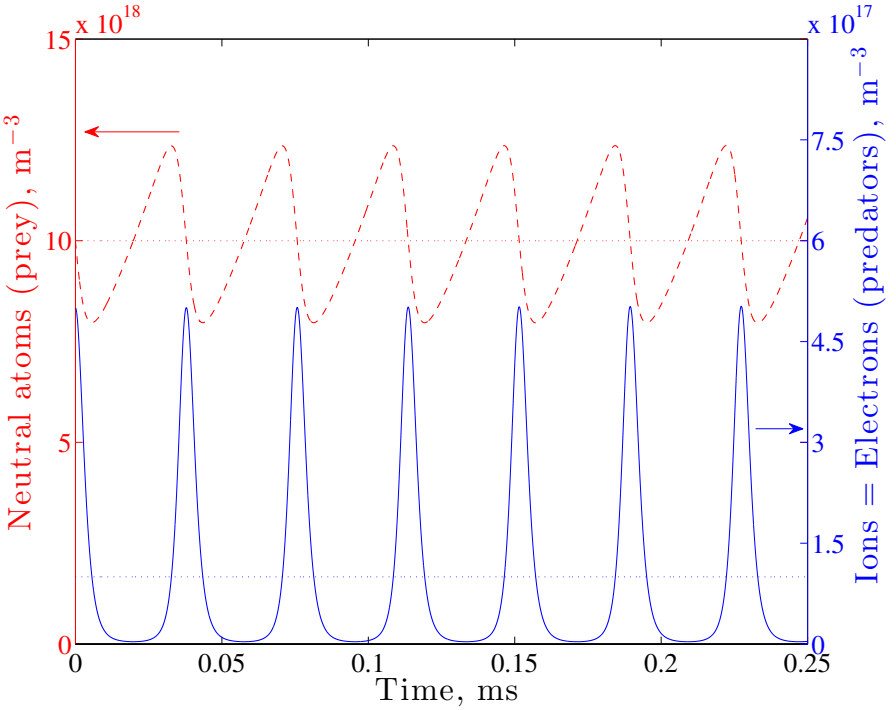


Figure 6.2: Lotka-Volterra model: Initial ion density is $5N_{i0}$.

evolution is no longer linear, thus higher order perturbation quantities must be included.

Although the predator-prey model may capture some of the discharge and plasma oscillations in HETs, the source of the oscillation is due to the initial condition that differs from the equilibrium values. From the predator-prey model, the excitation and stabilization of the discharge oscillations cannot be discussed.

In order to model the discharge oscillation of HETs more accurately, there are two assumptions that need to be reconsidered. First, as pointed out by Barral and Ahedo,[110] the neutral inflow rate in the actual HET operation is fixed at the anode and the outflow varies, so Eq. (6.2) is inaccurate. The meaning of Eq. (6.2) is simply to satisfy the predator-prey model. Second, $L$ is not well-defined and is often assumed to be on the order of the channel length. Therefore, a more complete model must be considered to study the mechanism of the ionization oscillation.

## 6.3 Complete Perturbation Theory

A 0D (zero-dimensional) model is useful to investigate the time evolution of a spatially-averaged quantity, which may not capture all of the detailed physics but provides a low order estimate. In the low temperature plasma community, a global model is often used to calculate the number densities of all chemical species.[113] Such models account for chemical reactions and some of the important physical phenomena, including diffusion, gas flow, and power input. In this section, a framework similar to global models is constructed to perform a perturbation analysis to investigate the excitation and stabilization of ionization oscillations in HETs.

### 6.3.1 Heavy Species Transport: Ion and Neutral Atom Continuity Equations

In order to construct the correct theory of ionization oscillations, we first define the geometry. Figure 6.3 shows a simplified HET schematic used in the present model. The discharge plasma is assumed to be confined inside the discharge channel. Although the one-dimensional flow in the axial direction is of interest, the radial plasma diffusion also plays an important role. One can take an approach similar to a finite-volume method in which

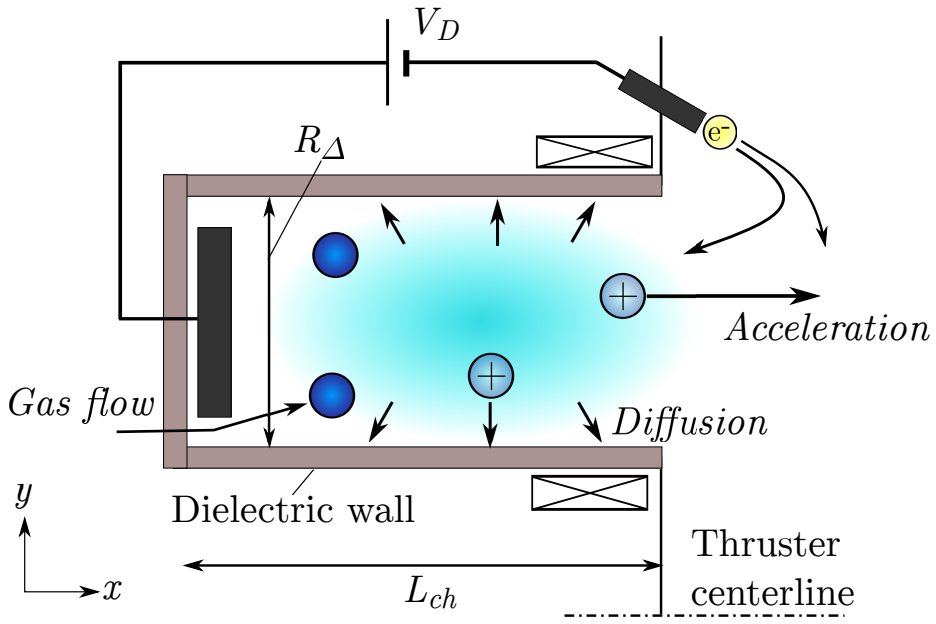


Figure 6.3: Schematic of the Hall thruster discharge region.

the state variables are volume averaged and the fluxes at interfaces are modeled. Without employing the undefined ionization length, ion and neutral continuity equations are more correctly given by

$$\frac{\partial N_i}{\partial t} + \frac{N_i U_i}{L_{ch}} + \frac{2 N_i U_{i,w}}{R_\Delta} = N_i N_n \xi_{ion} \tag{6.7}$$

$$\frac{\partial N_n}{\partial t} + \frac{(N_n - N_{int}) U_n}{L_{ch}} = -N_i N_n \xi_{ion}, \tag{6.8}$$

where $N_{int}$ is the number density of neutral atoms at the anode, $U_{i,w} = (eT_e/m_i)^{1/2}$ is the ion acoustic speed, $L_{ch}$ is the channel length, and $R_\Delta$ is the channel width. Ion diffusion toward the channel walls is taken into account assuming that Bohm's condition is satisfied at the sheath edge near the channel walls. Any spatial variations are neglected inside the box due to the zero-dimensional assumption. Since there is no radial diffusion for the neutral atoms, their transport can be described only by accounting for the axial transport.

The first thing that can be noted is that the ionization length $L$ in the predator-prey model can be described by relating the ion continuity equation in Eq. (6.7), where geometric

parameters are used, and Eq. (6.1) that assumes a hypothetical 1D ionization box:

$$L = L_{ch}\left(1 + \frac{2U_{i,w}}{U_i}\frac{L_{ch}}{R_\Delta}\right)^{-1}. \tag{6.9}$$

Ionization length in the predator-prey model is now defined using the geometric parameters and plasma properties for the first time. Eq. (6.9) shows that $L$ decreases when $T_e$ increases since the plasma diffusion becomes stronger, *i.e.*, $U_{i,w}$ increases for given $U_i$, $L_{ch}$, and $R_\Delta$. Thus, $L$ is a function of $T_e$ and the geometry of the channel.

From Eqs. (6.7) - (6.9), the equilibrium densities of ions and neutral atoms are given by

$$N_{n,0} = \frac{U_i}{L\xi_{ion}} \tag{6.10}$$

$$N_{i,0} = (N_{int} - N_{n,0})\frac{U_n}{U_i}\frac{L}{L_{ch}}. \tag{6.11}$$

Equation (6.10) is identical to Eq. (6.3). Both $N_{n,0}$ and $N_{i,0}$ are a function of $T_e$ because $\xi_{ion} = \xi_{ion}(T_e)$. Eq. (6.11) provides the first condition to have a steady-state plasma generated in the channel, *i.e.* $N_{i,0} > 0$ or $N_{int} > N_{n,0}$ must be satisfied. From Eq. (6.10),

$$\underbrace{N_{int}\xi_{ion}}_{\text{Maximum ion production}} > \underbrace{\frac{U_i}{L}}_{\text{Ion acceleration}}, \tag{6.12}$$

where the left hand side is the ionization frequency when ionizing all the inflow neutral gas and the right hand side is the characteristic frequency due to ion acceleration. For instance, the ionization rate needs to be sufficiently large to sustain a steady-state plasma when the ion outflow is fast. Given all the other parameters, the minimum $T_e$ ($= T_{e,min}$) can be calculated when the two terms in Eq. (6.12) are equal. It can be seen from Eq. (6.12) that an increased $U_i$ (via discharge voltage) or decreased $N_{int}$ (via anode mass flow) increases $T_{e,min}$. Thus, the condition of having a steady-state plasma becomes more severe.

Figures 6.4 and 6.5 show the results of $T_{e,min}$ and $L$ for a wide range of operation parameters. The expression for the ionization rate coefficient $\xi_{ion}$ of ground-state xenon

atoms proposed by Goebel and Katz[112] is used

$$\xi_{ion} \approx [AT_e^2 + B\exp(-C/T_e)] \left(\frac{8eT_e}{\pi m}\right)^{1/2}, \tag{6.13}$$

where $A = -1.0 \times 10^{-24}$, $B = 6.386 \times 10^{-20}$, and $C = 12.13$. The configuration of an SPT-100ML thruster[4] is assumed: $L_{ch} = 2.5$ cm, $R_\Delta = 2$ cm. For instance, the minimum electron temperature required to have a steady-state plasma is $T_{e,min} = 12.4$ eV for $V_D = 300$ V and $N_{int} = 1.6 \times 10^{19}$ m$^{-3}$.

### Minimum Electron Temperature

As shown in Fig. 6.4, a higher electron temperature is required to sustain the discharge plasma for higher discharge voltage and/or lower mass flow rate. This is because the ionization rate coefficient must be larger for a decreasing $N_{int}$ and increasing $U_i$, as can be seen from Eq. (6.12).

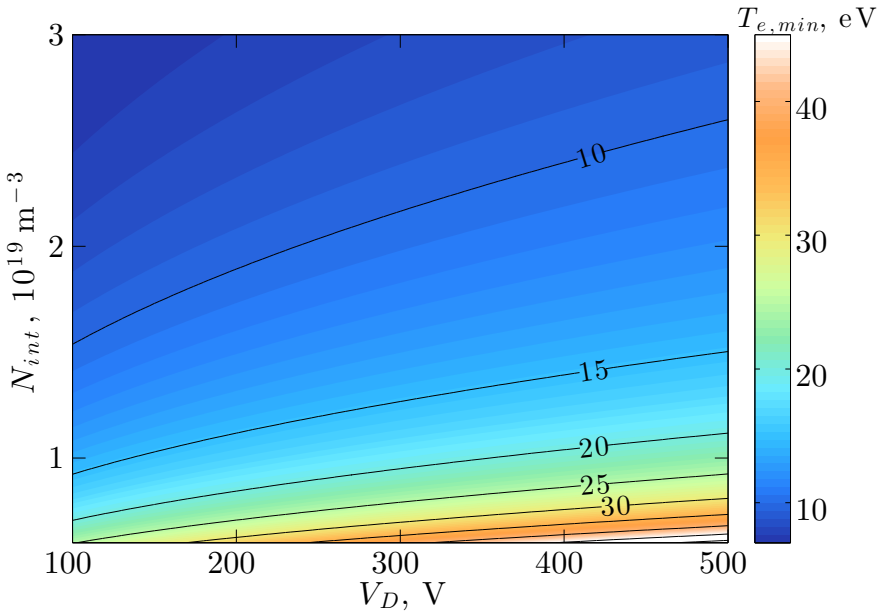


Figure 6.4: Minimum $T_e$ required to sustain a plasma. $N_{i,0} > 0$ from Eq. (6.11). The geometric parameters of a SPT-100 thruster are considered: $L_{ch} = 2.5$ cm, $R_\Delta = 2$ cm.

One notable trend is that $T_{e,min}$ is more sensitive to the inflow neutral atom density, *i.e.* the anode mass flow, than the discharge voltage. High power HETs are being designed in-

cluding the High Voltage Hall Accelerator (HiVHAC) at NASA Glenn Research Center[114] and the magnetically shielded HETs at NASA Jet Propulsion Laboratory.[27] Figure 6.4 suggests that the anode mass flow rate needs to be increased as a higher discharge voltage is used. However, this discussion only indicates the electron temperature required to have a steady-state discharge plasma. It will be shown from the complete perturbation theory that ionization oscillations can be excited even when the discharge plasma can operate in a steady state.

**Ionization Length**

Figure 6.5 shows the ionization length as a function of discharge voltage and electron temperature under the same geometric configuration as Fig. 6.4. The ionization length decreases as $T_e$ increases due to the enhanced plasma diffusion via $U_{i,w}$ in Eq. (6.9). On the other hand, the axial ion velocity $U_i$ increases as the discharge voltage $V_D$ increases, so $L/L_{ch}$ increases. Note that $L/L_{ch}$ in Eq. (6.9) is not dependent on the neutral atom density.

In Fig. 6.5, $T_{e,min}$ to sustain a steady-state plasma is obtained assuming $N_{int} = 1.6\times10^{19}$ $\mathrm{m}^{-3}$. If the inflow neutral atom density, *i.e.* the anode mass flow rate, decreases, $T_{e,min}$ will be larger, as shown in Fig. 6.4. In this situation, it can be seen that the operation condition to have a steady-state discharge plasma will be more severe. Furthermore, if $T_{e,min}$ is very large, there may not be any operation condition that produces a steady-state discharge plasma depending on the maximum threshold of the electron energy due to any physical effects, *e.g.* plasma-wall interactions. It is likely that the discharge plasma enters a pulsed mode rather than a continuous plasma flow. The breathing mode is due to discharge and ionization oscillations when a steady-state discharge plasma is produced. Mathematically, this corresponds to an unstable solution from the linear perturbations around a steady-state equilibrium solution.

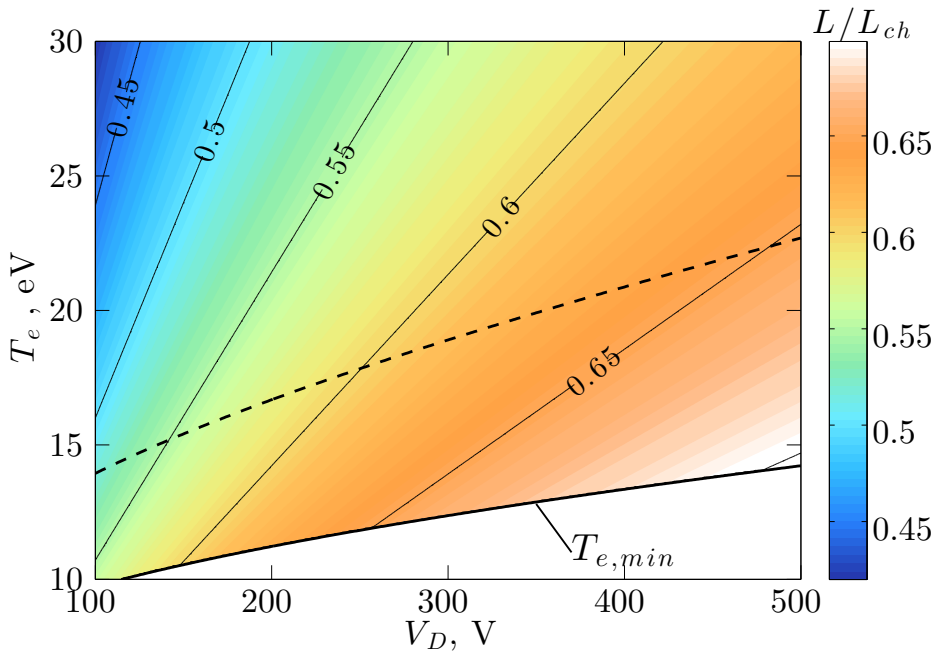


Figure 6.5: Ratio of ionization length and channel length for various $V_D$ and $T_e$ obtained from Eq. (6.9). Same geometric parameters as Fig. 6.4 is used. $N_{int} = 1.6\times10^{19}$ $\mathrm{m}^{-3}$ is considered for $T_{e,min}$ in solid line. Dashed line illustrates $T_{e,min}$ for $N_{int} = 1 \times 10^{19}$ $\mathrm{m}^{-3}$.

**Linear Perturbation**

The first-order perturbation equations of Eq. (6.7) and (6.8) can be described as a system of equations

$$\begin{bmatrix} -i\omega & -N_{i,0}\xi_{ion} \\ \frac{U_i}{L} & -i\omega + \frac{N_{int}}{N_{int}-N_{n,0}}N_{i,0}\xi_{ion} \end{bmatrix} \cdot \vec{Q} = \mathbf{O} \tag{6.14}$$

for $\vec{Q} = [N_i', N_n']^T$. The wave frequency can be calculated by solving the determinant of the matrix:

$$-\omega^2 - i\omega\frac{N_{int}}{N_{int}-N_{n,0}}N_{i,0}\xi_{ion} + N_{n,0}N_{i,0}\xi_{ion}^2 = 0. \tag{6.15}$$

The frequency can be written as the real frequency and the growth rate as $\omega = \omega_r + i\gamma$, where $\omega_r$ and $\gamma$ are always real numbers, assuming the perturbation to follow $\exp(-i\omega t)$.

The solution to Eq. (6.14) is given by

$$\omega_r = \pm \left(N_{i,0} N_{n,0} \xi_{ion}^2 - \gamma^2\right)^{\frac{1}{2}} \tag{6.16}$$

$$\gamma = -\frac{1}{2} \frac{N_{int}}{N_{int} - N_{n,0}} N_{i,0} \xi_{ion}. \tag{6.17}$$

If $\gamma = 0$, Eq. (6.16) reduces to the predator-prey model in Eq. (6.6). Under the same condition as Fig. 6.5 the real part of the solution is $0 < \omega_r < 2 \times 10^5$ rad/s for $T_{e,min} (= 12.4$ eV$) < T_e < 30$ eV when $V_D = 300$ V. Most importantly, Eq. (6.17) shows that the growth rate of the oscillation is always negative, *i.e.* the imaginary part of the oscillation contributes as damping, since $N_{int} > N_{n,0}$ to have a steady-state plasma. Therefore, only solving the two continuity equations shows that the oscillation is always damped.

### 6.3.2 Including Ion Momentum and Electron Energy Equations

It is shown from Eqs. (6.16) and (6.17) that ionization oscillations always damp when there is no perturbation in the ionization rate coefficient $\xi_{ion}$, or equivalently the electron temperature $T_e$. In addition to the continuity equations for ions and neutral atoms, the perturbations in ion momentum and electron temperature are now taken into consideration.

First, using the relation in Eq. (6.9), the ion momentum equation in the axial direction is given by

$$\frac{\partial}{\partial t} \left(N_i U_i\right) + \frac{N_i U_i^2}{L} = \frac{e}{M_i} N_i E, \tag{6.18}$$

where $E$ is the electric field. The pressure term is neglected since the ions are assumed to be cold, *i.e.* $T_i \approx 0$. Next, the electron energy equation is taken into consideration.

$$\frac{\partial}{\partial t} \left(\frac{3}{2} N_e T_e\right) + \frac{5}{2} \frac{N_e U_e T_e}{L} = S_{joule} - S_{wall} - S_{coll}, \tag{6.19}$$

where $S_{joule} = -N_e U_e E$ is the energy gain due to Joule heating, $S_{wall} = N_e \epsilon_w(T_e) \nu_w(T_e)$ is the energy loss due to the channel walls, and $S_{coll} = \sum_j N_e N_n \xi_j(T_e) \epsilon_j$ denotes inelastic collisions, $j$, that contribute to energy loss. For simplicity, the contributions from electron pressure and heat conductivity are neglected. The convective energy flux at the exit is carried into the system since the electron velocity $U_e$ is negative in HETs and it is assumed

that the electron energy is sufficiently low at the anode so that there is no convective flux towards the anode. In the present model, it is also assumed that the electron mobility and the electric field are constant in time and the electron kinetic energy is negligible although the effect of the kinetic energy should be included in HETs where the $E \times B$ drift is strong.[2] Finally, a quasineutral assumption is used $N_i = N_e$.

In order to investigate the perturbation in the right hand side of Eq. (6.19), we introduce models for each term. The wall collision frequency[90] is given by

$$\nu_w = \frac{1}{R_\Delta}\sqrt{\frac{eT_e}{M_i}}\frac{1}{1-\sigma}, \tag{6.20}$$

where $\sigma$ is the effective secondary electron emission (SEE) rate, which is identical to Eq. (5.4). The energy loss to the wall[112] is written as

$$\epsilon_w = 2T_e + (1-\sigma)\phi_w, \tag{6.21}$$

where $\phi_w = -T_e \log[(1-\sigma)/(2\pi m_e/M_i)^{1/2}]$ is the sheath potential. Only singly charge ionization and excitation from the ground state atoms are considered. $S_{coll}$ is further assumed as $S_{coll} = \chi N_i N_n \xi_{ion}(T_e)\epsilon_{ion}$, where $\chi$ is the ionization cost that includes the effect of excitation and $\epsilon_{ion}$ is the ionization energy loss. Since the expression for the ionization rate coefficient is complicated as can be seen from Eq. (6.13), the perturbation form of that is assumed to follow $\xi_{ion}(T_e) \approx \xi_{ion,0}(T_e/T_{e,0})^\kappa$ for simplicity, where $T_{e,0}$ is the equilibrium electron temperature and $\xi_{ion,0}$ is the ionization rate coefficient for $T_{e,0}$ given in Eq. (6.13). This form has been chosen due to the monotonic increase in $\xi_{ion}(T_e)$ for the range of $T_e$ that is considered, *e.g.* $5 < T_e < 30$ eV.

For simplicity, the perturbations of $L$, $\chi$, and $\sigma$ are neglected, *i.e.* frozen. The first-order terms of the quantities above are given by

$$(\nu_w)' = \frac{1}{2}\nu_{w,0}\frac{T_e'}{T_{e,0}} \tag{6.22}$$

$$(\epsilon_w)' = \left[2 + (1-\sigma)\frac{\phi_{w,0}}{T_{e,0}}\right]T_e' \tag{6.23}$$

$$(\xi_{ion})' = \kappa\xi_{ion,0}\frac{T_e'}{T_{e,0}} \tag{6.24}$$

Using the quasineutral assumption, the perturbation equations for $\vec{Q} = [N_i', N_n', U_i', T_e']^T$ can be written as

$$\begin{bmatrix} -i\omega & -N_{i,0}\xi_{ion} & \frac{N_{i,0}}{L} & -N_{i,0}\frac{U_{i,0}}{L}\frac{\kappa}{T_{e,0}} \\ \frac{U_i}{L} & -i\omega + \frac{N_{int}}{N_{int}-N_{n,0}}N_{i,0}\xi_{ion} & 0 & N_{i,0}\frac{U_{i,0}}{L}\frac{\kappa}{T_{e,0}} \\ -i\omega U_{i,0} & 0 & N_{i,0}\left(-i\omega + \frac{2U_{i,0}}{L}\right) & 0 \\ -i\omega\frac{3}{2}T_{e,0} & N_{i,0}\xi_{ion}\chi\epsilon_{ion} & 0 & N_{i,0}\left(-i\frac{3}{2}\omega + \Lambda\right) \end{bmatrix} \cdot \vec{Q} = \mathbf{O}, \tag{6.25}$$

where $N_{i,0} > 0$ to have a steady-state plasma, and

$$\Lambda = \frac{3}{2}\frac{\epsilon_{w,0}}{T_{e,0}}\nu_{w,0} + \frac{U_{i,0}}{L}\frac{\kappa}{T_{e,0}}\chi\epsilon_{ion} + \frac{5}{2}\frac{U_e}{L} \tag{6.26}$$

is the effective electron energy relaxation frequency that has contributions from the energy loss mechanisms such as wall loss, inelastic collisions, and the convective energy flux.

In the present study, $T_{e,0}$ is taken as a parameter as well as $U_e$ instead of the operational parameters such as $B$ and $V_D$. The balance between the loss mechanisms and the Joule heating determines $T_{e,0}$ dynamically and non-locally in actual HETs.[2] Also, $\kappa = 1$ is assumed. The determinant of Eq. (6.25) can be written as

$$-\omega^4 + i\omega^3 F_1 + \omega^2 F_2 + i\omega F_3 + F_4 = 0, \tag{6.27}$$

where the coefficients $F_k$ $(k = 1, 2, 3, 4)$ are functions of the plasma parameters. Since it is difficult to derive the solutions analytically, we analyze the stability criteria using representative values of the flow in a SPT-100 thruster in the next section.

## 6.4 SPT-100 Results

In addition to the values used in Sec. 6.3.1, the SEE model proposed in Refs. 90 and 2 is used. $\sigma = \max(\sigma_{max}, T_e/25)$, where $\sigma_{max} = 0.986$ is the SCL SEE coefficient. A SCL sheath is assumed to form at $T_e = 24.6$ eV. The nominal conditions are $N_{int} = 1.6 \times 10^{19}$ $\mathrm{m}^{-3}$ and $V_D = 300$ V. In order to investigate the stability of ionization oscillations in the SPT-100 thruster, $U_e$ is varied from 0 to $-U_i$ and $T_e$ is varied from $T_{e,min} = 12.4$ eV to 25

eV.

$U_e$ is related to the current utilization efficiency $\eta_c \equiv I_i/I_D$, where $I_i$ is the ion current and $I_D$ is the total discharge current. Assuming only singly charge ions and quasineutrality,

$$\eta_c = \frac{U_i}{U_i + |U_e|} = \left(1 + \frac{|U_e|}{U_i}\right)^{-1}. \tag{6.28}$$

From the literature, $0.72 < \eta_c < 0.86$ for the NASA-173Mv2 thruster[106], $0.70 < \eta_c < 0.92$ for the 6kW laboratory Hall thruster at the University of Michigan[115] and $0.68 < \eta_c < 0.85$ for the BHT-2000 thruster[116] across a range of parameters. While these thrusters exhibit 50 - 70% total efficiency, SPT-100 thrusters exhibit total efficiency of 35 - 50%,[18, 117, 118] so it can be extrapolated that $\eta_c$ becomes worse than that for NASA-173Mv2 or BHT-2000 thrusters. In fact, it has been reported in Ref. 119 that the current utilization efficiency for a SPT-100 thruster is $\eta_c \approx 0.6$ at optimal operation and can decrease down to $\eta_c \approx 0.4$ at lower discharge voltage. In this dissertation, the range for $U_e$ considered is from $-U_i$ to 0, which corresponds to $0.5 < \eta_c < 1$ from Eq. (6.28).

### 6.4.1 Growth Rate

As shown in Fig. 6.6, there is an undamped oscillation solution, *i.e.* $\gamma > 0$, when including the perturbation in electron temperature. The results without the electron energy perturbation only have damped solutions as shown in Eq. (6.17). Although not shown in this study, only including the ion momentum equation in addition to the two continuity equations results unconditionally in damping as well. For convenience, the two stable regions are labeled as Regions I and II as shown in Figs. 6.6 and 6.7.

The damped region for smaller $T_{e,0}$, Region I in Fig. 6.6, is possibly due to the combination of the reduced energy source as well as the small ion number density. The growth rate decreases as $|U_e/U_i|$ decreases for all $T_{e,0}$. From Eq. (6.26), the wall heat flux and inelastic collision terms serve as an energy sink, while the convective heat flux is a source. A large $|U_e|$ can provide more energy into the HET discharge channel while a smaller $|U_e|$ results in a smaller energy source at constant $T_{e,0}$. In addition, the ion number density decreases as the electron temperature decreases. Therefore, it is likely that the ionization oscillations

are damped due to the large energy sink with respect to the small ion number density.

Region II in Fig. 6.6 is mainly due to the energy loss due to the wall heat flux, $S_{wall}$ in Eq. (6.19). For a large energy loss, any perturbation in the ionization oscillations may be damped. This will be further discussed in Sec. 6.5.1.

### 6.4.2 Real Frequency

The corresponding real frequency in the unstable region is shown in Fig. 6.7. It can be seen that $\omega_r$ increases as $T_{e,0}$ increases but decreases after there is a maximum peak for a constant $U_e$ particularly in large $|U_e/U_i|$, or small $\eta_c$. However, for small $|U_e/U_i|$, the increase in $\omega_r$ with increasing $T_{e,0}$ is rather monotonic.

The magnitude of the oscillation frequency agrees with the results from the previous predator-prey models and experimental observations. $\omega_r = (1-2) \times 10^5$ rad/s corresponds

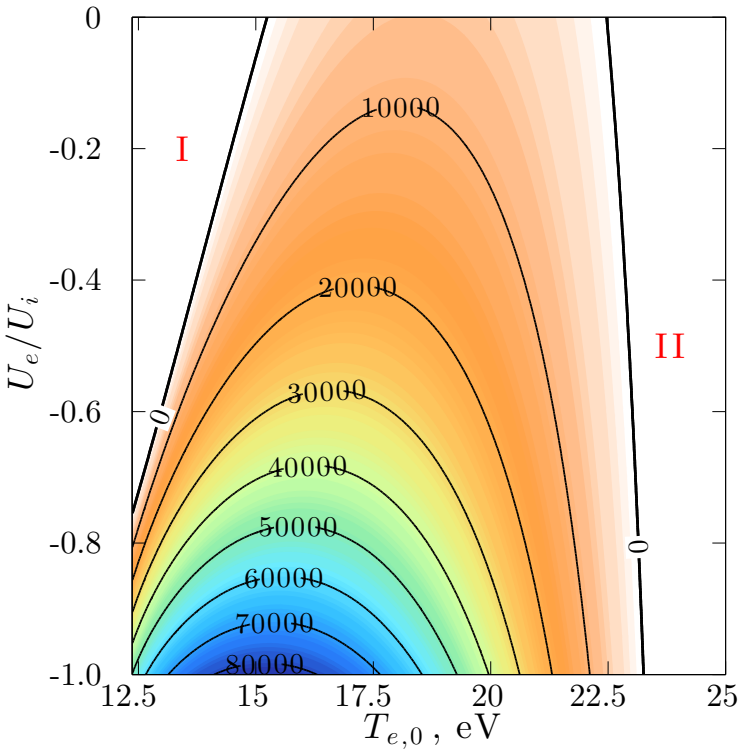


Figure 6.6: Growth rate in units of rad/s for various ($T_{e,0}$, $U_e$). The region where $\gamma < 0$ is not shown since the ionization oscillation is damped. $V_D = 300$ V and $N_{int} = 1.6 \times 10^{19}$ m$^{-3}$. The two stability regimes are labeled as I and II.

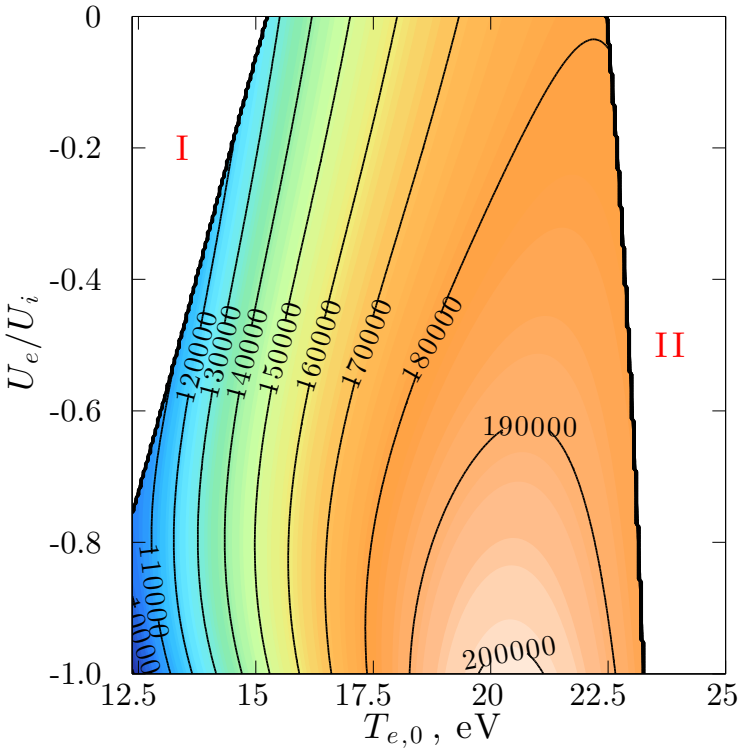


Figure 6.7: Real frequency in units of rad/s for various ($T_{e,0}$, $U_e$). Same condition as Fig. 6.6.

to $f = 16$ to 31.8 kHz. For instance, the SPT-100 simulation results in Fig. 5.6(b) show the breathing mode frequency from 21 to 25 kHz, which is within the range of the theoretical predictions. With these predictions of the growth rates, we can discuss the cause of the discharge oscillation mode transition and the direct cause of discharge oscillations in HETs.

## 6.5 Discussion

The cause of discharge oscillation is discussed in terms of the electron energy relaxation frequency. Although the electron energy relaxation frequency $\Lambda$, shown in Eq. (6.26), is one or two orders larger than the ionization oscillation frequency, ionization oscillations can be excited and/or stabilized depending on the high-frequency components. Qualitative agreement with experimental observations are also shown.

### 6.5.1 Cause of Discharge Oscillations

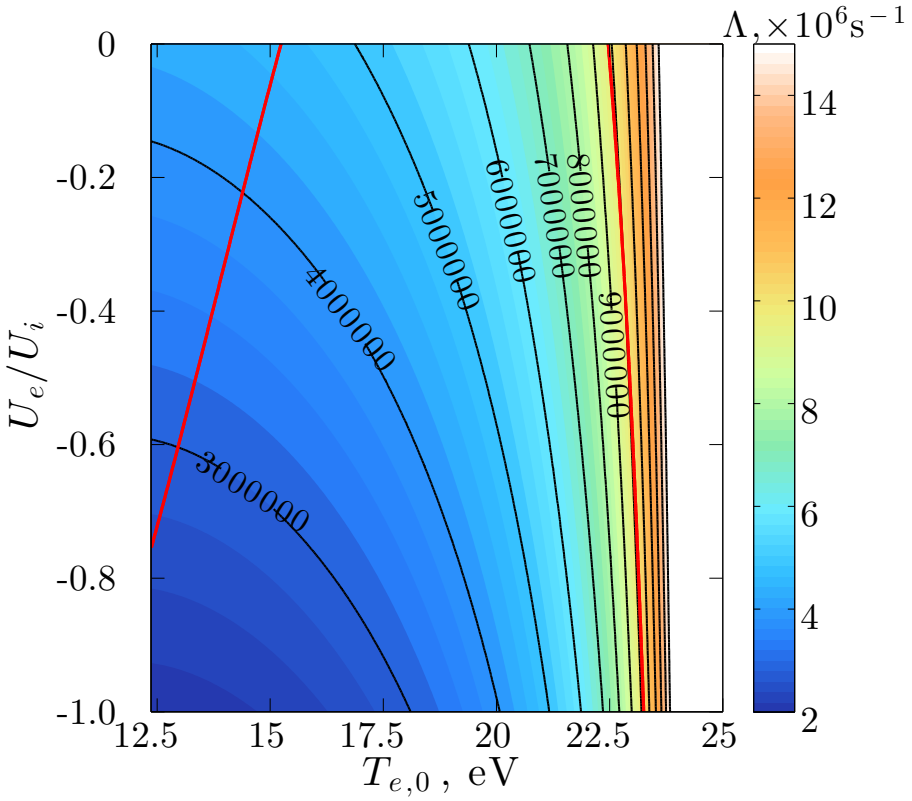


Figure 6.8: Electron energy relaxation frequency $\Lambda$ in units of $s^{-1}$ for various ($T_{e,0}$, $U_e$). White region corresponds to $\Lambda > 1.5 \times 10^7$ $s^{-1}$. Same condition as Figs. 6.6 and 6.7. Red line indicates $\gamma = 0$ as shown in Figs. 6.6 and 6.7.

The cause of the ionization oscillations in HETs has often been explained by insufficient neutral atom flow using the predator-prey model,[9, 11, 110] in which electron transport has been neglected. In the present study, it is shown that the ionization oscillations in HETs are strongly related to electron energy perturbations, in particular the electron energy relaxation frequency $\Lambda$ as shown in Fig. 6.8. This framework can be used to estimate the stability region of ionization oscillations in HETs although it is difficult to obtain a simple analytic formula due to the complexity of the equations as shown in Eq. (6.27).

The present theory supports the observation in a recent numerical simulation of the mode transition,[2] which is compared with experiments of the SPT-100[4] and H6 thrusters.[7] As shown in Figs. 6.6 and 6.7, increased wall losses via increased $T_{e,0}$ result in damping

of the ionization oscillations in Region II. From the simulation results in Ref. 2, $|U_e|$ is reduced and $T_e$ approaches the SCL regime as the discharge oscillation stabilizes when increasing the magnetic field strength $B$. Since $|U_e|$ is usually a decreasing function of $B$, the increase in $B$ results in a decrease in $|U_e|$. The mode transition observed in Ref. 2 corresponds to the mode transition from the linearly unstable region to Region II in Figs. 6.6 and 6.7. However, in order to directly compare experiments and the present theory, the internal electron temperature profile and the electron current need to be known in detail. The values of $U_e$ (or $\eta_c$) and $T_{e,0}$ need to be examined in the experiments since the mode transition of the ionization oscillation is determined by the electron transport. For instance, a small change in the cathode mass flow may also change the mode transition.[120] This phenomenon can be related to the change in $U_e$ from the plume into the channel.

### 6.5.2 Electron Energy Relaxation Frequency

As can be seen from Figs. 6.6 - 6.8, smaller $\Lambda$ corresponds to larger $\gamma$. However, Region I predicts damping of the ionization oscillations at small $T_e$ and small $|U_e|$, which is possibly due to the small convective heat flux and small plasma density. Note that the region where $T_e < T_{e,min}$ is unstable since the steady-state plasma is not satisfied. The other damped solution, Region II, appears when the heat loss due to plasma-wall interaction increases so that $\Lambda$ increases as $T_{e,0}$ increases. The relaxation of the electron energy is fast enough to damp other frequencies in the system so that there will be no low-frequency ionization oscillations.

Most importantly, Fig. 6.8 shows that the stability condition for Regime II corresponds to $\Lambda \approx 1 \times 10^7$ s$^{-1}$. This boundary is almost a straight line indicating that $T_{e,0}$ mainly plays an important role for the stability. The electron temperature for $\gamma = 0$ is approximately 23 eV, which is slightly below the electron temperature for the space charge limited sheath, $T_e \approx 24.6$ eV.

Similar concepts as the electron energy relaxation frequency in the present study have been used in the low temperature plasma community to discuss the effect of nonequilibrium electrons.[121, 122] However, the discharge plasma in the HETs and other low temperature plasmas can be significantly different. The discharge plasma in HETs is more complicated

since there is electron flow, heat loss through the channel walls, and inelastic collisions whereas the electrons mainly undergo diffusion and inelastic collisions in low temperature plasma systems and the energy relaxation length is often defined as $\lambda_\epsilon \sim (D_e/\nu_{eff})^{1/2}$ where $D_e$ is the diffusion coefficient and $\nu_{eff}$ is the effective collision frequency. In this study, $\Lambda$ has contributions from the electron convective heat flux, wall heat flux, and inelastic collisions.

### 6.5.3 Comparison with Experiments

Here, the results from the perturbation theory are compared with Ref. 7 and some discussions are made for the observations in Ref. 4.

#### Increasing Discharge Voltage and Anode Mass Flow Rate

Sekerak[7] observed that the range of magnetic field strength for a stable discharge operation mode becomes narrower as the discharge voltage is increased as well as the anode mass flow rate, as shown in Fig. 6.9. For a given magnetic field strength, it can be seen that the discharge oscillation can be excited when increasing the discharge voltage and anode mass flow rate, particularly at $B_r/B_r^* = 0.5 - 0.7$.

Some aspects of the present theoretical framework can explain the experimental observations. Figure 6.10 illustrates the growth rate for two cases: higher discharge voltage and higher neutral atom density at the inflow.

First, an increased $V_D$ requires $T_{e,min}$ to be larger so that a steady-state plasma discharge can be generated, as shown in Figs. 6.4 and 6.5. Thus, the first condition for a steady-state discharge is more severe, *i.e.* narrower, than the baseline case in Fig. 6.6. In addition, even if the electron temperature stays constant when increasing $V_D$, the axial electron velocity $|U_e|$ is likely to increase. If the magnetic field strength is constant, the electric field increases, the $E \times B$ drift in the azimuthal direction increases, so $|U_e| \approx |(E/B)\Omega^{-1}|$ increases as well. Thus, the operation point is likely to shift down in Fig. 6.10(a), meaning that the growth rate can be larger compared to Fig. 6.6.

Second, the theoretical prediction for the larger anode mass flow rate case is shown in Fig. 6.10(b). Although $T_{e,min}$ decreases, *i.e.* the condition for a steady-state discharge plasma is larger, the instability region, where $\gamma > 0$, is wider than Fig. 6.6. The two

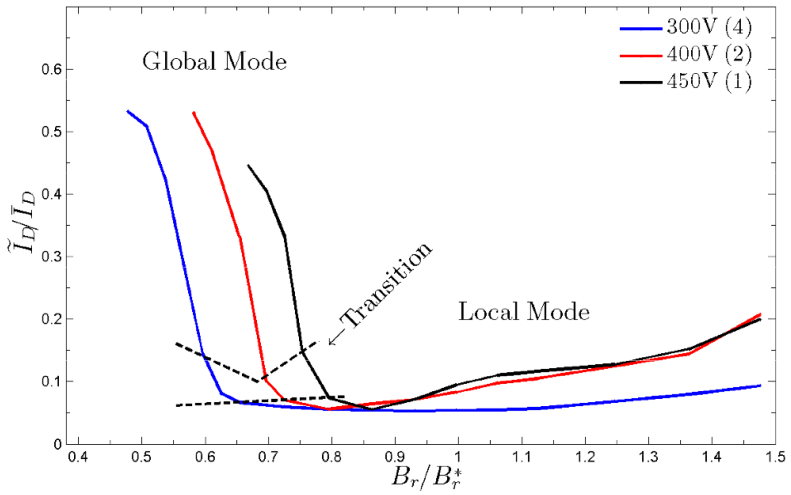


(a) Discharge voltage

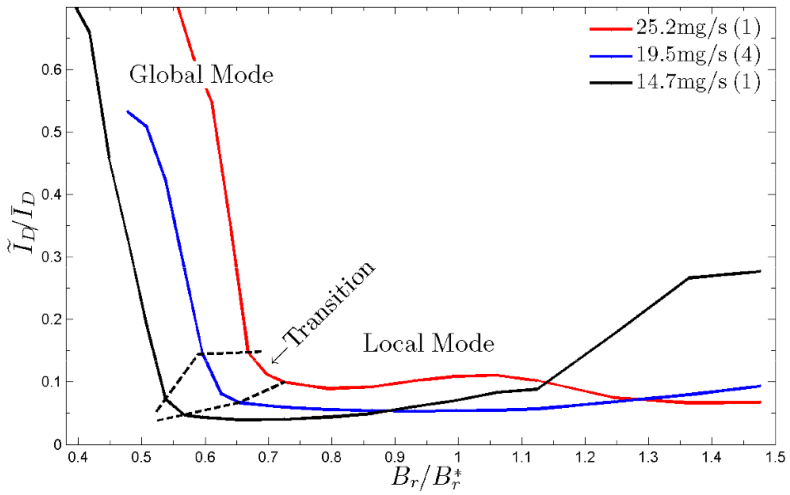


(b) Anode mass flow rate

Figure 6.9: Measurements of discharge current oscillation amplitudes in the H6 thruster. Reproduced from Figs. 4.2 and 4.3 of Ref. 7:

stable regions, Regions I and II, are both narrower. In addition, even when the operation point, $U_e/U_i$ and $T_{e0}$, is kept the same when increasing $N_{int}$, the growth rate increases. For instance, at $(T_{e,0}, U_e/U_i) = (20\text{ eV}, -0.4)$, $\gamma = 3 \times 10^4$ rad/s in Fig. 6.10(b) whereas $\gamma = 1.2 \times 10^4$ rad/s in Fig. 6.6. These observations indicate that the stability condition is more severe for increased $V_D$ and $N_{int}$, which agrees qualitatively with the experiments.

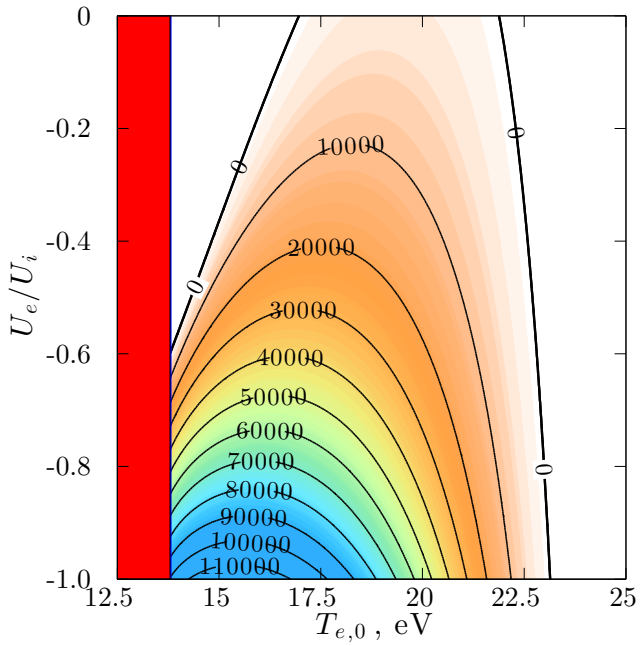


(a) $V_d = 450$ V, $N_{int} = 1.6 \times 10^{19}$ m$^{-3}$. Red region shows the unstable region due to $N_{i,0} < 0$.

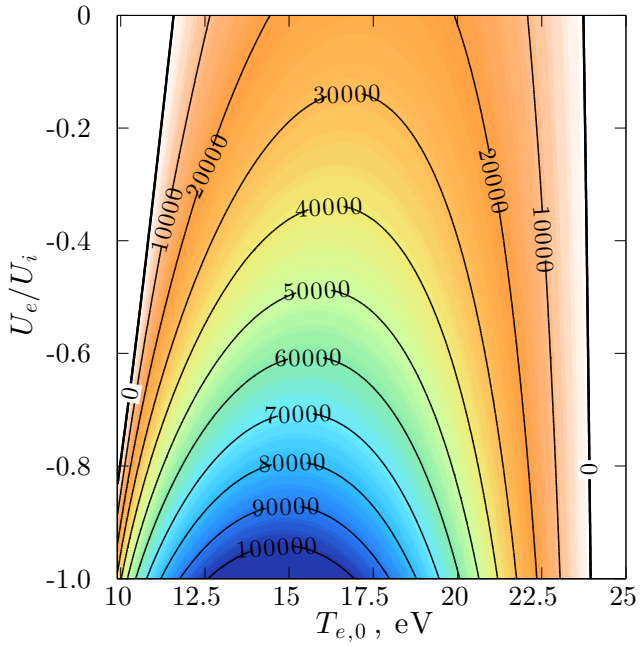


(b) $V_d = 300$ V, $N_{int} = 2.2 \times 10^{19}$ m$^{-3}$.

Figure 6.10: Perturbation theory results for different conditions. Note that the electron temperature range (horizontal axis) is different.

**Discharge Oscillation Mode at Larger Magnetic Field**

In Ref. 4, discharge oscillations also have been observed when further increasing the magnetic field after a stable discharge mode. This can be also seen from Fig. 6.9 that the discharge oscillation amplitudes increase for larger $B_r/B_r^*$. It was discussed in Ref. 95 that a different strong ionization oscillation may be related to plasma diffusion towards the anode. The plasma diffusion or acceleration to the anode has not been taken into consideration in this model. Including this effect into the model is reserved for future work.

In addition, the theory can be applied when changing the propellant. For instance, lighter noble gases such as argon and krypton are used in some thrusters. The mass of the heavy species can alter the ionization length in Eq. (6.9), the inelastic collision rate coefficients in Eq. (6.13), and the wall heat flux in Eqs. (6.20) and (6.21).

### 6.5.4 Nonlinear Saturation of Ionization Oscillations

The non-sinusoidal shape of the discharge current can be explained from the growth rate of the linearized oscillation wave. Some examples of the discharge current oscillations can be found in Refs. 4, 7, and 2.

When the growth rate of the linear perturbation of the ionization oscillation is positive, the perturbation in all quantities will grow exponentially, and the perturbed values may reach some threshold value, say $N_{i,0} > 0$ and $N_{int} > N_{n,0} > 0$. This results in so-called avalanche ionization.[90] After the avalanche ionization, the decay is also exponential. Therefore, the shape of the discharge current becomes an exponential rise and then exponential decay. In addition, as the avalanche ionization is a fast process, the plasma needs to wait for the depleted neutral atoms to fill in the ionization box, which is the slowest process in the system, and is similar to the Lotka-Volterra model in Fig. 6.2.

The growth rate of the linear perturbations in the present study may not exactly predict the behavior of discharge oscillations in HETs since the plasma parameters of the ionization oscillations can change dynamically and the oscillations are likely to be a nonlinear phenomenon. However, the significance of this analysis is the observation of the unstable solutions from the linear perturbations in the discharge plasma of HETs. Linear instabil-

ity grows and nonlinearity can play an important role for $\gamma > 0$ whereas a linearly stable system, $\gamma < 0$, will damp any ionization oscillations. In actual operation, the plasma has some spatial structure inside the ionization region. The growth rate of an ionization oscillation may be large in some area while it might be damping in other areas. The discharge oscillation, *i.e.* the global ionization oscillation, will be determined globally in the thruster.

## 6.6 Time-Varying Analysis

In this section, a matlab code is developed to investigate the ionization oscillations, similar to Figs. 6.1 and 6.2. Equations (6.7) and (6.8) are solved with and without perturbation in the ionization rate instead of solving the electron energy equation. The simplified equations can be written as

$$\frac{\partial N_i}{\partial t} + \frac{N_i U_i}{L} = N_i N_n \xi_{ion}[1 + \Xi \cos(\omega_{r0} t)] \tag{6.29}$$

$$\frac{\partial N_n}{\partial t} + \frac{(N_n - N_{int}) U_n}{L} = -N_i N_n \xi_{ion}[1 + \Xi \cos(\omega_{r0} t)], \tag{6.30}$$

where $\Xi$ is the magnitude of ionization rate perturbation and $\omega_{r0}$ is the prescribed oscillation frequency, which is not needed when $\Xi = 0$.

### 6.6.1 Damping due to Heavy Species Transport

Figure 6.11 shows the heavy species transport model with a constant ionization rate. Thus, $\Xi = 0$ in Eqs. (6.29) and (6.30). The oscillation frequency will be found naturally without prescribing $\omega_{r0}$. The equilibrium values are $N_{i0} = 1 \times 10^{17}$ m$^{-3}$, $N_{n0} = 1 \times 10^{19}$ m$^{-3}$, and $\xi_{ion} = 2 \times 10^{-13}$ m$^6$s$^{-1}$, which are the same as those employed for Figs. 6.1 and 6.2. The initial conditions are the same as Fig. 6.2, where a strong ionization oscillation is observed using the Lotka-Volterra model: $N_i = 5N_{i0}$ and $N_n = N_{n0}$. The inflow neutral atom density $N_{int}$ is added in Eqs. (6.29) and (6.30), which is chosen to be $N_{int} = 2N_{n0} = 2 \times 10^{19}$ m$^{-3}$.

It can be seen that the first oscillation cycle is similar to the Lotka-Volterra model. The large ion density yields a large ionization rate and the neutral atoms are consumed rapidly. The ion density also reaches a very small value. After one cycle, it can be already seen that

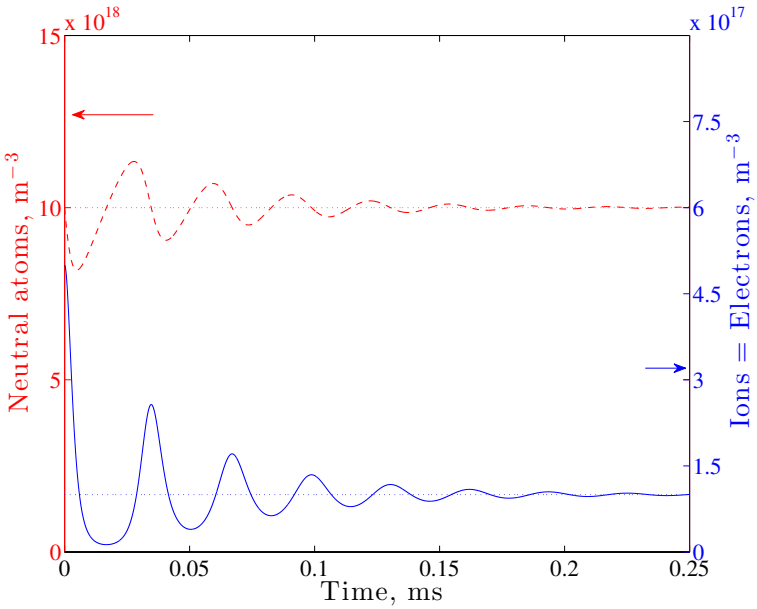


Figure 6.11: Heavy species transport model with constant ionization rate. Similar condition as Fig. 6.2: Initial ion density is 5 $N_{i0}$, but $N_{int} = 2 \times 10^{19}$ m$^{-3}$ is also used.

the ionization oscillations start to damp. This is due to the fixed neutral atom density at the inlet $N_{int}$. Then, the ion and neutral atom densities relax to the equilibrium values.

### 6.6.2 Excitation of Ionization Oscillations

Instead of solving the electron energy equation, shown in Eq. (6.19), a perturbation in the ionization rate is allowed. Thus, $\Xi \neq 0$ in Eqs. (6.29) and (6.30). The values used are $N_{int} = 2N_{n0} = 2 \times 10^{19}$ m$^{-3}$, $N_i = 2N_{i0}$,$N_n = N_{n0}$, and $\omega_{r0} = 2 \times 10^5$ s$^{-1}$. The perturbation of ionization rate is chosen to be $\Xi = 1 \times 10^{-3}$, 0.01, and 0.05.

In Fig. 6.12, the ionization oscillations are damped for $\Xi = 1 \times 10^{-3}$. The results are similar to Fig. 6.11. The neutral atom density of the inlet is fixed and damps the ionization oscillations that occur due to the initial conditions. It can be considered that the ionization oscillations are essentially damped although the ionization oscillations are not completely damped due to a finite $\Xi$.

Figure 6.13 shows the ionization oscillations for a moderate perturbation of the ionization rate, $\Xi = 0.01$. The results look very similar to Fig. 6.1, in which a small perturbation is allowed in the Lotka-Volterra model. Sinusoidal oscillations are observed for both the ion

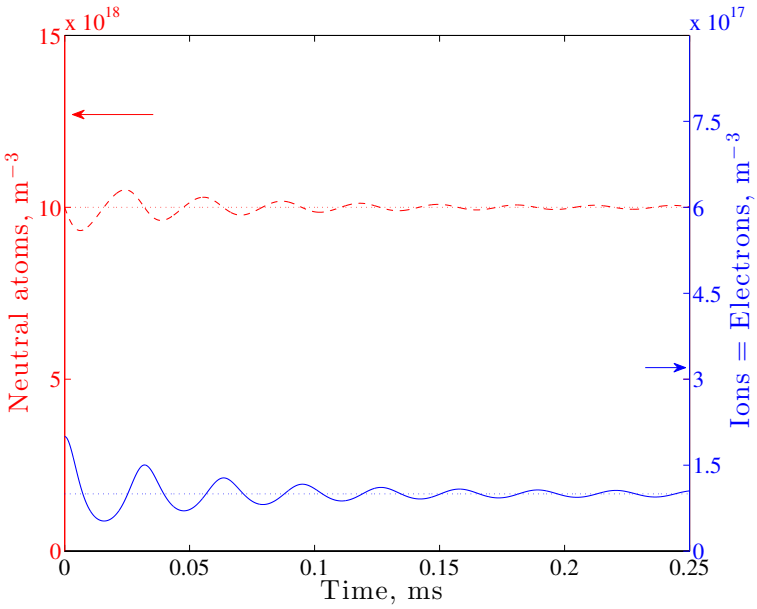


Figure 6.12: Heavy species transport model with perturbation of ionization rate: 0.1 %.

and neutral atom densities. The magnitude of the ionization oscillations is approximately 50 %, which is significantly larger than $\Xi = 0.01$. Thus, it can be concluded that the perturbed ionization rate excites an ionization oscillation. The most striking result of Fig. 6.13 is that the ionization oscillations can be excited with a small perturbation in the ionization rate, or equivalently the electron temperature.

Figure 6.14 shows the ionization oscillations for a strong perturbation of the ionization rate, $\Xi = 0.05$. The results look very similar to Fig. 6.2, in which a strong perturbation is prescribed in the Lotka-Volterra model. The ion and neutral atom densities oscillate in a non-sinusoidal manner. The magnitude of the ionization oscillations exceeds that of the initial perturbation. Although the electron energy perturbation is not solved for in this analysis, the non-sinusoidal oscillations are likely to occur when the growth rate is large for the perturbation theory.

These examples show that the Lotka-Volterra model, *i.e.* the predator-prey model, is valid as long as the ionization oscillation exists and the growth rate of the linear perturbation of the discharge plasma is large enough. The significance of the perturbation theory presented in this chapter is that the growth and damping of the ionization oscillations are understood by taking the perturbation of electron energy into account.

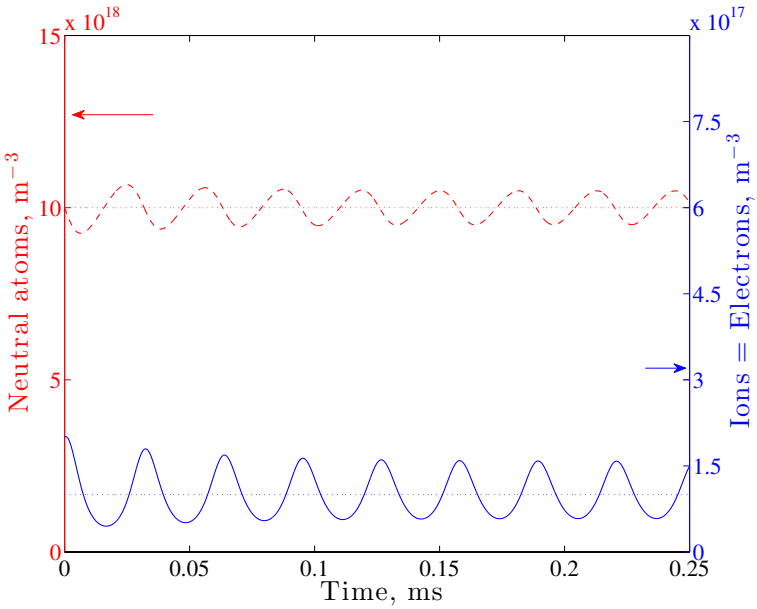


Figure 6.13: Heavy species transport model with perturbation of ionization rate: 1 %.

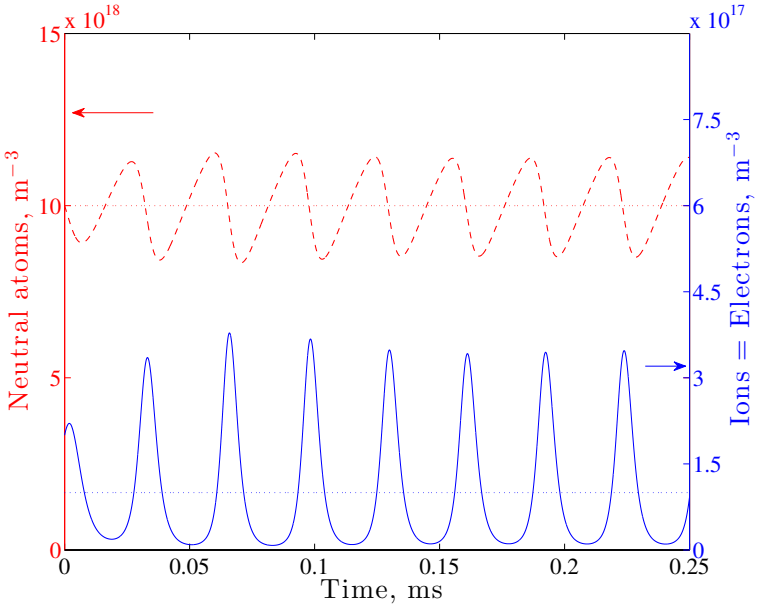


Figure 6.14: Heavy species transport model with perturbation of ionization rate: 5 %.

## 6.7 Summary

A complete perturbation theory of the ionization instability in HETs is developed including the ion and neutral continuity, ion momentum, and electron energy equations. There are three observations in comparison with the previous predator-prey type models.

- Without perturbations in electron energy, the ionization oscillations are always damped. The fixed neutral atom flow from the anode contributes to damping of the oscillation.
- The ionization length $L$, which is frequently used in the literature, is defined using the plasma and geometric parameters.
- The minimum electron temperature to sustain a steady-state discharge plasma is obtained from the continuity equations of ion and neutral atom.

It is further shown that the ionization oscillations in HETs are caused by the perturbation in the electron energy. This significantly advances the understanding of the breathing mode, for which only heavy species transport has been considered in the literature. Inclusion of the electron energy perturbation allows an undamped solution for the linear perturbations of the ionization oscillation wave. The parameters discussed in the present model are $U_e$ (or $\eta_c$) and $T_e$. In addition, the present theory suggests the stabilization mechanism of ionization oscillations. Reduced electron transport and increased electron temperature yields a transition from an undamped oscillation mode to a stabilized mode. This theoretical observation supports recent numerical simulation results in Ref. 2. In order to investigate the ionization oscillations in experiments of HETs, the electron transport properties such as the electron current and electron temperature must be measured.

# CHAPTER VII

# Two-Dimensional Hybrid Modeling of Plasma Transport in Hall Thrusters

## 7.1 Introduction

A variety of two-dimensional (2D) simulation techniques have been developed for the Hall thruster discharge plasma. One of the first was by Komurasaki and Arakawa[123], who developed a steady, 2D formulation using an ion flux-tube method with an electron continuum model.

Unsteady, 2D Hall thruster models have been developed by many researchers. A hybrid-PIC model, called HPHall, by Fife and Martinez-Sanchez[10] has been used the most in the HET community. A 2D PIC method is used for ions and neutral atoms and a quasi-1D continuum approach is used for electrons. HPHall was further extended by Parra *et al.*[94] to include the Bohm condition on the ion flow. Cheng and Martinez-Sanchez[124] further coupled an erosion model to HPHall to investigate the life time of Hall thrusters. Koo and Boyd[13] developed a similar 2D model in order to investigate the effects of anomalous electron transport on the discharge plasma. A 2D hybrid-PIC simulation, based on the 1D hybrid-DK type simulation by Boeuf and Garrigues[11], was further developed by Hagelaar *et al.*[73], which uses a similar formulation as HPHall.

2D fully continuum models have been developed due to their simplicity and low computational cost. Keidar *et al.*[15] developed a 2D continuum simulation with a detailed plasma-wall interaction model and investigated the effect of secondary electron emission (SEE) on the discharge plasma. Mikellides *et al.*[68] have developed a 2D continuum model, called

Hall2De. This method is primarily used to model the magnetically shielded Hall thrusters. A magnetic field aligned mesh is used and the domain can be extended into the far-field plume because of the reduced computation cost compared to particle methods. Geng *et al.*[125] revisited the thermalized potential assumption used in the state-of-the-art hybrid-PIC simulations, in which they suggested that a full 2D potential solver is required.

2D full-PIC methods have also been used to model small-scale turbulence effects and plasma-wall interactions. One of the first developments was by Hirakawa and Arakawa.[126] Szabo[69] developed a fully-PIC/DSMC simulation in the radial-axial directions. Cho [71] also presented a similar full-PIC method analyzing the effects of artificial mobility and permittivity. A 2D axial-azimuthal simulation by Adam *et al.*[21] showed that a high frequency turbulence type oscillation exists at the exhaust of the thruster. A similar numerical simulation was recently presented by Coche and Garrigues.[72]

In this section, a 2D hybrid-DK simulation is constructed. A 2D axial-azimuthal hybrid-PIC simulation was recently presented by Lam *et al.*,[76] but it was shown that there were numerical instabilities that made the solver stop at 0.1 $\mu$s, which is too short to discuss any low-frequency oscillations. A 2D continuum model was used for the electrons in their model. One advantage of using DK simulation is that the statical noise in PIC is eliminated, so the hybrid-DK simulation may generate numerically stable results. The validity of the 2D electron continuum model presented in Ref. 76 is discussed and a new quasi-1D type approach is proposed in this section.

## 7.2 Azimuthal Oscillations

In addition to the discharge oscillations that result from ionization oscillations in the axial direction, the azimuthal ionization instability is considered to play an important role in electron transport.

### 7.2.1 High-Frequency Rotating Spokes

Rotating spokes have become an interesting topic as many radial-axial ($r-z$) Hall thruster studies[10, 13, 74] suggest that anomalous electron mobility is one of the key

processes that determine the entire discharge plasma. One of the first experimental observations was by Janes and Lowder[127] that the anomalous diffusion contributes to the electron transport as collisional diffusion alone cannot explain the measured electron currents across magnetic fields. Such anomalous mobility is considered to be strongly dependent on the plasma fluctuations in the azimuthal direction. Yoshikawa and Rose[128] showed that plasma fluctuations can contribute to the anomalous electron transport across magnetic fields. In a cross-field device, this is often the electric field in the $E \times B$ direction.

One of the first azimuthal simulations shown in the HET community was the work of Hirakawa.[126, 129] It was suggested that azimuthally oscillating electric fields can contribute to the axial electron transport. Coche and Garrigues[72] showed that the electron-cyclotron drift instability, in the range of MHz and wave number on the order of 3000 rad/m,[1] is formed in the region of the negative gradient of magnetic fields. Their 2D simulation was compared with an earlier full-PIC simulation by Adam *et al.*[21] and a theory proposed by Ducrocq *et al.*[130]

### 7.2.2 Low-Frequency Rotating Spokes

Several experiments have successfully observed low-frequency rotating spokes in Hall thrusters. Parker *et al.*[131] showed the correlation between plasma density, light emission, and electron currents, using high-speed cameras and Langmuir probes. It was also observed that the spoke rotates in the $E \times B$ direction with a speed of 1200$-$ 2800 m/s, which is significantly smaller than the $E \times B$ drift. Ellison[12] measured the electron current induced by rotating spokes using a segmented anode in cylindrical Hall thrusters. It was concluded that over half of the total current is conducted by the spoke. Through the use of high-speed Langmuir probe systems[111] and high-speed cameras,[92] azimuthally rotating spokes have been investigated by Sekerak at the University of Michigan.[7] One example from Ref. 7 is shown in Fig. 7.1. It can be seen that the emitted light intensity oscillates coherently in the azimuthal direction. In addition, $m = 1$ spoke modes are observed in cylindrical HETs whereas $m > 2$ are observed in the H6 annular thruster.

[1] $k_\theta = 3000$ rad/m corresponds to a wavelength of $L = 2\pi/k_\theta = 2$ mm. For a standard SPT-100 thruster, the azimuthal length is approximately 25 cm. Therefore, the spoke order $m$ is $m = 125$, which can be considered as *small-scale* azimuthal oscillation waves.

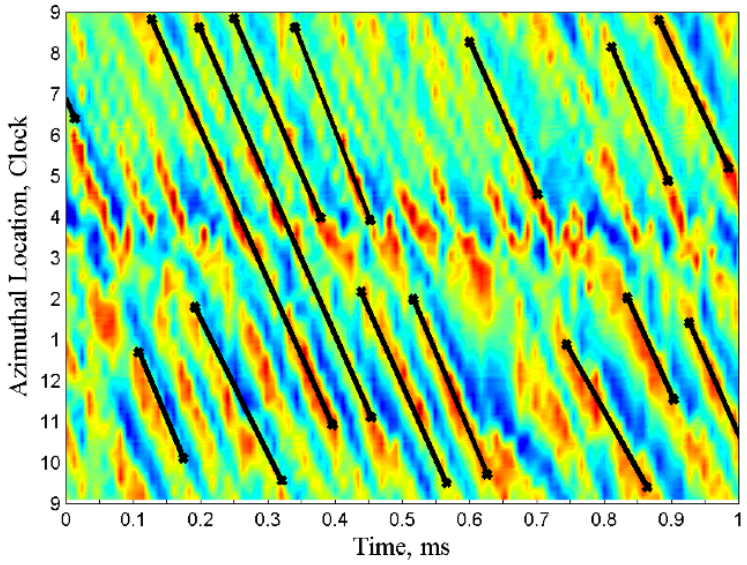


Figure 7.1: Low-frequency azimuthally rotating spokes. Shown is the normalized spoke surface processed from the light intensity obtained from images from a FastCam video. Reproduced from Fig. 5.2 of Ref. 7.

A full-PIC simulation of Boeuf[132] on the rotating spokes in a magnetron discharge showed that a rotating structure moves in the direction of $E \times B$ drift due to a "moving sheath", *i.e.* a double layer. This simulation was in the radial-azimuthal $(r - \theta)$ directions as the electric field is in the radial direction and the magnetic field is in the axial direction in a magnetron. Similar to plasma-sheaths, the ions are accelerated to the ion acoustic speed at the sheath edge, then enter a non-neutral region, where charge separation occurs. It was shown that the speed of the rotating structure is on the order of the ion acoustic speed. Another possible mechanism of rotating spokes is the *critical ionization velocity* hypothesis.[133] It is postulated that a strong increase in the ionization rate occurs if the ion velocity across the magnetic field, $v_{0,\perp}$, exceeds the critical ionization velocity, $v_c$:

$$v_{0,\perp} > v_c = \sqrt{\frac{2eU_i}{m_i}},$$

where $U_i$ is the ionization potential. For a Xenon plasma, $U_i = 12.1$ eV and $m_i = 131$ amu, hence $v_c \approx 4200$ m/s. This is higher than experimental observations in HET discharges.

### 7.2.3 Hypotheses for Low-Frequency Spokes

Sekerak made two hypotheses about the low-frequency rotating spokes in Ref. 7. It was indicated that the rotating spokes are an oscillation wave that results from (1) stabilization of the ionization front and (2) interaction with the outer channel wall.

The first hypothesis is supported by the observation that local ionization oscillations in the azimuthal direction disappear when global ionization mode, *i.e.* breathing mode, occurs. The second is supported by another observation in magnetically shielded Hall thrusters, where azimuthal spokes are not seen despite the stronger magnetic field strengths compared to conventional thrusters. It was shown that the only occasion for the spokes to appear is when the magnetic shielding is imperfect and the hot plasma touches the (*outer*) wall at high magnetic field strengths. In addition, several dispersion relation analyses were performed in Ref. 7, but all the high-frequency oscillations related to electron transport disagree with the spoke characteristics. The low-frequency oscillations suggests that the oscillation frequency is heavily dependent on the slow neutral atom flow, similar to the breathing mode oscillations discussed in Chapter VI.

A hypothesis that can be answered using the 2D hybrid kinetic-continuum model is whether an azimuthally rotating spoke is generated by a local ionization oscillation event. As shown in Fig. 7.2, the ions move axially and electrons move azimuthally. The observed spoke velocity in Ref. 7 was $1500 - 2200$ m/s in the azimuthal direction whereas the $E \times B$ drift of electrons is on the order of $10^6$ m/s at maximum. Sekerak[7] proposed a simple mechanism of the azimuthally rotating spokes as an ambipolar diffusion from the energy balance. Ambipolar diffusion sets an electric field that accelerates ions to the Bohm velocity, which is the ion acoustic speed. In this case, it can be assumed that the electron energy is dominated by the $E \times B$ drift, so

$$v_\theta = \sqrt{\frac{\frac{1}{2} m_e v_{E\times B}^2}{m_i}} \approx \sqrt{\frac{m_e}{m_i}} v_{E\times B}$$

A similar mechanism was also suggested by Boeuf[132]. The spoke velocity is explained as *critical ionization velocity*. Ions gain energy across the moving sheath that is on the order

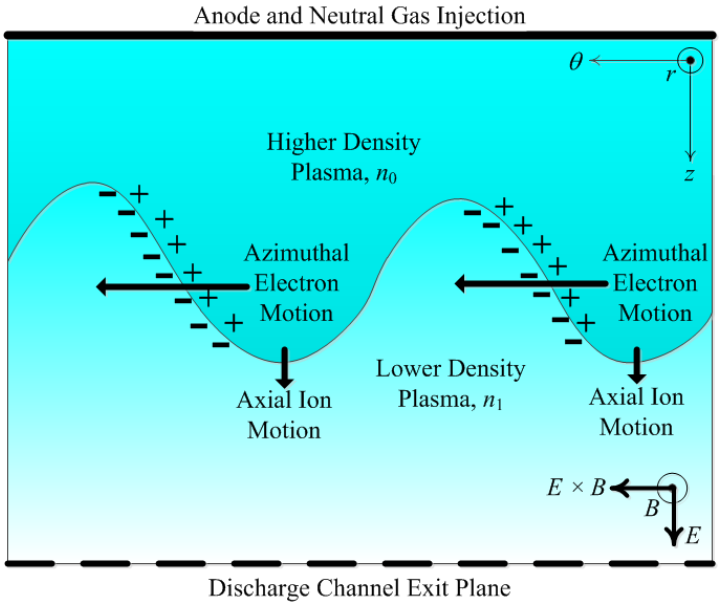


Figure 7.2: Possible mechanism of the rotating spokes. Diagram of $z-\theta$ plasma of discharge channel shown exaggerated ionization front. Reproduced from Fig. 5.19 of Ref. 7.

of the ionization potential for xenon atoms. $v_\theta = (2e\Delta\phi/m_i)^{1/2}$, where $\Delta\phi$ is the ionization potential, *e.g.* $\Delta\phi \approx 12.1$ eV for xenon atoms.

Note that the spoke velocity is not equal to the ion mean velocity in the azimuthal direction. This is supported by an experimental observation in Ref. 8. It was indicated that the ion swirl velocity, *i.e.* the ion mean velocity in the azimuthal direction, is approximately 250 m/s, which is much smaller than the rotating spoke velocity obtained from experiments. In addition, in this situation, the spoke velocity must be a strong function of magnetic field strength, but Sekerak's experiment showed that spoke velocity and magnetic field strengths are uncorrelated.

Finally, the use of a 2D axial-azimuthal simulation is justified by the observations that spokes fill the channel radially from the inner wall to the outer. Thus, the plasma structure can essentially be averaged in the radial direction. The experiments in Ref. 7 showed that the azimuthal spokes have wave numbers in the range of $k_\theta = 30 - 80$ rad/m. It was stated by Sekerak[7] that "*What is needed is a $z-\theta$ simulation, either kinetic, fluid, PIC or a hybrid of any of these, that can resolve time steps of 1 $\mu$s or less (in order to resolve 10's kHz oscillation) and wave numbers less than 100 rad/m. The domain should be from the anode*

*out at least one channel width downstream of the exit plane for a time duration of several hundred micro-seconds. Finally, in the limit of 1D in the z-direction, it should recover the 10-30 kHz axial breathing mode.*" The purpose of the present 2D hybrid-DK simulation is to fulfill these criteria and observe low-frequency, low wavenumber oscillations.

## 7.3 2D Kinetic Model

The axial-azimuthal domain in a cylindrical coordinate is approximated as a 2D planar domain. This significantly reduces the computational cost, as the third dimension in velocity space (here, the radial direction) can be neglected. If the total number of discretized phase space elements for a 2D2V simulation is $N_{4V}$, then it is $N_{4V}N_V$ for a 2D3V simulation, where $N_V$ is the number of velocity bins in the extra dimension. Thus, the computational cost increases by at least a factor of $N_V$ when adding another dimension.

Before coupling the DK simulation with a 2D continuum model, the DK simulation is tested with a collisionless, nonmagnetized, neutral atom flow. Without any electric field and source terms, the neutral atom DK solver is compared with MONACO,[134] a DSMC solver, for benchmarking purposes. The problem chosen is an effusion type problem, where neutral atoms are injected from a hole (3D) or a slit (2D). Good agreement of the two kinetic simulations is shown in Appendix D.

### 7.3.1 2D Axial-Azimuthal Kinetic Simulation

The schematic diagram of the 2D axial-azimuthal simulation is shown in Fig. 7.3. Figure 7.3(a) shows the cylindrical coordinates in a Hall thruster discharge channel. The radial direction pointing outwards follows the magnetic field orientation. In the 2D domain, shown in Fig. 7.3(b), the axial and azimuthal coordinates correspond to the $x$ and $y$ directions, respectively. Therefore, the $E_x \times B_r$ drift is in the $y$ direction, $v_x B_r$ is in the $y$ direction, and $v_y B_r$ is in the $-x$ direction.

The 2D kinetic equation can be written as

$$\frac{\partial f}{\partial t} + v_x \frac{\partial f}{\partial x} + v_y \frac{\partial f}{\partial y} + \frac{e}{m_i}(E_x - v_y B_r)\frac{\partial f}{\partial v_x} + \frac{e}{m_i}(E_y + v_x B_r)\frac{\partial f}{\partial v_y} = S. \tag{7.1}$$

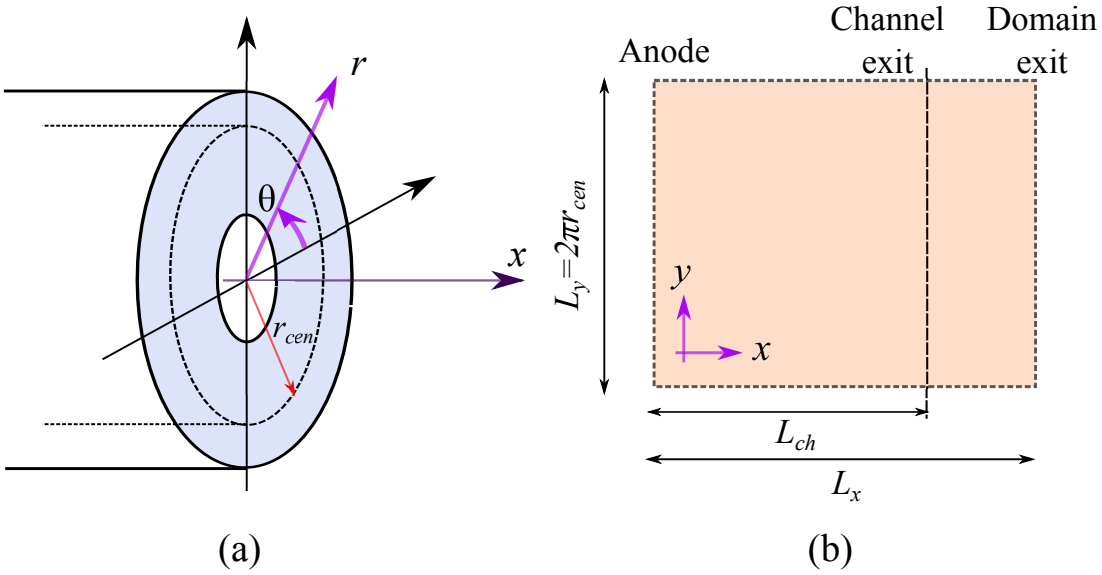


Figure 7.3: The 2D setup. (a) Cylindrical Coordinates in an annulus, representing a Hall thruster discharge channel. The dashed line in (a) is the plane of interest, expanded into 2D in (b).

The anode is set at $x = 0$ m and the domain exit is $x = 0.035$ m. The $y$ direction uses a periodic boundary condition. In addition, the Lorentz force can be turned on and off in order to investigate the effect of the gyromotion of ions in the 2D domain. The centrifugal force due to the radial transport is neglected. Equation (7.1) is based on a magnetic field line pointing outwards of the channel. However, this direction of the magnetic field can also be flipped so that $B_r < 0$.

### 7.3.2 Discretized 2D DK Model

For the 2D DK model, there are four dimensions, *i.e.* 2D2V. Strang's time splitting becomes more complicated and requires more intermediate time steps for a four dimensional system. The next obvious choice is to split the physical and velocity update, which is similar to a leap-frog scheme in particle methods. This will yield second order accuracy in time integration, but would require 2D and 2V updates to be second order accurate. The time integration used in the dissertation is a second-order accurate Runge-Kutta method without

any dimensional splitting. Equation (7.1) without the source term can be written as

$$\frac{\partial f}{\partial t} + L[f(x, y, v_x, v_y)] = 0,$$

where $L[f(x, y, v_x, v_y)]$ consists of the physical and velocity advection terms. Then, a second-order Runge-Kutta method can be written as

$$f^* = f^n + \Delta t L(f^n),$$

$$f^{n+1} = f^n + \frac{\Delta t}{2}\left[L(f^n) + L(f^*)\right].$$

The discretized VDF can be written as $f_{ix,iy,jx,jy}$ where $ix$, $iy$, $jx$, and $jy$ are the cell numbers in the $x$, $y$, $v_x$, and $v_y$ directions, respectively. Then, the discretized flux terms can be written as

$$v_x\frac{\partial f}{\partial x} = \frac{v_x}{\Delta x}(f_{ix+1/2,iy,jx,jy} - f_{ix-1/2,iy,jx,jy}),$$

$$v_y\frac{\partial f}{\partial y} = \frac{v_y}{\Delta y}(f_{ix,iy+1/2,jx,jy} - f_{ix,iy-1/2,jx,jy}),$$

$$a_x\frac{\partial f}{\partial v_x} = \frac{a_x}{\Delta v_x}(f_{ix,iy,jx+1/2,jy} - f_{ix,iy,jx-1/2,jy}),$$

$$a_y\frac{\partial f}{\partial v_y} = \frac{a_y}{\Delta v_y}(f_{ix,iy,jx,jy+1/2} - f_{ix,iy,jx,jy-1/2}),$$

where $a_x = e(E_x - v_y B_r)/m_i$ and $a_y = e(E_y + v_x B_r)/m_i$. The subscripts $+1/2$ and $-1/2$ denote the cell interfaces. For each flux evaluation, the finite volume method with a modified Arora-Roe limiter is used. Note that $a_x$ and $a_y$ are independent of $v_x$ and $v_y$, respectively.

The time step is restricted by the CFL condition. For the 2D2V DK model using a second-order Runge-Kutta time integration, the time step must follow:

$$\max\left(\frac{v_x\Delta t}{\Delta x} + \frac{v_y\Delta t}{\Delta y} + \frac{a_x\Delta t}{\Delta v_x} + \frac{a_y\Delta t}{\Delta v_y}\right) \leq \alpha, \tag{7.2}$$

where $\alpha$ is the safety factor. In this model, $\alpha = 0.9$ is used. Equation (7.2) needs to be satisfied for numerically stable integration. Thus, if the left hand side is above $\alpha$, the time step is reduced as $\Delta t = \Delta t/N_{CFL}$, where $N_{CFL}$ is the left hand side of Eq. (7.2) divided

by $\alpha$. For instance, if the left hand side of Eq. (7.2) is 1.5, $N_{CFL} = 2$ and thus the time step is reduced in half. The collision term is added after the left hand side of Eq. (7.1) is updated.

The domain size and discretization are provided in Table 7.1. The axial discretization is chosen small enough similar to the 1D hybrid model in Chapters IV and V. However, the azimuthal discretization can be larger as the main interest is to capture low-frequency large scale oscillations.

Table 7.1: Discretization of 2D DK simulation

| | | |
|---|---|---|
| Axial domain length | $L_x$ | 3.5 cm |
| Channel length | $L_{ch}$ | 2.5 cm |
| Inner Radius | $r_{in}$ | 3.5 cm |
| Outer Radius | $r_{out}$ | 5 cm |
| Azimuthal length | $L_y$ | $\pi(r_{in} + r_{out}) = 26.7$ cm |
| Velocity space in axial direction | $[v_{x,min}, v_{x,max}]$ | [-15000 m/s, 35000 m/s] |
| Velocity space in azimuthal direction | $[v_{y,min}, v_{y,max}]$ | [-10000 m/s, 10000 m/s] |
| The number of cells in physical space | $[N_x, N_y]$ | [70, 32] |
| The number of cells in velocity space | $[N_{vx}, N_{vy}]$ | [200, 100] |
| Cell size in physical space | $[\Delta x, \Delta y]$ | [0.5 mm, 8.3 mm] |
| Cell size in velocity space | $[\Delta v_x, \Delta v_y]$ | [250 m/s, 200 m/s] |

### 7.3.3 2D Ion Simulation with a Static Electric Field

Here, a static electric field is prescribed and the effect of magnetic fields on the ion acceleration is investigated. For this test case, the source term is neglected: $S = 0$ in Eq. (7.1). The orientation must be kept the same for electrons.

#### Electric Field

The prescribed electric field in the $x$ direction is given by.

$$E_x = \frac{7V_d}{L_x}\left(\frac{x}{L_x}\right)^6, \tag{7.3}$$

and the electric field in the $y$ direction is zero: $E_y = 0$. This corresponds to

$$\phi = V_d\left[1 - \left(\frac{x}{L_x}\right)^7\right],$$

where $\phi$ is the plasma potential. In the simulations, $V_d = 300$ V is assumed. The ions enter the domain at the anode $x = 0$ with a half-Maxwellian. Note that assigning a half-Maxwellian at the ghost cell adjacent to the anode yields a biased-Maxwellian at the anode plane because the probability of particles is shifted with their own velocity. The inlet number density is $n_0 = 10^{15}$ m$^{-3}$ and the ion mean velocity is $u_0 = (\pi k_B T/2m_i)^{1/2}$. For $T = 750$ K and xenon singly charged ions, *i.e.* $m_i = 131$ amu, the ion mean velocity is 273 m/s at the anode.

**Magnetic Field**

The magnetic field in these simulations is inward pointing, *i.e.* $B_r < 0$. The shape of the magnetic field is the same as the 1D simulations:

$$B_r(x) = B_{max} \exp\left[-\left(\frac{x - L_{ch}}{\Delta L}\right)^2\right]$$

Four different cases are tested: $B_{max} = 0$, 120, 240, and 400 G.

**Analytic Solutions**

The macroscopic quantities can be calculated analytically. The ions follow a biased-Maxwellian at the anode region and are accelerated through the potential field. Therefore, the analytic VDFs at the anode are given by

$$f_i(x = 0, v_x, v_y) = n_0 \left(\frac{m_i}{2\pi k_B T}\right)^{1/2} \frac{m_i}{k_B T} v_x \exp\left[-\frac{m_i}{2k_B T}\left(v_x^2 + v_y^2\right)\right],$$

for $v_x > 0$. Note that $f_i(x = 0, v_x, v_y) = 0$ for $v_x \leq 0$. The analytic solution for the ion VDFs at any location inside the domain can be obtained from energy conservation: $\frac{1}{2}m_i v_{x0}^2 = \frac{1}{2}m_i v_x^2 + e\Delta\phi$, where $\Delta\phi = \phi - V_d < 0$. Then the ion VDFs at an arbitrary position $x$ can be written as

$$f_i(x, v_x, v_y) = n_0 \left(\frac{m_i}{2\pi k_B T}\right)^{1/2} \frac{m_i}{k_B T} \left(v_x^2 + \frac{2e\Delta\phi}{m_i}\right)^{1/2} \exp\left[-\frac{m_i\left(v_x^2 + v_y^2\right) + e\Delta\phi}{2k_B T}\right], \quad (7.4)$$

for $v_x > (2e|\Delta\phi|/m_i)^{1/2}$. However, since the macroscopic quantities are difficult to obtain analytically from Eq. (7.4), the ion density and mean velocity are calculated by assuming cold ions with zero temperature. The number density can be written as

$$n = n_0 \left(1 + \frac{2e\Delta\phi}{m_i}\right)^{-1}$$

where $\Delta\phi = \phi - V_d$ is the potential drop from the anode. The ion mean velocity in the $x$ direction can be written as

$$u_{ix} = \left(u_0^2 - \frac{2e\Delta\phi}{m_i}\right)^{1/2}.$$

It can be expected that there are discrepancies between the numerical simulations and the analytic formulae using the cold-ion assumption but these analytic solutions work well near the anode (inlet) and the outlet. At the outlet, due to the ion acceleration, the ion temperature will decrease and essentially form a beam.

**Results**

Figure 7.4 shows the steady-state ion number density and mean velocity in the $x$ direction obtained from the DK simulation. Good agreement between the numerical simulations and theory is shown. The effects of the magnetic field on these macroscopic results are small. It can be also seen that there are some discrepancies near $x = 0.01$ m. The relative error can be given by $|\Delta e| = |u_n - u_a|/|u_a|$, where $u$ is the solution and subscripts $n$ and $a$ represent numerical and analytical, respectively. The maximum relative error in $0.007 < x < 0.012$ m can be as large as 8 % for both the ion density and mean velocity. However, it is found that the relative error reduces to within 0.5% in the region at $x > 0.015$ m.

The ion mean velocity in the $y$ direction is shown in Fig. 7.5. It can be seen that the magnetization yields the ion mean velocity up to 550 m/s at the domain exit. This suggests that a helical structure can be formed for the ion flows in the presence of a radial magnetic field. Such helical structure is reported in Hall thrusters by Sekerak[7] and Smith[135] as well as in a helicon discharge by Siddiqui.[136]

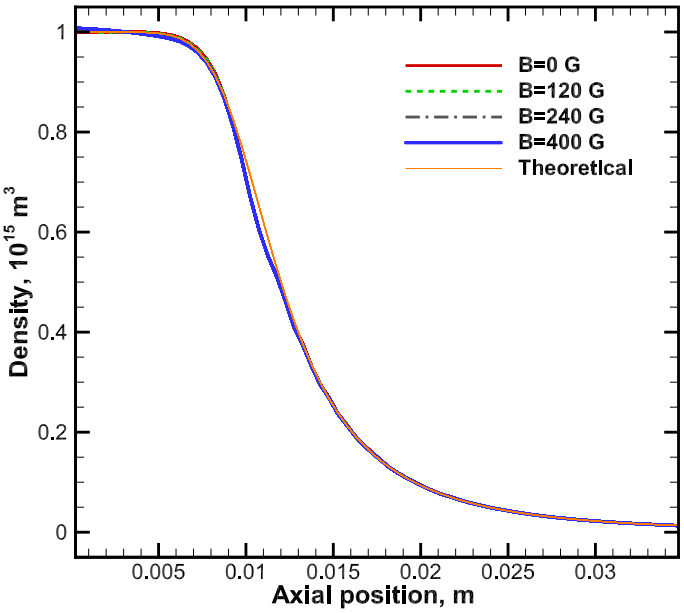


(a) Ion number density

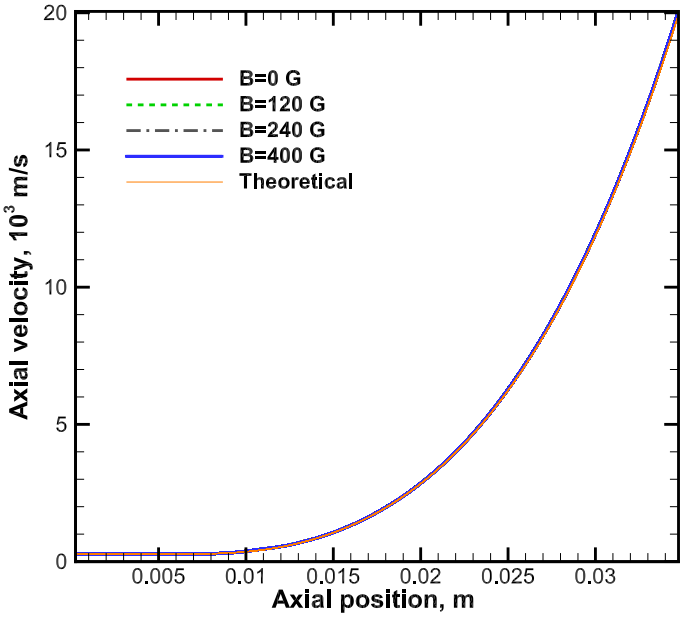


(b) Ion mean velocity in the $x$ direction

Figure 7.4: Static electric field case using the DK simulation.

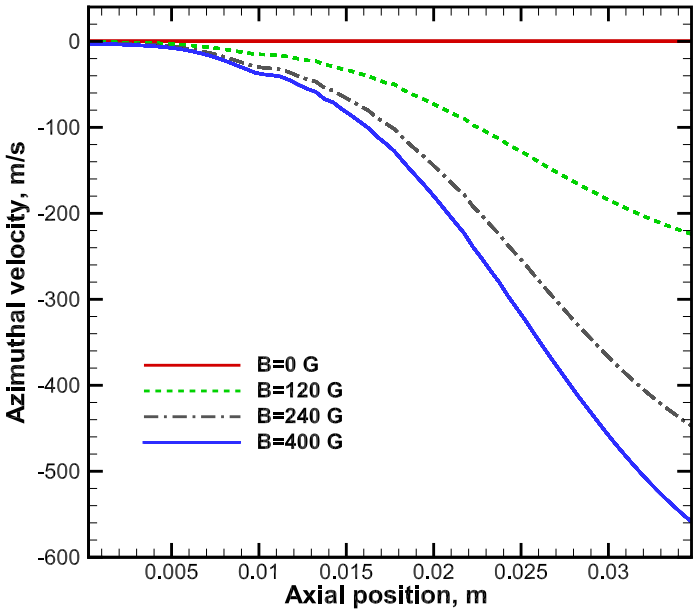


Figure 7.5: Ion mean velocity in the $y$ direction for the static electric field case using the DK simulation. Note that the azimuthal velocities are negative because the direction of the magnetic field lines is pointing inwards.

The ion VDFs at the inlet, *i.e.* $x = 0$ m, and the domain exit, *i.e.* $x = 0.035$ m, are shown in Fig. 7.6 for $B = 0$ G and $B = 400$ G. The ion VDFs are symmetric in the $v_y$ for the nonmagnetized case and shifted downwards for the magnetized case due to the Lorentz force. Although not shown in the figure, the ion VDFs at the inlet will have some negative $v_x$ components due to the magnetization. The force in *thex* direction is given by $F_x = v_y B_r$. In other words, the Lorentz force acts as a rotation in the phase space, as shown in Figs. 7.6(b) and 7.6(c). The helix angle or pitch angle is approximately 1.5°. Note that the ion distributions become wider, particularly in $v_x$ direction, due to the numerical error associated with the finite-volume MUSCL method. However, despite the wider distribution function, the ion mean velocity in the $x$ direction agrees well with the theoretical curve. As discussed in Chapter IV, the numerical error in the DK simulation contributes to a wider distribution, *i.e.* an increase in temperature, but does not alter the mean velocity. As collisions related to the ion temperature are not important for the Hall thruster discharge plasma, the DK simulation works well for the ion kinetic modeling.

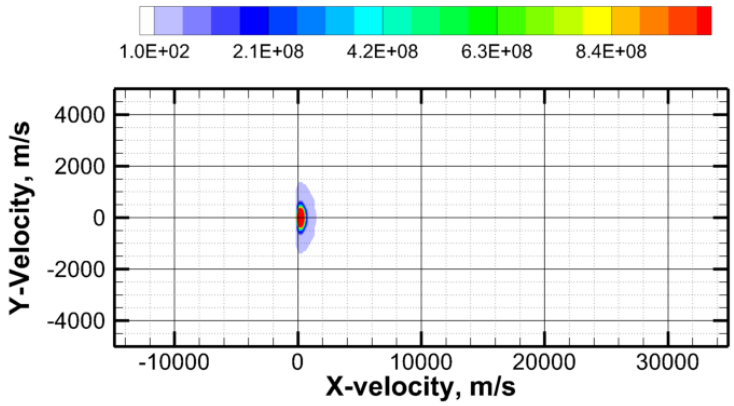


(a) At the inlet: $B = 0$ G

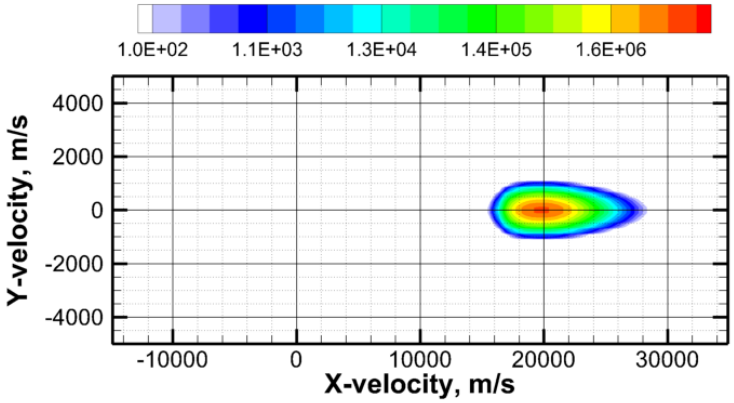


(b) At the domain exit: $B = 0$ G

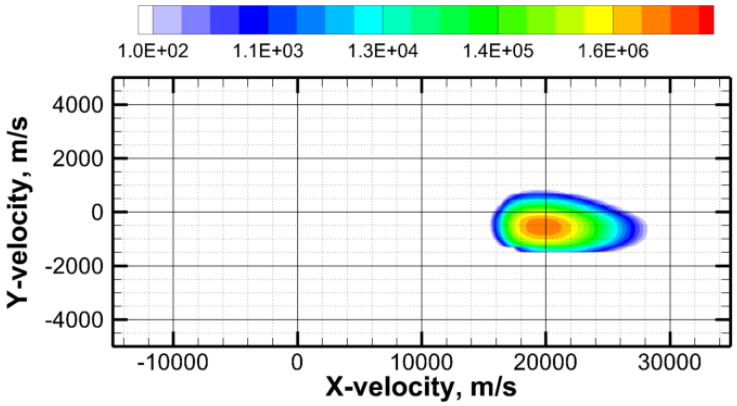


(c) At the domain exit: $B = 400$ G

Figure 7.6: The steady-state ion VDFs at the inlet, $x = 0$ m, and the domain exit, $x = 0.035$ m. The color bars are in logarithmic scales. Note that the range of the color bar is different in (a) from the other two.

## 7.4 2D Electron Continuum Model

In order to capture the low-frequency oscillations in the axial and azimuthal directions of the discharge plasma, the present model neglects the effect of radial transport. Hence, a two-dimensional assumption is used. Detailed derivation of the 2D electron continuum model is provided in Appendix E.

The electron continuum model is very sensitive to the discharge plasma. The use of a quasineutral assumption is valid for the ion time scales but not for electrons. Some discussions are made on the validity of the quasineutral assumption in Appendix F. There are two equations that are not needed to be solved by using the quasineutral assumption: the electron continuity equation and the Poisson equation. Instead, ions and electrons are related to each other through the charge conservation equation assuming only singly-charged ions and electrons.[2] The Poisson equation can no longer be used to calculate the electric field or the plasma potential as the right hand side of the Poisson equation is zero. Thus, the electric field needs to be calculated from the charge conservation equation that requires a *linear* dependence of the electron momentum on the electric field. The most common technique in the low-temperature plasma community is to use a drift-diffusion approximation.[3] Once the *nonlinearity* of electron momentum, *e.g.* inertia,[4] is introduced, then the charge conservation equation with the nonlinear electron momentum cannot be solved. In this situation, a time-dependent solution to the nonlinear equations may become the only option, which will be discussed in Chapter VIII.

Another concern in the 2D axial-azimuthal simulation is the validity of the continuum model. As discussed in Chapter I, continuum models are inaccurate for a large Knusden number flow. The collision frequency must be larger than the characteristic frequency of the flow so that the distribution functions relax to a Maxwellian. If the flow speed is faster, nonequilibrium effects will be present and continuum models may not be accurate.

[2]Charge conservation equation is derived by the ion and electron continuity equations.

[3]Drift-diffusion approximation works if the diffusion effects are dominant in the system and the spatial profile of electron current or flux is smooth.

[4]The inertial term plays an important role when the electron mean velocity has non-smooth profile, such as discontinuity.

### 7.4.1 Electron Momentum

The electron momentum equation also needs to be taken into account. The electron flux is required for the charge conservation equation in order to solve for the electric field, or the plasma potential, when using a quasineutral assumption.

#### Validity of Continuum Approach

The validity of the continuum approach is determined by the Knudsen number, as discussed in Chapter I. The Knudsen number is again given by

$$Kn = \frac{\lambda_{MFP}}{L},$$

where $\lambda_{MFP}$ is the mean free path and $L$ is the characteristic length. One important spatial scale in plasmas is the Debye length $\lambda_D = (\epsilon_0 k_B T_e / e^2 n_0)^{1/2}$. As can be seen from Fig. 1.3 in Chapter II, the Debye length in a Hall thruster is on the order of 0.1 mm to 1 $\mu$m. Thus, if the Debye length is resolved, a fully-kinetic approach must be taken due to the large Knudsen number. On the other hand, if the Debye length is not resolved, a continuum model can be used as long as $Kn$ is small.

As the electron transport is significantly reduced in the axial direction due to the radial magnetic fields, $\lambda_{MFP}$ in that direction can be considered very small. The electrons can drift in the azimuthal direction for a while and then move in the axial direction by collisions or other mechanisms, such as turbulence type anomalous transport. Thus, it is likely that $\lambda_{MFP}$ is much smaller than any characteristic length in the axial direction. This suggests that a continuum approach can be applied for axial transport.

However, for the azimuthal transport, the electrons may undergo a significant $E \times B$ drift, particularly in the region where the magnetic field strength is at maximum. The $E \times B$ drift can be on the order of $10^6 - 10^7$ m/s. The collision frequency is determined by $\nu = n_n < \sigma g >$, where $n_n$ is the neutral atom number density, $\sigma$ is the collision cross section, and $g$ is the relative velocity between electrons and other species, which is essentially equal to the electron velocity. In the azimuthal direction, the electron velocity can be approximated as a beam due to the $E \times B$ drift, so $\nu = n_n \sigma(v) v$. Thus, $\lambda_{MFP} = [n_n \sigma(v)]^{-1}$, where $v$

is the $E \times B$ drift. The cross section of electron-neutral collisions is on the order of $10^{-19}$ $\mathrm{m}^2$[16] and $n_n$ in the Hall thruster discharge channel is on the order of $10^{18} - 10^{19}$ $\mathrm{m}^{-3}$. Thus, the Knudsen number in the azimuthal direction is on the order of $1 - 10$, which is in a transitional regime between a fully equilibrium state and a nonequilibrium state. A continuum approach may be invalid for the electron transport in the azimuthal direction.

**Axial-Azimuthal Momentum Model**

The axial momentum equation can be written in a continuum form as

$$mn\left[\frac{\partial u_{ex}}{\partial t} + u_{ex}\frac{\partial u_{ex}}{\partial x} + u_{ey}\frac{\partial u_{ex}}{\partial y}\right] = -\frac{\partial p}{\partial x} - en(E_x - u_{ey}B_r) - mnu_{ex}\nu_m. \tag{7.5}$$

Based on the consideration that continuum approaches are invalid, the azimuthal momentum equation is written as

$$0 = -eu_{ex}B_r - mu_{ey}\nu_m. \tag{7.6}$$

The drift-diffusion approximation is assumed, so the left hand side of Eqs. (7.5) is zero. For the azimuthal transport, this approximation is essentially identical to assuming $E_y + 1/(en)\partial p/\partial y \approx 0$, in a continuum formulation. Therefore, the axial and azimuthal electron momentum equations can be written as

$$u_{ex} = -\mu_\perp\left(E_x + \frac{1}{en}\frac{\partial p}{\partial x}\right) \tag{7.7}$$

$$u_{ey} = -\Omega u_{ex} = +\mu_\perp\Omega\left(E_x + \frac{1}{en}\frac{\partial p}{\partial x}\right), \tag{7.8}$$

where $\mu_\perp = \mu(1+\Omega^2)^{-1}$ is the cross-field electron mobility, $\mu = e/m\nu_m$ is the electron mobility, and $\Omega = eB_r/m\nu_m$ is the Hall parameter. Note that Eq. (7.8) reduces to

$$u_{ey} = \frac{1}{B}\left(E_x + \frac{1}{en}\frac{\partial p}{\partial x}\right),$$

for $\Omega \gg 1$. The azimuthal electron mean velocity is the sum of the $E \times B$ drift and the diamagnetic drift, which can be derived from the collisionless guiding center theory. Note that the drift velocities calculated from the guiding center motion are already time-averaged

quantities.[5] It is further assumed that the spatial derivative of the electron momentum in the $y$ direction follows

$$\frac{\partial}{\partial y}(nu_{ey}) \simeq \frac{n}{B}\frac{\partial}{\partial x}\left(E_y + \frac{1}{en}\frac{\partial p}{\partial y}\right) \approx 0, \tag{7.9}$$

so that the electron momentum in the $y$ direction can be neglected in the 2D charge conservation equation.

### 7.4.2 Reviewing the One-Dimensional Case

In the 1D axial case, the quasineutral assumption is used. This formulation shown in Chapter IV is based on an integration technique to evaluate the electric field. From a continuum perspective, the 1D charge conservation equation with a quasineutral assumption yields

$$0 = \frac{\partial J_{ix}}{\partial x} + \frac{\partial J_{ex}}{\partial x},$$

where $J_{ex}$ can be given as $J_{ex} = nu_{ex} = n\mu_{\perp}E_x$ for simplicity. Thus, using $E_x = -\partial\phi/\partial x$, the 1D charge conservation equation can be written as

$$\frac{\partial}{\partial x}\left(n\mu_{\perp}\frac{\partial \phi}{\partial x}\right) = \frac{\partial J_{ix}}{\partial x}, \tag{7.10}$$

which is now a 2nd-order elliptic PDE that can be solved using linear algebra methods. In discrete form, this equation can be written as

$$\frac{1}{\Delta x}\left(\frac{a_i\phi_{i+1} - b_i\phi_i}{\Delta x} - \frac{b_i\phi_i - c_i\phi_{i-1}}{\Delta x}\right) = S_i,$$

where $a_i$, $b_i$, and $c_i$ are the coefficients, $\phi_i$ is the potential, and $S_i$ is the source term at point $i$. The coefficients are $a_i = (n\mu_{\perp})_{i+1}$, $b_i = (n\mu_{\perp})_i$, and $c_i = (n\mu_{\perp})_{i-1}$, which are the product of ion number density and the transverse electron mobility. In a vector form, this

[5] For instance, consider an electric field in $x$ direction, a magnetic field in the $y$ direction, the $E \times B$ drift is in $z$ direction. The velocity components can be written as $v_y = v_{\parallel}$, $v_x = v_{\perp}\cos(\omega_B t + A)$, and $v_z = v_{E\times B} + v_{\perp}\sin(\omega_B t + A)$, where $v_{\parallel}$ and $v_{\perp}$ are the parallel and perpendicular velocities, $\omega_B$ is the electron gyrofrequency. Therefore, $< v_z >= v_{E\times B}$ is the time averaged electron velocity in $z$ direction averaged over gyro motions.

can be written as

$$\mathbf{A}\vec{\phi} = \vec{S}, \tag{7.11}$$

where $\mathbf{A}$ consists of $a_i$, $b_i$, and $c_i$.

**Condition number**

The condition number of a matrix defines how well- or ill-conditioned the matrix is. Ill-conditioned matrix means that the matrix is closer to a singular matrix, so it is difficult or impossible to find the solutions. This is characterized by the condition number, typically given as

$$\text{cond}(A) = \frac{\lambda_{\max}}{\lambda_{\min}}, \tag{7.12}$$

where $\lambda_{\max}$ and $\lambda_{\min}$ are the maximum and minimum eigenvalues of the $\mathbf{A}$ matrix. When the condition number is large, the matrix is more ill-conditioned. In this situation, the matrix should not be solved in the form shown in Eq. (7.11). For instance, in the Hall thruster discharge plasma, an integration technique is used. The spatially integrated information is used so that the total current and the discharge voltage can be related.

Consider a simple case in which the shape of magnetic field strength and ion density is assumed to follow $\sim \exp\{-[(x - L_{exit})/\Delta L]^2\}$, where $L_{exit} = 0.025$ m and $\Delta L = 0.0125$ m. In calculating the condition number, $B_{max} = 0.018$ T and $n_{i,max} = 10^{18}$ m$^{-3}$ are used. In addition, the momentum transfer collision frequency is assumed to be constant at $\nu_m = 10^7$ s$^{-1}$. The transverse electron mobility is given by

$$\mu_\perp = \frac{e}{m_e \nu_m}\left[1 + \left(\frac{\omega_B}{\nu_m}\right)^2\right]^{-1},$$

where $\omega_B = eB/m_e$ is the gyrofrequency. Figure 7.7(a) shows the input conditions to calculate the condition number of the matrix in Eq. (7.11). It can be seen that the electron mobility can be very small for $\omega_B \gg \nu_m$, which occurs in the regions where the magnetic field strength is at maximum. On the other hand, the electron mobility near the anode can become orders of magnitude larger than that near the channel exit.

It can be seen from Fig. 7.7(b) that the condition number is over 10,000, which is very

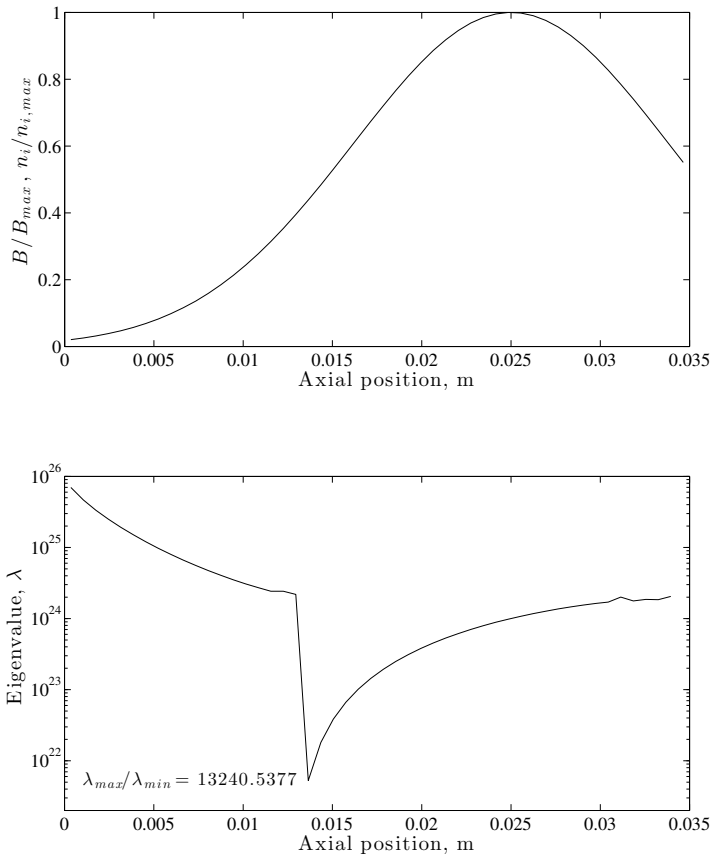


Figure 7.7: Example of a 1D axial case. (Top) Prescribed magnetic field and assumed ion density. $B_{max} = 0.018$ T and $n_{i,max} = 10^{18}$ m$^{-3}$ are assumed. (Bottom) Eigenvalues estimated using the MATLAB EIG function assuming Dirichlet Boundary conditions for potential. The Condition number is 13,240.

large for a matrix. This means that a small perturbation around the maximum eigenvalue, *e.g.* $10^{-4}$, can result in a larger perturbation, *e.g.* $\sim O(1)$ around the minimum eigenvalue. The condition number is calculated using the EIG function in MATLAB. The result suggests that Eq. (7.11) cannot be converged to obtain a solution. The coefficients of matrix **A** are orders of magnitude smaller near the channel exit than those near the anode. Therefore, a small change (error) of the potential near the anode can lead to a large change of the potential calculation near the channel exit.[6]

[6]With added collision frequency near the anode, the matrix **A** in Eq. (7.11) becomes more well-conditioned so that the elliptic PDE can be solved. Hall2De[27, 68, 137] uses an anomalous electron frequency near the anode and solves the 2D electron momentum equation in the $r - z$ directions.

The inability to find numerical convergence can also be explained from a physical perspective. If $n\mu_\perp$ is large, the electron axial velocity $|U_e|$ can be large even with a small electric field. Then, the expression for the electron flux is no longer valid because the $U_e$ can have a strong axial spatial gradient: $\partial U_e/\partial x \neq 0$. The assumption that the left hand side of the momentum equation can be neglected becomes incorrect. Adding the inertia term can also be beneficial from the numerical perspective because the inertial term can essentially serve as an additional collision frequency. However, evaluation of the inertial term is truly nonlinear and is difficult without including the time derivative term.[7]

**Integration Method**

Instead of solving the second-order elliptic PDE, an integration technique, explained in Chapter IV, can be useful for solving the system. As there are no issues related to condition numbers, the electron momentum equation can be solved with any values of coefficients in Eq. (7.11). In particular, the quasi-1D approximation in the state-of-the-art computational methods, such as in HPHall and other 2D models, essentially use a similar integration technique. Equation (7.10) can be integrated once over the axial direction to obtain

$$J_{ix} + J_{ex} = J_d,$$

where $J_d$ is the total current or the sum of ion and electron currents at the anode. Another integration yields

$$V_D = J_d \int \frac{1}{n\mu_\perp} dx - \int \frac{J_{ix}}{n\mu_\perp} dx,$$

which is identical to Eq. (4.7).

### 7.4.3 2D Charge Conservation Equation

The charge conservation equation can be given by

$$\frac{\partial \sigma}{\partial t} + \nabla \cdot \mathbf{J} = 0. \tag{7.13}$$

[7]This suggests that a time-varying magnetohydrodynamic (MHD) type simulation where a quasineutral assumption is not used is required to accurately model the electron dynamics. This will be further discussed in the future work section in Chapter VIII .

where $\sigma = n_i - n_e$ is the charge and $\mathbf{J} = \mathbf{J}_i - \mathbf{J}_e$ is the total flux. This can be derived from ion and electron mass conservation equations under the assumption that the right hand side is identical, which is only valid when single-charged ions are considered.

**Model Proposed by Lam *et al.*[76]**

In a 2D system, using only the quasi-neutral assumption for Eq. (7.13) yields

$$\frac{\partial}{\partial x}(J_{ix} - J_{ex}) + \frac{\partial}{\partial y}(J_{iy} - J_{ey}) = 0. \tag{7.14}$$

It can be seen that any small error, either numerical or physical, of $\partial J_{ey}/\partial y$ can act as a source term for the other three terms due to $J_{ey} \gg J_{ex} \sim J_{ix} > J_{iy}$. This makes the 2D matrix very ill-conditioned, for the same reason as Fig. 7.7.

In addition, in Lam's model, the electron momentum equation in the azimuthal direction is explicitly used without assuming an ambipolar type diffusion instead of Eq. (7.6). Therefore, $E_y$ is added in to Eq. (7.14) and a 2D elliptic PDE is solved.[8]

**New Model**

Assuming $J_{ix} \ll J_{iy}$, the ion flux component in the $y$ direction can be neglected. Another assumption is $\partial J_{ey}/\partial y \approx 0$ from Eq. (7.9). Thus, Eq. (7.14) reduces to

$$\frac{\partial}{\partial x}[J_{ix}(x,y) - J_{ex}(x,y)] = 0. \tag{7.15}$$

One-step integration over the $x$ direction gives

$$J_{ix}(x,y) - J_{ex}(x,y) = J_d(y)$$

Therefore, Eq. (7.15) can be solved for each $y$ coordinate using an integration technique. The anode current, $J_d$, is calculated as a function of $y$ and the total anode current can be

[8]This model was first implemented in the 2D hybrid-DK simulation but the electron continuum model, namely the electron momentum component, had difficulty achieving convergence for the elliptic PDE. This is the reason why an integration type method is used for the hybrid framework in this dissertation.

calculated as

$$J_{tot} = \int J_d(y)dy. \tag{7.16}$$

### 7.4.4 Electron Energy

The electron energy equation is given by

$$\frac{\partial}{\partial t}(n\varepsilon) + \nabla \cdot [(n\varepsilon + p)\mathbf{u}_e] = \nabla \cdot (\kappa_e \nabla T_e) - en\mathbf{u}_e \cdot \mathbf{E} - S_i - S_w, \tag{7.17}$$

where $\kappa_e$ is the heat conductivity, $S_i$ is the electron energy transfer due to inelastic collisions, including electron-impact ionization, stepwise ionization, and excitation, and $S_w$ is the wall collision term, given by

$$\kappa_e = 2.4 \cdot nT_{eV}k_B\frac{\mu}{1+\Omega^2}$$

$$S_i = \sum_j n\nu_j\Delta\epsilon_j$$

$$S_w = n\nu_w\Delta\epsilon_w.$$

Note that elastic collision transfer is assumed to be negligible. The total energy is given as the sum of the electron thermal energy, *i.e.* the electron temperature, and the kinetic energy

$$\varepsilon = \frac{3}{2}T_{eV} + K_{eV},$$

where $K_{eV}$ is the kinetic energy. Here, one approximation is employed. The electron pressure gradient and the electric field in the azimuthal direction are neglected in the momentum equation. As the electron velocity in the azimuthal direction is much larger than that in the axial direction, even a small electric field in the azimuthal direction can lead to a significant heat source.[9] Therefore,

$$\frac{\partial}{\partial t}(n\varepsilon) + \nabla \cdot (n\varepsilon\mathbf{u}_e) + \frac{\partial pu_{ex}}{\partial x} = \nabla \cdot \left(\kappa_e \nabla \frac{2}{3}\varepsilon\right) - enu_{ex}E_x - S_i - S_w \tag{7.18}$$

[9]Physically speaking, Joule heating may not be applicable in the azimuthal direction due to its large Knudsen number.

is solved. Note that the thermal conductivity term is assumed to follow the effective electron temperature including the effect of kinetic energy instead of the actual electron temperature. The right hand side is explicitly obtained using the variables at the current time step. In the present model, the conductive flux and the convective heat flux are assumed to be implicit and the other terms are explicit in time. In addition, the convective heat flux employs first-order upwind discretization.

Assuming $\partial n/\partial t = 0$, Eq. (7.18) can be written as

$$\frac{\partial \varepsilon}{\partial t} = F(\varepsilon) + G(\varepsilon),$$

where $F(\varepsilon)$ is the operator that uses a time-implicit method and $G(\varepsilon)$ is solved in a time-explicit manner. Specifically,

$$F(\varepsilon) = \frac{1}{n}\left[-\nabla \cdot (n\varepsilon \mathbf{u}_e) + \nabla \cdot \left(\kappa_e \nabla \frac{2}{3}\varepsilon\right)\right],$$

$$G(\varepsilon) = \frac{1}{n}\left[-\frac{\partial p u_{ex}}{\partial x} - enu_{ex}E_x - S_i(\varepsilon) - S_w\right],$$

where the inelastic energy loss term is a function of $\varepsilon$ but is chosen to be frozen in time. The 2nd-order Crank-Nicolson's method can be written as,

$$\frac{\varepsilon^{n+1} - \varepsilon^n}{\Delta t} = \frac{1}{2}\left[F(\varepsilon^n) + F(\varepsilon^{n+1})\right] + G(\varepsilon^n).$$

Then, an equation with a matrix can be constructed, given by

$$\left(1 - \frac{\Delta t}{2}\mathbf{F}\right)\vec{\varepsilon}^{n+1} = \vec{b}(\varepsilon^n),$$

where the matrix $\mathbf{F}$ contains the coefficients of $F(\varepsilon^{n+1})$. The left hand side of the equation consists of a matrix and the vector solution for the electron energy whereas the right hand side is a vector.

In the 2D simulation, hypre, a linear algebra library developed at LLNL, is used to solve for the system of equations. The Generalized Minimal Residual (GMRES) method

with a multigrid preconditioner is used for convergence. Tolerance is set to $10^{-14}$ and the maximum number of iteration is 50. However, convergence for the time-implicit electron energy equation usually only takes less than 5 iterations.[10] Thus, the computational cost for the linear algebra subroutine for the electron continuum model is much smaller than the ion kinetic module. Note that in a 1D setup, a tridiagonal matrix solver can be used.[11]

### 7.4.5 Summary of 2D Electron Continuum Model

The equations to be solved are

$$u_{ex} = -\mu \frac{1}{1+\Omega^2}\left[E_x + \frac{1}{n}\frac{\partial n T_{eV}}{\partial x}\right]$$

$$u_{ey} = \mu \frac{\Omega}{1+\Omega^2}\left[E_x + \frac{1}{n}\frac{\partial n T_{eV}}{\partial x}\right]$$

$$J_d(y) = \left(\int \frac{1}{n\mu_\perp} dx\right)^{-1}\left[V_D + \int \frac{J_{ix}}{n\mu_\perp} dx\right],$$

$$\frac{\partial}{\partial t}(n\varepsilon) + \nabla\cdot(n\varepsilon \mathbf{u}_e) + \frac{\partial p u_{ex}}{\partial x} = \nabla\cdot\left(\kappa_e \nabla \frac{2}{3}\varepsilon\right) - e n u_{ex} E_x - S_i - S_w$$

with

$$\Omega = \frac{\omega_b}{\nu_m} = \frac{1}{\nu_m}\frac{eB}{m}$$

$$\nu_m = \nu_{en} + \nu_{ei} + \nu_w + \nu_B$$

$$\mu = \frac{e}{m_e \nu_w}$$

The plasma density and ion fluxes are calculated from the ion kinetic solver. The potential is obtained as

$$E_x = \frac{J_D}{n_i \mu_\perp} - \frac{1}{n_i}\frac{\partial (n_i T_{eV})}{\partial x}$$

$$\phi(x,y) = -\int E_x dx$$

[10] Note that numerical convergence of the elliptic PDE for the plasma potential was very severe for the 2D drift-diffusion approximation both in the axial and azimuthal directions.

[11] Before starting the 2D simulation, the 1D hybrid-DK simulation is updated. Mode transition is reproduced again.

$$E_y = -\frac{\partial \phi}{\partial y}$$

In addition, the total anode current is given by

$$J_{tot} = \int J_d(y) dy,$$

which will be plotted against time in order to investigate the discharge current oscillations.

## 7.5 Test Cases

Table 7.2 shows the four test cases performed using the 2D hybrid-DK simulation. The notation G and L denote the global and local oscillation modes for $B = 120$ G and $B = 180$ G, respectively. The effect of ion gyromotion on the discharge plasma oscillation is first investigated by turning on and off the Lorentz force.

Table 7.2: Test cases performed using the 2D hybrid-DK simulation

| | $B = 120$ G<br>Global mode | $B = 180$ G<br>Local mode |
|---|---|---|
| 1D Hybrid-DK | 1D-G | 1D-L |
| With $\mathbf{v} \times \mathbf{B}$ | G-yes | L-yes |
| Without $\mathbf{v} \times \mathbf{B}$ | G-no | L-no |

The 1D hybrid-DK simulations are the baseline cases. As shown in Chapter V, the mode transition of the discharge current is well captured by the axial 1D simulation. It is thus expected that the 2D hybrid-DK simulations will capture the azimuthal transport or oscillations while observing the same mode transition phenomena as the 1D hybrid simulations.

Due to the use of a time-dependent electron energy solver, some updates are made for the hybrid-1D simulation.

- The anomalous electron mobility[12] is evaluated using $\nu_{ea,in} = \omega_B/64$ and $\nu_{ea,out} = \omega_B/16$. Higher anomalous mobility was required to obtain similar mode transition when changing the electron energy equation from a steady-state model used in Chapters IV and V to a time-implicit model in this chapter.

[12]The old model employed $\nu_{ea,in} = \omega_B/160$.

- The discontinuity in the anomalous electron mobility near the channel exit is alleviated by assuming a linear increase from $\nu_{ea,in}$ to $\nu_{ea,out}$
- The region of nonmagnetized electron mobility near the anode is extended. $\mu = (1-\alpha)\mu_{\parallel} + \alpha\mu_{\perp}$ for $x < 0.6L_{ch}$, where $\alpha = x/(0.6L_{ch})$.
- The conductive heat flux at the anode, $q_a$ is included for the boundary condition: $dT_e/dx = -q_a/\kappa_e$, where $q_a = 2T_eJ_e$, $J_e = n\bar{c}_e/4$ is the mass flux, and $\bar{c}_e = (8k_BT_e/\pi m_e)^{1/2}$ is the thermal velocity.

Using these updates in the electron continuum model, the 1D hybrid-DK simulation captures the mode transition of discharge current across various magnetic field strengths. Thus, these conditions are used in the 2D electron continuum model as well.

## 7.6 Mode Transition Results

Here, the mode transition of discharge oscillations is studied comparing the 1D hybrid-DK simulation used in Chapter V and the present 2D hybrid-DK simulation. Similar to Chapter V, the results for two magnetic field strengths $B = 120$ G and $B = 180$ G are compared.

### 7.6.1 1D Hybrid-DK Simulation

The 1D hybrid-DK simulation results serve as the baseline for the 2D hybrid-DK simulations. The main purpose of the 2D simulations is to capture the mode transition and investigate azimuthally rotating structures.

Figure 7.8 shows the mode transition results obtained from the 1D hybrid-DK simulation. It can be seen that the discharge current oscillations are strong for $B = 120$ G and stabilized for $B = 180$ G. The mean discharge current is about 20 % larger than experimental data of the SPT-100 thruster, which is due to the anomalous electron mobility terms used in the simulations. Although the time-averaged numerical results differ from the experiments, the mode transition is well captured by the 1D hybrid-DK simulation.

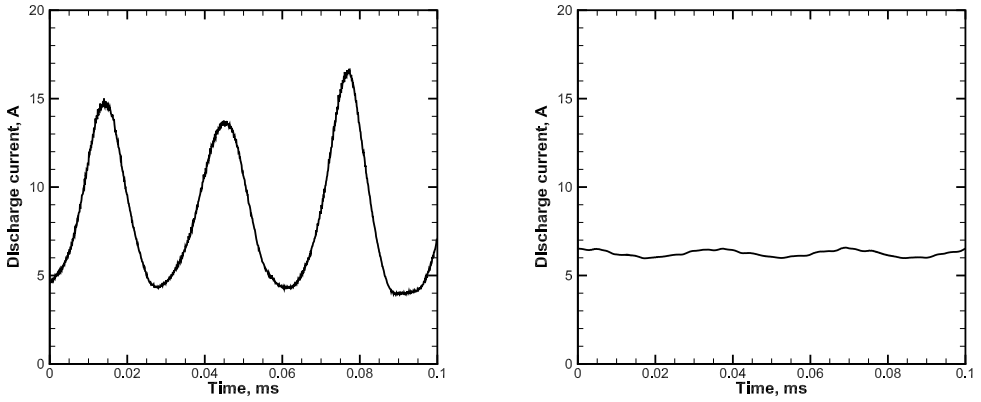


(a) Case 1D-G, $B = 120$ G (b) Case 1D-L, $B = 180$ G

Figure 7.8: Discharge oscillations obtained from the 1D hybrid-DK simulation. Note that y-axis is from $I_d = 0 - 20$ A.

### 7.6.2 Results Including Ion Magnetization

Figure 7.9 shows the discharge current oscillations obtained from the 2D hybrid-DK simulation with ion magnetization included. The differences between the present 2D simulation and the previous 1D simulation are ion 2D transport in physical space and velocity space, including the electric field and Lorentz force, the 2D electric field structure, and the azimuthal heat flux in the electron energy equation.

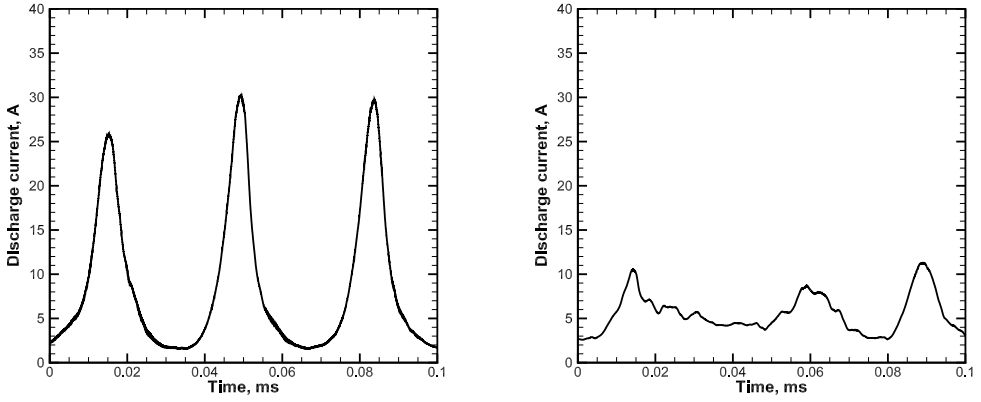


(a) Case G-yes, $B = 120$ G (b) Case L-yes, $B = 180$ G

Figure 7.9: Discharge oscillations obtained from the 2D hybrid-DK simulation with Lorentz force. Note that y-axis is from $I_d = 0 - 40$ A.

In comparison to the 1D hybrid-DK simulation, the discharge oscillations are slightly larger in the 2D hybrid-DK simulation. For instance, the maximum and minimum currents obtained from the 1D cases are 17 A and 4 A, whereas those from the 2D cases are 30A and 2 A, respectively, at $B = 120$ G. A similar trend is observed at $B = 180$ G. However, the results for $B = 180$ G exhibit stabilization of the discharge current compared to the results for $B = 120$ G while some high-order oscillatory modes are present. Thus, it can be concluded that mode transition of discharge oscillations are captured with the 2D hybrid-DK simulation. The plasma oscillations are discussed in more detail in the next section.

### 7.6.3 Results Without Ion Magnetization

Figure 7.10 shows the discharge current oscillations when only the ion Lorentz force is turned off in the 2D hybrid-DK simulation. One notable observation is that the discharge current oscillations are stronger at both magnetic field strengths compared to Fig. 7.9. The results strongly suggest that ion magnetization plays some role in the discharge and plasma oscillations in the axial and azimuthal directions in HETs.

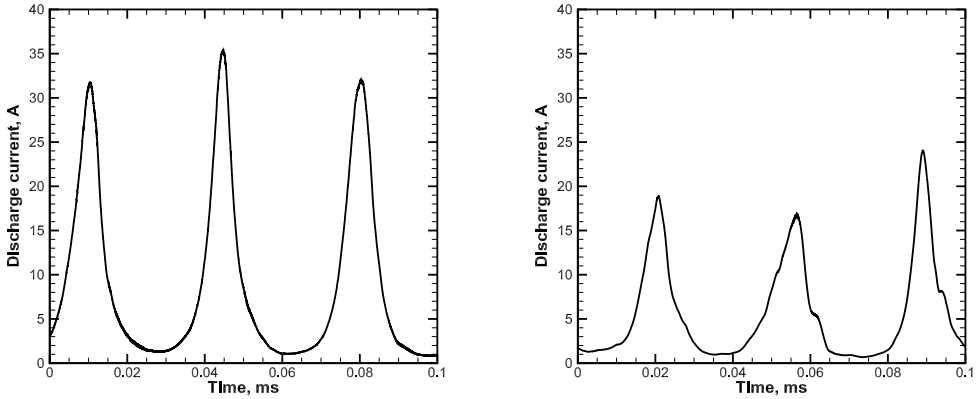


(a) Case G-no, $B = 120$ G

(b) Case L-no, $B = 180$ G

Figure 7.10: Discharge oscillations obtained from the 2D hybrid-DK simulation without Lorentz force. Note that y-axis is from $I_d = 0 - 40$ A.

Note that the discharge oscillations at $B = 180$ G are also observed without the ion Lorentz force when a different number of processors is used. Thus, the possibility of MPI or parallel partitioning producing any oscillations is eliminated. One possibility is that

the Lorentz force, *i.e.* rotation in phase space, serves as a diffusion type effect. Diffusion in phase space may help coupling the plasma transport between the azimuthal and axial directions.

## 7.7 Plasma Oscillations

The low-frequency plasma oscillations are investigated in this section for the global and local oscillation modes at $B = 120$ G and $B = 180$ G. The results shown are the 2D hybrid-DK simulations with ion magnetization on, *i.e.* Cases G-yes and L-yes listed in Table 7.2.

### 7.7.1 Global Oscillation Mode

Discharge current oscillations are due to the ionization oscillations in the Hall thruster discharge channel. Figures 7.11 and 7.12 show the ion number density and ground-state neutral atom density at two different time steps. $t = t_{id,max}$ corresponds to the time at which the discharge current is at maximum while $t = t_{id,min}$ is when the discharge current is at minimum. For instance, $t_{id,min} = 0.03$ ms and $t_{id,max} = 0.047$ ms in Fig. 7.9(a).

An increase in the ion density is associated with depletion of neutral atoms when the discharge current is at maximum. As the ions are accelerated out of the channel and also diffuse to the anode walls, the ion density inside the channel decreases. The ion density is almost an order of magnitude smaller at $t = t_{id,min}$ compared to that at $t = t_{id,max}$. It can be seen that the neutral atoms fill up the ionization region at $t = t_{id,min}$.

Some examples of the ion VDFs are shown in Fig. 7.13 for the global oscillation modes. The three locations chosen are $x = 0$, $x = L_{ch} = 0.025$ m, and $x = L_x = 0.035$ m. These are all at $y = L_y/2 \approx 0.13$ m. It can be seen that the ions near the anode diffuse or accelerate to the anode. At the channel exit, the ions are not fully accelerated. The peak of the VDFs is approximately $14 - 15$ km/s, *i.e.* 150 eV. The small populations due to the ionization inside the channel are resolved in the low $v_x$ components. At the domain exit, the peak of the ion VDFs is observed around $20-21$ km/s, *i.e.* 300 eV, which also agrees with the 1D simulations.

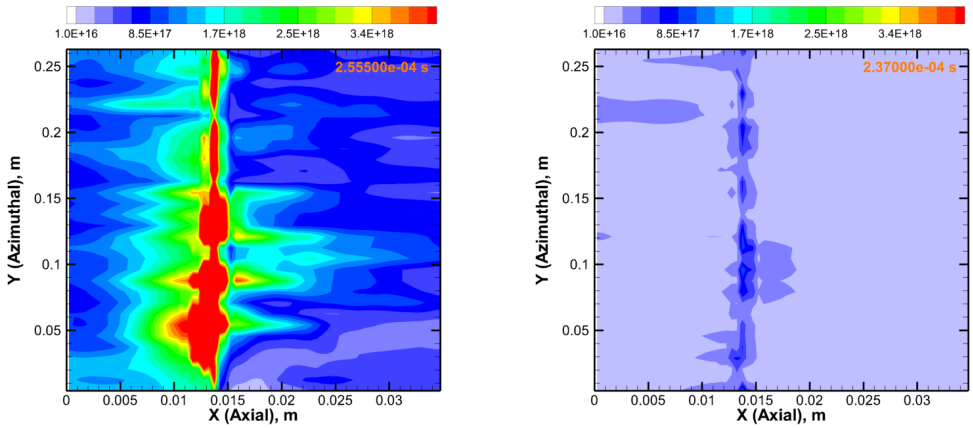


(a) $t = t_{id,max}$ (b) $t = t_{id,min}$

Figure 7.11: Ion number density in global oscillation mode: $B = 120$ G. The units are in $\mathrm{m}^{-3}$.

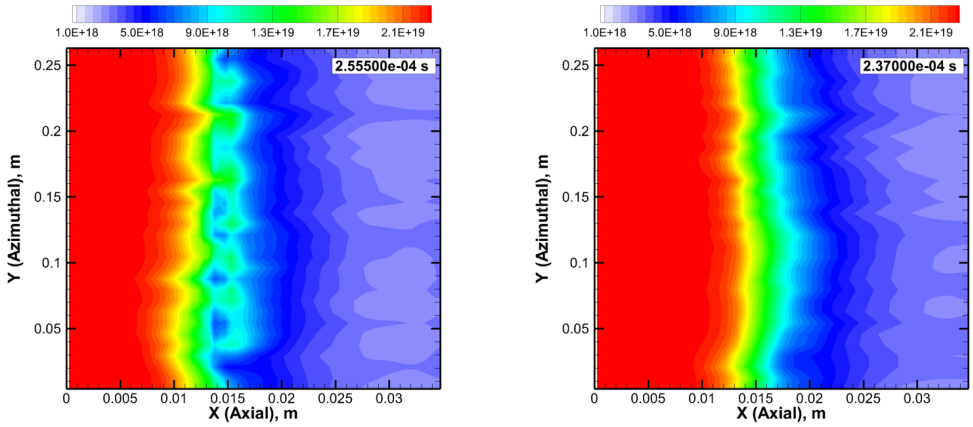


(a) $t = t_{id,max}$ (b) $t = t_{id,min}$

Figure 7.12: Ground-state neutral atom density in global oscillation mode: $B = 120$ G. The units are in $\mathrm{m}^{-3}$.

The ion VDFs shown in Figs. 7.13(e) and 7.13(f) are shifted in the positive-$v_y$ direction. This is due to the local azimuthal electric field, illustrated in Fig. 7.14. The azimuthal electric field is generated due to the difference in the potential, determined by the axial electric field due to the electron continuum model used here. When the discharge current is at maximum, the azimuthal electric field can increase up to $6 - 8$ kV/m. Note that the direction of the azimuthal electric fields at $y = 0.13$ m in Fig. 7.14 is consistent with the

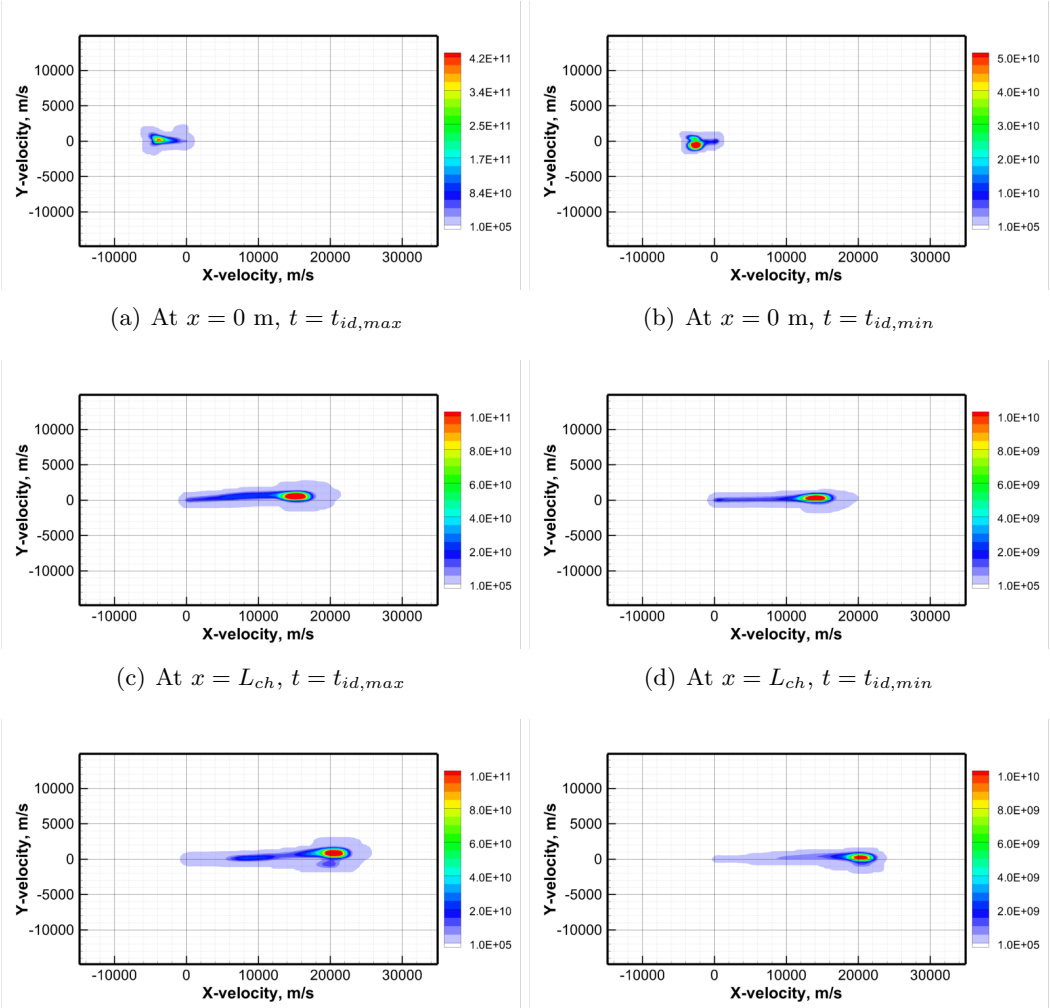


(a) At $x = 0$ m, $t = t_{id,max}$

(b) At $x = 0$ m, $t = t_{id,min}$

(c) At $x = L_{ch}$, $t = t_{id,max}$

(d) At $x = L_{ch}$, $t = t_{id,min}$

(e) At $x = L_x$, $t = t_{id,max}$

(f) At $x = L_x$, $t = t_{id,min}$

Figure 7.13: Examples of ion VDFs at $y = L_y/2$ in global oscillation mode and $B = 120$ G.

velocity shift in the $v_y$ direction in Figs. 7.13.

A 2D PIC simulation by Coche and Garrigues[72] showed that the azimuthal electric field can be as high as 30 kV/m. It was suggested in Ref. 72 that the high-frequency azimuthal instability is due to the resonant coupling of electron Bernstein modes with an ion acoustic wave. From their analysis, the most unstable mode of such instability occurs at $k_y V_{E\times B} = n\omega_B$, where $k_y$ is the wave number, $v_{E\times B}$ is the azimuthal drift velocity, $n$ is an integer, and $\omega_B$ is the electron cyclotron frequency. For instance, $B = 120$ G and $v_{E\times B} = 2 \times 10^6$ m/s yield the most unstable modes at $k_y \approx 1000n$ rad/m. The first mode for this instability occurs at $k_y = 1000$ rad/m, which corresponds to a wavelength of 6 mm.

The grid size in this simulation is $\Delta y = 8.3$ mm, as shown in Table 7.1. Therefore, such instabilities cannot be captured by the present 2D hybrid-DK simulation.

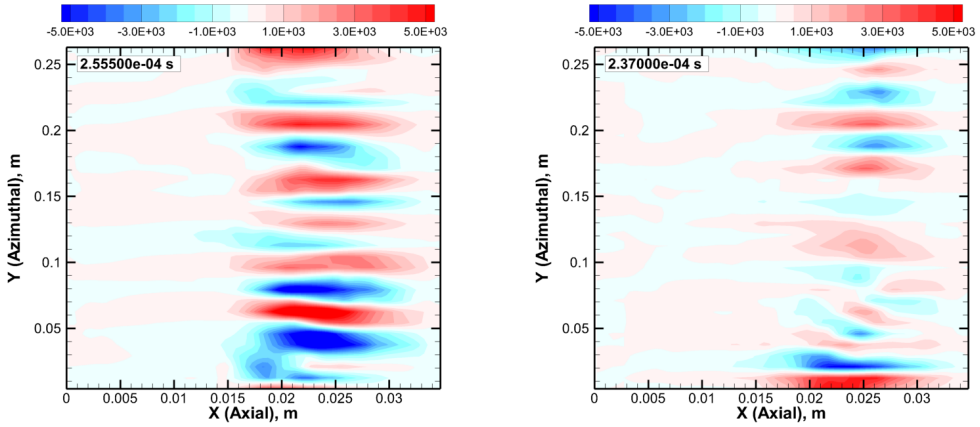


(a) $t = t_{id,max}$ (b) $t = t_{id,min}$

Figure 7.14: Azimuthal electric field in global oscillation mode: $B = 120$ G. The units are in V/m.

The azimuthal electric fields shown in Fig. 7.14 are large-scale phenomena, $m \approx 7$, where $m$ is the spoke order. However, such azimuthal modes are not important in a global ionization mode because the low-frequency plasma oscillations in the axial direction due to heavy species, *i.e.* ion and neutral atoms, dominate in the discharge channel.

Shown in Fig. 7.15 are the axially-integrated ion number densities as a function of the cell numbers in the azimuthal direction, *i.e.* the $y$ direction, at four different time steps. There are some azimuthal structures, particularly at $t = t_{id,max}$, that can also be seen from the 2D contour map in Fig. 7.11(a). However, these azimuthal oscillations may not be important in the global oscillation mode since ionization oscillations occur globally inside the channel and dominate any azimuthal fluctuation. It can also be seen that the number density level at $t = t_{id,min} + \Delta T$ is on the same order with that at $t = t_{id,max} + \Delta T$, where $\Delta T = 0.5(t_{id,max} - t_{id,min})$ is half of the time difference between $t_{id,max}$ and $t_{id,min}$. This agrees with the discharge current oscillation that is almost symmetric in time around $t = t_{id,max}$.

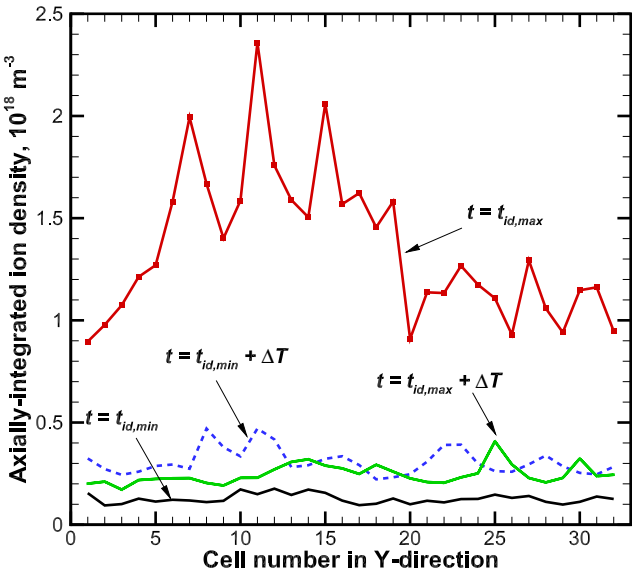


Figure 7.15: Axially-integrated ion number density for each azimuthal location at four different time steps. Note that $\Delta T = 0.5(t_{id,max} - t_{id,min})$ is half of the time difference between $t_{id,max}$ and $t_{id,min}$.

### 7.7.2 Local Oscillation Mode

Figure 7.16 shows the ion number densities at the four time points, namely $t = 0.02$, 0.04, 0.06, 0.08 ms in Fig. 7.9(b). The number density stays mostly unchanged over time with a slight fluctuation, particularly at $t = 0.06$ ms. An increased ion density corresponds to an increase in the discharge current. One notable result is that a low-frequency ionization oscillation in the azimuthal direction cannot be directly observed from these results.

The transition between the global mode and local mode in Ref. 7 was discussed extensively using a so-called spoke surface plot. The spoke surfaces are calculated from the light intensity obtained from images using a FastCam video, pixelating the images and converting them into a contour map. Then, the post-processed plots (see Fig. 7.1 in this dissertation) look like a 2D contour map of the light intensity with horizontal axis being time and vertical axis being the azimuthal locations.

Here, the time evolution of axially-integrated ion density profiles obtained from the 2D hybrid-DK simulation is shown in Fig. 7.17. Although this may not be exactly the same as

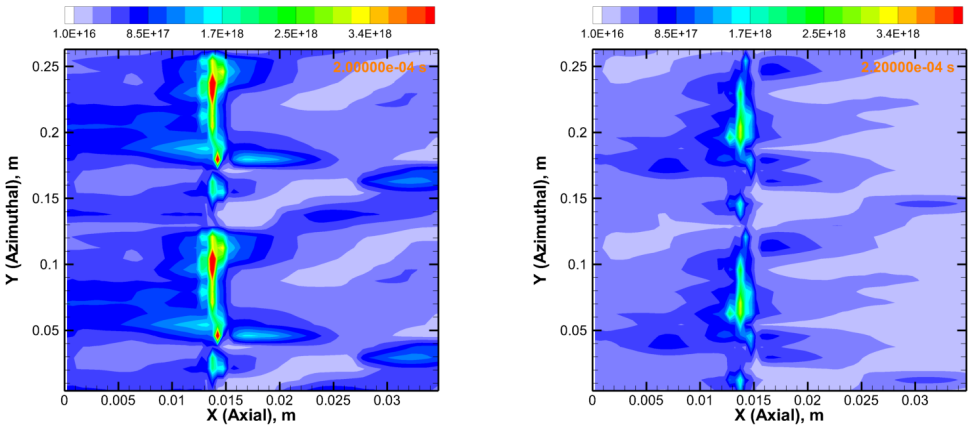


(a) Point 1: $t = 0.02$ ms

(b) Point 2: $t = 0.04$ ms

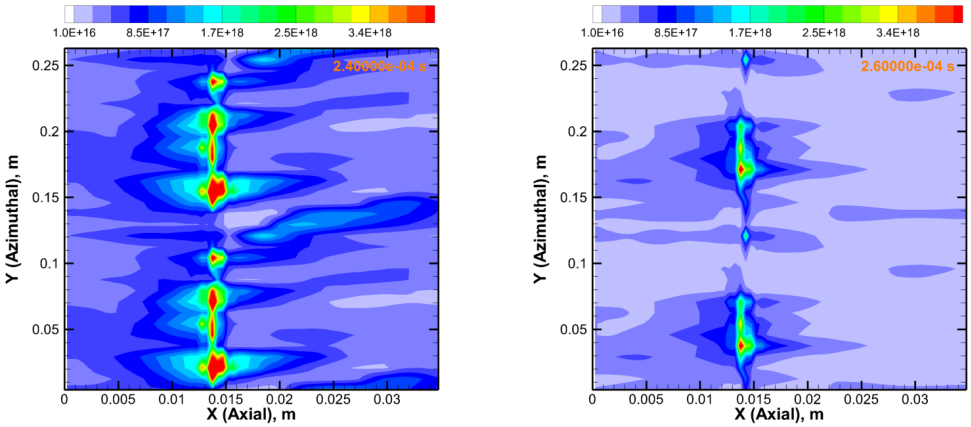


(c) Point 3: $t = 0.06$ ms

(d) Point 4: $t = 0.08$ ms

Figure 7.16: Ion number density in local oscillation mode: $B = 180$ G. The unit is $\mathrm{m}^{-3}$.

the experimental data, it can be assumed that the ion density fluctuations are correlated to the light intensity, which is discussed in Ref. 2.

It can be seen from Fig. 7.17 that the axial ionization oscillations are reduced in local mode compared to global mode, which agrees with the stabilization of discharge current oscillations. However, no characteristic azimuthal oscillation waves can be observed. One further assumption that can be made is that the axial oscillation needs to be significantly suppressed in order to observe the azimuthal spokes. This also agrees with Sekerak's observations that it was difficult to observe the rotating structures in the presence of a strong global oscillation. It can be considered that a strong axial oscillation mode can hinder the

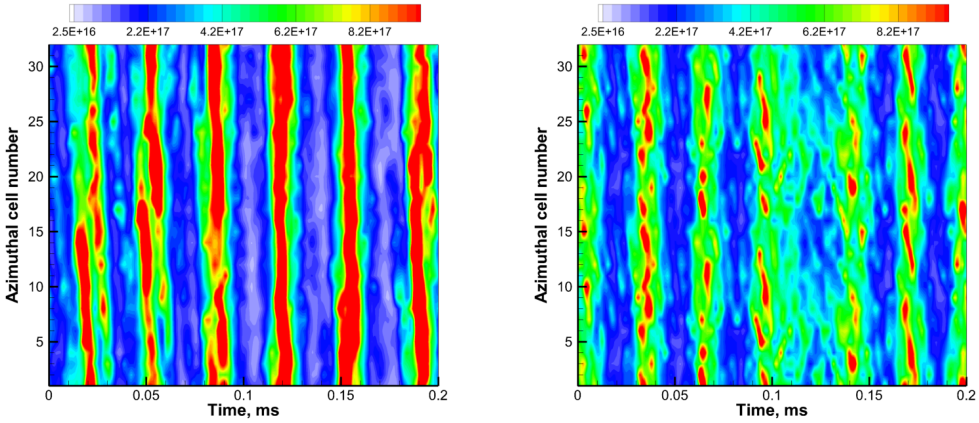


(a) $B = 120$ G (b) $B = 180$ G

Figure 7.17: Surface plot of the axially-integrated ion number density.

azimuthal oscillations.

Therefore, the relative intensity of the ion number densities can be investigated assuming that axial global oscillations are stabilized. The relative intensity of a quantity $Q$ can be defined as

$$\Sigma_Q(J,t) = 2\frac{Q(J,t) - Q_{mid}(t)}{Q_{max(t)} - Q_{min}(t)}, \tag{7.19}$$

where $Q_{max}$, $Q_{min}$, and $Q_{mid}$ are the maximum, minimum, and average of the maximum and minimum of the signal $Q$, and $Q$ is a function of time $t$ and the azimuthal cell number $J$. This essentially transforms $\Sigma_Q$ between -1 to 1, which is similar to the method used to obtain the normalized spoke surface plots in Refs. 138 and 7. An example is shown in Fig. 7.1 here, where the red and blue contours correspond to bright and dim regions, respectively.

Figure 7.18 shows the relative intensity of the axially-integrated ion number density calculated from Eq. (7.19). A dashed line is manually drawn indicating an azimuthally rotating structure. The speed of the rotating structure calculated from the slope is approximately $650-800$ m/s, which is smaller than that of the azimuthal spokes observed in Sekerak's experiments, *i.e.* $1500 - 2200$ m/s. This disagreement is likely due to the geometric difference as the SPT-100 thruster is assumed in the simulation whereas Sekerak's experiment used the H6 thruster.

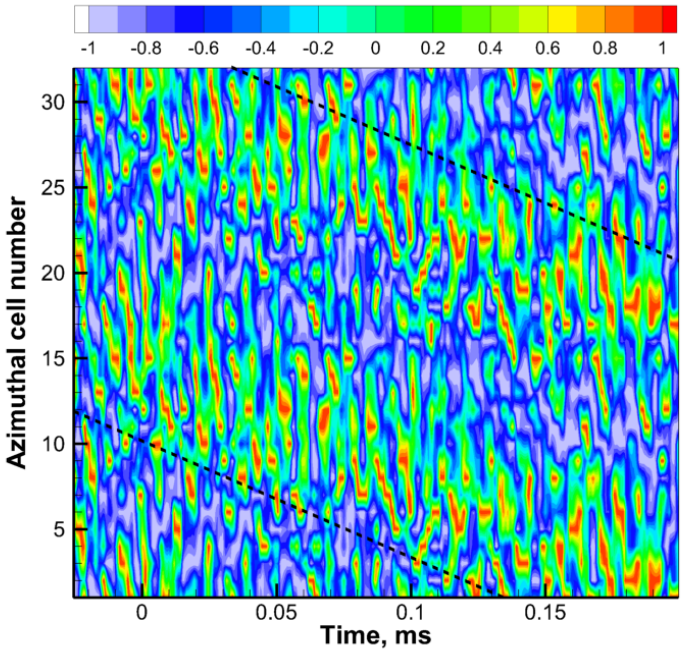


Figure 7.18: Normalized surface plot of local mode obtained from the 2D hybrid-DK simulation. A line is manually drawn that indicates an azimuthal structure.

It can be noted that the direction of the rotation is in the $-E\times B$ drift since $+y$ direction is the direction of the $E \times B$ drift. Experiments on the cylindrical HET by Parker[131] and on the H6 by Sekerak[7] both showed that the azimuthal spokes propagate in the $+E \times B$ direction. However, it may be worth mentioning that there are observations of the rotating structures in the $-E \times B$ direction in another $E \times B$ device.[139]

The rotating spokes can be explained by gradient-drift waves, which occur when spatial gradients exist in plasma properties. The simplest gradient drift wave is the interaction between a density gradient, $\nabla n$, and the magnetic field, $B$. Since a drift wave will be generated in the $\nabla n \times B$ direction, any gradient based drift wave will be in the direction of $E \times B$ if $\nabla n \parallel E_x$. Note that Frias *et al.*[140] showed that the gradient drift instability can occur when the axial electric field is negative for $\nabla(n/B) < 0$. Here in the simulations, it was found that the axial electric field is negative locally in the region where the ion density at maximum and the region of the maximum ion density is inside the channel, *e.g.* $x = 0.015$ m. It has been observed from experiments, for instance, in internal measurements of the

H6 by Reid,[29] that the maximum ion density peak is still inside the channel but much closer to the channel exit. Therefore, it is likely that the direction of the density gradient is the cause of the azimuthal spokes rotating in the opposite direction in the hybrid-DK simulation.

## 7.8 Discussion

The results of the test cases are shown in Table 7.3. It can be seen that the effect of ion Lorentz force on the discharge plasma is not negligible. Although the discharge oscillations are not completely stable, they become much more stabilized in local mode at $B = 180$ G in comparison to $B = 120$ G.

Table 7.3: Results of the 2D hybrid-DK simulation

| | $B = 120$ G<br>Global mode | $B = 180$ G<br>Local mode |
|---|---|---|
| 1D Hybrid-DK | Oscillatory | Very Stable |
| With $\mathbf{v} \times \mathbf{B}$ | Oscillatory | Stable |
| Without $\mathbf{v} \times \mathbf{B}$ | Oscillatory | Oscillatory |

Global oscillation mode and stabilization of the global oscillations are both obtained by the hybrid-DK simulation. The low-frequency azimuthally rotating spokes are captured by taking the relative intensity of the axially-integrated ion number density. It is assumed that global modes are completely stabilized. The propagation of the azimuthal structure is in the $-E \times B$ direction, but this is attributed to the density gradient in the simulations being opposite from experimental observations.

One improvement from the 2D hybrid-PIC simulation by Lam *et al.* is that the simulation never ends due to the numerical instability issue that was reported in Ref. 76. This is due to the use of a simplified electron continuum model, which essentially reduces the 2D system into 1D axial transport. Derivation of the present electron model suggests that a 2D model in the azimuthal direction is numerically difficult as the matrix of the constructed elliptic PDE becomes ill-conditioned, which means that either a different numerical method must be used, such as an integration method, or the physical model must be changed.

Although some low-frequency azimuthally rotating structures are captured by the 2D

hybrid-DK simulation, there are still remaining questions about rotating spokes. Boeuf [141] showed low-frequency rotating spokes in a magnetron discharge using a 2D full-PIC simulation. It was suggested that the rotating spoke is a double layer, *i.e.* sheath, in the azimuthal direction. A strong charge separation occurs at the edge of the spokes. In addition, it was observed that a small region near the inner wall (the cathode in their simulations) carries a large amount of azimuthal electron current where the spoke is absent. Sekerak[7] also hypothesized that spokes are associated with plasma-wall interactions. It was found that spokes occur only when the discharge plasma was exposed to the outer channel wall in some extreme cases. Although the present 2D hybrid-PIC simulation indicates the existence of a low-frequency azimuthal oscillation, the previous observations suggest that a kinetic simulation taking the channel walls into account is required even for a low-frequency large wavelength azimuthal oscillation wave.

# CHAPTER VIII

# Summary

## 8.1 Conclusions

Due to complex operational mechanisms, the discharge plasma in a HET is known to be in a nonequilibrium state. Although several numerical methods such as continuum and particle methods have been developed in order to model the detailed physics of such a plasma, a high-fidelity kinetic simulation that captures the small-scale phenomena and the nonequilibrium effects is needed. In the dissertation, a grid-based direct kinetic (DK) simulation, in which kinetic equations are directly solved on discretized phase space, is developed.

### 8.1.1 Part I: Development of a Grid-based DK Solver

First, verification test problems, including the plasma-sheath and nonlinear plasma waves, are presented. Good agreement between the numerical results obtained from the collisionless DK (Vlasov) solver and theoretical predictions is shown for both cases. In particular, the plasma-sheath in the presence of secondary electron emission is investigated and a virtual cathode due to a space charge limited sheath is observed near the wall. Nonlinear plasma waves including electron plasma waves and ion acoustic waves are studied in a one-wavelength long system and compared with a theoretical nonlinear dispersion relation due to particle trapping. Furthermore, a novel trapped particle instability is investigated by constructing a solver to generate a BGK solution, developing new diagnostic tools, and reformulating the theory to obtain improved estimates of the growth rates.

Second, the DK simulation is benchmarked against a standard PIC simulation using a hybrid framework in a Hall thruster discharge plasma. A simplified electron continuum model is compared and the two kinetic methods are used for benchmarking purposes. It is shown that ionization events can be captured more accurately, at every time step and in every velocity bin by the DK approach. Statistical noise in the PIC simulation can propagate nonlinearly through the electron continuum model and generate significant plasma oscillations. This is shown in the time-averaged ion energy distribution functions in comparison to experimental data. Both hybrid-DK and hybrid-PIC simulations captured the so-called wave-riding effect, where the ion energy becomes larger than the prescribed discharge voltage. The ionization events in the low-velocity regions also are captured without any numerical noise in the DK simulation as can be seen from the empty velocity bins in the hybrid-PIC simulation. Through this benchmarking study, the difference between the DK and the PIC simulations are better understood, and thus it was decided to use the hybrid-DK simulations to study discharge plasma oscillations in the HETs in detail.

### 8.1.2 Part II: Hybrid-DK Simulations of Ionization Oscillations in Hall Thrusters

Mode transition of the low-frequency discharge and plasma oscillations in HETs is investigated using the hybrid-DK simulation. The motivation of this series of work is based on the experimental effort by Sekerak [7], in which the mode transition in discharge oscillations is observed. Two major improvements from the old hybrid simulation are that the electron continuum model differentiates electron kinetic energy from the thermal energy and that the time evolution of electronically-excited neutral atoms is explicitly taken into account. At smaller magnetic field, the $E \times B$ drift is larger so the wall heat flux is reduced. This yields an imbalance in the electron energy transfer as the Joule heating is large but the wall heat flux is small. Therefore, conductive heat flux is required to balance the energy source and sink. It is found that the electron transport and electron temperature play an important role in the discharge oscillations.

This observation is further supported by the constructed perturbation analysis of ionization oscillations in HETs. The common explanation of discharge current oscillations was an insufficient neutral atom flow. However, the mode transition experiments and numerical

simulations suggest that electron transport triggers or stabilizes the ionization oscillations as the oscillation mode can significantly change when varying the magnetic field strength while keeping the discharge voltage and anode mass flow rate the same. It is observed from the perturbation theory that adding linear perturbation of the electron energy yields an unstable solution, *i.e.* positive growth rate, of the ionization oscillations. The ionization oscillations cannot be excited when the electron energy perturbation is zero or small. The ionization oscillations are also shown using the time-varying analysis where a small perturbation in the electron energy is allowed in the heavy species transport. The significance of the linear perturbation analysis is that the excitation and stabilization of the ionization oscillations, and hence the discharge oscillations, can be discussed in terms of the growth rate of a linear perturbation. Although the nonlinear mode of the instability cannot be obtained, the growth rate suggests how quickly the nonlinear mode can occur.

Finally, a 2D hybrid-DK simulation is constructed to analyze the low-frequency large-scale oscillations in HETs, namely the axial and azimuthal ionization oscillations. As Chapters V and VI discuss the axial ionization oscillations in detail, a 2D model is required to investigate the azimuthal oscillations. The major assumptions in the electron continuum model are that: a continuum formulation is (1) valid in the axial direction, and (2) not valid in the azimuthal direction. It was assumed that the electron momentum is uniform in the azimuthal direction so that the 2D charge conservation equation can be reduced to a quasi-1D formulation. A 2D DK simulation is tested using a neutral atom solver compared with a DSMC solver and an ion solver with prescribed electric field compared with analytical solutions. The ion DK simulation demonstrates that the ion magnetization can be captured since the azimuthal ion mean velocity increases as a function of the magnetic field strength. The 2D hybrid-DK simulation captures the global oscillation mode and stabilization of the global mode. Although low-frequency large-wavelength spokes are not observed clearly, the surface plots obtained from relative intensity show some promising structure in the azimuthal direction. As other studies suggest that a quasineutral assumption cannot be used for azimuthal spokes, development of a fully-kinetic simulation is reserved for future work.

## 8.2 Contributions

The key contributions of the research efforts represented in this thesis include

- development of a grid-based direct kinetic simulation and code verification for basic plasma phenomena including plasma-wall sheath and nonlinear plasma waves;
- construction of a hybrid kinetic-continuum method and benchmarking the grid-based kinetic method against a particle-based method for the discharge plasma of HETs;
- investigation of discharge oscillations in HETs using a hybrid kinetic-continuum method with a novel electron continuum model and a linear perturbation theory of ionization oscillations in HETs; and
- development of a two-dimensional grid-based kinetic simulation and demonstration of the multidimensional hybrid method for HET discharge plasmas.

The research topics are mainly focused to gain understanding of Hall thruster discharge plasmas in this dissertation but several test cases consider other plasma phenomena, including plasma sheaths and nonlinear plasma waves. The capability of the grid-based kinetic simulation is not limited to EP plasmas, but can also be applied to other low and high temperature plasma physics.

## 8.3 Future Work

### 8.3.1 Improving the Kinetic Method

The present kinetic method is second-order accurate in time and space. As shown in the broadening of the ion VDFs through an electric field in both 1D and 2D calculations, the accuracy of the kinetic method needs to be improved. The benefit of higher-order numerical schemes is that a similar error level can be achieved with a small number of grid points compared to a lower-order scheme. Therefore, higher-order schemes may be beneficial in not only obtaining more accurate results but also reducing the computational cost. However, the difficulty of high-order methods is that numerical wiggles, *i.e.* undershoots and overshoots, are often generated, which violates the positivity preserving requirement.

In the dissertation, the DK simulation is used for ions and neutral atoms for the Hall thruster simulations. Ion-ion and neutral-neutral collisions are neglected as the Knudsen number of the ion and neutral atoms flows is relatively large. However, as suggested in Sec. 2.1, an electron DK simulation requires more types of collisions including electron-neutral elastic collisions, inelastic collisions, and possibly Coulomb collisions. Implementation of such collision models is required for a full-DK simulation.

No scalability test has yet been performed for the 2D DK simulation. As speed up may not be ideal, this needs to be investigated. The physical space of the domain is partitioned, but velocity space can also be partitioned among processors for a better speed up. This is required when performing much larger-scale computations using the DK simulation method.

### 8.3.2 Plasma Sheath and Presheath Simulations

A generalized boundary condition for the sheath edge is proposed in Sec. 3.2.3. This is likely to resolve the source sheath problem that has existed for a while.[50] In the dissertation, a circular boundary condition that resembles this novel boundary condition is used. The proposed boundary condition should work for DK simulations as well as PIC methods.

In order to investigate the effects associated with the Bohm condition, *e.g.* it is predicted that classical sheaths collapse under a strong SEE,[23, 51] a simulation that includes presheath and bulk plasma regions is required. Preliminary calculations of a presheath-sheath simulation are performed in Ref. 54. The boundary condition uses a circular type boundary condition at the interface of the bulk plasma and presheath, but an easier condition is to set two walls for the boundary or cut the domain in half so that one boundary is the wall while the other is at the channel center. Plasma-wall interactions can be investigated in detail using a detailed presheath simulation.

### 8.3.3 Chemistry Models of Hall Thruster Discharge Plasma

In the Hall thruster simulations discussed in Chapter V, electron-impact ionization, excitation, stepwise ionization, spontaneous emission from the excited state, and wall diffusion are taken into account. In order to investigate the transport of the electronically excited neutral atoms, only one state is assumed for simplicity.

There are more states and reactions involved in a Xenon plasma. For instance, doubly and triply charged ions as well as the electronically excited state of the ions exist in the system. One major assumption used in the present analysis is that the spontaneous emission from the electronically excited state neutral atom corresponds to the light observed in experiments, but the photon emission from excited Xenon atom is in the frequency range that is not visible to the naked eye. The blue light emitted from the Xenon plasma corresponds to photons with a wavelength of 450-500 nm and there are no persistent lines due to the electronically-excited Xenon neutral atoms in that range. Therefore, the excited states for Xenon ions must also be taken into account.

### 8.3.4 Hall Thruster Performance Study

The hybrid-DK simulation can be used to study the Hall thruster performance with different wall materials, anode mass flow rate, and magnetic field structure and strengths. As shown in Chapter IV, the DK simulation works well for neutral atom flows as well as low VDF regions in the phase space. The background pressure inside the vacuum chamber is known to affect the thruster performance as the number density is at least one order of magnitude smaller than that inside the channel. For instance, the number density can be calculated as $n = p/(k_B T)$ using the ideal gas law. For $1 \times 10^{-5}$ Torr and 300 K, the number density is $n = 3.2 \times 10^{17}$ m$^{-3}$, which is smaller than the number density inside the channel, *e.g.* $\approx 10^{19}$ m$^{-3}$. The effects of background neutral atoms can be investigated using a DK simulation.

### 8.3.5 Ionization Oscillation Theory

The perturbation theory of ionization oscillation shown in Chapter VI can be extended to include more realistic phenomena, including ion diffusion and one-dimensional spatial information. It can be also applied to investigate the azimuthally rotating spokes by taking the azimuthal transport into account. Similar to a kink instability that occurs in tokamak plasmas, the growth rates of the instability depending on the spoke order, $m$, in the azimuthal direction can be investigated. Although ionization oscillations are rarely observed in other devices, the formulation of the perturbation theory can be applied to other related

phenomena.

### 8.3.6 2D Axial-Azimuthal or Radial-Azimuthal Simulation

Sekerak[7] suggested that rotating spokes are related to plasma-wall interactions. Boeuf[132] also showed that a large electron current can pass near the walls in the presence of spokes in magnetron discharges. A radial-azimuthal simulation that accounts for plasma-wall interactions in a cross-field setup is required to investigate such effects. However, in actual HET operation, it can be expected that axial transport cannot be neglected. For instance, the plasma properties averaged over the axial coordinate may not capture the electron transport accurately.

As Boeuf[132, 141] suggested that rotating spokes are moving sheaths, *i.e.* double layers, one-dimensional kinetic simulation in the azimuthal direction can also be useful to simulate such phenomena. Iizuka *et al.*[142] showed that double layer formation is due to the Buneman instability, namely electron-ion two stream instability, as well as the Pierce instability, which traps ions in potential wells, in the presence of a strong current. The ion trapping then leads to the formation of a double layer. As the present DK simulation is useful for investigating instabilities, investigation of instabilities associated with the formation of a double layer can serve as a good test case for the full-kinetic simulation. In addition, a theory proposed by Smolyakov *et al.*[17] investigated a similar phenomenon in a wall bounded system. It was shown that ion acoustic waves can be unstable in the presence of a strong $E \times B$ drift and the cross-field electron transport can be enhanced by such instabilities. These problems can be tested using a full-DK or hybrid-DK simulation.

### 8.3.7 2D Radial-Axial Hybrid-DK Simulation

The community needs a high-fidelity radial-axial simulation that can resolve low-frequency oscillations. The detailed electron transport may be due to the azimuthal components, but it is more important to have a predictive model to obtain the thruster performance accurately for engineering purposes. One of the most used state-of-the-art radial-axial simulations is HPHall, in which a quasi-1D approximation is used for the electron transport and no parallel computing capabilities exist.

It has been understood that the quasi-1D approximation in the electron continuum model cannot capture the electron transport accurately. For instance, see Refs. 68 and 125. A 2D electron continuum model coupled with either a continuum, PIC, or DK simulation for ions is therefore required.

### 8.3.8 Multidimensional Time-Varying MHD solver

As discussed in Sec. 7.4.2, a drift-diffusion approximation, which gives a *linear* relation between the electron momentum and the electric field, is used extensively for low temperature plasmas. This can be coupled with the charge conservation equation to obtain an elliptic PDE for the plasma potential, by using a quasineutral assumption. The only variable that can be adjusted is the collision frequency, which is exactly why additional anomalous collision frequencies are required.[137] In the dissertation, it is briefly mentioned that the PDE obtained from the electron continuum model can be ill-conditioned. It is mathematically impossible to solve an ill-conditioned matrix, which suggests that the physical model is incorrect. One example is the electron axial velocity near the anode. The strong inertia effect cannot be included using the quasineutral assumption and drift-diffusion approximation because the inertia term is a *nonlinear* term. The only option to include the nonlinear effects of electron transport is to develop a time-varying electron continuum model.

Although this is not a kinetic method and equilibrium assumptions still need to be used, a time-varying magnetohydrodynamic (MHD) type solver will be useful to investigate macroscopic turbulence type effects that may exist in Hall thrusters. The time-varying MHD solver must be tested with other problems where the drift-diffusion approximation is valid. After benchmarking or validation test cases are performed, the Hall thruster discharge plasma can be investigated in small temporal and spatial scales.

# APPENDICES

# APPENDIX A

# Derivation of Conservation Equations from the Boltzmann Equation

## Moments of the Vlasov equation

The Vlasov equation is given by

$$\frac{\partial f}{\partial t} + \mathbf{v} \cdot \frac{\partial f}{\partial \mathbf{x}} + \frac{q}{m}(\mathbf{E} + \mathbf{v} \times \mathbf{B}) \cdot \frac{\partial f}{\partial \mathbf{v}} = 0. \tag{A.1}$$

Conservation of mass, momentum, and energy can be analyzed by taking moments of Eq. (A.2). Specifically, the moment of a VDF is given by

$$\langle Q(\mathbf{x}) \rangle = \int_{-\infty}^{\infty} Q(\mathbf{x}) f(\mathbf{x}, \mathbf{v}) d\mathbf{v}, \tag{A.2}$$

for an arbitrary function $Q$.

For the zeroth moment equation, $n = \int f d\mathbf{v}$ and $n\mathbf{u} = \int \mathbf{v} f d\mathbf{v}$. Note that $\int (\partial f / \partial \mathbf{v}) d\mathbf{v} = [f]_{-\infty}^{\infty} = 0$.

For the first moment equation, consider $\mathbf{v}$ as a sum of the mean velocity $\mathbf{u}$ and the thermal (random) velocity $\mathbf{v}'$. The first moment involves directionality, so assume $\mathbf{v} = (v_1, v_2, v_3)$. The spatial convective term becomes $\int m v_i \mathbf{v} f(\mathbf{v}) d\mathbf{v} = m \int v_i (\mathbf{u} + \mathbf{v}') f(\mathbf{v}) d\mathbf{v} = \sum_{j=1}^{3} mnu_i u_j + p$, where $p = \int m v_i' \mathbf{v}' f(\mathbf{v}) d\mathbf{v} = \int m (v_i')^2 f(v_i) dv_i$ is the pressure[1]. The last

[1]Pressure is a macroscopic force due to the thermal spread of the particles.

term in Eq. (A.2) can be written as $\int \vec{Q}\mathbf{v}(\partial f/\partial \mathbf{v})d\mathbf{v} = \int \vec{Q} f d\mathbf{v} = n\vec{Q}$.

For the second moment equation, $\int m|\mathbf{v}|^2 f(\mathbf{v})d\mathbf{v} = mn|\mathbf{u}|^2 + 3p$ because $\int m|\mathbf{v}'|^2 f(\mathbf{v})d\mathbf{v} = \sum_{i=1}^{3} \int m(v_i')^2 f(v_i)dv_i = 3p$ when the isotropic condition is satisfied. $\int |\mathbf{v}|^2 \mathbf{v} f(\mathbf{v})d\mathbf{v}$ contains convective, compression, and conductive heat fluxes. $(1/2)\int |\mathbf{v}|^2(\partial f/\partial \mathbf{v})d\mathbf{v} = \int \mathbf{v} f d\mathbf{v} = n\mathbf{u}$. Finally, $\mathbf{v} \cdot (\mathbf{v} \times \mathbf{B}) = 0$.

Then, the conservation equations can be written as

$$\frac{\partial n}{\partial t} + \nabla \cdot (n\mathbf{u}) = 0, \tag{A.3}$$

$$\frac{\partial}{\partial t}(mn\mathbf{u}) + \nabla \cdot (mnu_j\mathbf{u} + p) - qn(\mathbf{E} + \mathbf{u} \times \mathbf{B}) = 0, \tag{A.4}$$

$$\frac{\partial}{\partial t}\left(\frac{1}{2}mn|\mathbf{u}|^2 + \frac{3}{2}p\right) + \nabla \cdot \left[\left(\frac{1}{2}mn|\mathbf{u}|^2 + \frac{3}{2}p\right)\mathbf{u} + p\mathbf{u} + \mathbf{q}\right] - qn\mathbf{u} \cdot \mathbf{E} = 0. \tag{A.5}$$

The $\mathbf{u} \cdot \mathbf{E}$ term in the energy equation is often called Joule heating but is a collisionless heating as opposed to collisional (resistive) heating, which is shown later. The total energy is often written as $\rho e = \rho|\mathbf{u}|^2/2 + (3/2)p$ in the Euler equations, where $\rho = mn$ is the gas density. Note that the Euler equations can be derived by neglecting the electromagnetic forces and the conductive heat flux, $\mathbf{q}$.

First, Eq. (A.4) can be written in terms of the mean velocity instead of the flux as

$$m\mathbf{u}\left[\frac{\partial n}{\partial t} + \nabla \cdot (n\mathbf{u})\right] + mn\frac{\partial \mathbf{u}}{\partial t} + mn\mathbf{u}(\nabla \cdot \mathbf{u}) + \nabla p - qn(\mathbf{E} + \mathbf{u} \times \mathbf{B}) = 0.$$

From Eq. A.3, the momentum equation can be given as the equation for the mean velocity:

$$mn\left(\frac{D\mathbf{u}}{Dt}\right) + \nabla p - qn(\mathbf{E} + \mathbf{u} \times \mathbf{B}) = 0, \tag{A.6}$$

where $D/Dt$ is the total derivative term that consists of the time derivative and spatial inertial term.

Next, the energy conservation equation can be written as

$$\begin{aligned}&\frac{1}{2}m|\mathbf{u}|^2\left[\frac{\partial n}{\partial t}+\nabla\cdot(n\mathbf{u})\right]+\mathbf{u}\cdot\left[mn\left(\frac{\partial}{\partial t}+\mathbf{u}\cdot\nabla\right)\mathbf{u}+\nabla p-qn(\mathbf{E}+\mathbf{u}\times\mathbf{B})\right]\\&+\left[\frac{\partial}{\partial t}\left(\frac{3}{2}p\right)+\nabla\cdot\left(\frac{3}{2}p\mathbf{u}+\mathbf{q}\right)\right]+p\nabla\cdot\mathbf{u}=0.\end{aligned}\tag{A.7}$$

Therefore, the total energy conservation equation can be written in terms of the thermal energy conservation, or temperature, as

$$\left[\frac{\partial}{\partial t}\left(\frac{3}{2}p\right)+\nabla\cdot\left(\frac{3}{2}p\mathbf{u}+\mathbf{q}\right)\right]+p\nabla\cdot\mathbf{u}=0,\tag{A.8}$$

which can be also written as

$$\left[\frac{\partial}{\partial t}\left(\frac{3}{2}p\right)+\nabla\cdot\left(\frac{5}{2}p\mathbf{u}+\mathbf{q}\right)\right]-\mathbf{u}\cdot\nabla p=0.\tag{A.9}$$

### Moments of the Boltzmann equation

Here, the conservation equations including the collision terms are discussed. The equations shown here are the conservation equations for electrons experiencing ionization, momentum exchange, and inelastic collisions. Note that all viscous terms are neglected.

$$\frac{\partial n}{\partial t}+\nabla\cdot(n\mathbf{u})=S,\tag{A.10}$$

$$\frac{\partial}{\partial t}(mn\mathbf{u})+\nabla\cdot(mn|\mathbf{u}|^2+p)-qn(\mathbf{E}+\mathbf{u}\times\mathbf{B})=\mathbf{R},\tag{A.11}$$

$$\frac{\partial}{\partial t}\left(\frac{1}{2}mn|\mathbf{u}|^2+\frac{3}{2}p\right)+\nabla\cdot\left[\left(\frac{1}{2}mn|\mathbf{u}|^2+\frac{3}{2}p\right)\mathbf{u}+p\mathbf{u}+\mathbf{q}\right]-qn\mathbf{u}\cdot\mathbf{E}=S_e-S_i,\tag{A.12}$$

where each term will be explained further.

#### Mass conservation

The source term is given by

$$S=\int\left(\frac{\partial f}{\partial t}\right)_{coll}d\mathbf{v},$$

where $(\partial f/\partial t)_{coll}$ contains the collisions that contribute to a change in the mass density. Some physical processes that should be taken into account include chemical processes, such as inelastic collisions and recombination.

**Momentum conservation**

The right hand side of the momentum conservation equation is due to collisional friction. Fast particles may collide with other slow particles, which may decrease their velocity. The total collisional friction term can be written as

$$\mathbf{R} = \int \mathbf{v} \left(\frac{\partial f}{\partial t}\right)_{coll} d\mathbf{v},$$

where $\mathbf{v} = \mathbf{u} + \mathbf{u}_r$ where $\mathbf{u}$ is the mean velocity and $\mathbf{u}_r$ is the thermal (random) velocity, which is related to the thermal energy (temperature). Then, the total collision friction can be written as

$$\mathbf{R} = \mathbf{u} \int \left(\frac{\partial f}{\partial t}\right)_{coll} d\mathbf{v} + \int \mathbf{u}_r \left(\frac{\partial f}{\partial t}\right)_{coll} d\mathbf{v} = Q\mathbf{u} + \mathbf{M},$$

where $\mathbf{M}$ is the momentum exchange due to thermal particles. Note that decoupling $\mathbf{u}$ and $\mathbf{u}_r$ only works when the mean velocity, *i.e.* directed velocity, is much smaller than the thermal component, *i.e.* random velocity. An additional assumption is that the velocity distribution function is isotropic. Now, instead of Eq. (A.6), the momentum conservation equation becomes

$$mn\left[\frac{\partial \mathbf{u}}{\partial t} + \mathbf{u}(\nabla \cdot \mathbf{u})\right] + \nabla p - qn(\mathbf{E} + \mathbf{u} \times \mathbf{B}) = \mathbf{M} \tag{A.13}$$

where the momentum exchange rate due to electron-neutral collisions is assumed to follow Krook's operator:

$$\mathbf{M} \approx -mn(\mathbf{u} - \mathbf{u}_N)\nu_m \approx -mn\nu_m \mathbf{u}$$

and $\nu_m(T)$ is the momentum exchange collision frequency as a function of temperature, which is from the random velocity components, and $\mathbf{u}_N$ is the velocity of the neutral atoms. For electron-neutral collisions, the neutral atom velocity can be neglected since it is much

smaller than electron velocity. Note that Krook's operator is a first order estimate of the collision term. Higher order corrections can be derived, as shown in Ref. 45.

**Energy conservation**

The total energy equation includes kinetic and thermal energies.

$$\frac{\partial}{\partial t}\left(\frac{1}{2}mn|\mathbf{u}|^2+\frac{3}{2}p\right)+\nabla\cdot\left[\left(\frac{1}{2}mn|\mathbf{u}|^2+\frac{3}{2}p\right)\mathbf{u}+p\mathbf{u}+\mathbf{q}\right]-qn\mathbf{E}\cdot\mathbf{u}=S_e-S_i, \quad \text{(A.14)}$$

where $S_e$ and $S_i$ are the rates of energy transfer due to elastic and inelastic collisions, respectively.

Similarly to Eq. (A.7), the total electron energy can be written in the presence of collisions as

$$\begin{aligned}&\frac{1}{2}m|\mathbf{u}|^2\left[\frac{\partial n}{\partial t}+\nabla\cdot(n\mathbf{u})\right]+\mathbf{u}\cdot\left[mn\left(\frac{\partial}{\partial t}+\mathbf{u}\cdot\nabla\right)\mathbf{u}+\nabla p-qn(\mathbf{E}+\mathbf{u}\times\mathbf{B})\right]\\&+\left[\frac{\partial}{\partial t}\left(\frac{3}{2}p\right)+\nabla\cdot\left(\frac{3}{2}p\mathbf{u}+\mathbf{q}\right)\right]+p\nabla\cdot\mathbf{u}=S_e-S_i.\end{aligned} \quad \text{(A.15)}$$

Then, the continuity equation in Eq. (A.10) and the momentum equation in Eq. (A.13) can be substituted into Eq. (A.15):

$$\left[\frac{\partial}{\partial t}\left(\frac{3}{2}p\right)+\nabla\cdot\left(\frac{5}{2}p\mathbf{u}+\mathbf{q}\right)\right]-\mathbf{u}\cdot\nabla p=S_e-S_i-\mathbf{u}\cdot\mathbf{M}-\frac{1}{2}m|\mathbf{u}|^2Q. \quad \text{(A.16)}$$

The source of the electron temperature is now due to collisional friction $\mathbf{u}\cdot\mathbf{M}$ instead of the Joule heating $\mathbf{u}\cdot\mathbf{E}$ in the total energy equation. It can be seen that there are a couple of terms on the right hand side of Eq. (A.16) added from Eq. (A.9).

Note that the kinetic energy equation can be derived from the momentum equation in Eq. (A.13):

$$n\left[\frac{\partial E_{kin}}{\partial t}+\mathbf{u}\cdot\nabla E_{kin}\right]=-\mathbf{u}\cdot\nabla p+qn\left[\mathbf{u}\cdot\mathbf{E}+\cancel{\mathbf{u}\cdot(\mathbf{u}\times\mathbf{B})}\right]+\mathbf{u}\cdot\mathbf{M}, \quad \text{(A.17)}$$

where $E_{kin}=(1/2)mu^2$ is the kinetic energy. Here, it can be seen that the kinetic energy is determined from the balance between the heating due to the electric field and the pressure

gradient as well as the collisional friction heat source. For a nonmagnetized case where $\mathbf{B} = 0$, the right hand side of Eq. (A.17) is zero. Thus, kinetic energy is unchanged and zero in a nonmagnetized plasma, which means that the total energy can be approximated only using the thermal energy, or the temperature.

# APPENDIX B

## Reduction of Kinetic Description to Hobbs and Wesson's Theory for Secondary Electrons

Here, we prove that the secondary electron VDF in the limit of $T_w \to 0$ reduces to an electron beam, which is assumed in Hobbs and Wesson's theory. In particular, the number density of secondary electrons is written as

$$n_{see} = n_{see0} \exp\left[\frac{-e(\phi - \phi_w)}{kT_w}\right]\left[1 - \mathrm{erf}\sqrt{\frac{e(\phi - \phi_w)}{kT_w}}\right], \tag{B.1}$$

in Eq. (3.16) for a half-Maxwellian with temperature $T_w$, where

$$n_{see0} = \sigma\frac{n_{0e}}{2}\exp\left(\frac{e\phi_w}{kT_e}\right)\sqrt{\tau}, \tag{B.2}$$

which is identical to Eq. (3.18). In the limit of $T_w \to 0$, or $\tau = T_e/T_w \to \infty$, Eq. (B.1) must be consistent with the number density assuming a cold electron beam. The limit for

the following function can be given, using L'Hospital's rule, as

$$\begin{aligned}
&\lim_{X\to\infty} X\exp(X^2)\left[1-\mathrm{erf}(X)\right] \\
&= \lim_{X\to\infty} \frac{X\left[1-\mathrm{erf}(X)\right]}{\exp(-X^2)} \\
&= \lim_{X\to\infty} \frac{\left(\left[1-\mathrm{erf}(X)\right] - \frac{2X}{\sqrt{\pi}}\cancel{\exp(-X^2)}\right)}{\cancel{-2X\exp(-X^2)}} \\
&= \frac{1}{\sqrt{\pi}}.
\end{aligned} \tag{B.3}$$

Let us define normalized quantities: $\Phi = e\phi/kT_e$, $\Phi_w = e\phi_w/kT_e$, and $\tau = T_e/T_w$. Eq. (B.1) can be written as

$$n_{see} = \sigma\frac{n_{0e}}{2}\exp\left(\Phi_w\right)\sqrt{\tau}\exp[-(\Phi-\Phi_w)\tau]\left[1-\mathrm{erf}\sqrt{(\Phi-\Phi_w)\tau}\right]. \tag{B.4}$$

Using $X = (\Phi-\Phi_w)\tau$,

$$n_{see} = \sigma\frac{n_{0e}}{2}\exp\left(\Phi_w\right)\frac{1}{\sqrt{\Phi-\Phi_w}}X\exp(-X^2)\left[1-\mathrm{erf}(X)\right]. \tag{B.5}$$

Finally, in the limit of $\tau\to\infty$, Eq. (B.3) can be used to evaluate Eq. (B.5).

$$\lim_{\tau\to\infty} n_{see} = \sigma\frac{n_{0,e}}{2}\exp(\Phi_w)\left[\pi(\Phi-\Phi_w)\right]^{-1/2}. \tag{B.6}$$

From the current conservation equation: $n_0u_0/(1-\sigma) = n_{0e}(kT_e/2\pi m_e)^{1/2}\exp(e\phi_w/kT_e)$, Eq. (B.6) reduces to the formulation of Hobbs and Wesson in Eq. (3.19)

$$n_{see}^{HW} = \frac{\sigma}{1-\sigma}n_0\left[\frac{m_eu_0^2}{2e(\phi-\phi_w)}\right]^{1/2}. \tag{B.7}$$

## APPENDIX C

# Derivation of Trapped Particle Theory

Consider linear perturbations about a stationary nonlinear wave, namely, a BGK mode that is characterized by $\omega_L$ and $k_L$.[60, 143, 144] Here, a periodic system is considered. Decomposition of the Vlasov and Poisson equations in Fourier series leads to Bloch-type modes, the superposition of Fourier components $\delta E_n$ with frequency $\omega_n = \delta\omega + n\omega_L$ and wavenumber $k_n = \delta k + nk_L$ for integers $n = 0, \pm 1, \pm 2, \ldots$. The corresponding effective eigenvalue problem is given by

$$\sum_{n'} \epsilon_{n,n'}(\delta k, \delta\omega)\delta E_{n'} = 0, \tag{C.1}$$

with the dielectric coupling matrix element, $\epsilon_{n,n'}(\delta k, \delta\omega) = \delta_{n,n'} + \chi_{n,n'}(\delta k, \delta\omega)$, where $\chi_{n,n'}(\delta k, \delta\omega)$ is the susceptibility coupling matrix elements. The susceptibility has contributions from untrapped $\chi^u_{n,n'}$ and trapped particles $\chi^t_{n,n'}$. The untrapped particles are assumed to be highly passing and have contributions only for $n = n'$, *i.e.* $\chi^u_{n,n'} = \chi^u_n \delta_{n,n'}$. The susceptibility of trapped particles can be given as[60, 145] $\chi^t_{n,n'} = q^2 I^t_{n,n'}/(m\epsilon_0\lambda_L)$ with

$$I^t_{n,n'} = \sum_{p=1}^{\infty} \int \frac{2\tau(p\Omega)^2}{\delta\omega_S^2 - (p\Omega)^2} \frac{C_p(k_n\Lambda)}{k_n} \frac{C_p^*(k_{n'}\Lambda)}{k_{n'}} f' dW, \tag{C.2}$$

where $\delta\omega_S = \delta\omega - \delta k v_\phi$ is the frequency in the wave frame, $\Omega$ is the bounce frequency, $\tau = 2\pi/\Omega$ is the bounce period, $\Lambda(W)$ is the amplitude of the trapped particle trajectory in physical space, and $f' = df(W)/dW$ for the unperturbed trapped distribution function

$f(W)$. Approximating the potential wells as harmonic, the coefficients $C_p$ are expressed in terms of Bessel functions $J_p$ of order $p$, $C_p = i^p J_p(k\Lambda)$, and $\cos(\Lambda) = -W/(e\phi)$. Including only the leading order Bessel function $p = 1$, the summation in Eq. (C.2) is removed. For a sufficiently narrow trapped particle distribution, one can approximate $\chi^t_{n,n'}$ by a dyadic form: $\chi^t_{n,n'} \simeq Z_n Z_{n'}$, with $Z_n = (\chi^t_{n,n})^{1/2}$. This relation is exact in the limiting case where $f'$ has zero width, which is the case considered here. From Eq. (C.1),

$$\bar{\epsilon}_n \delta E_n + Z_n \sum_{n'} Z_{n'} \delta E_{n'} = 0, \tag{C.3}$$

where $\bar{\epsilon}_n$ is defined as $\bar{\epsilon}_n = 1 + \chi^u_n$. Multiplying $Z_n/\bar{\epsilon}_n$ and taking the summation over $n$,

$$\left(1 + \sum_n \frac{Z_n^2}{\bar{\epsilon}_n}\right) \sum_{n'} Z_{n'} \delta E_{n'} = 0. \tag{C.4}$$

Finally, one obtains the dispersion relation

$$1 + \sum_n \frac{\chi^t_{n,n}}{\bar{\epsilon}_n} = 0, \tag{C.5}$$

with $\chi^t_{n,n} = Z_n^2$. For the simplest model describing the sideband instability,[143, 144] $\Omega$ is assumed constant in Eq. (C.2) and only $n = \pm 1$ are retained in Eq. (C.5) as the corresponding Fourier components nearly satisfy the dispersion relation of Langmuir waves.

To enable the description of the NMI as well, one must account for the energy dependence of $\Omega = \Omega(W)$, or equivalently the dependence $\Omega = \Omega(J)$ in the action $J$, in the potential wells. We consider a single wavelength system with periodicity, *i.e.* $\delta k = 0$ and thus $k_n = n k_L$. Assuming, as can be verified *a posteriori*, $1/\bar{\epsilon}_n + 1/\bar{\epsilon}_{-n} \approx 2$, the dispersion relation can be written from Eq. (C.5) as $1 + 2\sum_{n>0} \chi^t_{n,n} = 0$. In order to calculate the dispersion relation correctly, it is important to note that $\Lambda$ is a function of $W$, *i.e.* $\Lambda = \Lambda(W)$, so that $\sum_{n>0}[C_{p=1}(k_n\Lambda)/k_n]^2$ is performed before the integration over $W$ in Eq. (C.2). Furthermore, due to the deeply trapped assumption $k_L\Lambda \ll 1$, a good estimate for this sum is given by $(\Lambda/k_L)\int[C_{p=1}(\xi)/\xi]^2 d\xi$, where $\xi = n k_L \Lambda$. The integral is performed from $\xi = 0$ to $\infty$, and one obtains $\int[C_{p=1}(\xi)/\xi]^2 d\xi = 4/(3\pi)$ since $C_p^2 = J_p^2$, where $J_p$ is the

Bessel function. Hence, the dispersion relation can be given as

$$1 + 2M_0\omega_t^2\sqrt{J_0}\int_0^{J_{max}} \frac{\sqrt{J\Omega/\Omega_0}}{\delta\omega_S^2 - \Omega(J)^2}F'(J)dJ = 0, \tag{C.6}$$

where $J = m\Omega\Lambda^2/2$ is the canonical action for deeply trapped particles assuming harmonic oscillation, $F(J) = 2\pi f(J)/(mn_t)$ is the normalized distribution function, $\omega_t = (n_t/n_p)^{1/2}\omega_{pe}$ is the trapped particle frequency, $n_t$ and $n_p$ are the number density of trapped particles and the plasma density, respectively, $M_0 = 16/(3\pi k_L\Lambda_0) \approx 1.70/(k_L\Lambda_0)$, $J_0 = m\Omega_0\Lambda_0^2/2$, $\Omega_0 = \Omega(J = J_0)$, and $\Lambda_0 = \Lambda(J = J_0)$.

Equation (C.6) can be analytically solved when $F(J) = \delta(J - J_0)$.[59, 60] Using integration by parts assuming $F(J) = 0$ at the limits,

$$1 - \frac{(1-\alpha_0)\beta_0}{w} + \frac{4\alpha_0\beta_0}{w^2} = 0, \tag{C.7}$$

where $w = (\delta\omega/\Omega_0)^2 - 1$, $\alpha_0 = \alpha(J = J_0)$, and $\beta_0 = M_0\omega_t^2/\Omega_0^2$ with $\alpha(J) = -J/\Omega(d\Omega/dJ)$. Note that the numerical values of $\Omega$ and $\alpha$ in a sinusoidal wave field with amplitude $\phi_0$ are explicitly shown in Ref. 60:

$$\Omega(W) = \Omega_{deep}\frac{\pi}{2}\frac{1}{K(\mu)} \tag{C.8}$$

$$\alpha(W) = \frac{[E(\mu) + (\mu-1)K(\mu)]^2}{\mu(1-\mu)K^2(\mu)} \tag{C.9}$$

where $\Omega_{deep} = k_L(e\phi_0/m)^{1/2}$ is the deeply trapped bounce frequency, $K(\mu) = \int_0^{\pi/2}(1 - \mu\sin^2\theta)^{-1/2}d\theta$ and $E(\mu) = \int_0^{\pi/2}(1 - \mu\sin^2\theta)^{+1/2}d\theta$ are the complete elliptic integral of the first and second kind, respectively, and $\mu = (W + e\phi_0)/(2e\phi_0)$. Due to the deeply trapped assumption, $\alpha \ll 1$. Therefore, the solution to Eq. (C.7) can be found as $\delta\omega \simeq \pm\Omega_0(1 + \beta_0/4) + i\gamma$, where the growth rate is

$$\gamma = \omega_t\left[M_0\alpha_0\left(1 - \frac{\beta_0}{16\alpha_0}\right)\right]^{1/2} \tag{C.10}$$

when $\alpha_0 > \beta_0/16$. Note that the difference between Eq. (C.10) and the growth rate when including $(1 - \alpha_0)$ term in Eq. (C.7) is negligible for the simulations considered here. If

$\beta_0$ is negligible, $\gamma \simeq \omega_t \left(\alpha_0 M_0\right)^{1/2} = \left(f_t \alpha_0 M_0\right)^{1/2} \omega_{pe}$ from which one can see that the NMI growth rate is primarily dependent on $f_t$, $W_0 = W(J_0)$ via $\alpha_0$, and $M_0$. We have improved calculation of the coefficient $M_0$ compared with Refs. 59 and 60.

# APPENDIX D

## 2D Collisionless Kinetic Simulation Compared to DSMC

Collisionless neutral atom simulations are performed using the present DK simulation and MONACO,[134] an implementation of the direct simulation Monte Carlo (DSMC) developed at the University of Michigan. As MONACO has been used for various neutral atom flows,[146, 147] comparison of the DK simulation with MONACO serves as a good benchmarking test case. For the DK simulation, the 2D kinetic equation can be simply written as

$$\frac{\partial f}{\partial t} + v_x \frac{\partial f}{\partial x} + v_y \frac{\partial f}{\partial y} = 0,$$

without the electromagnetic force. The domain is assumed to be 2D planar.

Diffuse reflection is assumed for the particles that collide with walls. The diffuse reflection means that the VDFs of the particles follow a Maxwellian with the wall temperature after a collision event. The particles that approach the walls will not have any effect from the wall until they collide. Therefore, the boundary conditions for the VDFs on the wall are (1) an outflow boundary condition for $v_{\hat{n}} \geq 0$ and (2) a half-Maxwellian for $v_{\hat{n}} < 0$, where $v_{\hat{n}}$ is the velocity normal to the wall. Another type of reflection is called specular, or mirror reflection, where the direction of the particle velocity normal to the wall is flipped in sign without any change in magnitude of the velocity as well as the tangential velocity parallel to the wall.

The neutral atom flow from a slit at $(X, Y) = (0\ \text{m}, 0.04\text{m})$[1] and diffuse reflection at

[1]Here, the units for the $X$ and $Y$ locations are further dropped.

all walls are assumed. $Y = 0$ is the centerline, so any particles crossing that plane are reflected back. Outlet boundary condition is used at $X = 0.09$ and $Y = 0.08$, *i.e.* particles will leave the domain and no background atoms are introduced. Anode mass flow rate of 5 mg/s is assumed to leave the slit which is 2 mm wide, *i.e.* 2 cells. The cell size in physical space is $\Delta X = \Delta Y = 1$ mm. For the DK simulation, the cell size in velocity space is $\Delta v_X = \Delta v_Y = 30$ m/s for $v_X \in [-1000, 2000]$ m/s and $v_Y \in [-1500, 1500]$ m/s. The time step is $\Delta t = 10^{-7}$ s and the simulation stops at 1 s. For MONACO, a grid size similar to that of the DK simulation is used. The main difference is that a Cartesian mesh is used in the DK simulation but triangular cells are used in MONACO. The number of particles per cell required to obtain good statistics is approximately 20 for MONACO. Streamlines are shown in black solid lines with arrows on top of the number density contours.

Figure D.1 shows that the DK simulation captures the neutral atom flow well, particularly inside the discharge channel where the neutral atom density is large. The most important difference between the two kinetic simulation is that the DK results are obtained from only 1 time step whereas the MONACO results are time-averaged over a number of time steps. Therefore, a true *steady-state* solution can be obtained from the DK simulation without any numerical noise.

However, it can be seen that there is a decrease in the density in the plume near the channel centerline at $Y = 0.04$ in the DK results. This is due to the discrete velocity space. The neutral atoms far from the slit will have a much narrower distribution function in the Y direction. As shown in Fig. D.2(a), the VDFs in the Y direction integrated over the X-velocity, *i.e.* $g(v_X) = \int f(v_X, v_Y) dv_Y$, at $X = 0.04$ and $X = 0.08$ are very narrow and are almost like a dirac delta function. This is because finite Y-velocity components near the slit advect in the Y direction and the only particles that reach the channel centerline are beam-like with a velocity of $v_Y = 0$. For instance, consider a slit that is infinitesimally small at $(X, Y) = (0, 0)$ and a domain without any walls. At a point $(X_0, Y_0)$, the particles that reach that point must satisfy $V_X/V_Y = X_0/Y_0$ for $Y_0 \neq 0$ and $\forall V_X > 0, V_Y = 0$ for $Y_0 = 0$. Note that the number density decreases as the flow expands into a larger domain.

Also shown in Fig. D.2(a) is the VDF at the cell adjacent to the slit. The VDF is fairly close to the theoretical distribution, *i.e.* a full-Maxwellian, because the VDF of the

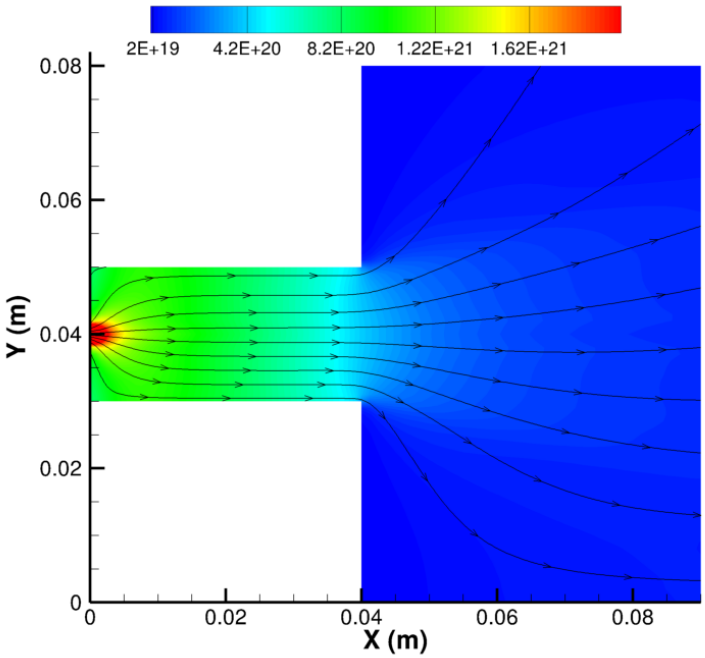


(a) DK solver

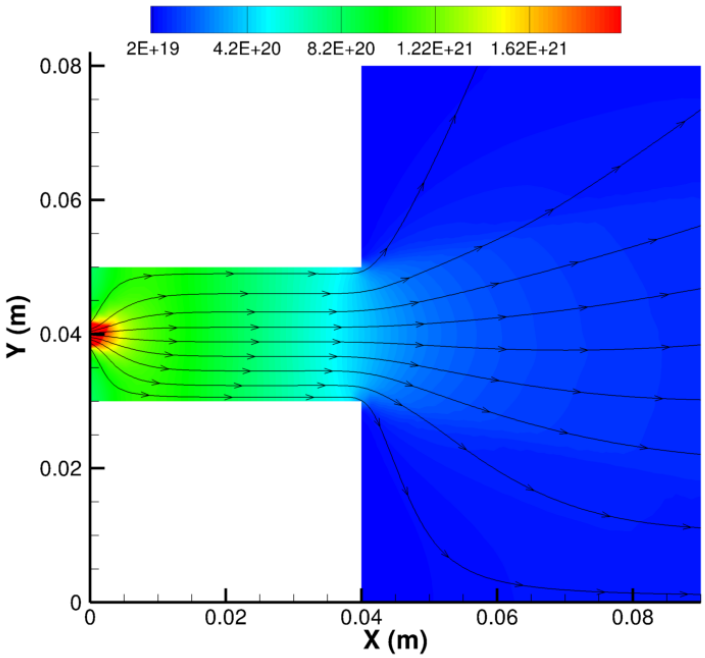


(b) MONACO (DSMC)

Figure D.1: Collisionless neutral atom simulation.

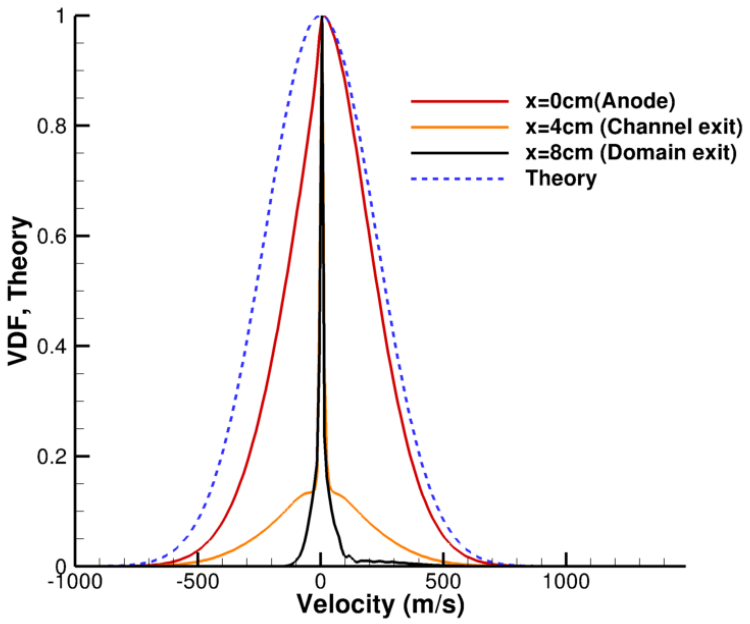


Figure D.2: The VDFs as a function of Y-velocity averaged over X-velocity obtained from the collisionless DK simulation at $(X, Y) = (0.001, 0.04)$, $(0.039, 0.04)$, and $(0.08, 0.04)$ m. Theory curve is a Maxwellian.

Y-velocity is a full-Maxwellian at the slit. The calculated VDF shows a slight deviation from the full-Maxwellian as the VDF is measured at the cell-center of the first cell, not the plane from which particles are injected. The cell-center position of the cell is $(X, Y) = (\Delta X/2, \Delta Y/2 + 0.04)$ not at the plane of the slit. Because the cell is shifted by $\Delta Y/2$ from the centerline of the slit, the positive Y-velocity components agree with the full-Maxwellian better than the negative Y-velocity components. In addition, the VDFs at $X = 0.04$ consist of a beam type distribution, mentioned above, as well as a full-Maxwellian distribution due to the diffuse reflection inside the channel. Any particles that collide with the walls inside the channel will be thermalized to a Maxwellian.

Figure D.3 shows the VDFs as a function of X-velocity averaged over Y-velocity. $h(v_X) = \int f(v_X, v_Y) dv_Y$. At $X = 0$, there are particles with negative velocity, meaning that some particles are approaching the slit from the domain $X > 0$. This is because the diffuse reflection at the wall can yield particles generated downstream that come back to the anode.

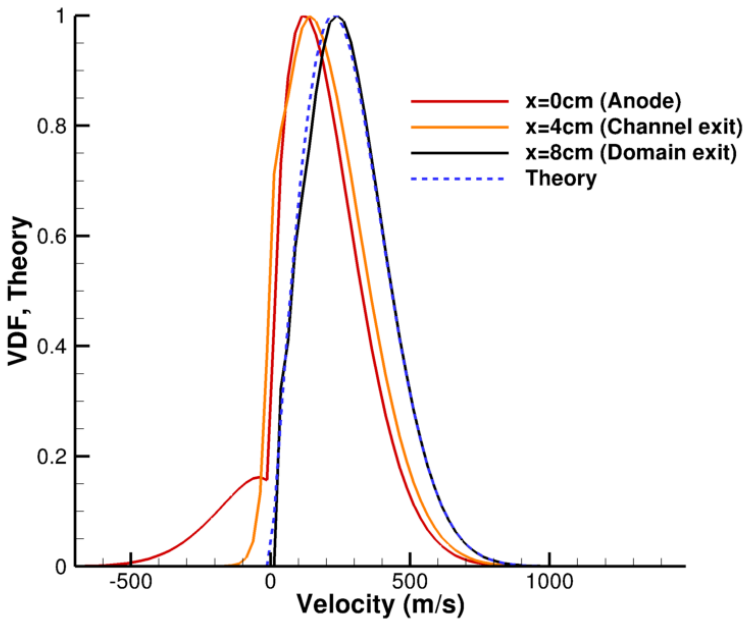


Figure D.3: The VDFs as a function of X-velocity averaged over Y-velocity obtained from the collisionless DK simulation at $(X, Y) = (0.001, 0.04)$, $(0.039, 0.04)$, and $(0.08, 0.04)$ m. Theory curve is a Maxwellian biased with the X-velocity.

The theory curve shown in Fig. D.3 is a Maxwellian biased with the X-velocity: $\sim v_X \exp[-m(v_X^2 + v_Y^2)/(2k_BT)]$. The VDFs obtained from the DK simulation in the down stream, *e.g.* $X = 0.08$, exhibit good agreement with the theory curve since the particles ejected through the slit will have the biased-Maxwellian. Particles with higher velocity will have higher probability of being ejected. In addition, no particles with negative velocity or zero velocity will escape from the slit. The Y-velocity averaged VDFs agree well with the theoretical curve because there are no effects from the walls in the plume. On the other hand, the VDFs inside the channel show a distribution not like the biased-Maxwellian due to the wall effects. The particles that collide with the wall follow a Maxwellian, *i.e.* isotropic in all directions. Therefore, the particles moving in Y direction are likely to have small X-velocity. Thus, the VDFs are shifted more towards a slower velocity inside the channel.

# APPENDIX E

# Axial-Azimuthal Electron Continuum Model

## Electron Momentum Equation

Let us normalize the momentum equation in the axial-azimuthal direction. Consider the electron conservation equations in Eq. (A.13) in the time scale of ions. $\tilde{n} = n/n_0$, $\tilde{U_x} = U_x/U_{x0}$, $\tilde{U_y} = U_y/U_{y0}$, $\tilde{\nabla} = \nabla/(1/L)$, $\tilde{T_e} = T_e/T_{e,0}$, $\tilde{\phi} = \phi/\phi_0$, $\tilde{B} = B/B_0$, and $\tilde{t} = \omega_{pi}t = (e^2 n_0/m_i\epsilon_0)^{1/2}t$. The quantities in different directions shall be considered separately. Here, electrons are considered so $q = -e$. Raizer[46] simply states that the left hand side of the momentum equation can be negligible since the electron mass is much smaller than the ion mass. Here, we try to do a more careful analysis.

1. **Time derivative:**

$$mn_0U_{x0}\omega_{pi}\tilde{n}\frac{\partial\tilde{U_x}}{\partial\tilde{t}} = \left[\left(\frac{U_{x0}}{U_{th}}\right)\left(\frac{\omega_{pi}L_x}{U_{th}}\right)\frac{n_0kT_{e0}}{L_x}\right]\tilde{n}\frac{\partial\tilde{U_x}}{\partial\tilde{t}}$$

$$mn_0U_{y0}\omega_{pi}\tilde{n}\frac{\partial\tilde{U_y}}{\partial\tilde{t}} = \left[\left(\frac{U_{y0}}{U_{th}}\right)\left(\frac{\omega_{pi}L_y}{U_{th}}\right)\frac{n_0kT_{e0}}{L_y}\right]\tilde{n}\frac{\partial\tilde{U_y}}{\partial\tilde{t}}$$

   where $U_{th} = (kT_e/m)^{1/2}$ is the electron thermal velocity.

2. **Inertial terms:**

$$\frac{n_0kT_{e0}}{L_x}\left\{\left[\left(\frac{U_{x0}}{U_{th}}\right)^2\right]\tilde{n}\tilde{U_x}\frac{\partial\tilde{U_x}}{\partial\tilde{x}} + \left[\left(\frac{U_{x0}}{U_{th}}\right)\left(\frac{U_{y0}}{U_{th}}\right)\frac{L_x}{L_y}\right]\tilde{n}\tilde{U_y}\frac{\partial\tilde{U_x}}{\partial\tilde{y}}\right\}$$

$$\frac{n_0 kT_{e0}}{L_y}\left\{\left[\left(\frac{U_{x0}}{U_{th}}\right)\left(\frac{U_{y0}}{U_{th}}\right)\frac{L_y}{L_x}\right]\tilde{n}\tilde{U_x}\frac{\partial\tilde{U_y}}{\partial\tilde{x}}+\left[\left(\frac{U_{y0}}{U_{th}}\right)^2\right]\tilde{n}\tilde{U_y}\frac{\partial\tilde{U_y}}{\partial\tilde{y}}\right\}$$

where $\tilde{x}=x/L_x$ and $\tilde{y}=y/L_y$. $L_x$ and $L_y$ are the characteristic length.

3. **Pressure gradient:**

$$\frac{\partial p}{\partial x}=\frac{n_0 kT_{e0}}{L_x}\frac{\partial\tilde{p}}{\partial\tilde{x}}$$

$$\frac{\partial p}{\partial y}=\frac{n_0 kT_{e0}}{L_y}\frac{\partial\tilde{p}}{\partial\tilde{y}}$$

where $p=nkT_e$.

4. **Electric field:**

$$qnE_x=-\left[\frac{n_0 kT_{e0}}{L_x}\frac{q\phi_0}{kT_{e0}}\right]\tilde{n}\frac{\partial\tilde{\phi}}{\partial\tilde{x}}$$

$$qnE_y=-\left[\frac{n_0 kT_{e0}}{L_y}\frac{q\phi_0}{kT_{e0}}\right]\tilde{n}\frac{\partial\tilde{\phi}}{\partial\tilde{y}}$$

where $E=-\nabla\phi$.

5. **Lorentz force:**

$$qnU_yB_r=\left[\frac{n_0 kT_{e0}}{L_x}\frac{U_{y0}}{U_{th}}\frac{\omega_B L_x}{U_{th}}\right]\tilde{n}\tilde{U_y}\tilde{B_0}$$

$$qnU_xB_r=\left[\frac{n_0 kT_{e0}}{L_y}\frac{U_{x0}}{U_{th}}\frac{\omega_B L_y}{U_{th}}\right]\tilde{n}\tilde{U_x}\tilde{B_0}$$

6. **Collision terms:**

$$-mn\nu_m U_x=-\left[\frac{n_0 kT_{e0}}{L_x}\frac{U_{x0}}{U_{th}}\frac{\nu_{m0}L_x}{U_{th}}\right]\tilde{n}\tilde{\nu_m}\tilde{U_x}$$

$$-mn\nu_m U_y=-\left[\frac{n_0 kT_{e0}}{L_y}\frac{U_{y0}}{U_{th}}\frac{\nu_{m0}L_y}{U_{th}}\right]\tilde{n}\tilde{\nu_m}\tilde{U_y}$$

**Normalized Momentum Equation**

The normalized momentum conservation equation is

$$\left[\frac{U_{x0}}{U_{th}}\frac{\omega_{pi}L_x}{U_{th}}\right]\tilde{n}\frac{\partial\tilde{U}_x}{\partial\tilde{t}}+\left[\left(\frac{U_{x0}}{U_{th}}\right)^2\right]\tilde{n}\tilde{U}_x\frac{\partial\tilde{U}_x}{\partial\tilde{x}}+\left[\frac{U_{x0}}{U_{th}}\frac{U_{y0}}{U_{th}}\frac{L_x}{L_y}\right]\tilde{n}\tilde{U}_y\frac{\partial\tilde{U}_x}{\partial\tilde{y}}$$
$$=-\frac{\partial\tilde{p}}{\partial\tilde{x}}+\left[\frac{e\phi_0}{kT_{e0}}\right]\tilde{n}\frac{\partial\tilde{\phi}}{\partial\tilde{x}}-\left[\frac{U_{y0}}{U_{th}}\frac{\omega_B L_x}{U_{th}}\right]\tilde{n}\tilde{U}_y\tilde{B}_0-\left[\frac{U_{x0}}{U_{th}}\frac{\nu_{m0}L_x}{U_{th}}\right]\tilde{n}\tilde{\nu_m}\tilde{U}_x \qquad \text{(E.1)}$$

$$\left[\frac{U_{y0}}{U_{th}}\frac{\omega_{pi}L_y}{U_{th}}\right]\tilde{n}\frac{\partial\tilde{U}_y}{\partial\tilde{t}}+\left[\frac{U_{x0}}{U_{th}}\frac{U_{y0}}{U_{th}}\frac{L_y}{L_x}\right]\tilde{n}\tilde{U}_x\frac{\partial\tilde{U}_y}{\partial\tilde{x}}+\left[\left(\frac{U_{y0}}{U_{th}}\right)^2\right]\tilde{n}\tilde{U}_y\frac{\partial\tilde{U}_y}{\partial\tilde{y}}$$
$$=-\frac{\partial\tilde{p}}{\partial\tilde{y}}+\left[\frac{e\phi_0}{kT_{e0}}\right]\tilde{n}\frac{\partial\tilde{\phi}}{\partial\tilde{y}}+\left[\frac{U_{x0}}{U_{th}}\frac{\omega_B L_y}{U_{th}}\right]\tilde{n}\tilde{U}_x\tilde{B}_0-\left[\frac{U_{y0}}{U_{th}}\frac{\nu_{m0}L_y}{U_{th}}\right]\tilde{n}\tilde{\nu_m}\tilde{U}_y \qquad \text{(E.2)}$$

1. **Axial direction:**

   Several assumptions can be made from physical observations, as shown below.

   - The pressure gradient and electric field terms are $O(1)$.
   - The time derivative term can be neglected depending on the fluctuation level of $U_x$. Electron transport over a time scale larger than ion time scales follows ion transport.
   - $U_{x0}/U_{th} \ll 1$, thus, the inertial term in the axial direction is negligible.
   - The azimuthal inertia term can be potentially important. A spatial variation of the axial drift in the azimuthal direction can lead to an additional collision frequency, given by

     $$\nu_{rot}=\frac{U_y}{U_x}\frac{\partial U_x}{\partial y},$$

     which has been never considered in Hall thruster simulations. However, this can be important in the presence of rotating spokes. As discussed by Ellison[12], spokes can carry electron currents, so there are possibilities that the axial electron mean velocity has some azimuthal variation.
   - $U_{y0}\omega_B \gg U_{x0}\nu_{m0}$. This is equivalent to $\Omega(U_{y0}/U_{x0}) \gg 1$. Therefore, the axial transport equation suggests that the axial electric field and pressure gradient

terms determine the electron azimuthal velocity $U_y$. Accordingly, $U_{x0}$ will be much smaller

Neglecting the axial and azimuthal inertia effects, the axial transport can be written as

$$0 = -\frac{\partial p}{\partial x} - en(E_x + U_y B_r) - mn\nu_m U_x. \tag{E.3}$$

Strictly speaking, the collision frequency term can be comparable to the axial and azimuthal inertia terms. Consider $U_{x0} = O(10^4$ m/s), $U_{y0} = U_{th} = O(10^6$ m/s), $\nu_{m0} = O(10^7$ 1/s), $L_x = O(10^{-2}$ m), and $L_y = O(10^{-1}$ m). The axial inertia term is on the order of $O(10^{-4})$, the azimuthal inertia term is $O(10^{-3})$, and the collision term is $O(10^{-3})$. Therefore, a time-varying simulation is required. In other words, the anomalous collision frequency assumed in the electron continuum model also includes the effects of such inertial nonlinear transport.

2. **Azimuthal direction:** It is discussed that the continuum approach may be invalid in the azimuthal direction in Sec. 7.4.1. If there are no collisions, the equations of motion or individual particles can be given by

$$m\frac{dv_x}{dt} = -e(E_x - v_y B_r),$$

$$m\frac{dv_y}{dt} = -e(E_y + v_x B_r),$$

which yield $v_x = v_\perp \cos(\omega_B t) - \frac{E_y}{B_r}$ and $v_y = v_\perp \cos(\omega_B t) + \frac{E_x}{B_r}$. Therefore, the time-averaged guiding center velocities can be given by

$$u_x = \langle v_x \rangle = -\frac{E_y}{B_r},$$

$$u_y = \langle v_y \rangle = \frac{E_x}{B_r},$$

which neglect the pressure gradient in both directions. Here, it is shown that the guiding-center type solution can be recovered from the continuum model. Consider

the following equations:

$$0 = -e(E_x - u_y B_r) - \frac{1}{n}\frac{\partial p}{\partial x} - m u_x \nu_m,$$

$$0 = -e(E_y + u_x B_r) - \frac{1}{n}\frac{\partial p}{\partial y} - m u_y \nu_m,$$

where the drift diffusion approximation is used in both axial and azimuthal directions. Then, the axial and azimuthal velocities can be calculated as

$$u_x = -\mu_\perp \left[ \left( E_x + \frac{1}{en}\frac{\partial p}{\partial x} \right) + \Omega \left( E_y + \frac{1}{en}\frac{\partial p}{\partial y} \right) \right], \tag{E.4}$$

$$u_y = -\mu_\perp \left[ \left( E_y + \frac{1}{en}\frac{\partial p}{\partial y} \right) - \Omega \left( E_x + \frac{1}{en}\frac{\partial p}{\partial x} \right) \right]. \tag{E.5}$$

Note that Lam *et al.*[76] explicitly used Eqs. (E.4) and (E.5) with the charge conservation equation. However, the issue related to the large condition number of the elliptic PDE is discussed in Sec. 7.4.2. In the limit of $\Omega \gg 1$, assuming $E_y + (1/en)\partial p/\partial y \approx 0$ gives

$$u_x = -\mu_\perp \left( E_x + \frac{1}{en}\frac{\partial p}{\partial x} \right), \tag{E.6}$$

$$u_y = \frac{1}{B_r} \left( E_x + \frac{1}{en}\frac{\partial p}{\partial x} \right), \tag{E.7}$$

which is similar to the guiding center equation for the azimuthal velocity while the axial velocity is written in a continuum form. This formulation is chosen due to Sekerak's suggestion,[7] namely to construct a 2D model that can be reduced to a 1D model.

3. **Considerations for Azimuthal transport:** Assuming that the continuum equations are valid in the azimuthal direction, some assumptions can be made from physical observations.

   - The axial inertia term can be comparable to the Lorentz force and the collision

term. The axial inertia term can be characterized by

$$\nu_{shear} = \frac{\partial U_y}{\partial x}.$$

This corresponds to the shear assumed in Scharfe's shear-based model.[148]

- The azimuthal drift may also be on the same order as the pressure and electric field because $U_{y0} \approx U_{th}$. Using a continuum approach suggests that the Knudsen number is small enough. If this is the case and $U_{y0}/U_{th} = O(1)$, then it is likely that a *shock* occurs.

Eq. (E.7) can be recovered when assuming that (1) the time derivative, (2) the inertia terms, (3) the pressure, and (4) the electrostatic force can be neglected in the full continuum formulation.

### Electron Energy Equation

Instead of separating out the energy equation into kinetic and thermal energy equations, one should solve the total energy equation since the right hand side cannot be separated out clearly. From Eq. (A.14),

$$\frac{\partial}{\partial t}(n\varepsilon) + \nabla \cdot [(n\varepsilon)\,\mathbf{u} + p\mathbf{u} + \mathbf{q}] = qn\mathbf{u} \cdot \mathbf{E} + S_e - S_i. \tag{E.8}$$

In the 2D hybrid-DK model, Eq. (E.8) is solved in a 2D domain. Several models are reviewed here.

The assumptions used in Hara *et al.* in Ref. 2 are that (1) the electron thermal energy is calculated from the total energy and kinetic energy to evaluate the wall heat flux, (2) $\nabla \cdot \mathbf{q} = 0$ in the axial and azimuthal directions but $\nabla \cdot \mathbf{q} = S_w$ in the radial direction that accounts for the wall heat flux, (3) $S_e \approx 0$ since $S_e \sim m_e/M_i = O(10^{-6})$, (4) the average mean energy is $\varepsilon = (3/2)T_{eff}$, and (5) the time derivative of the electron energy density is zero, *i.e.* frozen in the ion time scale.

$$\cancel{\frac{\partial}{\partial t}(n\varepsilon)} + \frac{\partial}{\partial x}\left(\frac{5}{3}n\varepsilon u_x\right) = qnu_xE_x - S_i - S_w. \tag{E.9}$$

Further assume $\partial(nu_x)/\partial x = 0$,

$$nu_x \cdot \frac{\partial}{\partial x}\left(\frac{5}{3}\epsilon\right) = -enu_xE_x - S_i - S_w. \tag{E.10}$$

## APPENDIX F

# Validity of the Quasineutral Assumption

### General Case

In order to evaluate the quasineutral assumption, the Poisson equation is considered:

$$\epsilon_0 \nabla^2 \phi = -e\sigma, \tag{F.1}$$

or equivalently Gauss's law:

$$\epsilon_0 \nabla \cdot \mathbf{E} = e\sigma. \tag{F.2}$$

- **Local Thermal Equilibrium**: Charge, potential, and space can be normalized by a characteristic density variation $\delta n$, electron temperature $k_B T_e/e$, and the characteristic length $R$, respectively. If an equilibrium number density $n_0$ is assumed and using the Debye length $\lambda_D = (\epsilon_0 k_B T_e/e^2 n_0)^{1/2}$, the normalized Poisson equation can be written as

$$\left(\frac{\lambda_D}{R}\right)^2 \tilde{\nabla}^2 \tilde{\phi} = -\frac{\delta n}{n_0}\tilde{\sigma}.$$

  The quasineutral assumption is valid as long as $\lambda_D \ll R$ so that $\delta n \ll n_0$. This equation also suggests that quasineutrality is not valid in the plasma-sheath, where the characteristic length $R \sim \lambda_D$. As the potential drop is also on the order of $T_e$, $\delta n \sim n_0$. Another observation of the quasineutral assumption is that the electric field

must be on the order of $\sim k_B T_e/eR$, which is valid when ambipolar type diffusion occurs.[1]

- **Drifting Plasma**: The other situation is when the drift current is greater than the diffusion current. $\mathbf{u} \simeq \mu_e \mathbf{E}$ (P.32 in Ref. 46). Here, the diffusion across magnetic fields is neglected. From the Einstein relation $D = (k_B T_e/e)\mu_e$, where $D$ is the diffusion coefficient, $\mathbf{E} \sim (k_B T_e/e)\mathbf{u}/D$. For the velocity that satisfies thermal velocity: $u^2 \sim D\nu = k_B T_e/m$, the energy relaxation length can be written as $\Lambda_u = u/\nu = D/u$. Therefore, the normalized Gauss's law can be given by

$$\left(\frac{\lambda_D}{R}\right)\left(\frac{\lambda_D}{\Lambda_u}\right)\tilde{\nabla}\cdot\tilde{\mathbf{E}} = \frac{\delta n}{n_0}\tilde{\sigma}.$$

  Therefore, the quasineutral assumption can become invalid if $\Lambda_u \ll \lambda_D$. $\Lambda_u$ can be small when $u$ is small and $\nu$ is large.

Evaluation of the length scale becomes less clear for magnetized cases. However, quasineutrality is likely to hold when simulating a large-scale phenomena as the characteristic length $R$, typically determined by the cell size in simulations, is much larger than the Debye length.

### 2D Axial-Azimuthal Transport

The quasineutrality assumption in the 2D axial-azimuthal electron continuum model is discussed. The charge conservation equation can be derived using Ampere's law:

$$\nabla \times \mathbf{B} = \mu_0 \left(\mathbf{j} + \epsilon_0 \frac{\partial \mathbf{E}}{\partial t}\right), \tag{F.3}$$

where $\mu_0$ is the permeability of free space and $\mathbf{j} = e\mathbf{J}$ is the current density. Taking the divergence of Eq. (F.3), the left hand side is zero: $\nabla \cdot \nabla \times \mathbf{B} = 0$. Then, the right hand side of Eq. (F.3) can be written as $e\nabla \cdot \mathbf{J} + \epsilon_0[\partial(\nabla \cdot \mathbf{E})/\partial t] = 0$. From Gauss's law in Eq. (F.2), $\epsilon_0[\partial(\nabla \cdot \mathbf{E})/\partial t] = \epsilon_0[\nabla \cdot (\partial \mathbf{E}/\partial t)] = e(\partial\sigma/\partial t)$. These two relations reduce to the charge

[1] For situations when the pressure gradient is balanced with the electric field and $\mathbf{u} \approx 0$, from $\mathbf{E} \sim (k_B T_e/e)(\nabla n/n)$, the density gradient satisfies $\nabla n = O(n/R)$.

conservation equation, given by

$$\frac{\partial \sigma}{\partial t} + \nabla \cdot \mathbf{J} = 0, \tag{F.4}$$

where $\sigma = n_i - n_e$ is the charge and $\mathbf{J} = \mathbf{J}_i - \mathbf{J}_e$ is the total flux. First of all, neglect $\partial J_{iy}/\partial y$ as the ion rotation speed will be much smaller than other drift velocities. The charge, the currents of ion and electrons in the $x$-direction, the electron current in the $y$-direction, time, and space are normalized by a characteristic charge density $\delta n$, the anode current density $J_D$, the current density due to the $E \times B$ drift $J_{E\times B}$, the characteristic frequency of non-neutral plasma to become neutral $\omega_T$, and the characteristic length $L$, respectively. Assume that the anode total current density and the $E \times B$ current density follow $J_D = n_0 u_D$ and $J_{E\times B} = n_0 u_{E\times B}$, where $n_0$ is the equilibrium number density, $u_D$ is the characteristic velocity in the $x$-direction, and $u_{E\times B}$ is the $E \times B$ drift speed. Thus,

$$\frac{u_D}{L_x \omega_T} \frac{\partial}{\partial \tilde{x}} (\tilde{J}_{ix} - \tilde{J}_{ex}) + \frac{u_{E\times B}}{L_y \omega_T} \frac{\partial}{\partial \tilde{y}} \tilde{(-J)}_{ey} = -\frac{\delta n}{n_0} \frac{\partial \tilde{\sigma}}{\partial \tilde{t}}. \tag{F.5}$$

Here, let us define

$$C_x = \frac{u_D}{L_x \omega_T},$$

$$C_y = \frac{u_{E\times B}}{L_y \omega_T},$$

as the normalization coefficients in each direction. Depending on the temporal and spatial scales, one can discuss whether the quasineutral assumption is valid or not.

**Small-scale phenomena**

In a Hall thruster discharge channel, it is known that $u_{E\times B} \gg u_D$. If the characteristic lengths in the $x$ and $y$ directions, *i.e.* $L_x$ and $L_y$, are on the same order, the $y$-direction components will yield a strong non-neutral plasma. The spatial scales are $L_x = L_y \simeq \lambda_D = O(10^{-5})$ m and the associated time scale is $\omega_T = \omega_{pe} = O(10^{11})$ rad/s. For instance, using $u_D = O(10^4)$ m/s and $u_{E\times B} = O(10^6)$ m/s,

$$C_x = O\left(\frac{10^4}{10^{-5} \times 10^{11}}\right) = O(10^{-2}) \ll 1,$$

$$C_y = O\left(\frac{10^6}{10^{-5} \times 10^{11}}\right) = O(1).$$

Thus, the quasineutral assumption is no longer valid for small-scale plasma oscillations, particularly in the azimuthal direction. It can be seen that the axial transport still can be described using a quasineutral plasma for the given parameters only if the azimuthal transport is neglected or averaged.

**Large-scale phenomena**

In the present simulation, the targeted phenomenon is a low-frequency oscillation that is on the order of 10 kHz. From a physical perspective, the characteristic frequency of charge neutrality is no larger than the ion plasma frequency. Thus, $\omega_T \sim \omega_{pi} = (e^2 n_0/m_i\epsilon_0)^{1/2} = O(10^8 - 10^9)$ rad/s. It can be assumed that the electrons will follow the ion oscillations in this time scale. The characteristic length of the low-frequency phenomenon in the $x$-direction is $L_x = (10^{-2})$ m, as the characteristic length of breathing mode oscillations is on the order of the channel length, and that in the $y$-direction is $L_y = O(10^{-1})$ m because the dominant spoke modes are $m = O(1)$. Using the same velocity range as the small-scale phenomena, the normalization coefficients can be calculated as

$$C_x = O\left(\frac{10^4}{10^{-2} \times 10^8}\right) = O(10^{-2}) \ll 1,$$

and

$$C_y = O\left(\frac{10^6}{10^{-1} \times 10^8}\right) = O(10^{-1}) < 1.$$

Therefore, $\delta n/n_0 < 1$ and the quasineutrality assumption can be used.

# BIBLIOGRAPHY

# BIBLIOGRAPHY


[1] Sekerak, M. J., Longmier, B. W., Gallimore, A. D., Brown, D. L., Hofer, R. R., and Polk, J. E., "Mode Transitions in Hall Effect Thrusters," AIAA 2013-4116, San Jose, CA, July 2013.

[2] Hara, K., Sekerak, M. J., Boyd, I. D., and Gallimore, A. D., "Mode transition of a Hall thruster discharge plasma," *Journal of Applied Physics*, Vol. 115, No. 20, 2014. doi:10.1063/1.4879896.

[3] Tilinin, G. N., "High-frequency plasma waves in a Hall accelerator with an extended acceleration zone," *Sov. Phys. Tech. Phys.*, Vol. 22, 1977, pp. 974–978.

[4] Gascon, N., Dudeck, M., and Barral, S., "Wall material effects in stationary plasma thrusters. I. Parametric studies of an SPT-100," *Physics of Plasmas*, Vol. 10, No. 10, 2003, pp. 4123–4136. doi:10.1063/1.1611880.

[5] Barral, S., Makowski, K., Peradzynski, Z., Gascon, N., and Dudeck, M., "Wall material effects in stationary plasma thruster. II. Near-wall and in-wall conductivity," *Physics of Plasmas*, Vol. 10, No. 10, October 2003, pp. 4137–4152.

[6] Gascon, N., Perot, C., Bonhomme, G., Caron, X., Bechu, S., Lasgorceix, P., Izrar, B., and Dudeck, M., "Signal processing and non-linear behavior of a stationary plasma thruster: First results," AIAA 1999-2427, Los Angeles, CA, June 1999.

[7] Sekerak, M. J., *Plasma Oscillations and Operational Modes in Hall Effect Thrusters*, Ph.D. thesis, University of Michigan, 2014.

[8] Tremolizzo, E., Meier, H., and Estublier, D., "In-flight Disturbance Torque Evaluation of the SMART-1 Plasma Thruster," *Proceedings of the 18th International Symposium on Space Flight Dynamics (ESA SP-548)*, October 2004, pp. 303–306.

[9] Choueiri, E. Y., "Plasma Oscillations in Hall Thrusters," *Physics of Plasmas*, Vol. 8, 2001, pp. 1411–1426.

[10] Fife, J. M., *Hybrid-PIC Modeling and Electrostatic Probe Survey of Hall Thrusters*, Ph.D. thesis, MIT, 1998.

[11] Boeuf, J. P. and Garrigues, L., "Low Frequency Oscillations in a Stationary Plasma Thruster," *Journal of Applied Physics*, Vol. 84, No. 7, 1998, pp. 3541–3554. doi:10.1063/1.368529.

[12] Ellison, C. L., Raitses, Y., and Fisch, N. J., "Cross-field electron transport induced by a rotating spoke in a cylindrical Hall thruster," *Physics of Plasmas*, Vol. 19, 2012, pp. 013503.

[13] Koo, J. W. and Boyd, I. D., "Modeling of anomalous electron mobility in Hall thrusters," *Physics of Plasmas*, Vol. 13, No. 3, 2006. doi:10.1063/1.2172191.

[14] Hofer, R. R., Katz, I., Mikellides, I. G., Goebel, D. M., Jameson, K. K., Sullivan, R. M., and Johnson, L. K., "Efficacy of Electron Mobility Models in Hybrid-PIC Hall Thruster Simulations," AIAA 2008-4924, Hartford, CT, July 2008.

[15] Keidar, M., Boyd, I. D., and Beilis, I. I., "Plasma flow and plasma-wall transition in Hall thruster channel," *Physics of Plasmas*, Vol. 8, No. 12, December 2001, pp. 5315–5322.

[16] Sydorenko, D., Smolyakov, A., Kaganovich, I., and Raitses, Y., "Modification of Electron Velocity Distribution in Bounded Plasmas by Secondary Electron Emission," *IEEE Transactions on Plasma Science*, Vol. 34, No. 3, June 2006, pp. 815–824.

[17] Smolyakov, A. I., Frias, W., Kaganovich, I. D., and Raitses, Y., "Sheath-Induced Instabilities in Plasmas with $\mathbf{E}_0 \times \mathbf{B}_0$ Drift," *Phys. Rev. Lett.*, Vol. 111, Sep 2013, pp. 115002. doi:10.1103/PhysRevLett.111.115002.

[18] Garrigues, L., Boyd, I. D., and Boeuf, J. P., "Computation of Hall Thruster Performance," *Journal of Propulsion and Power*, Vol. 17, No. 4, July 2001, pp. 772–779.

[19] Smith, B. D., Boyd, I. D., and Kamhawi, H., "Influence of Triply-Charged Ions and Ionization Cross-Sections in a Hybrid-PIC Model of a Hall Thruster Discharge," AIAA 2014-3429, Cleveland, OH, July 2014.

[20] Zhurin, V. V., Kaufman, H. R., and Robinson, R. S., "Physics of closed drift thrusters," *Plasma Sources Science and Technology*, Vol. 8, No. 1, 1999, pp. R1.

[21] Adam, J. D., Heron, A., and Laval, G., "Study of stationary plasma thrusters using two-dimensional fully kinetic simulation," *Physics of Plasmas*, Vol. 11, No. 1, January 2004, pp. 295 –305.

[22] Frias, W., Smolyakov, A. I., Kaganovich, I. D., and Raitses, Y., "Long wavelength gradient drift instability in Hall plasma devices. I. Fluid theory," *Physics of Plasmas (1994-present)*, Vol. 19, No. 7, 2012, pp. –. doi:10.1063/1.4736997.

[23] Campanell, M. D., Khrabrov, A. V., and Kaganovich, I. D., "General Cause of Sheath Instability Identified for Low Collisionality Plasmas in Devices with Secondary Electron Emission," *Phys. Rev. Lett.*, Vol. 108, Jun 2012, pp. 235001. doi:10.1103/PhysRevLett.108.235001.

[24] Yim, J. T., *Computational Modeling of Hall Thruster Channel Wall Erosion*, Ph.D. thesis, University of Michigan, 2008.

[25] Smith, B. D. and Boyd, I. D., "Computation of Total and Differential Sputter Yields of Boron Nitride Using Molecular Dynamics," *Proceedings of the 33rd International Electric Propulsion Conference*, IEPC 2013-156, Washington D. C., October 2013.

[26] Sawlani, K., *Effects of Secondary Electron Emission on the Electron Energy Distribution and Sheaths in Crossed Field Plasma Devices*, Ph.D. thesis, University of Michigan, 2015.

[27] Hofer, R. R., Goebel, D. M., Mikellides, I. G., and Katz, I., "Magnetic shielding of a laboratory Hall thruster. II. Experiments," *Journal of Applied Physics*, Vol. 115, No. 4, 2014. doi:10.1063/1.4862314.

[28] Raitses, Y., Smirnov, A., Staack, D., and Fisch, N. J., "Measurements of secondary electron emission effects in the Hall thruster discharge," *Physics of Plasmas*, Vol. 13, 2006, pp. 014502.

[29] Reid, B. M., *The Influence of Neutral Flow Ratein the Operation of Hall Thrusters*, Ph.D. thesis, University of Michigan, 2009.

[30] Huismann, T., *Improving Hall Thruster Plume Simulation through Refined Characterization of Near-field Plasma Properties*, Ph.D. thesis, University of Michigan, 2011.

[31] Boyd, I. D. and Dressler, R. A., "Far field modeling of the plasma plume of a Hall thruster," *Journal of Applied Physics*, Vol. 92, No. 4, 2002, pp. 1764–1774. doi:10.1063/1.1492014.

[32] Galitzine, C., *On the Accuracy and Efficiency of the Direct Simulation Monte Carlo Method*, Ph.D. thesis, University of Michigan, 2015.

[33] Cheng, C. and Knorr, G., "The integration of the vlasov equation in configuration space," *Journal of Computational Physics*, Vol. 22, No. 3, 1976, pp. 330 – 351. doi:10.1016/0021-9991(76)90053-X.

[34] Filbet, F. and Sonnendrucker, E., "Comparison of Eulerian Vlasov solvers," *Computer Physics Communications*, Vol. 150, No. 3, 2003, pp. 247 – 266. doi:10.1016/S0010-4655(02)00694-X.

[35] Qiu, J.-M. and Christlieb, A., "A conservative high order semi-Lagrangian WENO method for the Vlasov equation," *Journal of Computational Physics*, Vol. 229, No. 4, 2010, pp. 1130 – 1149. doi:10.1016/j.jcp.2009.10.016.

[36] Rossmanith, J. A. and Seal, D. C., "A positivity-preserving high-order semi-Lagrangian discontinuous Galerkin scheme for the Vlasov–Poisson equations," *Journal of Computational Physics*, Vol. 230, No. 16, 2011, pp. 6203 – 6232. doi:10.1016/j.jcp.2011.04.018.

[37] Banks, J. W. and Hittinger, J. A. F., "A New Class of Nonlinear Finite-Volume Methods for Vlasov Simulation," *IEEE Transactions on Plasma Science*, Vol. 38, No. 9, Sept. 2010, pp. 2198–2207.

[38] Lee, W. W., "Gyrokinetic approach in particle simulation," *Physics of Fluids (1958-1988)*, Vol. 26, No. 2, 1983, pp. 556–562.

[39] Hirsch, C., *Numerical Computation of Internal and External FFlow: Fundamentls of Computational Fluid Dynamics*, John Wiley and Sons, Ltd, 2007.

[40] Arora, M. and Roe, P. L., "A Well-Behaved TVD Limiter for High-Resolution Calculations of Unsteady Flow," *Journal of Computational Physics*, Vol. 132, No. 1, 1997, pp. 3 – 11. doi:10.1006/jcph.1996.5514.

[41] Van Leer, B., "Towards the ultimate conservative difference scheme. IV. A new approach to numerical convection," *Journal of Computational Physics*, Vol. 23, No. 3, 1977, pp. 276 – 299. doi:10.1016/0021-9991(77)90095-X.

[42] Kushner, M. J., "Hybrid modelling of low temperature plasmas for fundamental investigations and equipment design," *Journal of Physics D: Applied Physics*, Vol. 42, No. 19, 2009, pp. 194013.

[43] Cheng, Y., Christlieb, A. J., and Zhong, X., "Energy-conserving discontinuous Galerkin methods for the Vlasov–Ampère system," *Journal of Computational Physics*, Vol. 256, No. 0, 2014, pp. 630 – 655. doi:10.1016/j.jcp.2013.09.013.

[44] Lieberman, M. A. and Lichtenberg, A. J., *Principles of Plasma Discharges and Materials Processing*, Wiley, 2nd ed., 2005.

[45] Tanenbaum, B. S., *Plasma Physics*, McGraw-Hill, 1967.

[46] Raizer, Y. P., Allen, J. E., and Kisin, V. I., *Gas Discharge Physics*, Springer, September 1991.

[47] Barnes, M. S., Cotler, T. J., and Elta, M. E., "Largesignal timedomain modeling of lowpressure rf glow discharges," *Journal of Applied Physics*, Vol. 61, No. 1, 1987, pp. 81–89. doi:10.1063/1.338804.

[48] Shoucri, M., *Numerical Solution of Hyperbolic Differential Equations*, Nova Science Publishers, 2008.

[49] Kolobov, V. I. and Arslanbekov, R. R., "Towards Adaptive Kinetic-Fluid Simulations of Weakly Ionized Plasmas," *Journal of Computational Physics*, Vol. 231, No. 3, 2011, pp. 839–869.

[50] Schwager, L. A. and Birdsall, C. K., "Collector and source sheaths of a finite ion temperature plasma," *Physics of Fluids B: Plasma Physics (1989-1993)*, Vol. 2, No. 5, 1990, pp. 1057–1068. doi:10.1063/1.859279.

[51] Sheehan, J. P., Hershkowitz, N., Kaganovich, I. D., Wang, H., Raitses, Y., Barnat, E. V., Weatherford, B. R., and Sydorenko, D., "Kinetic Theory of Plasma Sheaths Surrounding Electron-Emitting Surfaces," *Phys. Rev. Lett.*, Vol. 111, No. 7, August 2013, pp. 075002.

[52] Hobbs, G. D. and Wesson, J. A., "Heat flow through a Langmuir sheath in the presence of electron emission," *Plasma Physics*, Vol. 9, 1967, pp. 85–87.

[53] Oksuz, L. and Hershkowitz, N., "Plasma, presheath, collisional sheath and collisionless sheath potential profiles in weakly ionized, weakly collisional plasma," *Plasma Sources Science and Technology*, Vol. 14, No. 1, 2005, pp. 201.

[54] Hara, K. and Boyd, I. D., "Analysis of secondary electron emission of dielectric materials using a direct kinetic simulation," San Francisco, CA, June 2013.

[55] Brunner, S. and Valeo, E. J., "Trapped-Particle Instability Leading to Bursting in Stimulated Raman Scattering Simulations," *Phys. Rev. Lett.*, Vol. 93, Sep 2004, pp. 145003. doi:10.1103/PhysRevLett.93.145003.

[56] Bernstein, I. B., Greene, J. M., and Kruskal, M. D., "Exact Nonlinear Plasma Oscillations," *Phys. Rev.*, Vol. 108, Nov 1957, pp. 546–550. doi:10.1103/PhysRev.108.546.

[57] Dewar, R. L., "Frequency Shift Due to Trapped Particles," *Physics of Fluids (1958-1988)*, Vol. 15, No. 4, 1972, pp. 712–714. doi:10.1063/1.1693969.

[58] Berger, R. L., Brunner, S., Chapman, T., Divol, L., Still, C. H., and Valeo, E. J., "Electron and ion kinetic effects on non-linearly driven electron plasma and ion acoustic waves," *Physics of Plasmas*, Vol. 20, No. 3, 2013, pp. 032107. doi:10.1063/1.4794346.

[59] Dodin, I. Y., Schmit, P. F., Rocks, J., and Fisch, N. J., "Negative-Mass Instability in Nonlinear Plasma Waves," *Phys. Rev. Lett.*, Vol. 110, May 2013, pp. 215006. doi:10.1103/PhysRevLett.110.215006.

[60] Brunner, S., Berger, R. L., Cohen, B. I., Hausammann, L., and Valeo, E. J., "Kinetic Simulations and Reduced Modeling of Longitudinal Sideband Instabilities in Non-Linear Electron Plasma Waves," *Physics of Plasmas (1994-present)*, 2014. doi:10.1063/1.4896753.

[61] Tennyson, J. L., Meiss, J. D., and Morrison, P. J., "Self-consistent chaos in the beam-plasma instability," *Physica D: Nonlinear Phenomena*, Vol. 71, February 1994, pp. 1–17. doi:10.1016/0167-2789(94)90178-3.

[62] Hara, K., Chapman, T., Banks, J. W., Brunner, S., Joseph, I., Berger, R. L., and Boyd, I. D., "Quantitative study of the trapped particle bunching instability in Langmuir waves," *Physics of Plasmas (1994-present)*, Vol. 22 (accepted), 2015. doi:10.1063/1.4903843.

[63] Huang, W., *Study of Hall Thruster Discharge Channel Wall Erosion via Optical Diagnostics*, Ph.D. thesis, University of Michigan, 2011.

[64] Huang, W., Gallimore, A. D., and Hofer, R. R., "Neutral Flow Evolution in a SIx-Killowatt Hall Thruster," *Journal of Propulsion and Power*, Vol. 27, No. 3, May 2011, pp. 553–563.

[65] William A Hargus, J. and Charles, C. S., "Near Exit Plane Velocity Field of a 200-Watt Hall Thruster," *Journal of Propulsion and Power*, Vol. 24, 2008, pp. 127–133.

[66] Mazouffre, S. and Bourgeois, G., "Spatio-temporal characteristics of ion velocity in a Hall thruster discharge," *Plasma Sources Science and Technology*, Vol. 19, No. 6, 2010, pp. 065018.

[67] Ahedo, E., Martinez-Cerezo, P., and Martinez-Sanchez, M., "One-dimensional model of the plasma flow in a Hall Thruster," *Physics of Plasma*, Vol. 8, No. 6, June 2001, pp. 3058–3068.

[68] Mikellides, I. G. and Katz, I., "Numerical simulations of Hall-effect plasma accelerators on a magnetic-field-aligned mesh," *Phys. Rev. E*, Vol. 86, Oct 2012, pp. 046703. doi:10.1103/PhysRevE.86.046703.

[69] Szabo, J. J., *Fully Kinetic Numerical Modeling of a Plasma Thruster*, Ph.D. thesis, MIT, 2001.

[70] Taccogna, F., Schneider, R., Longo, S., and Capitelli, M., "Kinetic simulations of a plasma thrusters," *Plasma Sources Sci. Technol.*, Vol. 17, 2008, pp. 024003.

[71] Cho, S., Komurasaki, K., and Arakawa, Y., "Kinetic particle simulation of discharge and wall erosion of a Hall thruster," *Physics of Plasmas (1994-present)*, Vol. 20, No. 6, 2013, pp. –. doi:10.1063/1.4810798.

[72] Coche, P. and Garrigues, L., "A two-dimensional (azimuthal-axial) particle-in-cell model of a Hall thruster," *Physics of Plasmas (1994-present)*, Vol. 21, No. 2, 2014, pp. –. doi:10.1063/1.4864625.

[73] Hagelaar, G. J. M., Bareilles, J., Garrigues, L., and Boeuf, J. P., "Two-dimensional model of a stationary plasma thruster," *Journal of Applied Physics*, Vol. 91, No. 9, May 2002, pp. 5592–5598. doi:10.1063/1.1465125.

[74] Bareilles, J., Hagelaar, G. J. M., Garrigues, L., Boniface, C., Boeuf, J. P., and Gascon, N., "Critical assessment of a two-dimensional hybrid Hall thruster model: Comparisons with experiments," *Physics of Plasmas*, Vol. 11, No. 6, June 2004, pp. 3035–3046.

[75] Scharfe, M. K., Gascon, N., Cappelli, M. A., and Fernandez, E., "Comparison of hybrid Hall thruster model to experimental measurements," *Physics of Plasmas*, Vol. 13, 2006, pp. 083505.

[76] Lam, C. M., Fernandez, E., and Cappelli, M. A., "A 2-D Hybrid Hall Thruster Simulation That Resolves the E  B A 2-D Hybrid Hall Thruster Simulation That Resolves the $\mathbf{E} \times \mathbf{B}$ Electron Drift Direction," *IEEE Transactions on Plasma Science*, Vol. 43, No. 1, 2015, pp. 86–84.

[77] Fox, J. M., Batishcheva, A. A., Batishchev, O. V., and Martinez-Sanchez, M., "Adaptively Meshed Fully-Kinetic PIC-Vlasov Model For Near Vaccum Hall Thrusters," AIAA 2006-4324, Sacramento, CA, July 2006.

[78] Garrigues, L., Heron, A., Adam, J. C., and Boeuf, J. P., "Hybrid and particle-in-cell models of a stationary plasma thruster," *Plasma Sources Sci. Technol.*, Vol. 9, No. 2, February 2000, pp. 219–226.

[79] Pullins, S., Chiu, Y.-H., Levandier, D. J., and Dressler, R. A., "Ion Dynamics in Hall Effect and Ion Thrusters: $Xe^+ + Xe$ Symmetric Charge Transfer," AIAA 2000-0603, Reno, NV, January 2000.

[80] Rapp, D. and Englander-Golden, P., "Total Cross Sections for Ionization and Attachment in Gases by Electron Impact. I. Positive Ionization," *The Journal of Chemical Physics*, Vol. 43, No. 5, 1965, pp. 1464–1479. doi:10.1063/1.1696957.

[81] Hara, K., Boyd, I. D., and Kolobov, V. I., "One-dimensional hybrid-direct kinetic simulation of the discharge plasma in a Hall thruster," *Physics of Plasmas*, Vol. 19, No. 11, 2012. doi:10.1063/1.4768430.

[82] Dorf, L., Raitses, Y., and Fisch, N. J., "Experimental studies of anode sheath phenomena in a Hall thruster discharge," *Journal of Applied Physics*, Vol. 2005, 97, pp. 103309.

[83] Keidar, M., "Anodic plasma in Hall thrusters," *Journal of Applied Physics*, Vol. 103, 2008, pp. 053309.

[84] Garrigues, L., Mazouffre, S., and Bourgeois, G., "Computed versus measured ion velocity distribution functions in a Hall effect thruster," *Journal of Applied Physics*, Vol. 111, 2012, pp. 113301.

[85] Puech, V. and Mizzi, S., "Collision Cross Sections and Transport Parameters in Neon and Xenon," *J. Phys. D: Appl. Phys.*, Vol. 24, 1991, pp. 1974–1985.

[86] Mikellides, I. G., Katz, I., Mandell, M. J., and Snyder, J. S., "A 1-D Model of the Hall-Effect Thruster with an Exhaust Region," AIAA 2001-3505, Salt Lake City, UT, July 2001.

[87] King, L. B. and Gallimore, A. D., "Ion-Energy Diagnostics in the Plasma Exhaust Plume of a Hall Thruster," *Journal of Propulsion and Power*, Vol. 16, No. 5, September 2000, pp. 916–922.

[88] Young, C. V., Lucca Fabris, A., and Cappelli, M. A., "Ion dynamics in an EB Hall plasma accelerator," *Applied Physics Letters*, Vol. 106, No. 4, 2015, pp. –. doi:10.1063/1.4907283.

[89] Durot, C. J., Gallimore, A. D., and Smith, T. B., "Validation and evaluation of a novel time-resolved laser-induced fluorescence technique," *Review of Scientific Instruments*, Vol. 85, No. 1, 2014, pp. –. doi:10.1063/1.4856635.

[90] Barral, S. and Ahedo, E., "Low-frequency model of breathing oscillations in Hall discharges," *Phys. Rev. E*, Vol. 79, Apr 2009, pp. 046401. doi:10.1103/PhysRevE.79.046401.

[91] Lobbia, R. B. and Gallimore, A. D., "Two-dimensional Time-resolved Breathing Mode Plasma Fluctuation Variation with Hall Thruster Discharge Settings," IEPC 2009-106, Ann Arbor, MI, September 2009.

[92] McDonald, M., Bellant, C., Pierre, B. S., and Gallimore, A. D., "Measurement of Cross-Field Electron Current in a Hall Thruster Due to Rotating Spoke Instabilities," AIAA 2011-5810, San Diego, CA, August 2011.

[93] Szabo, J., Warner, N., Martinez-Sanchez, M., and Batishchev, O., "Full Particle-In-Cell Simulation Methodology for Axisymmetric Hall Effect Thrusters," *Journal of Propulsion and Power*, Vol. 30, No. 1, 2014, pp. 197–208. doi:10.2514/1.B34774.

[94] Parra, F. I., Ahedo, E., Fife, J. M., and Martínez-Sánchez, M., "A two-dimensional hybrid model of the Hall thruster discharge," *Journal of Applied Physics*, Vol. 100, No. 2, 2006, pp. –. doi:10.1063/1.2219165.

[95] Hara, K. and Boyd, I. D., "Low Frequency Oscillation Analysis of a Hall Thruster Using a One-Dimensional Hybrid-Direct Kinetic Simulation," IEPC-2013-266, Washington D.C., October 2013.

[96] Bechu, S., Perot, C., Gascon, N., Lasgorceix, P., Hauser, A., and Dudeck, M., "Operating mode investigation of a Laboratory Stationary Plasma Thruster," AIAA 1999-2567, Los Angeles, CA, June 1999.

[97] Hebner, G. A. and Miller, P. A., "Behavior of excited argon atoms in inductively driven plasmas," *Journal of Applied Physics*, Vol. 87, No. 12, 2000, pp. 8304–8315. doi:http://dx.doi.org/10.1063/1.373542.

[98] Ton-That, D. and Flannery, M. R., "Cross sections for ionization of metastable rare-gas atoms (Ne*, Ar*, Kr*, Xe*) and of metastable $N_2$*, CO* molecules by electron impact," *Phys. Rev. A*, Vol. 15, Feb 1977, pp. 517–526. doi:10.1103/PhysRevA.15.517.

[99] Meunier, J., Belenguer, P., and Boeuf, J. P., "Numerical model of an AC plasma display panel cell in neon-xenon mixtures," *Journal of Applied Physics*, Vol. 78, No. 2, 1995, pp. 731–745. doi:10.1063/1.360684.

[100] Hayashi, M., "Determination of electron-xenon total excitation cross-sections, from threshold to 100 eV, from experimental values of Townsend's $\alpha$," *Journal of Physics D: Applied Physics*, Vol. 16, No. 4, 1983, pp. 581. doi:10.1088/0022-3727/16/4/018.

[101] Raitses, Y., Staack, D., Smirnov, A., and Fisch, N. J., "Space charge saturated sheath regime and electron temperature saturation in Hall thrusters," *Physics of Plasmas*, Vol. 12, No. 7, 2005, pp. 073507. doi:10.1063/1.1944328.

[102] McDonald, M. and Gallimore, A. D., "Comparison of Breathing and Spoke Mode Strengths in the H6 Hall Thruster Using High Speed Imaging," IEPC 2013-353, Washington D. C., October 2013.

[103] Sydorenko, D., Smolyakov, A., Kaganovich, I., and Raitses, Y., "Plasma-sheath instability in Hall thrusters due to periodic modulation of the energy of secondary electrons in cyclotron motion," *Physics of Plasmas*, Vol. 15, No. 5, 2008, pp. –. doi:10.1063/1.2918333.

[104] Jorns, B. A. and Hofer, R. R., "Low Frequency Plasma Oscillations in a 6-kW Magnetically Shielded Hall Thruster," AIAA 2013-4119, San Jose, CA, July 2013.

[105] Manzella, D. H., "Stationary Plasma Thruster Plume Emissions," IEPC-93-097, Seattle, WA, October 1993.

[106] Hofer, R. R. and Gallimore, A. D., "High-Specific Impulse Hall Thrusters, Part 2: Efficiency Analysis," *Journal of Propulsion and Power*, Vol. 22, No. 4, 2006, pp. 732–741.

[107] Yamamoto, N., Komurasaki, K., and Arakawa, Y., "Discharge Current Oscillation in Hall Thrusters," *Journal of Propulsion and Power*, Vol. 21, No. 5, 2005, pp. 870–876.

[108] Barral, S. and Peradzyński, Z., "Ionization oscillations in Hall accelerators," *Physics of Plasmas (1994-present)*, Vol. 17, No. 1, 2010. doi:10.1063/1.3292645.

[109] Peradzyński, Z., Makowski, K., Barral, S., Kurzyna, J., and Dudeck, M., "The Role of The Electron Energy Balance in Plasma Thruster Instabilities," *AIP Conference Proceedings*, Vol. 993, No. 1, 2008, pp. 435–438. doi:10.1063/1.2909169.

[110] Barral, S. and Ahedo, E., "On the Origin of Low Frequency Oscillations in Hall Thrusters," *AIP Conference Proceedings*, Vol. 993, 2008, pp. 439–442.

[111] Lobbia, R. B., *A Time-resolved Investigation of Hall Thruster Breathing Mode*, Ph.D. thesis, University of Michigan, 2010.

[112] Goebel, D. and Katz, I., *Fundamentals of Electric Propulsion: Ion and Hall Thrusters*, Wiley, 2008.

[113] Lee, C. and Lieberman, M. A., "Global model of Ar, O2, Cl2, and Ar/O2 highdensity plasma discharges," *Journal of Vacuum Science and Technology A*, Vol. 13, No. 2, 1995, pp. 368–380. doi:10.1116/1.579366.

[114] Jacobson, D. T., Manzella, D. H., Hofer, R. R., and Peterson, P. Y., "NASA's 2004 Hall Thruster Program," AIAA 2004-3600, Fort Lauderdale, FL, July 2004.

[115] Brown, D. L., Larson, C. W., Beal, B. E., and Gallimore, A. D., "Methodology and Historical Perspective of a Hall Thruster Efficiency Analysis," *Journal of Propulsion and Power*, Vol. 25, No. 6, November 2009, pp. 1163–1177.

[116] Ross, J. L., *Probe Studies of a Hall Thruster at Low Voltages*, Ph.D. thesis, Michigan Technological University, 2011.

[117] Garner, C. E., Brophy, J. R., Polk, J. E., and Pless, L. C., "Performance Evaluation and Life Testing of the SPT-100," AIAA 94-2856, Indianapolis, IN, June 1994.

[118] Nakles, M. R., Hargus Jr., W. A., Delgado, J. J., and Corey, R. L., "A Performance Comparison of Xenon and Krypton Propellant on an SPT-100 Hall Thruster," IEPC 2011-003, Weisbaden, Germany, September 2011.

[119] Kim, V., "Main Physical Features and Processes Determining the Performance of Stationary Plasma Thrusters," *Journal of Propulsion and Power*, Vol. 14, No. 5, September 1998, pp. 736–743.

[120] Sankovic, J. M., Hamley, J. A., and Haag, T. W., "Performance Evaluation of The Russian SPT-100 Thruster at NASA LeRC," IEPC-93-094, Seattle, WA, October 1993.

[121] Tsendin, L. D., "Electron kinetics in non-uniform glow discharge plasmas," *Plasma Sources Science and Technology*, Vol. 4, No. 2, 1995, pp. 200.

[122] Kaganovich, I. D., Demidov, V. I., Adams, S. F., and Raitses, Y., "Non-local collisionless and collisional electron transport in low-temperature plasma," *Plasma Physics and Controlled Fusion*, Vol. 51, No. 12, 2009, pp. 124003.

[123] Komurasaki, K. and Arakawa, Y., "Two-dimensional Numerical Model of Plasma Flow in a Hall Thruster," *Journal of Propulsion and Power*, Vol. 11, No. 6, November 1995, pp. 1317–1323.

[124] Cheng, S., *Modeling of Hall thruster lifetime and erosion mechanisms*, Ph.D. thesis, MIT, 2007.

[125] Geng, J., Brieda, L., Rose, L., and Keidar, M., "On applicability of the thermalized potential solver in simulations of the plasma flow in Hall thrusters," *Journal of Applied Physics*, Vol. 114, No. 10, 2013, pp. –. doi:10.1063/1.4821018.

[126] Hirakawa, M. and Arakawa, Y., "Numerical simulation of plasma particle behavior in a Hall thruster," AIAA Paper 96-3195, Lake Buena Vista, FL, July 1996.

[127] Janes, G. S. and Lowder, R. S., "Anomalous Electron Diffusion and Ion Acceleration in a LowDensity Plasma," *Physics of Fluids (1958-1988)*, Vol. 9, No. 6, 1966, pp. 1115–1123. doi:10.1063/1.1761810.

[128] Yoshikawa, S. and Rose, D. J., "Anamalous Diffusion of a Plasma across a Magnetic Field," *Physics of Fluids*, Vol. 5, No. 3, March 1962, pp. 334–40.

[129] Hirakawa, M., "Electron Transport Mechanism in a Hall Thruster," IEPC 97-021, 1997.

[130] Ducrocq, A., Adam, J. C., Heron, A., and Laval, G., "High-frequency electron drift instability in the cross-field configuration of Hall thrusters," *Physics of Plasmas (1994-present)*, Vol. 13, No. 10, 2006. doi:10.1063/1.2359718.

[131] Parker, J. B., Raitses, Y., and Fisch, N. J., "Transition in electron transport in a cylindrical Hall thruster," *Applied Physics Letters*, Vol. 97, No. 9, 2010, pp. –. doi:10.1063/1.3486164.

[132] Boeuf, J.-P., "Rotating structures in low temperature magnetized plasmas - Insight from particle simulations," *Frontiers in Physics*, Vol. 2, No. 74, 2014. doi:10.3389/fphy.2014.00074.

[133] Brenning, N. and Lundin, D., "Alfvn's critical ionization velocity observed in high power impulse magnetron sputtering discharges," *Physics of Plasmas (1994-present)*, Vol. 19, No. 9, 2012, pp. –. doi:10.1063/1.4752073.

[134] Boyd, I. D., Van Gilder, D. B., and Liu, X., "Monte Carlo Simulation of Neutral Xenon Flows in Electric Propulsion Devices," *Journal of Propulsion and Power*, Vol. 14, No. 6, 1998, pp. 1009–1015.

[135] Smith, A. W. and Cappelli, M. A., "Time and space-correlated plasma potential measurements in the near field of a coaxial Hall plasma discharge," *Physics of Plasmas (1994-present)*, Vol. 16, No. 7, 2009, pp. –. doi:10.1063/1.3155097.

[136] Siddiqui, M. U., Kim, J. F., Jackson, C. D., and Hershkowitz, N., "Presheath and boundary effects on helicon discharge equilibria," *Plasma Sources Science and Technology*, Vol. 24, 2015, pp. 015022.

[137] Mikellides, I. G., Katz, I., Hofer, R. R., and Goebel, D. M., "Hall-Effect Thruster Simulations with 2-D Electron Transport and Hydrodynamic Ions," IEPC-2009-114, Ann Arbor, Michigan, September 2009.

[138] McDonald, M., *Electron Transport in Hall Thrusters*, Ph.D. thesis, University of Michigan, 2012.

[139] Ito, T. and Cappelli, M., "High Speed Images of Drift Waves and Turbulence in Magnetized Microplasmas," *Plasma Science, IEEE Transactions on*, Vol. 36, No. 4, Aug 2008, pp. 1228–1229. doi:10.1109/TPS.2008.927347.

[140] Frias, W., Smolyakov, A. I., Kaganovich, I. D., and Raitses, Y., "Long wavelength gradient drift instability in Hall plasma devices. II. Applications," *Physics of Plasmas (1994-present)*, Vol. 20, No. 5, 2013, pp. –. doi:10.1063/1.4804281.

[141] Boeuf, J. P. and Bhaskar, C., "Rotating Instability in Low-Temperature Magnetized Plasmas," *Phys. Rev. Lett.*, Vol. 111, No. 15, October 2013. doi:10.1103/PhysRevLett.111.155005.

[142] Iizuka, S., Saeki, K., Sato, N., and Hatta, Y., "Buneman Instability, Pierce Instability, and Double-Layer Formation in a Collisionless Plasma," *Phys. Rev. Lett.*, Vol. 43, No. 19, Nov 1979, pp. 1404–1407.

[143] Kruer, W. L., Dawson, J. M., and Sudan, R. N., "Trapped-Particle Instability," *Phys. Rev. Lett.*, Vol. 23, Oct 1969, pp. 838–841. doi:10.1103/PhysRevLett.23.838.

[144] Goldman, M. V., "Theory of Stability of Large Periodic Plasma Waves," *Physics of Fluids (1958-1988)*, Vol. 13, No. 5, 1970, pp. 1281–1289. doi:10.1063/1.1693061.

[145] Liu, C. S., "Instability of a large-amplitude plasma wave due to inverted trapped particle population." *Journal of Plasma Physics*, Vol. 8, 1972, pp. pp 169–174. doi:10.1017/S0022377800007054.

[146] Sun, Q. and Boyd, I. D., "Evaluation of Macroscopic Properties in the Direct Simulation Monte Carlo Method," *Journal of Thermophysics and Heat Transfer*, Vol. 19, No. 19, July 2005, pp. 329–335.

[147] Dragnea, H., Boyd, I., Lee, B., and Yalin, A., "Characterization of Eroded Boron Atoms in the Plume of a Hall Thruster," *Plasma Science, IEEE Transactions on*, Vol. 43, No. 1, Jan 2015, pp. 35–44. doi:10.1109/TPS.2014.2320851.

[148] Scharfe, M. K., Thomas, C. A., Scharfe, D. B., Gascon, N., Cappelli, M. A., and Fernandez, E., "Shear-Based Model for Electron Transport in Hybrid Hall Thruster Simulations," *IEEE Transactions on Plasma Science*, Vol. 36, No. 5, October 2008, pp. 2058–2068.